Politechnika Wrocławska

FIELD OF SCIENCE: ENGINEERING AND TECHNOLOGY

DISCIPLINE OF SCIENCE: MECHANICAL ENGINEERING

DOCTORAL DISSERTATION

Balancing of slider-crank and Scotch-yoke mechanisms by the use of mechanical resonance.

mgr inż. Willy Prastiyo

Supervisor:
prof. dr hab. inż. Wiesław Fiebig

Keywords: slider-crank, Scotch-yoke, mechanism, linkage, resonance, dynamics, balancing

WROCŁAW 2026

Statements of Originality

I hereby declare that this dissertation is my own original work and has been written independently. The research presented herein has not been submitted, in whole or in part, for the award of any other degree or qualification at this or any other institution.

All sources of information, data, figures, and ideas that are not my own have been appropriately acknowledged through proper citation and referencing. Any previously published material included in this dissertation is clearly identified and used with due permission where required.

The original contributions of this dissertation include the synthesis, analysis, and experimental validation of resonance-based slider-crank and Scotch-yoke mechanisms aimed at reducing input torque fluctuations, joint reaction forces, and shaking forces and moments. The work further provides systematic investigation of the influence of system parameters—including reciprocating mass, spring stiffness, friction, gravity, and externally applied forces—on the dynamic performance of these mechanisms. The numerical models, experimental setups, and analyses presented were developed and executed by the author unless otherwise stated.

I confirm that this dissertation complies with the regulations governing research integrity and originality at Wrocław University of Science and Technology.

Acknowledgements

I would like to express my sincere gratitude to my supervisor for his guidance, expertise, and continuous support throughout the course of this research. His insightful discussions, constructive feedback, and encouragement were invaluable to the successful completion of this dissertation.

I would like to acknowledge the technical and administrative staff of the laboratory and department for their assistance during the experimental phase of this study, particularly in the design, fabrication, and testing of the physical prototypes. Their support was essential to the successful execution of the experimental investigations.

My appreciation also extends to my colleagues and fellow researchers for their discussions, collaboration, and collegial environment, which made the research process both productive and intellectually stimulating.

Finally, I would like to thank my family for their unwavering support, patience, and encouragement throughout my doctoral studies. Their understanding and motivation played a crucial role in sustaining me through the challenges of this work.

Abstract

Unbalanced inertia forces, moments, and torques in slider-crank and Scotch-yoke mechanisms negatively affects performance, causing stress, vibrations, and accelerated wear. This risks system reliability and durability which compromise overall energy efficiency. This dissertation presents the strategic application of mechanical resonance as a solution to mitigate these drawbacks. Modelling and investigations are carried out using multibody simulations involving both rigid and flexible bodies. The scope covers the detrimental effects of unbalanced forces, moments, and torques, the potential benefits of mechanical resonance, and an investigation of resonance utilization in diverse scenarios. Synthesis section defines the technique for generating resonance, achieving optimal reciprocating body positioning, gravity compensation, and configuring systems with multiple sliders. Analysis section highlights the impact of factors such as reciprocating body mass, spring element stiffness, damping, and external loads on resonance performance. Findings reveal substantially improved dynamics under resonance conditions for both mechanisms. In the absence of dissipative forces, resonance conditions in the slider-crank mechanism result in a significant reduction of up to 79.99% for peak joint reaction force, 76.74% for the RMS value, 81.6% for peak inertia torque, and 82.2% for RMS torque. Resonance in the Scotch-yoke mechanism entirely eliminates torque fluctuation due to the harmonic nature of slider motion, practically eliminating reaction forces at key kinematic pairs. Both mechanisms experience substantial reductions in strain energy under resonance—91.9% in peak and 94.5% in average for the slider-crank crank, and 99.1% in peak and 99.2% in average for the Scotch-yoke crank and connecting rod.

Keywords: slider-crank, Scotch-yoke, mechanism, linkage, resonance, dynamic, balancing.

Streszczenie

Niezrównoważone siły bezwładności, momenty oraz momenty skręcające w mechanizmach korbowo-suwakowych (slider-crank) oraz Scotch-yoke pogarszają ich działanie, powodując naprężenia, drgania i przyspieszone zużycie elementów, co prowadzi do obniżenia niezawodności, trwałości oraz ogólnej efektywności energetycznej układów. W rozprawie przedstawiono koncepcję wykorzystania rezonansu mechanicznego jako metody ograniczania tych niekorzystnych zjawisk. Modelowanie i badania przeprowadzono z wykorzystaniem symulacji układów wieloczłonowych obejmujących zarówno ciała sztywne, jak i podatne. Zakres pracy obejmuje analizę wpływu niezrównoważonych sił i momentów, ocenę potencjalnych korzyści wynikających z wykorzystania rezonansu mechanicznego oraz badanie możliwości jego zastosowania w różnych konfiguracjach układów. W rozdziale drugim, dotyczącym syntezy, przedstawiono metodę generowania rezonansu, wyznaczania optymalnego położenia elementu wykonującego ruch posuwisto-zwrotny, kompensacji sił grawitacyjnych oraz konfiguracji układów z wieloma elementami wykonującymi ruch posuwisto-zwrotny. W rozdziale trzecim, dotyczącym analizy, określono wpływ masy elementu posuwisto-zwrotnego, sztywności elementu sprężystego, tłumienia oraz obciążeń zewnętrznych na charakterystyki rezonansowe układu. Uzyskane wyniki wskazują na znaczną poprawę właściwości dynamicznych obu mechanizmów przy wykorzystaniu zjawiska rezonansu. W mechanizmie korbowo-suwakowym, przy braku sił dyssypacyjnych, uzyskano redukcję maksymalnej dynamicznej siły reakcji w przegubie do 79,99%, jej wartości skutecznej (RMS) do 76,74%, maksymalnego momentu bezwładności do 81,6% oraz wartości skutecznej momentu do 82,2%. W mechanizmie Scotch-yoke rezonans eliminuje fluktuacje momentu dzięki harmonicznemu charakterowi ruchu suwaka, praktycznie usuwając siły reakcji w kluczowych parach kinematycznych. W obu mechanizmach odnotowano również istotne zmniejszenie energii odkształcenia w warunkach rezonansu — o 91,9% (maksymalnie) i 94,5% (średnio) dla korby mechanizmu korbowo-suwakowego oraz o 99,1% (maksymalnie) i 99,2% (średnio) dla korby i cięgna mechanizmu Scotch-yoke.

Słowa kluczowe: mechanizm korbowo-suwakowy, mechanizm Scotch-yoke, mechanizm, układ dźwigniowy, rezonans, dynamika, wyważanie.

Contents

Nomenclature

General Variables and Functions

Symbol	Description	Unit
t	Time	s
$x(t)$	Translational displacement	m
$\dot{x}(t), \ddot{x}(t)$	Velocity and acceleration	$m \cdot s^{-1}$, $m \cdot s^{-2}$
$y(t)$	Base or excitation displacement	m
$F(t)$	External excitation force	N
F_0	Force amplitude	N
ω	Excitation angular frequency	$rad \cdot s^{-1}$
ω_n	Natural angular frequency	$rad \cdot s^{-1}$
ζ	Damping ratio	–
ϕ	Phase angle	rad
X_0, Y_0	Steady-state displacement amplitudes	m
K	Static compliance (inverse stiffness)	$m \cdot N^{-1}$
k	Linear stiffness	$N \cdot m^{-1}$
c	Viscous damping coefficient	$N \cdot s \cdot m^{-1}$
m, m_0	Mass parameters	kg

Kinematics

Symbol	Description	Unit
α	Crank angle	rad
$\dot{\alpha}, \ddot{\alpha}$	Angular velocity and acceleration	$rad \cdot s^{-1} rad \cdot s^{-2}$
β	Connecting rod angle	rad
l_1	Crank length	m
l_2	Connecting rod length	m
r_2	Offset distance	m
x_2	Connecting rod center-of-mass position	m
x_3	Slider center-of-mass position	m

Mass and Inertia Properties

Symbol	Description	Unit
m_2	Connecting rod mass	kg
m_3	Slider mass	kg
I_1	Crank moment of inertia	kg · m^{-2}
I_2	Connecting rod moment of inertia	kg · m^{-2}

Energies and Lagrangian Formulation

Symbol	Description	Unit
T	Kinetic energy	J
V	Potential energy	J
$\mathcal{L}$	Lagrangian	J
U	Strain energy	J
q	Generalized coordinate vector	–
ξ	Generalized coordinates	–
Φ	Constraint equations	–
Φ_q	Constraint Jacobian	–
λ	Lagrange multipliers	N

Forces, Torques, and Power

Symbol	Description	Unit
$\tau(\alpha)$	Input torque as a function of crank angle	N · m
$\tau_{\text{in}}(t)$	Time-dependent input torque	N · m
$\omega(t)$	Instantaneous angular velocity	rad · s^{-1}
$P(t)$	Instantaneous mechanical power	W
$\bar{P}$	Mean power over one cycle	W
$P_{\text{in}}(\alpha)$	Input power as a function of crank angle	W
$P_{\text{eff}}(\alpha)$	Effective (positive) input power	W
W	Work done per cycle	J
RMS	Root-mean-square value	–

Joint Forces and Constraints

Symbol	Description	Unit
$\boldsymbol{F}_{joint}$	Joint reaction force vector	N
λ_1, λ_2	Constraint force components	N

Gravity Compensation

Symbol	Description	Unit
m_t	Total reciprocating mass	kg
g	Gravitational acceleration	m · s^{-2}
θ	Mechanism orientation angle	rad
F_p	Spring preload force	N
x_p	Spring preload displacement	m

Electric Motor Model

Symbol	Description	Unit
I_a	Armature current	A
R_a	Armature resistance	Ω
E_s	Supply voltage	V
E_b	Back electromotive force	V
K	Motor torque constant	N · m · A^{-1}
z	Number of conductors	–
p	Number of pole pairs	–
a	Number of parallel paths	–
n	Rotational speed	rpm
ϕ	Magnetic flux per pole	Wb

Fluid and Pneumatic System Parameters

Symbol	Description	Unit
s	Instantaneous chamber length	m
x_0	Reference position	m
V	Chamber volume	m^3
d_p	Piston diameter	m
d_r	Rod diameter	m
F_l	Force acting towards the connecting	N
p	Pressure	Pa
p_1, p_2	Inlet and outlet pressures	Pa
p_c	Cracking pressure	Pa
p_{max}	Valve maximum opening pressure	Pa
Δp	Valve net opening pressure	Pa
o_v	Static fractional valve opening	–
$\dot{m}_d$	Mass flow rate	kg · s^{-1}
G	Relief valve mass flow rate pressure gradient	kg · s^{-1} · Pa^{-1}
R	Specific gas constant	J · kg^{-1} · K^{-1}

T	Absolute temperature	K

Electrical Power Measurement

Symbol	Description	Unit
$u(t)$	Instantaneous voltage	V
$i(t)$	Instantaneous current	A
P	Average electrical power	W

Chapter 1

Introduction

1.1. Background

The slider-crank and Scotch-yoke mechanisms, illustrated in Figure 1.1, are widely utilized in mechanical systems for converting rotational motion to translational motion, and vice versa. These mechanisms serve as core components in numerous applications, including internal combustion engines, compressors, and various forms of industrial machinery. Despite their broad utility and functional versatility, they exhibit inherent dynamic drawbacks, most notably unbalanced inertia forces, moment fluctuations due to mass distribution, and inertia-induced torques [1, 2]. These dynamic shortcomings are primarily attributed to the behavior

(a) Slider-crank mechanism.

(b) Scotch-yoke mechanism.

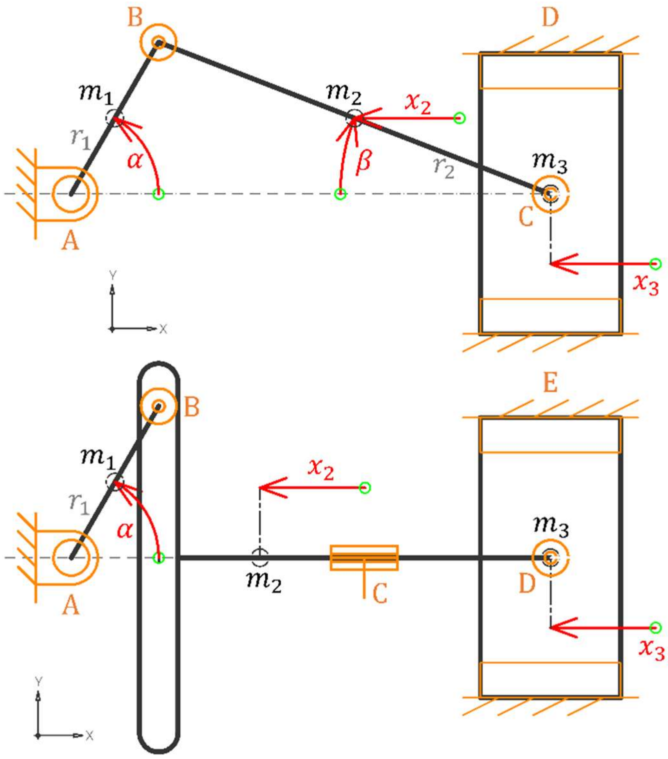

Figure 1.1. Conventional slider-crank (a) and Scotch-yoke (b) mechanism.

of reciprocating components, which experience continuous acceleration and deceleration throughout each motion cycle. As a result, they produce significant fluctuations in the inertia torque—also referred to as the input torque—required to maintain a constant angular velocity. Additionally, the oscillatory nature of these forces imposes variable reaction loads on the joints, which may compromise mechanical stability, operational efficiency, and component longevity.

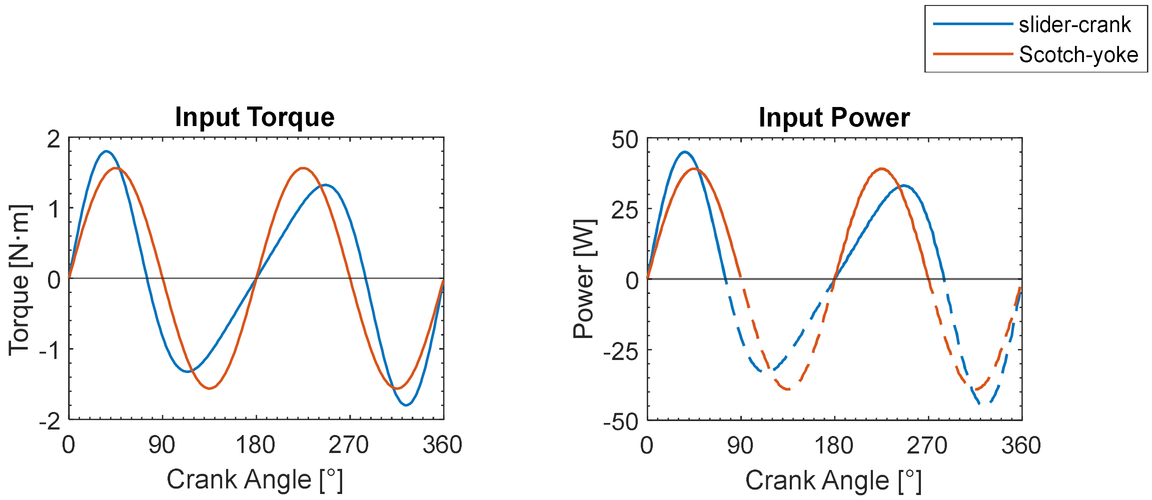

Figure 1.2. Example of typical input torque and input power in one cycle of the slider-crank and Scotch-yoke mechanism at certain constant angular velocity. Simulations are done without involving friction and externally applied and gravitational forces.

In the conversion of rotational motion to translational motion, the input torque required to maintain a constant angular velocity undergoes fluctuations, as illustrated in Figure 1.2. These variations originate from the inertial dynamics of the reciprocating components—primarily the connecting rod (m_2) and slider (m_3)—which experience alternating phases of acceleration and deceleration as they move between the top and bottom dead centers and the midpoint of the stroke. During acceleration, input torque is required to overcome the inertial resistance of the moving masses. Conversely, during deceleration, the input torque demand decreases as the kinetic energy of the reciprocating components is reduced. This cyclical behavior of torque results in corresponding fluctuations in instantaneous power demand on the driving source. Notably, the negative power that occurs during deceleration phases is typically not recovered by the driver and is instead dissipated through various forms of energy loss, thereby reducing the overall energy efficiency of the system.

The variability of the inertia load not only leads to fluctuations in the inertia torque transmitted to the driver and in the reaction forces at the joints—as illustrated in Figure 1.3—but also induces significant shaking forces and shaking moments on the frame or supporting structure [3]. The shaking forces, defined as the unbalanced dynamic forces transmitted from the mechanism to its frame, are shown in Figure 1.3 (SC & SY Joint A). These forces arise due to mass imbalances associated with the reciprocating components and can propagate vibratory disturbances throughout the mechanical system.

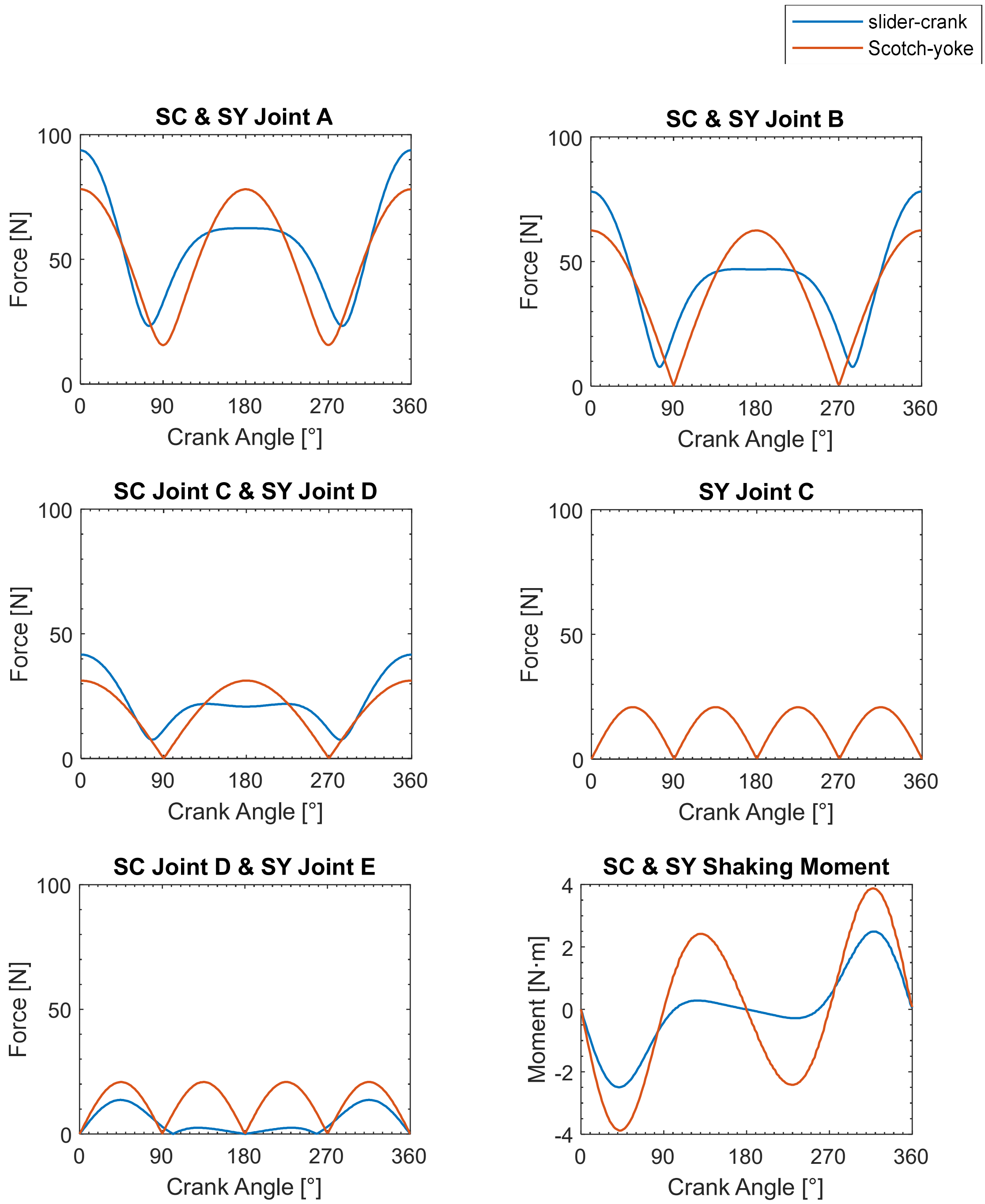

Figure 1.3. Example of typical reaction forces magnitude on the joints of the slider-crank (SC) and Scotch-yoke (SY) mechanisms in one cycle. Simulations are done without involving friction and externally applied and gravitational forces.

In addition, shaking moments—depicted in Figure 1.3 (SC & SY Shaking Moment)—are primarily caused by lateral (Y-axis) forces at the slider–ground interface. When these lateral forces are combined with the spatial offset between the slider–connecting rod and crank–ground pivot points, a moment about the frame is generated. These shaking moments can lead to torsional oscillations and localized stress concentrations in the structure, ultimately compromising its mechanical stability and fatigue life. Collectively, the interplay of fluctuating inertia torque, variable joint reaction forces, and the presence of shaking forces and moments results in a complex dynamic response, which can detrimentally impact the performance, precision, and durability of the mechanism.

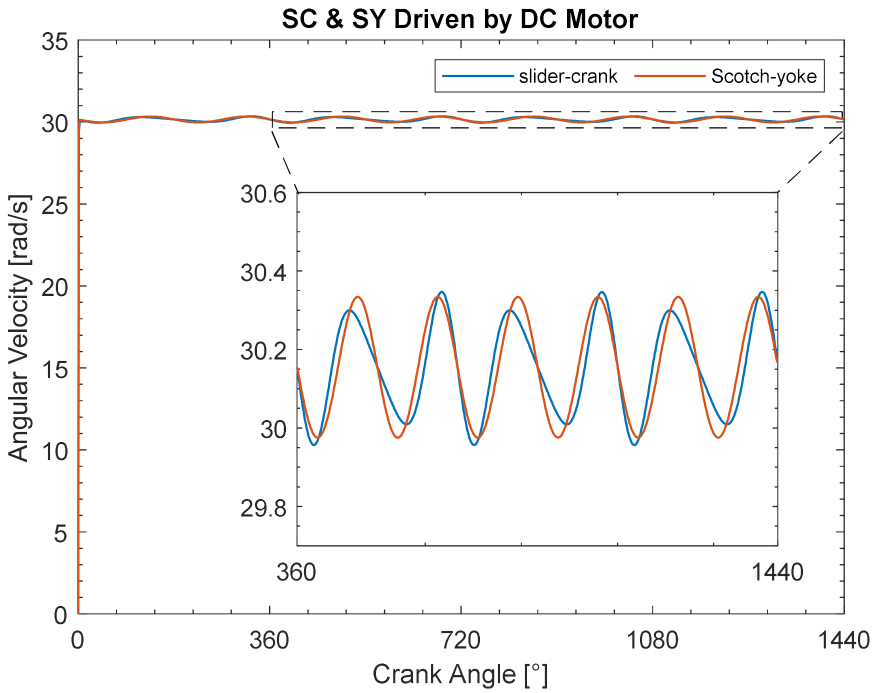

Figure 1.4. Example of the crank angular velocity of the conventional slider-crank and Scotch-yoke mechanism driven by the DC motor. Simulations are done without involving friction and externally applied and gravitational forces.

The presence of unbalanced forces, moments, and torques in these reciprocating machines can lead to several negative consequences that affect various aspects of their operation [4]. Significant variations in inertia torque can result in speed fluctuations of the driving unit [5, 6] and may induce torsional vibrations within the drivetrain [7]. This phenomenon is exemplified in Figure 1.4, which presents representative cases of slider-crank and Scotch-yoke mechanisms driven by a DC motor, a source of constant torque. In applications that demand high-precision motion, such torque irregularities can introduce undesirable kinematic disturbances due to time-varying loads imposed on the motor shaft [8]. Moreover, these torque fluctuations can amplify frictional interactions at sliding interfaces or contact points, leading to increased surface wear, elevated thermal loads, and additional energy dissipation losses [9]. The cyclic nature of the unbalanced inertia forces and torques also subjects mechanical components to time-varying stress amplitudes, which can accelerate fatigue damage and contribute to premature mechanical failure [10]. In practical applications, the requirement to overcome such torque fluctuations necessitates higher mechanical power input from the driver, thereby influencing actuator selection, increasing energy consumption, and elevating overall operational costs [11, 12, 13].

1.2. Literature Review

Balancing is the process of correcting or eliminating unwanted inertia forces and/or moments in rotating and reciprocating machinery [14, 15, 16]. Its origins can be traced back to early mechanical systems where counterweights were employed to compensate gravitational forces. As machinery evolved—particularly with the advent of steam engines and internal combustion engines in the late 19th and early 20th centuries—the focus shifted toward mitigating dynamic effects caused by high-speed reciprocating components [17, 18]. The need for smooth operation, reduced vibrations, and extended component life made mechanism balancing a central challenge in mechanical engineering.

One of the first formalized systematic approaches was introduced by Fischer in 1902 [19], who developed the principal vector method, locating "principal points" on mechanism links to define conditions for static balancing. Goryachkin [20] and Yudin [21] expanded on this method, while practical applications like the Lanchester balancer [22] employed counter-rotating shafts to balance inertia forces in automotive engines.

Mid-century research focused heavily on static mass substitution, in which distributed masses were replaced by concentrated point masses to simplify balancing. Crossley [23], Maxwell [24], and Smith [25] made notable advances in transforming dynamic balancing problems into equivalent rotating link problems. Hilpert [26] proposed pantograph mechanisms for balancing with minimal additional mass, while Kamenskii [27] explored cam-based solutions for continuous center-of-mass adjustment. In parallel, terminology evolved—what was once called “static balancing” became more precisely termed shaking force balancing to avoid confusion with overall dynamic balancing, which also addresses shaking moments (Berkof and Lowen [28]). Around the same time, linearly independent vector methods were introduced to decouple equations of motion, enabling simultaneous force and moment cancellation. Bagci [29] later expanded this concept into practical rotary balancer designs using idler parallelogram loops.

The 1980s marked the integration of computational techniques and flexible-body considerations. Kineto-elastodynamic balancing developed to account for link flexibility and its influence on vibration response [30, 31]. Spatial (3D) balancing methods [32] extended planar theories to more complex motion paths. Dynamic mass substitution, first explored in the 1970s, was further developed by Esat and Bahai [33] for complete force and moment cancellation. In the 1990s, optimization-based methods gained importance. Techniques such as least-squares minimization, Chebyshev approximation, and nonlinear programming [34] were applied to refine mass distribution and linkage parameters. Bagci's Completely Dynamically Equivalent Link (CDEL) concept [35, 36, 37] allowed the balancing of shaking forces, moments, and torque in multi-cylinder engines without harmonic balancers by holding each slider–crank loop's center of mass stationary.

Arakelian [38] provided a comprehensive historical and theoretical framework for mechanism balancing, formalizing the distinction between shaking force and shaking moment cancellation. The 2000s saw specialized adaptations for reciprocating machinery, notably slider–crank mechanisms. These are widely used in engines, and industrial machines but suffer from inherent unbalanced reciprocating motion. Conventional counterweight methods [39] remained the baseline solution but could not fully suppress unbalanced dynamics under varying load conditions. To address torque irregularities, Demeulenaere and De Schutter [40, 41, 42, 43] developed Cam-Based Centrifugal Pendulums (CBCP) and the Inverted Cam Mechanism (ICM), solving nonlinear cam design equations through optimization and Fourier analysis. Similar strategies by Wu and Angeles [44] and Tsay et al. [45] employed cam–spring systems and rational B-splines to reduce periodic torque fluctuations. During this period, Briot et al. [46, 47] applied optimal center-of-mass control in manipulators and integrated Scott–Russell linkages for full balancing without heavy counterweights.

From 2010 onward, research on slider–crank balancing diversified into passive mechanical solutions, active control methods, and optimization-based synthesis. Arakelian and Briot [48] introduced cam–spring mechanisms that balanced shaking forces while compensating input torque fluctuations. Later adaptations included dual-spring and pantograph-assisted systems [49, 50, 51], reducing RMS inertia forces without adding significant complexity. Active solutions, such as Sun and Yao's [52] servomotor-driven differential gear train, used control algorithms to cancel torque oscillations. Zi-Ming et al. [13] combined Fourier-based modeling with secondary balancing devices to reduce RMS torque by 22.7% and energy consumption by 6.54%. Chaudhary and Chaudhary [53, 54] used genetic algorithms and two-stage optimization (mass redistribution followed by link shape synthesis with cubic B-splines) to balance shaking forces and moments while optimizing transmission characteristics. Groza and Antonya [55, 56] proposed progressive spring-based methods targeting specific components of motion, while Moussafir and Arakelian [57] demonstrated single-cam devices for simultaneous force and torque balancing. Etesami et al. [58] addressed the effects of joint clearances using a bi-objective optimization framework to improve both balance and transmission angle, while Frantz et al. [59] applied Davies' method for systematic mass distribution optimization. In large-scale applications, Levecque et al. [60] developed a high-fidelity finite element model for reciprocating compressors, integrating experimental modal analysis with the Influence Coefficient Method for optimal balancing masses—demonstrating significant improvements over rotor-only balancing.

The Scotch-yoke mechanism, with its sinusoidal displacement profile, provides uniform slider velocity characteristics than the slider–crank but still generates significant inertial forces. Arakelian et al. [2, 61] introduced linear spring balancers to stabilize input torque without auxiliary linkages, reducing friction-induced wear. Kwon et al. [62] used curved cranks and coil springs in robotic fish propulsion for balanced torque distribution. Lee et al. [63] proposed the Rolling Scotch-Yoke Mechanism (RSYM), replacing sliding with rolling contact for friction reduction and oil-free operation. Advanced torque-balancing approaches include Funk and Han's [64] cam–spring systems and Yao and Yan's [65] non-circular gear drives. Shieh and Chou [66] introduced gear-pair spring balancers for gravitational compensation, while Nguyen and Shieh [67] extended such concepts to spatial articulated mechanisms.

Despite significant advances, the literature consistently notes trade-offs in added mass, complexity, and operational adaptability. Kochev [68] warned that full balancing may increase mechanism mass by factors of two to seven, potentially negating performance benefits. As a result, recent research emphasizes lightweight balancing strategies, and real-time adaptive control. Arising directions include integrated computational modeling (Ni et al., [69]), adaptive self-adjusting mechanisms (de Jong et al., [70]), and machine learning for real-time balancing in variable operating conditions. Finally, a chronological summary of the key contributions to mechanism balancing, with particular emphasis on slider–crank and Scotch-yoke systems as well as related topics such as input torque control, shaking force reduction, and shaking moment elimination, is presented in Table 1.1. This table consolidates more than a century of research progress, ranging from the earliest theoretical developments and static balancing techniques to modern optimization-based, adaptive, and mechanism-specific solutions.

Table 1.1. Structured literature summary table, organized chronologically by publication year and grouped by thematic focus.

Year	Author(s)	Mechanism / Focus	Key Contribution
1902	Fischer [19]	General planar mechanisms	Principal vector method for static balancing via principal points on links.
1914	Goryachkin [20]	General planar mechanisms	Extended principal vector method for broader balancing applications.
1914	Lanchester [22]	Engines	Counter-rotating shaft balancer for inertia force reduction.
1941	Yudin [21]	General planar mechanisms	Further refinement of principal vector method.
1954	Crossley [23]	General planar mechanisms	Static mass substitution for balancing.
1960	Maxwell [24]	General planar mechanisms	Formalized static mass substitution methods.

1967	Smith [25]	Four-bar linkage	Expanded point-mass substitution approaches.
1968	Kamenskii [27]	Four-bar linkage	Cam-based balancing for continuous center-of-mass adjustment.
1968	Hilpert [26]	General planar mechanisms	Pantograph mechanisms for shaking force compensation.
1969	Berkof & Lowen [28]	General planar mechanisms	Linearly independent vectors method for simultaneous force/moment cancellation.
1973	Berkof [71]	Inline four-bar linkage	Dynamic mass substitution for balancing.
1979	Berkof [17]	Historical/mechanical	Early historical perspective on balancing evolution.
1982	Bagci [29]	General planar mechanisms	Idler parallelogram loops to achieve shaking force/moment balance.
1986	Zobairi [30,31]	General planar mechanisms	Contribution of the kineto-elastodynamic inertia forces towards the shaking force and shaking moment while balancing planar mechanisms.
1987	Yu [32]	Spatial mechanisms	Extended balancing methods to 3D mechanisms.
1989	Liu & Huang [72]	Seven-bar linkage	Method of integration and elimination (MIE) on balancing input torques.
1991	Qi & Pennestrí [34]	Optimization methods	Applied least-squares, Chebyshev approximation, nonlinear programming to balancing.
1992	Bagci [35]	Various mechanisms	Completely Dynamically Equivalent Link (CDEL) concept for mechanism balancing.
1995	Bagci [36,37]	Engines	Eliminated shaking force, moment, and torque in multi- and single-cylinder engines without harmonic balancers.
1999	Esat & Bahai [33]	General planar mechanisms	Geared inertia counterweights as well as force counterweights for balancing.
2000	Arakelian [38]	General	Historical and theoretical framework; clarified static vs dynamic balancing terms.
2000	Kochev [68]	General planar mechanisms	Highlighted mass drawbacks of full balancing (up to $\times 7$ mass increase).
2001	Wu & Angeles [44]	Cam-based	Cam-spring mechanism to cancel periodic loads.
2002	Tsay et al. [45]	Cam-based	Used rational B-splines to reduce vibrations in globoidal cams.
2003	Yao & Yan [65]	Gear-based	Non-circular gear drives for balancing torque fluctuation.
2004	Demeulenaere & De Schutter [40]	Cam-based	Inverted cam mechanism with Fourier synthesis and optimization.

2005	Demeulenaere et al. [41,42]	Cam-based	Introduced Cam-Based Centrifugal Pendulum (CBCP); optimized via least-squares and Sequential Quadratic Programming (SQP).
2006	Arakelian [49]	Slider-crank	Dual-spring and pantograph-based balancing to reduce RMS inertia forces.
2007	Van Khang & Phong Dien [73]	Spatial mechanisms	Derived algebraic balancing conditions compatible with CAS tools.
2007	Chaudhary & Saha [74]	Four-bar linkage	Maximum recursive dynamic algorithm for the evaluation of the bearing forces.
2008	Demeulenaere et al. [43]	CBCP	Experimental validation in weaving looms for speed fluctuation reduction.
2009	Briot et al. [46]	Planar parallel manipulators	Integrated Scott-Russell linkages for full balance with fewer counter-rotations.
2009	Wijk et al. [75]	Double pendulum	Comparison of the existing balancing principles regarding the addition of mass and the addition of inertia.
2010	Arakelian & Briot [48]	Slider-crank	Cam–spring balancing for force and torque compensation.
2011	Sun & Yao [52]	Active control	Servomotor-driven differential gear train for torque cancellation.
2011	Levecque et al. [60]	Compressors	High-fidelity FE model with Influence Coefficient Method for optimal balancing.
2012	Briot et al. [47]	High-speed manipulators	Optimal center-of-mass control for shaking force reduction without counterweights.
2012	Erkaya & Uzmay [76]	Slider-crank	Studied balancing under joint clearance conditions.
2013	Arakelian et al. [77]	Slider-crank	Optimal crank motion control for ~35% shaking force reduction.
2013	Nehemiah et al. [39]	Slider-crank	Review of counterweight-based balancing methods.
2014	Chaudhary & Chaudhary [53]	Slider-crank	GA-based mass redistribution for shaking force/moment minimization.
2014	Lee et al. [63]	Scotch-yoke	Rolling Scotch-Yoke mechanism for friction reduction and oil-free operation.
2014	Ni et al. [69]	Computational modeling	Integrated computational modeling for balancing design.
2015	Zi-Ming et al. [13]	Slider-crank	Fourier-based modeling with secondary balancing device; torque reduction 22.7%.
2015	Arakelian et al. [2,61]	Scotch-yoke	Linear spring balancers for torque stabilization without auxiliary linkages.
2015	Shieh & Chou [66]	Gear-spring	Full gravitational balance using gear-pair spring balancer.
2015	Chaudhary & Chaudhary [54]	Slider-crank	Two-stage optimization: equimomental systems and cubic B-spline link shape synthesis.

2016	Groza & Antonya [55]	Slider-crank	Progressive spring-based method for separate balancing of piston and crank motion.
2016	Arakelian et al. [2]	Scotch-yoke	Extended linear spring balancer designs for torque stabilization.
2018	Kwon et al. [62]	Scotch-yoke	Curved crank and coil spring design for balanced torque in robotic propulsion.
2018	Frantz et al. [59]	Slider-crank	Used Davies' method for systematic mass distribution optimization.
2018	de Jong et al. [70]	General planar mechanisms	Developed self-adjusting balancing mechanisms.
2019	Nguyen & Shieh [67]	Scotch-yoke	Spatial gravitational balancing in articulated mechanisms.
2019	Destradi [78]	Slider-crank	Modern applications of Lanchester balancers.
2020	Moussafir & Arakelian [57]	Slider-crank	Single-cam device for simultaneous force and torque compensation.
2021	Etesami et al. [58]	Slider-crank	Clearance-inclusive dynamic model with bi-objective optimization.
2021	Funk & Han [64]	Cam-spring	Cam–spring system for torque balancing in various mechanisms.
2021	Arakelian [79]	Slider-crank	Coupled slider–crank systems with inertia-canceling springs for shaking force reduction.
2022	Buśkiewicz [80]	Spring-linkage	Energy-based discrete torque balancing using symbolic solution.
2024	Arakelian [50,51]	Slider-crank	Pantograph-based and optimized crank-motion balancing for inertia reduction.
2025	Groza & Antonya [56]	Slider-crank	Progressive spring method refinement for piston/crank separation in force balancing.
2025	Albaghdadi et al. [81]	Crank-rocker	Duplicated configuration with counterweights to reduce shaking force and moment.
2025	Prastiyo & Fiebig [87]	Slider-crank & Scotch-yoke	Input torque and shaking force/moment balancing using mechanical resonance.

1.3. Scope and Contribution

A fundamental strategy for enhancing the dynamic performance of mechanical systems involves minimizing the load imposed on the driving unit. In practical implementations, this objective is pursued through load reduction techniques and mechanism balancing methodologies. The primary aim of dynamic balancing is to reduce or eliminate time-varying forces and moments that arise due to inertial effects and induce vibratory responses within the system [82]. A mechanism is deemed dynamically balanced when the resultant inertial force vector and the net moment about the center of mass remain constant (or ideally zero) throughout the entire motion cycle of its components. Achieving such a balanced condition significantly reduces internal frictional forces at the kinematic pairs, thereby enhancing the mechanism's operational lifespan, reliability, and drive efficiency—all without compromising motion stability or positional accuracy.

Although extensive research has been devoted to the dynamic balancing of mechanisms—spanning conventional counterweight strategies to contemporary active and optimization-driven techniques—a notable gap persists in the systematic exploitation of mechanical resonance within this domain. The prevailing body of literature largely treats mechanical resonance as a detrimental phenomenon, focusing on its suppression or avoidance through damping or frequency detuning strategies. Conventional balancing approaches primarily emphasize mass redistribution, the incorporation of counter-rotating components, or the introduction of auxiliary balancing linkages. However, to date, no studies have rigorously investigated the potential of leveraging resonance phenomena as a passive means of mitigating shaking forces and inertia-induced torque fluctuations.

For instance, Arakelian's cam-spring balancing mechanisms [48, 57] and Groza's progressive spring-based designs [55] achieve partial dynamic equilibrium but require substantial auxiliary mechanical components, which introduce added mass, structural complexity, and potential reliability concerns. Arakelian [51] also stated that resonance is considered a phenomenon to be mitigated due to its potential to amplify oscillations and degrade performance in a mechanical system with reciprocating motion. Similarly, active balancing systems—such as the servomotor-based compensatory mechanisms proposed by Sun and Yao [52, 84]—offer high precision and adaptability but are often limited by increased energy consumption, control complexity, and elevated system cost. Optimization-based methodologies, including those utilizing genetic algorithms [53, 85, 86], have demonstrated efficacy in minimizing shaking forces and moments; however, they predominantly rely on computational parameter tuning rather than engaging with the system's inherent dynamic characteristics. Importantly, none of the aforementioned methods exploit on mechanical resonance as a beneficial dynamic effect—one that, if properly harnessed, could enable passive and energy-efficient balancing solutions with reduced mechanical complexity.

This dissertation introduces a novel concept in mechanism balancing by formulating a generalized framework that deliberately harnesses mechanical resonance within slider-crank and Scotch-yoke mechanisms. Contrary to the conventional engineering perspective, in which resonance is typically regarded as a destabilizing phenomenon to be avoided, this work demonstrates that, under appropriately controlled conditions, resonance can be transformed into a constructive dynamic feature [83, 87, 88, 89]. By integrating strategically tuned elastic elements and synchronizing the kinematic profiles of the mechanism components, the system's natural frequencies are exploited to achieve passive dynamic balancing.

The central thesis underpinning this approach is that when reciprocating mechanisms operate in proximity to their resonant frequencies, the cyclic exchange of energy between kinetic and potential forms can be utilized to counteract the inertial forces and moments typically responsible for shaking effects. This insight represents a significant departure from traditional balancing strategies, which have predominantly neglected the potential benefits of resonance-driven dynamics. The proposed methodology offers a fundamentally new direction for the design of dynamically efficient mechanical systems, characterized by reduced vibrational loading, improved energy efficiency, and minimal additional structural complexity.

Mechanical resonance is conventionally regarded as an undesirable or even hazardous phenomenon in mechanical systems due to its association with excessive vibrations and potential structural failure. However, when approached with a rigorous and controlled methodology, resonance can be strategically harnessed to yield advantageous dynamic behavior. At resonance, the system facilitates an efficient and sustained exchange between kinetic and potential energy, enabling the reciprocating body to receive kinetic energy more effectively when its excitation frequency coincides with the system's natural frequency [90].

In this context, the deliberate utilization of resonance phenomena in slider-crank and Scotch-yoke mechanisms—through the implementation of properly tuned elastic elements and frequency-matched excitation—can facilitate optimal energy transfer from the rotational input to the translational output. When the excitation frequency is aligned with the natural frequency of the system, the dynamic response of the reciprocating mass becomes more favorable, thereby reducing the reactive forces and torque demands on the driver. This, in turn, offers the potential to improve the dynamic efficiency of the mechanism and reduce overall energy consumption, presenting a compelling alternative to existing balancing methods.

This study makes three principal contributions to the field of mechanism dynamics, particularly in the context of dynamic balancing. First, it establishes the theoretical foundations of resonance-based balancing by deriving the analytical conditions under which system parameters—specifically, spring stiffness, body mass, and excitation frequency—interrelate to generate dynamically stabilizing effects. Second, through comprehensive multibody dynamics simulations, the study demonstrates that the proposed resonance-driven approach achieves a significant level of vibration reduction compared to that of conventional models, while avoiding their inherent disadvantages, such as increased structural mass, added inertia, and mechanical complexity. Third, the practical feasibility of the method is validated through experimental implementation using physical prototypes and application scenarios. The empirical results confirm that resonance-based balancing can substantially reduce inertia forces, moments, and torque fluctuations, offering a practical pathway to enhanced energy efficiency relative to traditional active balancing techniques.

What fundamentally differentiates this work from existing balancing strategies is its novel paradigm for addressing the dynamic imbalance problem. Whereas conventional existing methods rely on the incorporation of abundant compensatory elements—such as counterweights, auxiliary linkages, or actively controlled systems [91]—this approach leverages the intrinsic dynamic behavior of the mechanism itself. By precisely tuning the system parameters to operate within a favorable resonant region, it becomes possible to achieve significant reductions in shaking forces, moments, and input torque fluctuations without incurring the disadvantages of added mass, increased inertia, or mechanical complexity typically associated with traditional solutions.

The practical significance of this resonance-based methodology is especially pronounced in high-speed applications where mass minimization and dynamic efficiency are dominant—for example, in precision actuators, lightweight machinery, and energy-sensitive systems. This approach not only simplifies the mechanical design but also opens new possibilities for passive balancing strategies that are inherently more scalable, energy-efficient, and suitable for modern engineering applications.

1.4. Outlines of the Dissertation

The remainder of this dissertation is structured as follows. Chapter 2, the *Synthesis* chapter, presents the foundational development of the resonance condition, the optimization of reciprocating body positioning, and strategies for gravity compensation across various configurations. Chapter 3, titled *Analysis*, evaluates the dynamic behavior of the proposed systems through a detailed examination of input torque profiles, joint reaction forces, internal body stresses, and the influence of key design parameters such as reciprocating mass, spring stiffness, damping coefficients, and externally applied forces.

Chapter 4 addresses *Experimental Validation*, offering practical validation of the theoretical framework through controlled physical experiments. Building on this, Chapter 5 presents real-world *Application Examples*, confirming the efficacy of the proposed balancing methodology through comprehensive measurements and applied testing. Finally, Chapter 6 provides a *Summary* of conclusions, key contributions, and suggestions for future research directions.

Chapter 2
Synthesis

2.1. Achieving Resonance Condition

In the dynamic analysis of vibratory systems, it is crucial to account for the different forms of excitation that can influence the response behavior of a single-degree-of-freedom (SDOF) spring-mass system [92]. Three principal categories of external excitation are commonly identified in the literature: external forcing, base excitation, and rotor excitation [93–96]. Each excitation type corresponds to a distinct physical mechanism frequently encountered in engineering systems. Understanding the distinctive characteristics and effects of these excitation modes is fundamental for modeling, predicting, and controlling the vibrational response of mechanical systems.

External forcing excitation represents a class of vibratory systems in which a time-dependent external force is applied directly to the mass element, as illustrated in Figure 2.1. This excitation model is commonly used to represent systems subjected to external dynamic loads, such as those encountered in machinery under periodic or transient loading conditions. In most analytical formulations, the excitation force is assumed to be harmonic in nature, enabling tractable mathematical modeling. It is typically expressed as Equation 2.1, where F_0 denotes the amplitude of the applied force, and ω is the excitation (angular) frequency.

$$F(t) = F_0 \sin(\omega t) \tag{2.1}$$

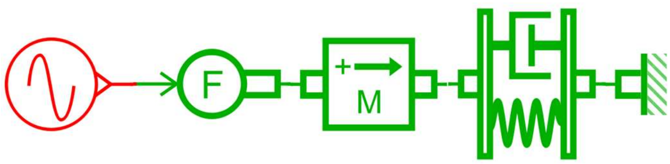

Figure 2.1. External forcing model.

The dynamic response of the system under external forced vibration is governed by the second-order linear differential equation of motion, expressed in Equation 2.2. This formulation incorporates the system's natural frequency ω_n, damping ratio ζ, and compliance K, which are defined in Equations 2.3, 2.4, and 2.5, respectively. In these expressions, m denotes the mass, k is the stiffness of the spring element, c is the damping coefficient, and $F(t)$ is the externally applied force.

$$\frac{1}{\omega_n^2}\frac{d^2x}{dt^2} + \frac{2\zeta}{\omega_n}\frac{dx}{dt} + x = KF(t) \tag{2.2}$$

$$\omega_n = \sqrt{\frac{k}{m}} \tag{2.3}$$

$$\zeta = \frac{c}{2\sqrt{km}} \tag{2.4}$$

$$K = \frac{1}{k} \tag{2.5}$$

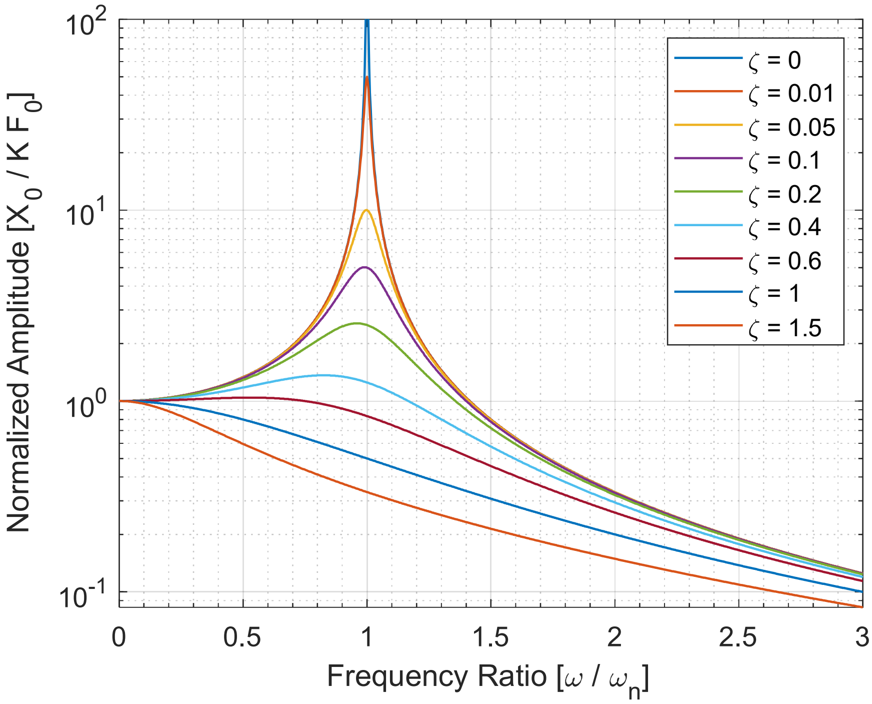

Figure 2.2. Amplitude of steady-state vibrations in a forced spring-mass system.

Under steady-state conditions, the displacement response $x(t)$ of the system to a harmonic excitation assumes the form given in Equation 2.6. This solution captures the sinusoidal nature of the response, where the phase angle ϕ between the excitation and the system response is defined by Equation 2.7, and the response amplitude X_0 is given by Equation 2.8. The amplitude-frequency response, as illustrated in Figure 2.2, shows a noticeable peak occurring near the natural frequency ω_n, indicating the resonance condition. At resonance, the system exhibits a significant amplification of its dynamic response, particularly when damping is low.

$$x(t) = X_0 \sin(\omega t + \phi) \tag{2.6}$$

$$\phi = \tan^{-1} \frac{-2\zeta\omega/\omega_n}{1 - \omega^2/\omega_n^2} \tag{2.7}$$

$$X_0 = \frac{KF_0}{\sqrt{(1 - \omega^2/\omega_n^2)^2 + (2\zeta\omega/\omega_n)^2}} \tag{2.8}$$

Secondly, *base excitation* refers to a dynamic scenario in which vibratory motion is induced by a prescribed displacement applied at the base of the spring-mass system, as depicted in Figure 2.3. The base displacement is typically modeled as a harmonic function expressed in Equation 2.9 where Y_0 is the amplitude of the imposed base motion and ω is the excitation frequency. The equation of motion for the system subjected to base excitation is given by Equation 2.10. In this case, the system parameters ω_n, ζ, and K retain the definitions established in Equations 2.3 and 2.4, with the compliance value K being set to 1 for base excitation cases.

$$y(t) = Y_0 \sin(\omega t) \tag{2.9}$$

$$\frac{1}{\omega_n^2}\frac{d^2x}{dt^2} + \frac{2\zeta}{\omega_n}\frac{dx}{dt} + x = K\left(y + \frac{2\zeta}{\omega_n}\frac{dy}{dt}\right) \tag{2.10}$$

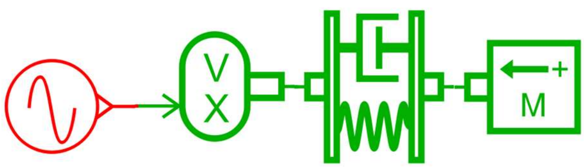

Figure 2.3. Base excitation model.

The system's steady-state response to base excitation also takes a sinusoidal form, as in Equation 2.6, but the phase angle ϕ and amplitude X_0 are determined by the expressions stated in Equation 2.11 and 2.12, respectively. The amplitude-frequency response for base excitation, illustrated in Figure 2.4, shows characteristics different from those of direct forcing. In particular, the system's response amplitude can peak below the natural frequency, especially in damped systems.

$$\phi = \tan^{-1} \frac{-2\zeta\omega^3/\omega_n^3}{1 - (1 - 4\zeta^2)\omega^2/\omega_n^2} \tag{2.11}$$

$$X_0 = \frac{KY_0\sqrt{1+(2\zeta\omega/\omega_n)^2}}{\sqrt{(1-\omega^2/\omega_n^2)^2+(2\zeta\omega/\omega_n)^2}} \tag{2.12}$$

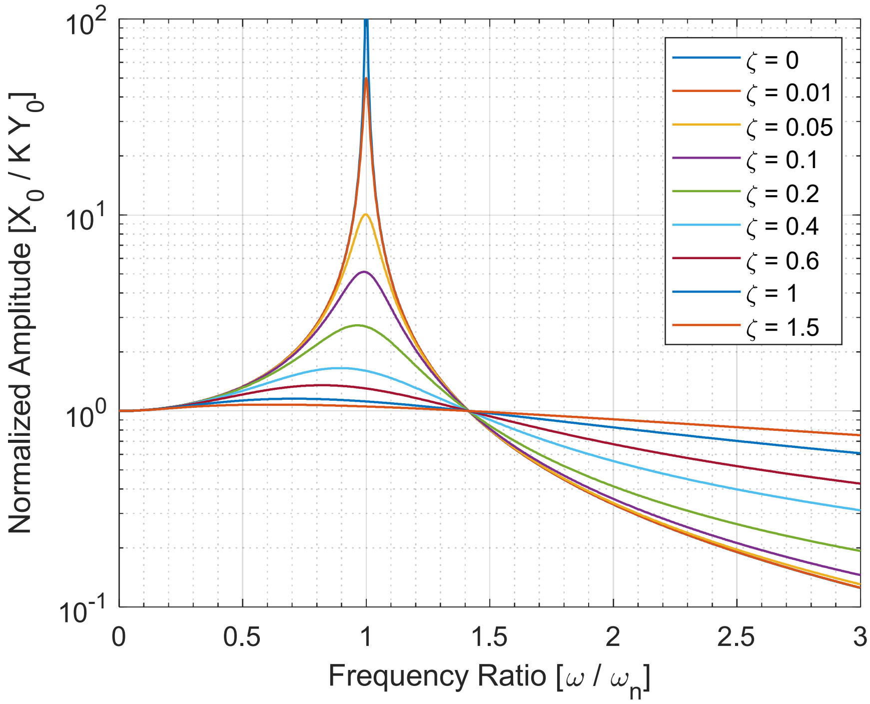

Figure 2.4. Amplitude of steady-state vibration in a spring-mass system excited at the base.

The third type of excitation—*rotor excitation*—models the dynamic response of a system subjected to periodic inertial forces generated by a rotating unbalanced mass, as illustrated in Figure 2.5. These forces arise due to the centrifugal effect of the mass imbalance, which produces a time-varying force component acting on the system. The excitation displacement of the unbalanced mass follows the same harmonic form introduced in Equation 2.9, with Y_0 representing the radius of rotation or the amplitude of the unbalanced mass trajectory.

The governing differential equation of motion for the system under rotor excitation is expressed as Equation 2.13 where the natural frequency of the combined mass system ω_n, the damping ratio ζ, and the compliance K representing the normalized influence of the unbalanced mass are defined in Equations 2.14, 2.15, and 2.16, respectively. Here, m denotes the primary mass, and m_0 is the rotating unbalanced mass contributing to the excitation.

$$\frac{1}{\omega_n^2}\frac{d^2x}{dt^2} + \frac{2\zeta}{\omega_n}\frac{dx}{dt} + x = -\frac{K}{\omega_n^2}\frac{d^2y}{dt^2} \tag{2.13}$$

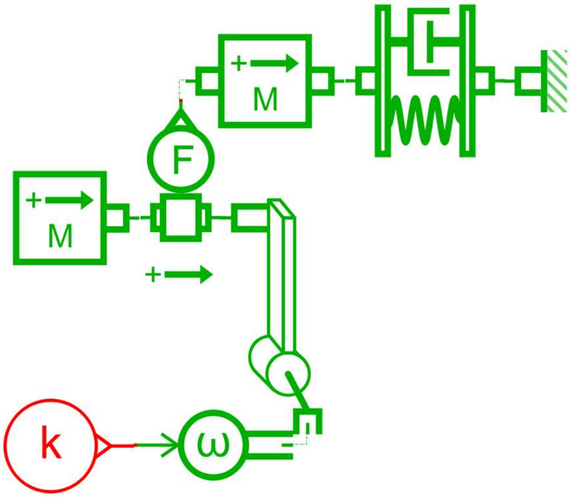

Figure 2.5. Rotor excitation model.

$$\omega_n = \sqrt{\frac{k}{(m+m_0)}} \tag{2.14}$$

$$\zeta = \frac{c}{2\sqrt{k(m+m_0)}} \tag{2.15}$$

$$K = \frac{m_0}{m+m_0} \tag{2.16}$$

$$X_0 = \frac{KY_0\omega^2/\omega_n^2}{\sqrt{(1-\omega^2/\omega_n^2)^2 + (2\zeta\omega/\omega_n)^2}} \tag{2.17}$$

Assuming a harmonic base displacement as stated in Equation 2.9, the inertial excitation force is proportional to the second derivative $\ddot{y}(t)$, resulting a forcing function consistent with periodic excitation at frequency ω. The steady-state displacement response $x(t)$ again follows the general sinusoidal form given in Equation 2.6, where the amplitude X_0 is given by Equation 2.17. The corresponding phase angle ϕ is determined as previously shown in Equation 2.7. The amplitude-frequency response is depicted in Figure 2.6. As expected, the response amplitude reaches a peak near the system's natural frequency ω_n, indicating resonance behavior.

Although real-world systems may encounter more complex excitation patterns, the three categories discussed—external forcing, base excitation, and rotor excitation—cover a broad spectrum of engineering applications and serve as the foundational models in vibration analysis. Each system's equations of motion reduce to a standard or well-known form when subjected to harmonic excitation. In all three scenarios, the excitation is assumed to be sinusoidal in time, and the system is considered to start from rest at its static equilibrium position.

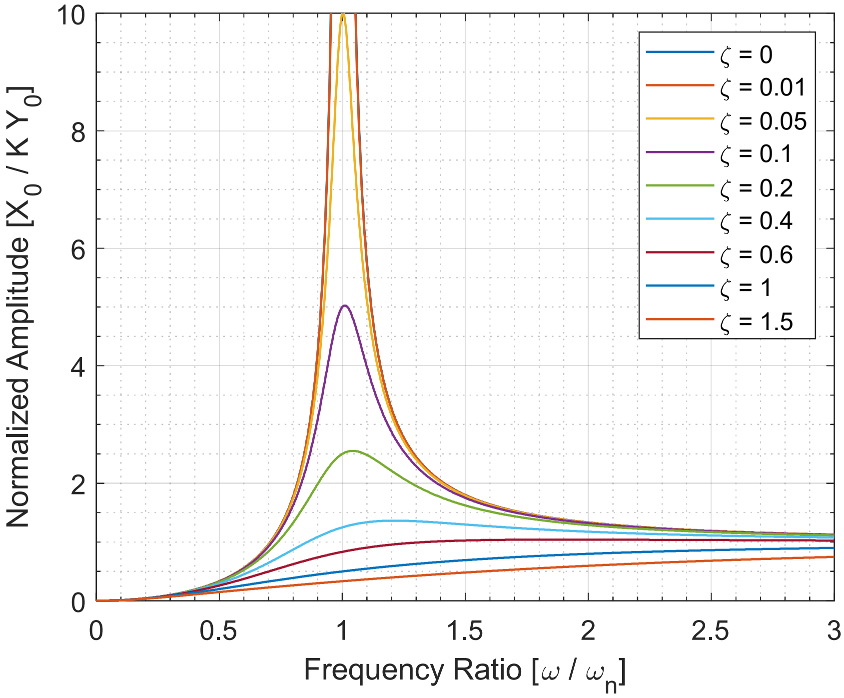

Figure 2.6. Amplitude of steady-state vibration in a spring-mass system excited by a rotor.

Consider a scenario where the system is initially displaced and released, resulting in free vibration at its natural frequency ω_n. If a harmonic external force is subsequently applied such that it is exactly in phase (i.e., zero phase difference) with the displacement of the oscillating mass, the resulting dynamics present a particular case regarding energy transfer in forced vibration.

Let the external force be defined as Equation 2.1 while the displacement of the mass as Equation 2.18; the external force and the displacement are synchronized in phase.

$$x(t) = X\sin(\omega_n t) \tag{2.18}$$

Mechanical power transfer is governed by the phase relationship between the external force and the velocity of the mass. Taking the time derivative of the displacement yields the velocity as expressed in Equation 2.19. This shows that the velocity is phase-shifted by 90 degrees with respect to both the displacement and the applied force.

$$\dot{x}(t) = \frac{d}{dt}x(t) = \omega_n X\cos(\omega_n t) \tag{2.19}$$

The instantaneous power delivered to the system by the external force is given by the product of force and velocity, stated in Equation 2.20. The power function oscillates sinusoidally about zero, indicating that energy is alternately transferred and returned during each half-cycle of motion. The average power input over a complete cycle is expressed in Equation 2.21 where $T = \frac{2\pi}{\omega_n}$ is the natural period of oscillation.

$$P(t) = F(t) \cdot \dot{x}(t) = F_0 \sin(\omega_n t) \cdot \omega_n X \cos(\omega_n t) = \frac{1}{2} F_0 \omega_n X \sin(2\omega_n t) \tag{2.20}$$

$$\overline{P} = \frac{1}{T} \int_0^T P(t)\, dt = 0 \tag{2.21}$$

As shown in Figure 2.7, the external force reaches its maximum when the mass velocity is zero (i.e., at maximum displacement) and crosses zero when the velocity is at its peak. This indicates that no net energy is transferred to the system when the external force is applied in phase with displacement. Consequently, the amplitude of oscillation remains constant, and the external force does not contribute to any sustained increase in the system's energy.

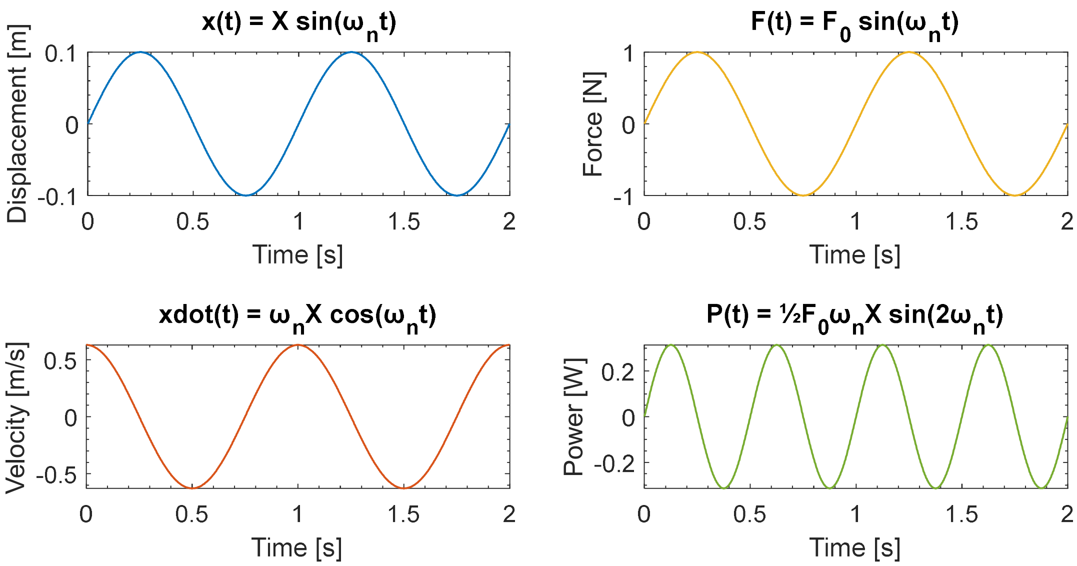

Figure 2.7. Time-domain plots of the displacement, velocity, applied force, and instantaneous power for an undamped mass-spring system. Parameters: Natural frequency 2π rad/s (1 Hz), force amplitude 1 N, and displacement amplitude 0.1 m. The force and displacement are in phase (0°), while the velocity leads by 90°. The power oscillates at twice the natural frequency with zero net work over a cycle.

The principle described earlier can be further leveraged to enhance the dynamics of slider-crank and Scotch-yoke mechanisms, as illustrated in Figure 2.8. These mechanisms consist of a crank (m_1), a connecting rod (m_2)—which incorporates a yoke in the case of the Scotch-yoke mechanism—and a slider (m_3). By incorporating a spring element, or an equivalent medium capable of storing and transferring mechanical potential energy, with stiffness k, connected between the slider and the ground or frame, resonance can be induced on the reciprocating bodies (m_2 and m_3). Simultaneously, the kinematic constraints inherent to these rigid-body systems restrict the motion of the components, confining their degrees of freedom and limiting the maximum reciprocating displacement. As a result, under resonant conditions, slider-crank and Scotch-yoke mechanisms are, in principle, characterized by a phase shift of 0°, wherein the motion of the reciprocating bodies is synchronized with the driving input.

In the subsequent discussions, the term "resonance setup, model, or configuration" refers to the analytical representation of the mechanism with a spring element mounted between the slider and the ground, tuned to the system's natural frequency. On the contrary, the term "conventional setup, model, or configuration" denotes the standard configuration without the spring element.

(a) Slider-crank mechanism.

(b) Scotch-yoke mechanism.

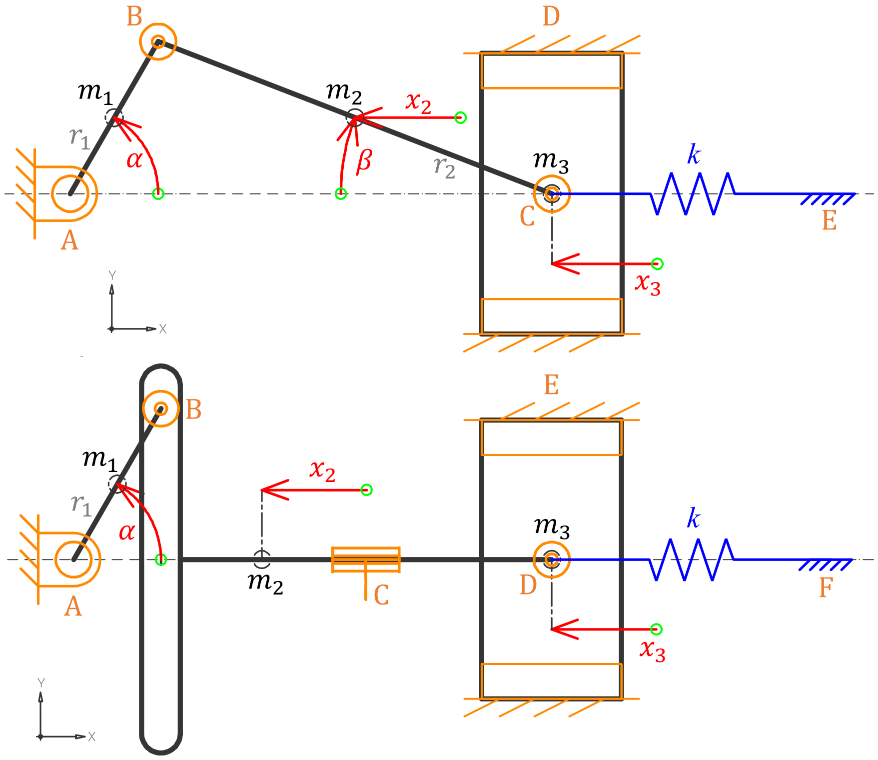

Figure 2.8. Slider-crank (a) and scotch-yoke (b) mechanism with mounted spring element from the slider to the ground/frame.

2.2. Equations of Motion

Referring to Figure 2.8, the general solution of the resonance model considers point masses for the crankshaft (m_1), connecting rod (m_2), and slider (m_3), with the spring element assumed to be massless. The total kinetic energy of the system (T) is composed of four components: the rotational kinetic energy of m_1 about the crank angle α (rotating around joint A); the translational kinetic energy of m_2 along its center-of-mass path x_2; the rotational kinetic energy of m_2 about angle β (rotating around joint C, applicable only to the slider-crank mechanism); and the translational kinetic energy of m_3 along the slider path x_3. Under this configuration, the total kinetic energy T is expressed as shown in Equations 2.22 and 2.23.

$$T = \tfrac{1}{2}I_1\dot{\alpha}^2 + \tfrac{1}{2}m_2{\dot{x}_2}^2 + \tfrac{1}{2}I_2\dot{\beta}^2 + \tfrac{1}{2}m_3{\dot{x}_3}^2 \quad \text{; for slider-crank mechanism} \tag{2.22}$$

$$T = \tfrac{1}{2}I_1\dot{\alpha}^2 + \tfrac{1}{2}m_2{\dot{x}_2}^2 + \tfrac{1}{2}m_3{\dot{x}_3}^2 \quad \text{; for Scotch-yoke mechanism} \tag{2.23}$$

The motion of the slider and connecting rod is governed by the rotation of the crankshaft. In the case of the slider-crank mechanism, the translational displacement of the slider x_3, the angular displacement of the connecting rod β, and its angular velocity $\dot{\beta}$ are described by Equations 2.24, 2.25, and 2.26, respectively.

$$x_3 = l_1 - l_1\cos\alpha + l_2 - l_2\cos\beta \tag{2.24}$$

$$\beta = \arcsin\left(\frac{l_1}{l_2}\sin\alpha\right) \tag{2.25}$$

$$\dot{\beta} = \frac{\dot{\alpha}l_1\cos\alpha}{\sqrt{{l_2}^2 - {l_1}^2\sin^2\alpha}} \tag{2.26}$$

By substituting Equation 2.25 into Equation 2.24, the slider displacement can be expressed as Equation 2.27, while its velocity, $\dot{x}$, is given by Equation 2.28.

$$x_3 = l_1 - l_1\cos\alpha + l_2 - \sqrt{{l_2}^2 - {l_1}^2\sin^2\alpha} \tag{2.27}$$

$$\dot{x}_3 = \dot{\alpha}l_1\sin\alpha + \frac{\dot{\alpha}{l_1}^2\sin 2\alpha}{2\sqrt{{l_2}^2 - {l_1}^2\sin^2\alpha}} \tag{2.28}$$

The translational displacement of the connecting rod, denoted as x_2, is given by Equations 2.29 and 2.30, while its velocity, $\dot{x}_2$, is provided in Equation 2.31.

$$x_2 = x_3 - (r_2 - r_2\cos\beta) \tag{2.29}$$

$$x_2 = \left(l_1 - l_1\cos\alpha + l_2 - \sqrt{{l_2}^2 - {l_1}^2\sin^2\alpha}\right) - \left(r_2 - r_2\sqrt{\frac{{l_2}^2 - {l_1}^2\sin^2\alpha}{{l_2}^2}}\right) \tag{2.30}$$

$$\dot{x}_2 = \dot{\alpha}l_1\sin\alpha + \frac{\dot{\alpha}{l_1}^2\sin 2\alpha}{2\sqrt{{l_2}^2 - {l_1}^2\sin^2\alpha}} - \frac{\dot{\alpha}r_2{l_1}^2\sin 2\alpha}{2{l_2}^2\sqrt{\frac{{l_2}^2 - {l_1}^2\sin^2\alpha}{{l_2}^2}}} \tag{2.31}$$

Hence, the total kinetic energy T of the slider-crank mechanism is expressed by Equation 2.32.

$$T = \frac{1}{2}I_1\dot{\alpha}^2 + \frac{1}{2}m_2\left(\dot{\alpha}l_1\sin\alpha + \frac{\dot{\alpha}{l_1}^2\sin 2\alpha}{2\sqrt{{l_2}^2 - {l_1}^2\sin^2\alpha}} - \frac{\dot{\alpha}r_2{l_1}^2\sin 2\alpha}{2{l_2}^2\sqrt{\frac{{l_2}^2 - {l_1}^2\sin^2\alpha}{{l_2}^2}}}\right)^2$$
$$+\frac{1}{2}I_2\left(\frac{\dot{\alpha}l_1\cos\alpha}{\sqrt{{l_2}^2 - {l_1}^2\sin^2\alpha}}\right)^2 \tag{2.32}$$
$$+\frac{1}{2}m_3\left(\dot{\alpha}l_1\sin\alpha + \frac{\dot{\alpha}{l_1}^2\sin 2\alpha}{2\sqrt{{l_2}^2 - {l_1}^2\sin^2\alpha}}\right)^2$$

In the case of the Scotch-yoke mechanism, the translational displacement of the slider x_3 varies sinusoidally with respect to the crank angle α. Accordingly, the displacement is defined by Equation 2.33, and the corresponding slider velocity $\dot{x}$ is obtained by differentiating the displacement with respect to time, as shown in Equation 2.34.

$$x_3 = l_1\sin\alpha \tag{2.33}$$

$$\dot{x}_3 = l_1\dot{\alpha}\cos\alpha \tag{2.34}$$

Since both m_2 and m_3 exhibit identical kinematic relationships with respect to the crank angle α, their motions can be described using the same displacement and velocity functions. As a result, the total kinetic energy T for the Scotch-yoke mechanism is expressed in Equation 2.35.

$$T = \frac{1}{2}I_1\dot{\alpha}^2 + \frac{1}{2}(m_2 + m_3)(l_1\dot{\alpha}\cos\alpha)^2 \tag{2.35}$$

The total potential energy of the system, denoted as V, comprises the contributions from the gravitational potential energy of the masses m_1, m_2 and m_3, as well as the elastic potential energy stored in the deformed spring element. However, as will be discussed in detail in Section 2.3, the gravitational force is compensated, allowing the term with g to be eliminated. Consequently, the potential energy expression simplifies to account solely for the spring deformation. The generalized expression for V in both the slider-crank and Scotch-yoke mechanisms is presented in Equation 2.36, with specific formulations for each mechanism provided in Equations 2.37 and 2.38, respectively.

$$V = \frac{1}{2}k{x_3}^2 \tag{2.36}$$

$$V = \frac{1}{2}k\left(l_1 - l_1\cos\alpha + l_2 - \sqrt{{l_2}^2 - {l_1}^2\sin^2\alpha}\right)^2 \quad ;\text{ for slider-crank mechanism} \tag{2.37}$$

$$V = \frac{1}{2}k(l_1\sin\alpha)^2 \quad ;\text{ for Scotch-yoke mechanism} \tag{2.38}$$

Table 2.1. Multibody model specification of both slider-crank and Scotch-yoke mechanisms.

Rigid Body		
Crank length l_1		50 mm
Connecting rod length l_2		150 mm
Mass of each body m_1, m_2, m_3		1 kg
Moments of inertia of each body I_{xx}, I_{yy}, I_{zz}		1 kg · mm^2
Flexible Body		
Crank length l_1		50 mm
Connecting rod length l_2		168 mm
Mass of the body	m_1	0.25 kg
	m_2	0.44 kg
	m_3	3 kg
Moments of inertia	I_{xx}, I_{yy}, I_{zz} of m_1	173.13 kg · mm^2, 144.95 kg · mm^2, 32.39 kg · mm^2
	I_{xx}, I_{yy}, I_{zz} of m_2	1400.47 kg · mm^2, 1371.71 kg · mm^2, 36.22 kg · mm^2
	I_{xx}, I_{yy}, I_{zz} of m_3	3829.31 kg · mm^2, 2552.87 kg · mm^2, 2552.87 kg · mm^2
Material		Steel
Element type and shape		Solid, tetrahedral
Element order		Linear
Edge shape		Straight
Angle per element		45 deg
Element size		Automatic
Joints		
Revolute	Pin Radius	10 mm
	Bending Reaction Arm	20 mm
	Friction Arm	5 mm
Cylindrical	Pin Radius	10 mm
	Initial Overlap	20 mm
Translational	Reaction Arm	26 mm
	Initial Overlap	32 mm
Spherical	Ball Radius	10 mm

Let the mechanisms be configured with identical basic parameters, as defined in Table 2.1. As shown in Figure 2.9, at constant angular velocity of the crankshaft—that is, the same given translational displacement of the crankshaft crank pin journal—, the slider-crank mechanism presents different displacement, velocity, and acceleration profiles for both the slider and the connecting rod when compared to the Scotch-yoke mechanism. Notably, in the slider-crank configuration, the center of mass of the connecting rod also undergoes motion along the Y-axis due to its rotational behavior, resulting in a vertical oscillation that is absent in the Scotch-yoke mechanism.

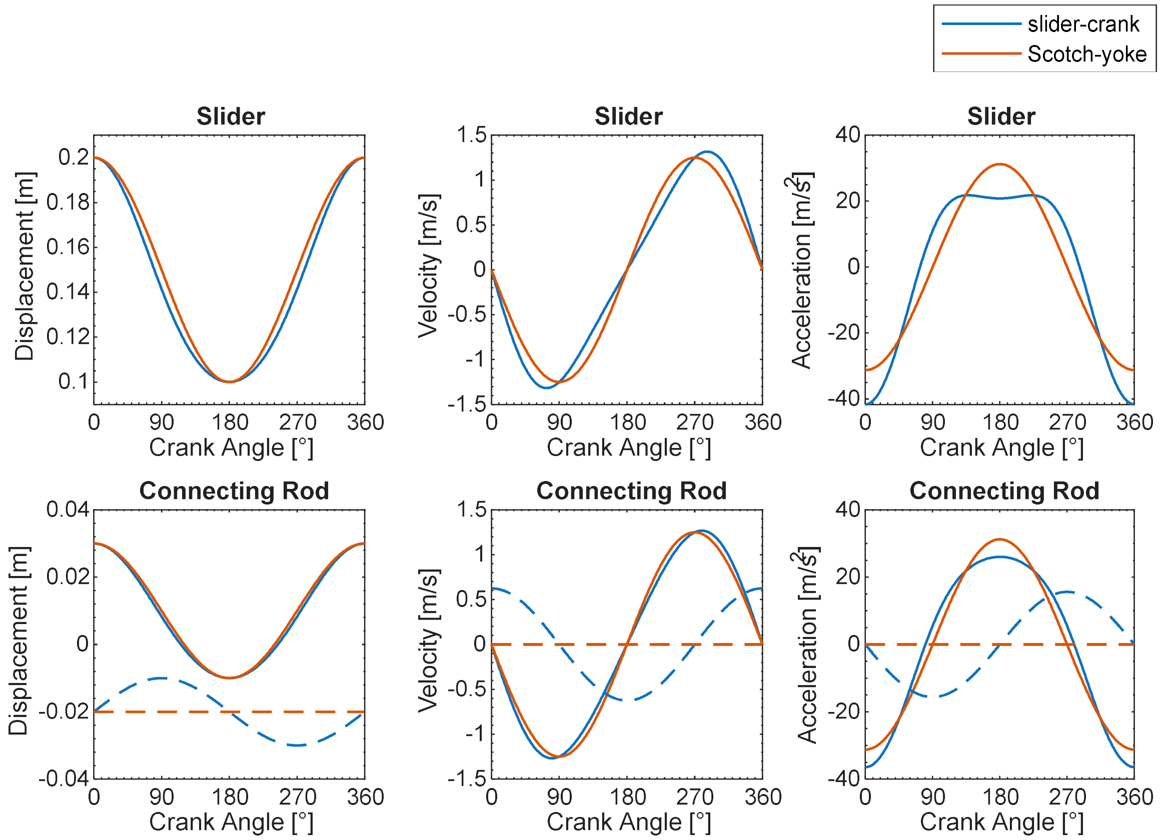

Figure 2.9. Absolute position, velocity, and acceleration of the center of mass of the crankshaft (m_1) and connecting rod (m_2) over one cycle of the slider-crank and Scotch yoke mechanisms at constant angular velocity of the crankshaft, measured relative to the global coordinate system. Solid-line curves correspond to motion along the X-axis, while dashed-line curves represent motion along the Y-axis.

The motion of the multibody system is governed by the Euler-Lagrange equation, as expressed in Equation 2.39, which is implemented in the solver used in this study. In this formulation, q denotes the generalized coordinates, and the Lagrangian $\mathcal{L}$ is defined as the difference between the total kinetic energy T and the total potential energy V, as shown in Equation 2.40. The term $\frac{d}{dt}\left(\frac{\partial \mathcal{L}}{\partial \dot{q}}\right)$ in Equation 2.39 captures the inertial (accelerative) effects of the system, while $\frac{\partial \mathcal{L}}{\partial q}$ represents the conservative forces derived from potential energy. Non-conservative or externally applied forces are captured in the generalized force vector Q. Additionally, constraint forces are incorporated through the term $\Phi_q^T \lambda$, where λ denotes the Lagrange multipliers corresponding to the constraint forces or torques necessary to enforce the system's kinematic constraints. The Jacobian matrix of the constraint equations, given in Equation 2.41, consists of the partial derivatives of the constraint functions with respect to the generalized coordinates.

$$\frac{d}{dt}\left(\frac{\partial \mathcal{L}}{\partial \dot{q}}\right) - \frac{\partial \mathcal{L}}{\partial q} + \Phi_q^T \lambda - Q = 0 \tag{2.39}$$

$$\mathcal{L} = T - V \tag{2.40}$$

$$\Phi_q = \frac{\partial \Phi}{\partial q} \tag{2.41}$$

Accordingly, the Lagrangian for the slider-crank mechanism is expressed in Equation 2.42. By computing the necessary partial derivatives with respect to the generalized coordinates and their time derivatives, and subsequently applying the total time derivative as required by the Euler-Lagrange formulation, the governing dynamic expressions are derived. The simplified results are presented in Equations 2.43, 2.44, and 2.45.

$$\begin{aligned}\mathcal{L} = \frac{1}{2} I_1 \dot{\alpha}^2 + \frac{1}{2} m_2 &\left(\dot{\alpha} l_1 \sin\alpha + \frac{\dot{\alpha} {l_1}^2 \sin 2\alpha}{2\sqrt{{l_2}^2 - {l_1}^2 \sin^2\alpha}} - \frac{\dot{\alpha} r_2 {l_1}^2 \sin 2\alpha}{2{l_2}^2 \sqrt{\frac{{l_2}^2 - {l_1}^2 \sin^2\alpha}{{l_2}^2}}} \right)^2 \\ &+ \frac{1}{2} I_2 \left(\frac{\dot{\alpha} l_1 \cos\alpha}{\sqrt{{l_2}^2 - {l_1}^2 \sin^2\alpha}} \right)^2 \\ &+ \frac{1}{2} m_3 \left(\dot{\alpha} l_1 \sin\alpha + \frac{\dot{\alpha} {l_1}^2 \sin 2\alpha}{2\sqrt{{l_2}^2 - {l_1}^2 \sin^2\alpha}} \right)^2 \\ &- \frac{1}{2} k \left(l_1 - l_1 \cos\alpha + l_2 - \sqrt{{l_2}^2 - {l_1}^2 \sin^2\alpha} \right)^2\end{aligned} \tag{2.42}$$

On the other hand, for the Scotch-yoke mechanism, the Lagrangian is given by Equation 2.46. Its partial derivative with respect to the generalized coordinate and its partial derivative with respect to the generalized velocity, along with the total time derivative of the latter, are presented in Equations 2.47, 2.48, and 2.49, respectively.

$$
\begin{aligned}
\frac{\partial \mathcal{L}}{\partial \alpha} = m_2 & \left(\dot{\alpha} l_1 \cos\alpha + \frac{\dot{\alpha} {l_1}^2 (2\cos 2\alpha)}{2\sqrt{{l_2}^2 - {l_1}^2 \sin^2\alpha}} - \frac{\dot{\alpha} r_2 {l_1}^2 (2\cos 2\alpha)}{2{l_2}^2 \sqrt{\frac{{l_2}^2 - {l_1}^2 \sin^2\alpha}{{l_2}^2}}} \right) \Bigg(\dot{\alpha} l_1 \sin\alpha \\
& + \frac{\dot{\alpha} {l_1}^2 \sin 2\alpha}{2\sqrt{{l_2}^2 - {l_1}^2 \sin^2\alpha}} - \frac{\dot{\alpha} r_2 {l_1}^2 \sin 2\alpha}{2{l_2}^2 \sqrt{\frac{{l_2}^2 - {l_1}^2 \sin^2\alpha}{{l_2}^2}}} \Bigg) \\
& + \frac{1}{2} I_2 \left(- \frac{\dot{\alpha}^2 l_1 \sin\alpha\cos\alpha}{\left(\sqrt{{l_2}^2 - {l_1}^2 \sin^2\alpha}\right)^3} - \frac{\dot{\alpha}^2 {l_1}^3 \sin\alpha\cos\alpha\sin 2\alpha}{2\left(\sqrt{{l_2}^2 - {l_1}^2 \sin^2\alpha}\right)^5} \right) \\
& + m_3 \left(\dot{\alpha} l_1 \cos\alpha + \frac{\dot{\alpha} {l_1}^2 (2\cos 2\alpha)}{2\sqrt{{l_2}^2 - {l_1}^2 \sin^2\alpha}} \right) \Bigg(\dot{\alpha} l_1 \sin\alpha \\
& + \frac{\dot{\alpha} {l_1}^2 \sin 2\alpha}{2\sqrt{{l_2}^2 - {l_1}^2 \sin^2\alpha}} \Bigg) \\
& + k \left(l_1 - l_1\cos\alpha + l_2 - \sqrt{{l_2}^2 - {l_1}^2 \sin^2\alpha} \right) l_1 \sin\alpha
\end{aligned} \tag{2.43}
$$

$$
\begin{aligned}
\frac{\partial \mathcal{L}}{\partial \dot{\alpha}} = I_1 \dot{\alpha} + m_2 & \left(\dot{\alpha} l_1 \sin\alpha + \frac{\dot{\alpha} {l_1}^2 \sin 2\alpha}{2\sqrt{{l_2}^2 - {l_1}^2 \sin^2\alpha}} - \frac{\dot{\alpha} r_2 {l_1}^2 \sin 2\alpha}{2{l_2}^2 \sqrt{\frac{{l_2}^2 - {l_1}^2 \sin^2\alpha}{{l_2}^2}}} \right) l_1 \sin\alpha \\
& + I_2 \frac{\dot{\alpha} {l_1}^2 \cos^2\alpha}{{l_2}^2 - {l_1}^2 \sin^2\alpha} + m_3 \left(\dot{\alpha} l_1 \sin\alpha + \frac{\dot{\alpha} {l_1}^2 \sin 2\alpha}{2\sqrt{{l_2}^2 - {l_1}^2 \sin^2\alpha}} \right) l_1 \sin\alpha
\end{aligned} \tag{2.44}
$$

$$
\begin{aligned}
\frac{d}{dt}\left(\frac{\partial \mathcal{L}}{\partial \dot{\alpha}}\right) = I_1 \ddot{\alpha} + m_2 & \Bigg(\ddot{\alpha} l_1 \sin\alpha + \frac{\ddot{\alpha} {l_1}^2 \sin 2\alpha}{2\sqrt{{l_2}^2 - {l_1}^2 \sin^2\alpha}} + \frac{\dot{\alpha}^2 l_1 \cos 2\alpha}{2\sqrt{{l_2}^2 - {l_1}^2 \sin^2\alpha}} \\
& - \frac{\dot{\alpha} r_2 {l_1}^2 \cos 2\alpha \sin 2\alpha}{2{l_2}^2 \sqrt{\frac{{l_2}^2 - {l_1}^2 \sin^2\alpha}{{l_2}^2}}} \Bigg) l_1 \sin\alpha \\
& + I_2 \left(\frac{\ddot{\alpha}^2 {l_1}^2 \cos^2\alpha}{{l_2}^2 - {l_1}^2 \sin^2\alpha} - \frac{2\dot{\alpha}^2 {l_1}^2 \sin\alpha\cos^3\alpha}{({l_2}^2 - {l_1}^2 \sin^2\alpha)^2} \right) \\
& + m_3 \left(\ddot{\alpha} l_1 \sin\alpha + \frac{\ddot{\alpha} {l_1}^2 \sin 2\alpha}{2\sqrt{{l_2}^2 - {l_1}^2 \sin^2\alpha}} + \frac{\dot{\alpha}^2 l_1 \cos 2\alpha}{2\sqrt{{l_2}^2 - {l_1}^2 \sin^2\alpha}} \right) l_1 \sin\alpha
\end{aligned} \tag{2.45}
$$

$$\mathcal{L} = \frac{1}{2}I_1\dot{\alpha}^2 + \frac{1}{2}(m_2+m_3)(l_1\dot{\alpha}\cos\alpha)^2 - \frac{1}{2}k(l_1\sin\alpha)^2 \tag{2.46}$$

$$\frac{\partial\mathcal{L}}{\partial\alpha} = -(m_2+m_3){l_1}^2\dot{\alpha}^2\sin\alpha\cos\alpha - k{l_1}^2\sin\alpha\cos\alpha \tag{2.47}$$

$$\frac{\partial\mathcal{L}}{\partial\dot{\alpha}} = I_1\dot{\alpha} + (m_2+m_3){l_1}^2\dot{\alpha}\cos^2\alpha \tag{2.48}$$

$$\frac{d}{dt}\left(\frac{\partial\mathcal{L}}{\partial\dot{\alpha}}\right) = I_1\ddot{\alpha} + (m_2+m_3){l_1}^2(\ddot{\alpha}\cos^2\alpha - 2\dot{\alpha}^2\sin\alpha\cos\alpha) \tag{2.49}$$

The constraint conditions imposed by the joints govern the relative motion between the connected bodies. These constraints can be mathematically described using vector loop equations [97]. For the slider-crank mechanism, the loop equation is given by Equation 2.50, and for the Scotch-yoke mechanism, by Equation 2.51.

$$\vec{\Phi}(\alpha,\beta,x_3) = (l_1\cos\alpha\,\hat{\imath} + l_1\sin\alpha\,\hat{\jmath}) + (l_2\cos\beta\,\hat{\imath} + l_2\sin\beta\,\hat{\jmath}) - (x_3\hat{\imath}) = 0 \tag{2.50}$$

$$\vec{\Phi}(\alpha,x_3) = (l_1\cos\alpha\,\hat{\imath} + l_1\sin\alpha\,\hat{\jmath}) - (x_3\hat{\imath}) = 0 \tag{2.51}$$

Here, $\hat{\imath}$ and $\hat{\jmath}$ denote unit vectors along the X- and Y-axes, respectively, in the ground reference frame; and l_1, l_2, α, β, and x_3 are geometric and kinematic parameters describing the mechanism configuration. In matrix notation, the vector loop equations are rewritten in terms of the time-dependent coordinates α, β, and x_3 as stated in Equations 2.52 and 2.53.

$$\Phi(\alpha,\beta,x_3) = \begin{pmatrix} l_1\cos\alpha + l_2\cos\beta - x_3 \\ l_1\sin\alpha + l_2\sin\beta \end{pmatrix} = 0 \quad \text{; for slider-crank mechanism} \tag{2.52}$$

$$\Phi(\alpha,x_3) = \begin{pmatrix} l_1\cos\alpha - x_3 \\ l_1\sin\alpha \end{pmatrix} = 0 \quad \text{; for Scotch-yoke mechanism} \tag{2.53}$$

After substitution and simplification, the constraint vector reduces to the expressions given in Equation 2.54 for the slider-crank mechanism and Equation 2.55 for the Scotch-yoke mechanism. The Jacobian matrices, $\Phi_\alpha = \frac{\partial\Phi}{\partial\alpha}$, representing the partial derivatives of the constraints with respect to α, are provided in Equations 2.56 and 2.57.

$$\Phi(\alpha) = \begin{pmatrix} 2l_1\cos\alpha - l_1 - l_2 + 2\sqrt{{l_2}^2 - {l_1}^2\sin^2\alpha} \\ 2l_1\sin\alpha \end{pmatrix} = 0 \tag{2.54}$$

$$\Phi(\alpha) = \begin{pmatrix} l_1\cos\alpha - l_1\sin\alpha \\ l_1\sin\alpha \end{pmatrix} = 0 \tag{2.55}$$

$$\Phi_\alpha = \begin{pmatrix} -2l_1 \sin\alpha - \frac{2{l_1}^2 \sin\alpha\cos\alpha}{\sqrt{{l_2}^2 - {l_1}^2 \sin^2\alpha}} \\ 2l_1 \cos\alpha \end{pmatrix} \quad \text{; for slider-crank mechanism} \tag{2.56}$$

$$\Phi_\alpha = \begin{pmatrix} -l_1 \sin\alpha - l_1 \cos\alpha \\ l_1 \cos\alpha \end{pmatrix} \quad \text{; for Scotch-yoke mechanism} \tag{2.57}$$

Finally, the constraint forces are incorporated into the equations of motion through the term $\Phi_\alpha^T \lambda$, representing the generalized forces arising from the constraints. For the slider-crank mechanism, this coupling is expressed by Equation 2.58, and for the Scotch-yoke mechanism by Equation 2.59.

$$\begin{aligned} \Phi_\alpha^T \lambda &= \begin{pmatrix} -2l_1 \sin\alpha - \frac{2{l_1}^2 \sin\alpha\cos\alpha}{\sqrt{{l_2}^2 - {l_1}^2 \sin^2\alpha}} & 2l_1 \cos\alpha \end{pmatrix} \begin{pmatrix} \lambda_1 \\ \lambda_2 \end{pmatrix} \\ &= \left(-2l_1 \sin\alpha - \frac{2{l_1}^2 \sin\alpha\cos\alpha}{\sqrt{{l_2}^2 - {l_1}^2 \sin^2\alpha}} \right) \lambda_1 + (2l_1 \cos\alpha)\lambda_2 \end{aligned} \tag{2.58}$$

$$\begin{aligned} \Phi_\alpha^T \lambda &= \begin{pmatrix} -l_1 \sin\alpha - l_1 \cos\alpha & l_1 \cos\alpha \end{pmatrix} \begin{pmatrix} \lambda_1 \\ \lambda_2 \end{pmatrix} \\ &= (-l_1 \sin\alpha - l_1 \cos\alpha)\lambda_1 + (l_1 \cos\alpha)\lambda_2 \end{aligned} \tag{2.59}$$

In summary, the dynamics of the mechanisms are governed by two sets of equations: a) the force-balance equations—Equations 2.43 and 2.45, coupled with the constraint force term in Equation 2.58 for the slider-crank mechanism; and Equations 2.47 and 2.49, along with Equation 2.59 for the Scotch-yoke mechanism; and b) the kinematic constraint equations—Equations 2.54 and 2.55. In the context of the conventional model, the term k is essentially zero.

Let again the mechanisms be configured with identical basic parameters—including mass, moment of inertia, and spring element stiffness—as specified in Table 2.1. The system response is evaluated under a ramp input in angular velocity, wherein the crankshaft experiences a constant angular acceleration of 1 rad/s^2. The analysis neglects friction, external forces, and gravitational effects. The Grübler criterion yields a degree of freedom (DOF) of zero for each mechanism, confirming the absence of redundant constraints in the simulated models.

As in contrast to the Scotch-yoke mechanism, wherein the connecting rod undergoes purely translational motion, the slider-crank mechanism involves both translational and rotational motion of the connecting rod. This primary difference in kinematic behavior leads to distinct dynamic responses between the two mechanisms. In the Scotch-yoke mechanism, the absence of rotational motion precludes the excitation of the connecting rod's mass moments of inertia. Consequently, the system's resonant frequency aligns with the predicted value based solely on the effective reciprocating mass and the stiffness of the spring element, as given by

Equation 2.3. In contrast, the rotational motion of the connecting rod in the slider-crank mechanism leads to different dynamic effects arising from its rotational inertia. As illustrated in Figure 2.9, the effective reciprocating mass of the connecting rod's—that is, the component of the connecting rod's mass contributing to motion along the X-axis—differs from the idealized sinusoidal pattern exhibited by the Scotch-yoke mechanism. This deviation becomes particularly noticeable at specific crank angular displacements, where the coupling between translational and rotational motion alters the inertial behavior of the system. As a result, the effective reciprocating dynamics of the slider-crank mechanism differ from those assumed in the nominal resonance prediction, leading to a slight shift in the observed resonant frequency from the value calculated using Equation 2.3. This deviation is evident in Figure 2.10, where the resonance is shown to occur at a frequency slightly different from the 25 rad/s estimated using Equation 2.3.

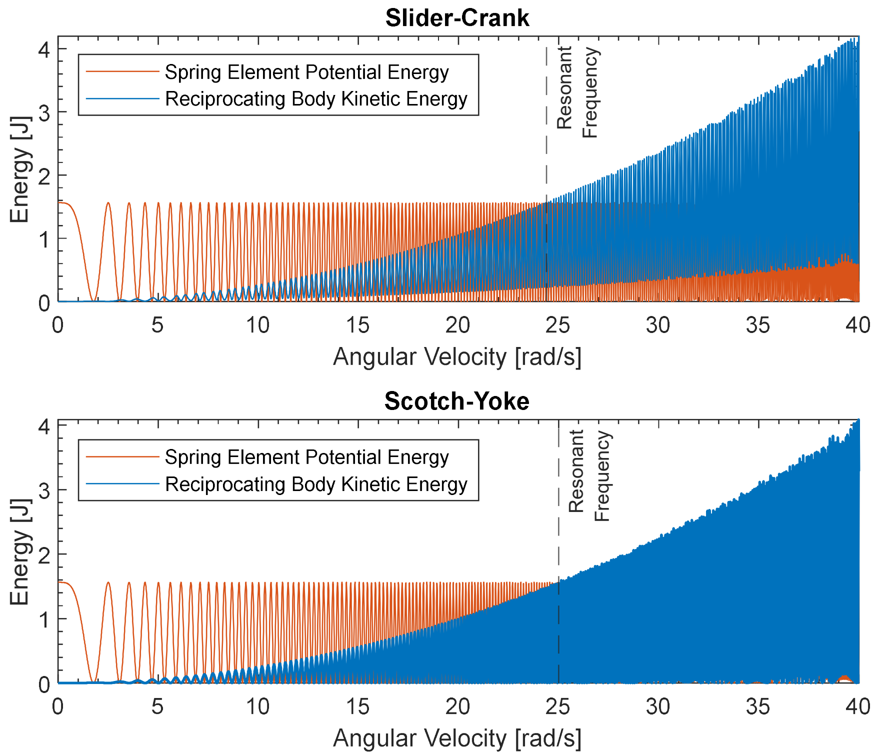

Figure 2.10. Spring element potential energy and reciprocating body kinetic energy of the slider-crank and Scotch-yoke mechanism under a ramp angular velocity input of the crank, simulated without involving friction, externally applied forces, and gravity.

As shown in Figure 2.10, at resonance, the peak values of the kinetic energy of the reciprocating body and the potential energy of the spring element are equal, though they occur at different phases of the motion cycle. The kinetic energy of the reciprocating body reaches its maximum when its velocity is highest—that is, at the equilibrium position—whereas the potential energy of the spring is zero at that point. Conversely, the potential energy of the spring peaks when the displacement is maximum (i.e., at the endpoints of motion), where the velocity—and thus the kinetic energy—of the reciprocating body is zero in the case of the Scotch-yoke mechanism; by contrast, in the slider–crank mechanism the kinetic energy reaches a minimum (but not zero), because the connecting rod undergoes purely rotational motion. In this state, the mechanism operates in its eigenmotion, which refers to a natural mode of vibration in which the total mechanical energy (the sum of kinetic and potential energy) remains constant in the absence of external energy input [98, 99]. This condition minimizes the requirement for active acceleration and deceleration, such that external energy is only needed to overcome passive resistances like friction and damping.

(a). Slider-crank mechanism

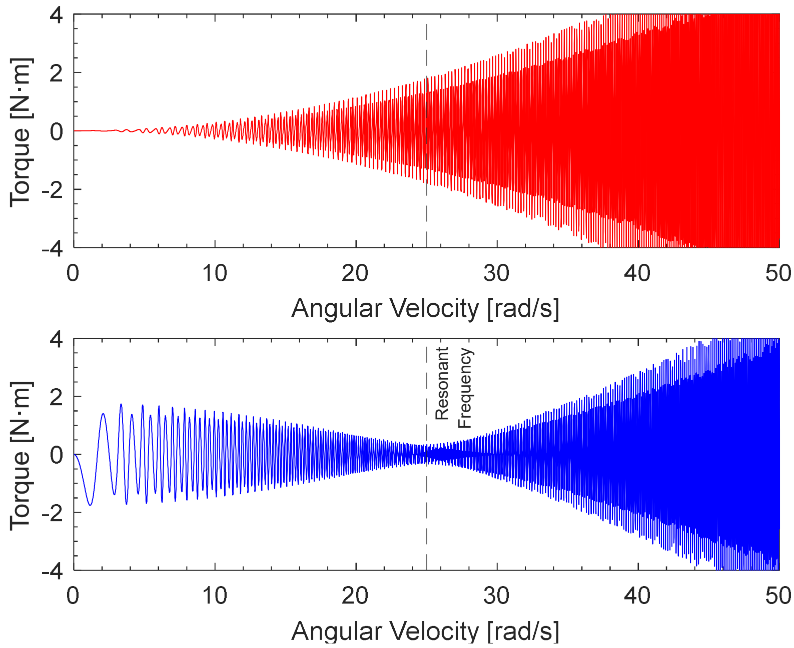

(b). Scotch-yoke mechanism

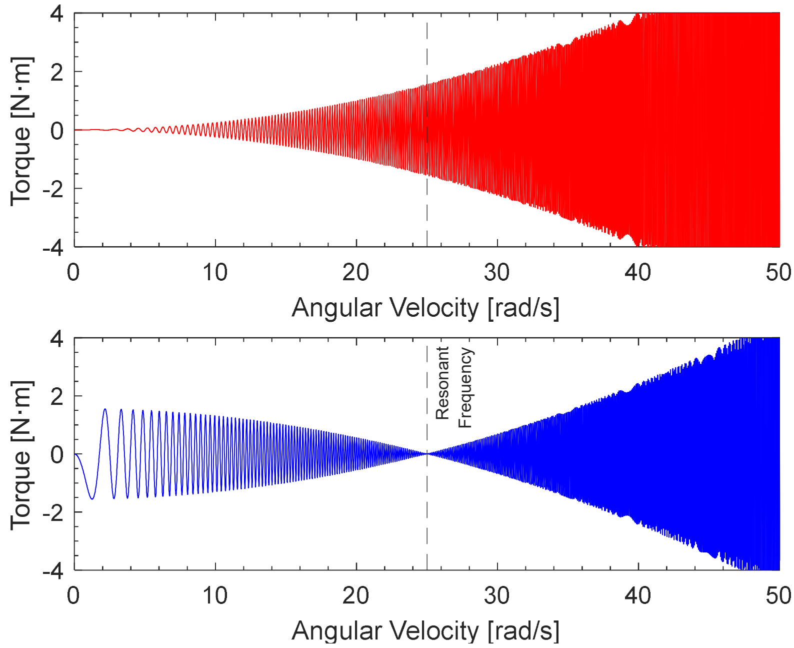

Figure 2.11. Input torques of the slider-crank (a) and Scotch-yoke mechanism (b) under a ramp angular velocity input of the crank, simulated without involving friction, externally applied forces, and gravity. The red line represents the torque in setups without a spring element, while the blue line represents the torque in setups with a spring element k = 1250 N/m.

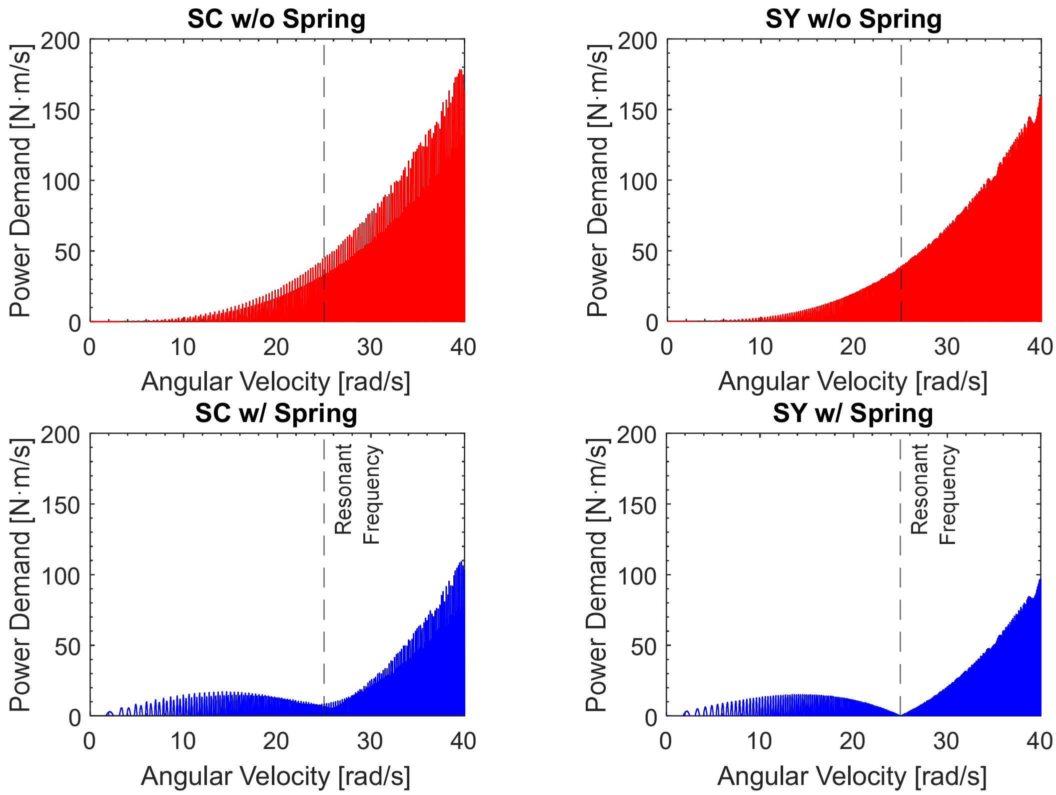

Figure 2.12. Power demand of input motions on the crank of the slider-crank and Scotch-yoke mechanism under a ramp angular velocity input of the crank, simulated without involving friction, externally applied forces, and gravity.

Figure 2.11 presents the crank input torque, equivalently expressed as the negated inertia torque, for both the slider-crank and Scotch-yoke mechanisms. Compared to the conventional setup—which excludes a spring element attached to the slider—the setup incorporating a spring element exhibits a significant reduction in input torque fluctuations, particularly as the crank's angular velocity approaches or coincides with the system’s natural frequency. Under resonant conditions, the slider-crank mechanism experiences a pronounced decrease in torque fluctuation, as the dynamic effects of the reciprocating mass are increasingly balanced by the restoring force of the spring. In the Scotch-yoke mechanism, torque fluctuations are effectively eliminated at resonance, owing to the inherently sinusoidal displacement profile of the slider, which enables complete cancellation of inertia forces by the spring's restoring action throughout the cycle. As a result, and as depicted in Figure 2.12, the setups incorporating spring element demand significantly lower mechanical input power than their conventional counterparts when operated at resonance, thereby in practice potentially enhancing the energy efficiency.

2.3. Reciprocating Body Positioning

When a spring element is incorporated into the mechanism as illustrated in Figure 2.8, the initial position of the reciprocating body at equilibrium becomes a critical factor in achieving favorable dynamic performance demonstrated in Section 2.2.

(a). Slider-crank mechanism.

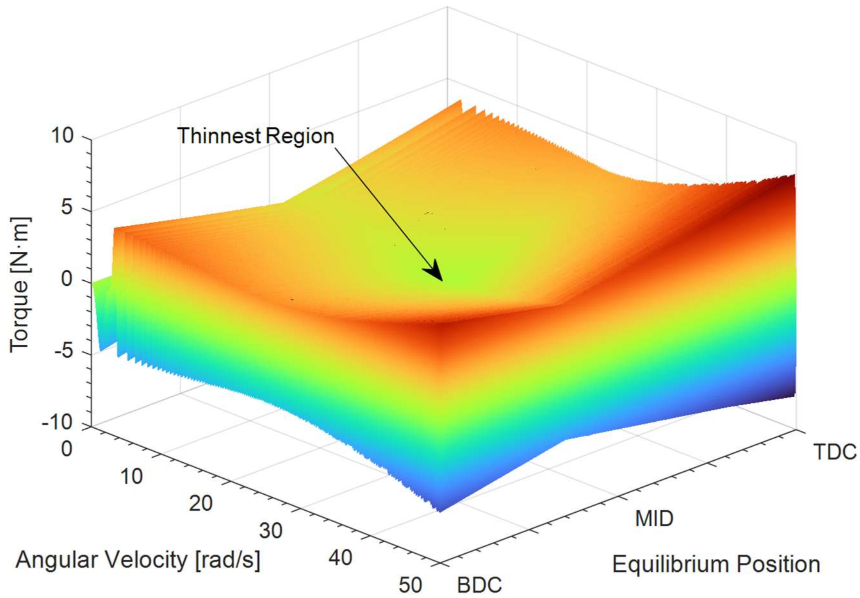

(b). Scotch-yoke mechanism

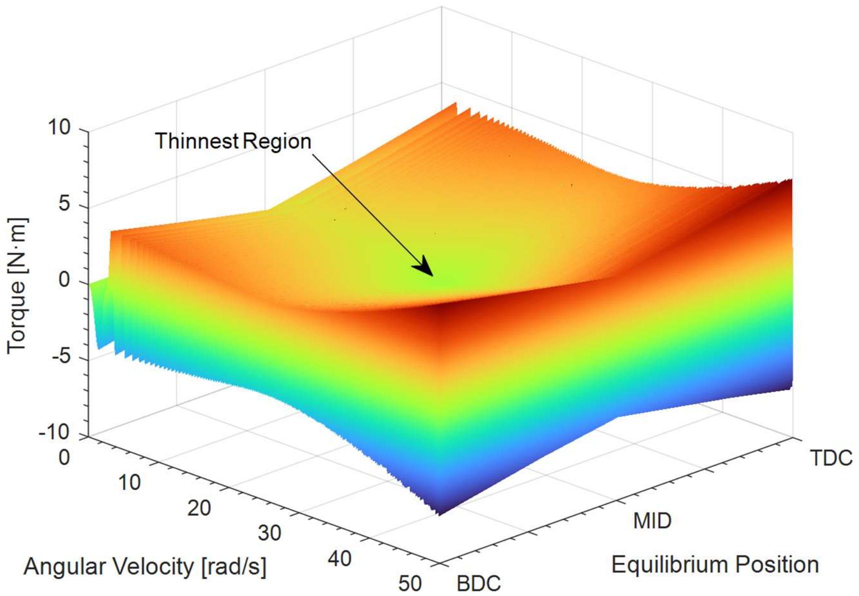

Figure 2.13. Input torques of the slider-crank (a) and Scotch-yoke mechanism (b) at different positions of the slider in equilibrium under a ramp angular velocity of the crank, simulated without involving friction, externally applied forces, and gravity.

Figure 2.13 illustrates the inertia torque responses of both the slider-crank and Scotch-yoke mechanisms to a ramp angular velocity input, evaluated at different equilibrium positions of the slider. In each plot, the thinnest region corresponds to the condition of minimal torque fluctuation, which occurs when the slider is positioned approximately at the midpoint of its stroke—denoted as MID—between bottom dead center (BDC) and top dead center (TDC). As the equilibrium position deviates from this midpoint, the thin region expands, indicating an increase in torque fluctuations. Therefore, to achieve optimal dynamic behavior, it is essential to configure the spring connection such that the slider is located at the midpoint of its stroke when the mechanism is at its equilibrium position, regardless of the presence of external conservative forces.

2.4. Gravity Compensation

The presence of gravity exerts an influence on the dynamic behavior of mechanical systems [100-104], primarily by altering the potential energy of the moving bodies over the course of the motion [105]. Gravity compensation is a critical consideration, as it enables a significant reduction in joint reaction forces and input torques in mechanisms operating under conservative forces such as gravity [106, 107, 108].

In applications, the slider-crank and Scotch-yoke mechanisms may be arranged in various spatial configurations, including vertical, horizontal, or inclined orientations. These configurations are illustrated in Figure 2.8, where gravitational acceleration is depicted as acting along the negative X-axis, the negative Y-axis, or along resultant directions incorporating components along both the negative X- and Z-axes (or their opposites). The gravitational alignment with respect to the mechanism's orientation directly influences the dynamic load paths, thereby affecting the joint reaction forces and the required input torque to maintain motion. As such, gravity must be accounted for in dynamic models to ensure efficient system behavior.

In subsequent discussions, the root mean square (RMS) values of force and torque over a complete cycle are calculated to quantitatively characterize the fluctuating behavior of these dynamic quantities [14, 109]. In practical applications, both the peak and RMS torque values are valuable criteria in the selection and specification of appropriate actuators or drivers. Within multibody dynamic simulations—where data are typically sampled at discrete time intervals—the RMS value is calculated using the discrete form presented in Equation 2.60.

$$RMS\ Value = \sqrt{\frac{1}{n}\sum_{i=1}^{n}(x_i)^2} \qquad (2.60)$$

In this expression, the RMS value corresponds to the root mean square of force, or torque, depending on the context. The variable x_i denotes the instantaneous value of the respective quantity at each discrete time step i within a complete motion cycle, and n represents the total number of data points recorded during that cycle.

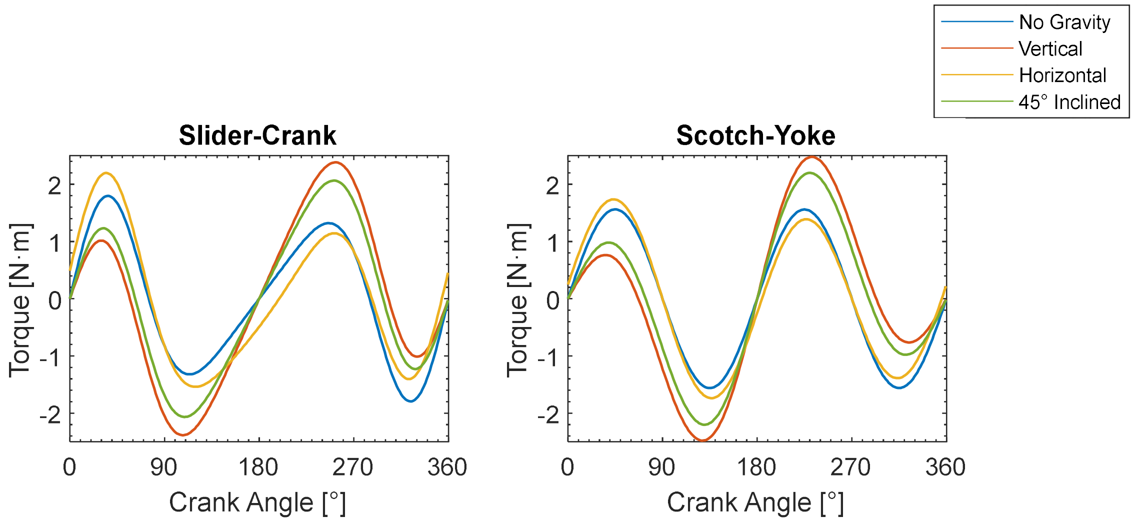

Figure 2.14. Input torques of the conventional slider-crank and Scotch-yoke mechanisms at 25 rad/s in various orientations of the slider with respect to gravity, simulated without involving friction and externally applied forces.

Table 2.2 Peak and RMS of input torques of the conventional slider-crank and Scotch-yoke mechanisms at 25 rad/s in various orientations of the slider with respect to gravity, simulated without involving friction and externally applied forces.

Mechanism	Peak Torque [N · m]				RMS Torque [N · m]			
	No Gravity	Vertical	Horizontal	Inclined	No Gravity	Vertical	Horizontal	Inclined
Slider-Crank	1.79	2.38	2.19	2.07	1.07	1.41	1.12	1.25
Scotch-Yoke	1.56	2.48	1.74	2.20	1.10	1.40	1.11	1.26

Figure 2.14 and Table 2.2 present a comparison of the input torque profiles for the conventional slider-crank and Scotch-yoke mechanisms across various orientations relative to gravity, while maintaining a constant operating speed of 25 rad/s. The curves indicate that both mechanisms exhibit the highest peak and RMS torque values when configured in the vertical orientation, whereas the horizontal orientation yields the lowest torque fluctuations. In the vertical configuration, bodies m_1, m_2, and m_3 undergo changes in gravitational potential energy throughout the motion cycle. By contrast, in the horizontal orientation, only bodies m_1 and m_2 in the slider-crank mechanism—and solely body m_1 in the Scotch-yoke mechanism—

experience such changes. This behavior illustrates that the number of bodies undergoing variation in potential energy directly influences the magnitude of torque fluctuations required from the input driver. Specifically, as more bodies contribute to potential energy variation, the resulting torque demand becomes more oscillatory.

In the case of slider-crank and Scotch-yoke mechanisms, gravitational potential energy varies periodically with the crank angle. Therefore, to maintain dynamic balance at all configurations during resonance, the potential energy stored in the spring element must also exhibit a periodic profile that compensates for the fluctuations in gravitational potential energy. In the presence of gravity, simply installing a spring between the slider and the ground is not sufficient to achieve the desired resonance behavior. As described in Section 2.3, the spring must be configured such that the slider resides at the midpoint of its stroke under static equilibrium—this condition must hold regardless of the influence of external conservative forces such as gravity. To ensure this equilibrium configuration, the gravitational force acting on the reciprocating mass must be precisely counteracted by a constant opposing force of equal magnitude. Only then can the spring provide a symmetric restoring force profile throughout the cycle, thereby preserving the resonance condition.

In the vertical orientation—regardless of whether the slider is positioned above or below the crank—the required opposing force can be established by applying a preload force F_p to the spring element. The magnitude of this preload is given by Equation 2.61, where m_t denotes the total reciprocating mass (comprising m_2 and m_3, as illustrated in Figure 2.8), g is the gravitational acceleration, and the inclination angle θ is taken as 0°. Note that the mass of the crank is not included as part of the reciprocating mass in Equation 2.61, since the force it exerts on the spring is not constant but varies sinusoidally. This is due to the crank being supported by a revolute joint at its axis of rotation, which allows its weight to be partially supported and periodically redistributed throughout the cycle.

$$F_p = m_t g \cos\theta \tag{2.61}$$

$$x_p = \frac{m_t g \cos\theta}{k} \tag{2.62}$$

In practice, this preload force can be implemented by introducing an initial displacement x_p in the spring element, as defined by Equation 2.62, where k is the spring stiffness. The effect of applying this spring preload is illustrated in Figure 2.15, in the curves labeled *SC Vertical* and *SY Vertical*. These plots compare configurations merely with the spring without preload attached at the geometric midpoint of the slider stroke (gray curves, labeled *w/o preload*) and those in which the spring also incorporates the proper preload (black curves, labeled *w/ preload*). The preloaded configuration produces a narrower torque fluctuation at the resonant frequency, closely approximating the torque behavior observed in the absence of gravity.

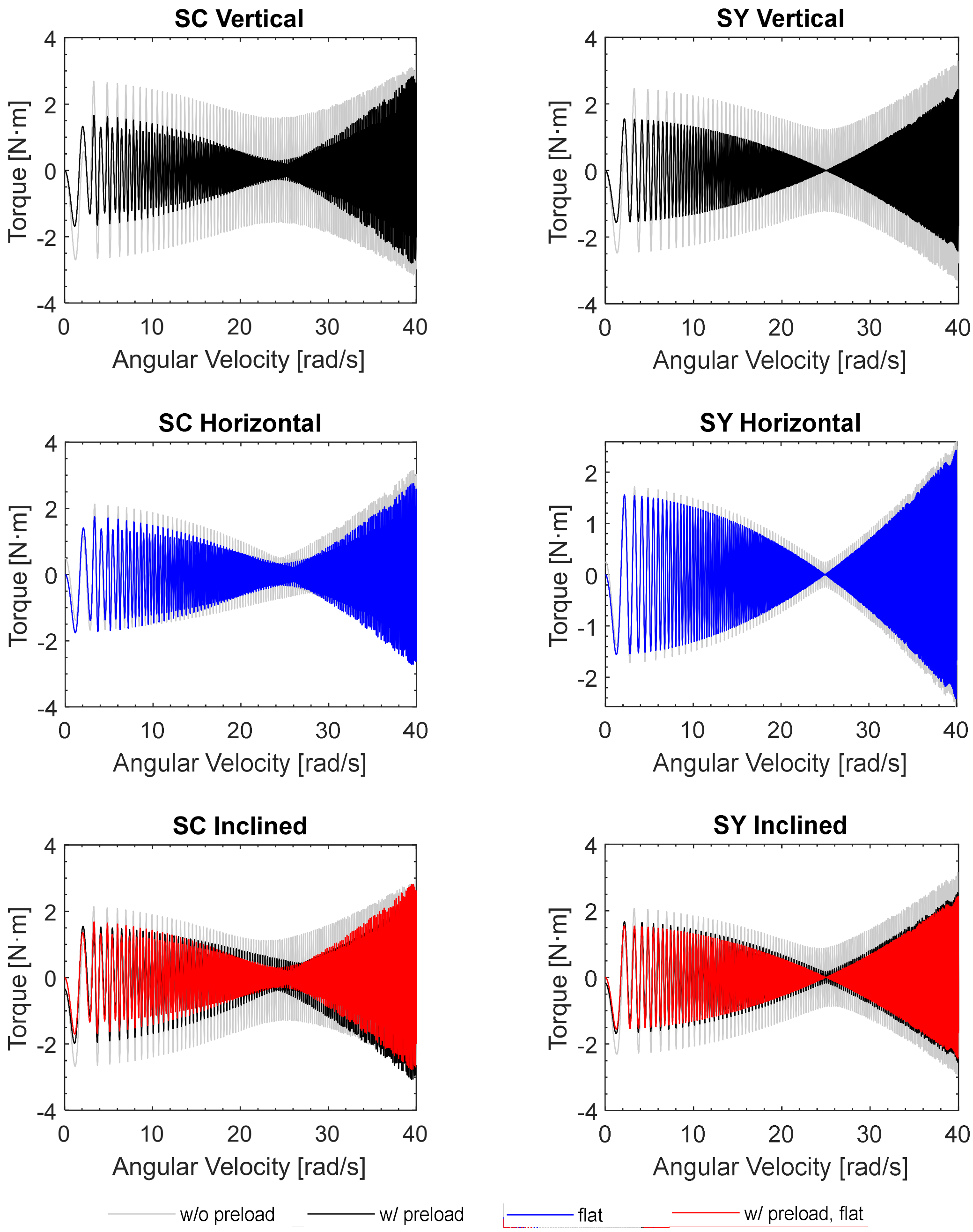

Figure 2.15. Input torques of the slider-crank (SC) and Scotch-yoke mechanism (SY) with mounted spring element k of 1250 N/m under a ramp angular velocity input of the crank in various orientations of the slider with respect to gravity, simulated without involving friction and externally applied forces.

In the horizontal orientation, applying a spring element preload is not an effective solution, as the primary motion of the reciprocating body occurs perpendicular to the direction of gravity. Instead, to minimize the influence of gravitational forces, the mechanism should be reoriented so that the crank's axis of rotation aligns with the direction of gravity. In practical terms, this means configuring the mechanisms in Figure 2.8 such that gravity acts along the positive or negative Z-axis. This orientation maintains constant gravitational potential energy for all moving bodies, thereby eliminating the effect of gravity on the input torque. The results of this reorientation strategy are demonstrated in Figure 2.15, particularly in the plots labeled *SC Horizontal* and *SY Horizontal*. Under resonance conditions, the horizontal orientation produces narrower torque fluctuations compared to the vertical or inclined orientations. However, adopting this "flat" orientation results in more improved dynamics, closely resembling a scenario where gravitational effects are negligible.

On the other hand, in the inclined orientation, the preload force must compensate for the component of the gravitational force that aligns with the motion of the slider. The required magnitude of this preload is given by Equation 2.61, where θ denotes the inclination angle of the axis along which the slider reciprocates, relative to the direction of gravity. Accordingly, the initial displacement of the spring element, x_p, necessary to generate this preload, is calculated using Equation 2.62.

The mechanisms can be inclined in arbitrary directions. For instance, they may operate on the XY plane while gravity acts at a 45° angle relative to the negative X-axis within the same plane. The plots labeled *SC Inclined* and *SY Inclined* in Figure 2.15 illustrate the behavior of the mechanisms with only a spring element (gray curves) and with a spring element incorporating preload (black curves). These results indicate that preload still offers benefits in such non-ideal configurations, provided that the reciprocating bodies are positioned at the midpoint of their strokes when the mechanism is in equilibrium. Nonetheless, it is best practice to orient the mechanism so as to minimize fluctuations in the potential energy of its moving components. In the previously explained case, the fluctuating potential energy of masses m_2 and m_3 is mitigated due to their motion path being tilted away from the direction of gravity. However, the rotating body m_1 does not benefit from this inclination, as its axis of rotation remains perpendicular to the gravitational direction. To further improve dynamic performance, the inclined orientation should be configured such that all moving bodies—including both reciprocating and rotating components—operate on the same inclined plane. As illustrated in Figure 2.8, this optimal configuration is achieved when the gravitational acceleration vector lies on the XZ plane, oriented at an angle to the X-axis. Under these conditions, the mechanisms demonstrate improved dynamic behavior, as reflected in the red curves (labeled *w/ preload, flat*), which closely resemble the performance observed under gravity-free conditions.

2.5. Optimization

Generally, an optimization problem involves the minimization or maximization of an objective function with respect to a set of design variables, subject to a series of constraints imposed on both design and state variables of the system [110]. The design process seeks to systematically manipulate these variables in order to derive an optimal configuration that satisfies all specified objectives and adheres to given constraints [110]. Optimization techniques offer a systematic and often analytical approach for determining theoretically optimal solutions [112]. The inherently iterative nature of most optimization procedures relies on algorithms and numerical methods, which, in this study, are applied within multibody dynamics simulations to manage the complexity and computational scale of the problem.

Specifically, the Modified Method of Feasible Directions (MMFD) algorithm, implemented through the MSC Automated Design Synthesis (MSCADS) software, is employed to conduct the optimization. Note that the optimization process described in this study is not intended to provide a comprehensive or great depth exploration. Rather, it serves to validate the advantageous effect of resonance-based design modifications, thereby demonstrating the potential of optimization-driven tuning.

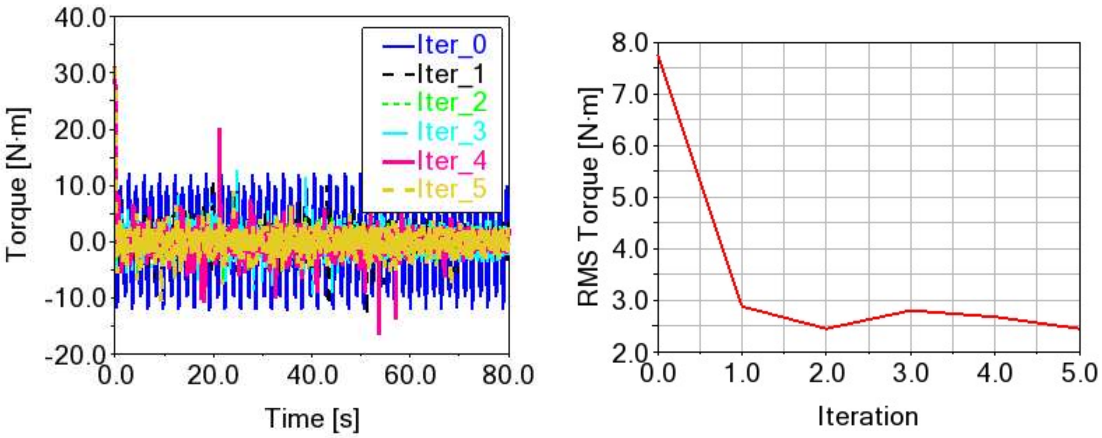

(a). Slider-crank mechanism.

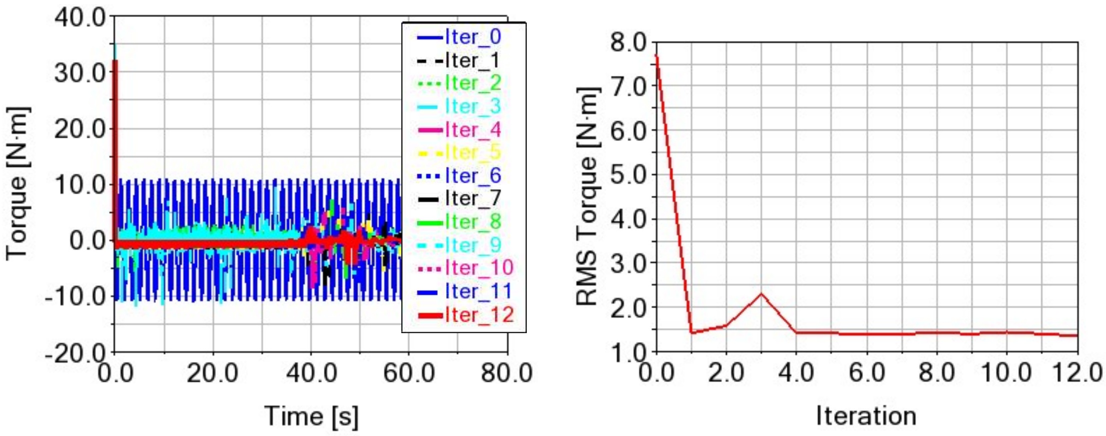

(b). Scotch-yoke mechanism.

Figure 2.17. Input torques of the slider-crank and Scotch-yoke mechanism under different crank angular velocities as the design variable.

2.5.1. Optimal Angular Velocity

In addition to the ramp angular velocity tests and the identification of regions exhibiting minimal torque fluctuation in the slider-crank and Scotch-yoke mechanisms with spring as presented earlier, optimization techniques can also be employed to determine the optimal angular velocity of the mechanism's motion driver. In this context, the design objective is to minimize the RMS value of the input torque fluctuation, with the angular velocity treated as the primary design variable. To focus on capturing the dominant dynamic behavior of the system, frictional effects are neglected, thereby eliminating energy dissipation.

The multibody model specifications for both mechanisms utilized in the optimization simulations are detailed in Table 2.3. The corresponding simulation results are illustrated in Figure 2.17 and also summarized in Table 2.3. For the slider-crank mechanism, the ramp angular velocity test indicates that the narrowest torque fluctuation occurs at approximately 47 rad/s, which coincides with the system's resonant frequency. The result is validated by this optimization study, which identifies the minimum RMS value of input torque at 47.67 rad/s. Similarly, for the Scotch-yoke mechanism, the ramp angular velocity test shows that the minimum torque fluctuation is achieved at 50 rad/s, precisely matching the system's resonant frequency. The optimization confirms this result, indicating the lowest RMS torque value at 50.26 rad/s.

Table 2.3. Summary of input angular velocity optimization using MSCADS-MMFD.

<table>
<tr><td colspan="5">Design Evaluation</td></tr>
<tr><td colspan="2">Optimization Algorithm</td><td colspan="3">MSCADS-MMFD</td></tr>
<tr><td colspan="2">Study Measure</td><td colspan="3">RMS of input torque</td></tr>
<tr><td colspan="2">Design Variable</td><td colspan="3">Crank angular velocity
Standard value = 2 rad/s
Value range = 1 – 80 rad/s</td></tr>
<tr><td colspan="2">Objective</td><td colspan="3">Minimize design measure</td></tr>
<tr><td colspan="5">Model Setup</td></tr>
<tr><td colspan="2">Crank length l_1</td><td colspan="3">50 mm</td></tr>
<tr><td colspan="2">Connecting rod length l_2</td><td colspan="3">168 mm</td></tr>
<tr><td></td><td>m [kg]</td><td>I_{xx} [$\mathrm{kg \cdot mm^2}$]</td><td>I_{yy} [$\mathrm{kg \cdot mm^2}$]</td><td>I_{zz} [$\mathrm{kg \cdot mm^2}$]</td></tr>
<tr><td>Crank</td><td>0.25</td><td>173.13</td><td>144.94</td><td>323.92</td></tr>
<tr><td>Connecting Rod</td><td>0.5</td><td>140.05</td><td>137.17</td><td>362.17</td></tr>
<tr><td>Slider</td><td>3</td><td>382.93</td><td>255.28</td><td>255.28</td></tr>
<tr><td colspan="2">Spring Stiffness</td><td colspan="3">8750 N/m</td></tr>
<tr><td colspan="5">Optimization Summary</td></tr>
<tr><td rowspan="2">Iteration</td><td colspan="2">Crank angular velocity [rad/s]</td><td colspan="2">RMS torque [$\mathrm{N \cdot m}$]</td></tr>
<tr><td>SC</td><td>SY</td><td>SC</td><td>SY</td></tr>
<tr><td>0</td><td>2.00</td><td>2.00</td><td>7.7667</td><td>7.7223</td></tr>
<tr><td>1</td><td>43.54</td><td>50.264</td><td>2.8832</td><td>1.4168</td></tr>
</table>

2	47.67	47.909	2.4536	1.5847
3	44.09	54.761	2.8069	2.3012
4	48.10	50.266	2.6816	1.4121
5	47.67	50.266	2.4536	1.4154
6	-	50.265	-	1.3826
7	-	50.263	-	1.3981
8	-	50.262	-	1.4270
9	-	50.260	-	1.4002
10	-	50.261	-	1.4404
11	-	50.261	-	1.4005
12	-	50.261	-	1.3518

2.5.2. Optimal Reciprocating Body Mass

Based on the findings presented in the preceding section, the optimal reciprocating mass for a system incorporating a spring and operating at a prescribed angular velocity is the one that yields a natural frequency close to—or coinciding with—the excitation (target) angular velocity. To validate this principle, the following example presents an optimization of the slider-crank and Scotch-yoke mechanisms, each equipped with a spring mounted between the slider and the ground. In this case, the slider mass is defined as the design variable, and the objective function is the RMS of the input torque. The optimization seeks to determine the mass value that minimizes this objective function.

The simulation results are summarized in Table 2.4. For the slider-crank mechanism, the optimal slider mass is found to be approximately 2.77 kg. In the case of the Scotch-yoke mechanism, the minimum RMS input torque is achieved with a mass of approximately 2.98 kg.

Table 2.4. Summary of reciprocating body optimization using MSCADS-MMFD.

Design Evaluation				
Optimization Algorithm	MSCADS-MMFD			
Study Measure	RMS of input torque			
Design Variable	Slider mass Standard value = 0.5 kg Value range = 0.25 – 5 kg			
Objective	Minimize design measure			
Model Setup				
Crank length l_1	50 mm			
Connecting rod length l_2	168 mm			
	m [kg]	I_{xx} [kg · mm^2]	I_{yy} [kg · mm^2]	I_{zz} [kg · mm^2]
Crank	0.25	173.13	144.94	323.92
Connecting Rod	0.5	140.05	137.17	362.17

Spring Stiffness	8750 N/m			
Crank Angular Velocity	50.4 rad/s			
Optimization Summary				
Iteration	Slider mass [kg]		RMS torque [N · m]	
	SC	SY	SC	SY
0	0.5000	0.5000	5.9788	5.7043
1	2.8984	3.1587	2.0816	1.2988
2	2.9821	2.9763	2.1301	1.2339
3	2.9942	3.2744	2.1387	1.4019
4	<u>2.7680</u>	2.9977	2.0467	1.2347
5	-	<u>2.9784</u>	-	1.2339

2.5.3. Optimal Spring Element Stiffness

Finally, Table 2.5 provides a summary of the optimization results for the spring stiffness in systems with a reciprocating mass of 3.5 kg and a target crank angular velocity of 50.4 rad/s. Based on the analytical approximation from Equation 2.3, the required spring stiffness k can be initially estimated as 8890.5 N/m. Though, optimization enables further refinement of this parameter to more effectively minimize the RMS value of input torque, accounting for the specific dynamic characteristics of each mechanism. The optimization results show that, for the slider-crank mechanism, the minimum RMS torque is achieved with an optimal spring stiffness of 8726.4 N/m. In comparison, the Scotch-yoke mechanism exhibits an optimal stiffness of 8751.4 N/m.

Table 2.5. Summary of spring element stiffness optimization using MSCADS-MMFD.

Design Evaluation				
Optimization Algorithm	MSCADS-MMFD			
Study Measure	RMS of input torque			
Design Variable	Spring element stiffness Standard value = 8740 N/m Value range = 8720 – 8770 N/m			
Objective	Minimize design measure			
Model Setup				
Crank length l_1	50 mm			
Connecting rod length l_2	168 mm			
	m [kg]	I_{xx} [kg · mm^2]	I_{yy} [kg · mm^2]	I_{zz} [kg · mm^2]
Crank	0.25	173.13	144.94	323.92
Connecting Rod	0.5	140.05	137.17	362.17
Slider	3	382.93	255.28	255.28
Crank Angular Velocity	50.4 rad/s			
Optimization Summary				
Iteration	Spring stiffness [N/m]		RMS torque [N · m]	

	SC	SY	SC	SY
0	8740.0	8740.0	1.712038	0.0087531
1	8726.4	8754.5	1.711998	0.0039356
2	8726.4	8753.8	1.711998	0.0033233
3		8753.2		0.0028272
4		8751.4		0.0012469

The optimization studies presented in this section demonstrate that across all three optimization cases—angular velocity, reciprocating mass, and spring stiffness—the optimal solutions consistently correspond to conditions where the system natural frequency closely matches the excitation frequency. From the energy use perspective, the RMS value of the input torque is adopted as the study measure in all three optimization cases, with the common objective of minimizing this design measure. This choice is determined by the fact that the RMS input torque provides a representative measure of the overall torque demand imposed on the motion driver, directly influencing its operating efficiency.

To sum up, in terms of practical application, the role of optimization in this work is not to serve as a control strategy, but rather as a design and tuning tool. The optimization results provide quantitative guidance for selecting operating speed, reciprocating mass, and elastic elements during the early design stage, or for retuning existing mechanisms to operate near resonance with minimal torque demand.

Chapter 3
Analysis

3.1. Input Torque

In simple rotating machinery, the input torque is essentially used to overcome frictional forces and perform useful work, and is often constant over time, as is the device's speed [17]. However, many mechanisms, such as the slider-crank and Scotch-yoke, incorporate non-rotating components and are characterized by non-constant work requirements. The input torque typically varies with time, though usually in a periodic manner. Due to the nature of their operation, it is often necessary to maintain prescribed limits on the maximum fluctuations of input angular velocity and, consequently, input torque. Input torque balancing in mechanisms addresses torque-induced speed fluctuations and vibrations. As briefly mentioned in Section 2.1, recent approaches range from passive counterweights to cam-based, spring-loaded, and centrifugal pendulum mechanisms, often coupled with optimization.

For both the slider-crank and Scotch-yoke mechanisms, the magnitude of the inertia torque is governed not only by the mass and mass moments of inertia of the moving components [7, 113], but also by the geometric configuration of each body and the angular velocity of the crank. As outlined in Chapter 2, the system dynamics are formulated using Lagrange's equations of the second kind. For the slider-crank mechanism, this results the general input torque expression presented in Equation 3.1. Under the condition of constant crank angular velocity, and in the absence of an elastic restoring force—that is, the case in the conventional model—the angular acceleration $\ddot{\alpha}$ and spring stiffness k terms become zero, thereby simplifying the torque expression to the form shown in Equation 3.2. In contrast, the resonance configuration incorporates the spring element, introducing an additional torque component associated with the spring's restoring force, leading to the expression in Equation 3.3.

A similar formulation is applied to the Scotch-yoke mechanism, for which the input torque is derived and presented in Equation 3.4. When assuming constant crank angular velocity, the conventional model simplifies the torque expression to that given in Equation 3.5, accounting solely for inertia-induced effects. In the resonance model, the inclusion of the spring element changes the torque profile, resulting in the modified form shown in Equation 3.6.

$$\begin{aligned}
\tau(\alpha) = I_1\ddot{\alpha} + m_2 l_1 \sin\alpha \left(\ddot{\alpha} l_1 \sin\alpha + \frac{\ddot{\alpha} {l_1}^2 \sin 2\alpha + \dot{\alpha}^2 l_1 \cos 2\alpha - \frac{\dot{\alpha} r_2 {l_1}^2 \cos 2\alpha \sin 2\alpha}{l_2}}{2\sqrt{{l_2}^2 - {l_1}^2 \sin^2\alpha}} \right) \\
+ I_2 \left(\frac{\dot{\alpha}^2 {l_1}^2 \cos^2\alpha}{{l_2}^2 - {l_1}^2 \sin^2\alpha} - \frac{2\dot{\alpha}^2 {l_1}^2 \sin\alpha \cos^3\alpha}{({l_2}^2 - {l_1}^2 \sin^2\alpha)^2} \right) \\
+ m_3 l_1 \sin\alpha \left(\ddot{\alpha} l_1 \sin\alpha + \frac{\ddot{\alpha} {l_1}^2 \sin 2\alpha + \dot{\alpha}^2 l_1 \cos 2\alpha}{2\sqrt{{l_2}^2 - {l_1}^2 \sin^2\alpha}} \right) \\
- m_2 \dot{\alpha}^2 \left(l_1 \cos\alpha + \frac{{l_1}^2 \cos 2\alpha}{\sqrt{{l_2}^2 - {l_1}^2 \sin^2\alpha}} - \frac{r_2 {l_1}^2 \cos 2\alpha}{l_2 \sqrt{{l_2}^2 - {l_1}^2 \sin^2\alpha}} \right) \left(l_1 \sin\alpha \right. \\
\left. + \frac{{l_1}^2 \sin 2\alpha}{2\sqrt{{l_2}^2 - {l_1}^2 \sin^2\alpha}} - \frac{r_2 {l_1}^2 \sin 2\alpha}{2 l_2 \sqrt{{l_2}^2 - {l_1}^2 \sin^2\alpha}} \right) \\
+ \frac{1}{2} I_2 \dot{\alpha}^2 \sin\alpha \cos\alpha \left(\frac{l_1}{\left(\sqrt{{l_2}^2 - {l_1}^2 \sin^2\alpha}\right)^3} + \frac{{l_1}^3 \sin 2\alpha}{2\left(\sqrt{{l_2}^2 - {l_1}^2 \sin^2\alpha}\right)^5} \right) \\
- m_3 \dot{\alpha}^2 \left(l_1 \cos\alpha + \frac{{l_1}^2 \cos 2\alpha}{\sqrt{{l_2}^2 - {l_1}^2 \sin^2\alpha}} \right) \left(l_1 \sin\alpha \right. \\
\left. + \frac{{l_1}^2 \sin 2\alpha}{2\sqrt{{l_2}^2 - {l_1}^2 \sin^2\alpha}} \right) \\
- k l_1 \sin\alpha \left(l_1 - l_1 \cos\alpha + l_2 - \sqrt{{l_2}^2 - {l_1}^2 \sin^2\alpha} \right)
\end{aligned} \tag{3.1}$$

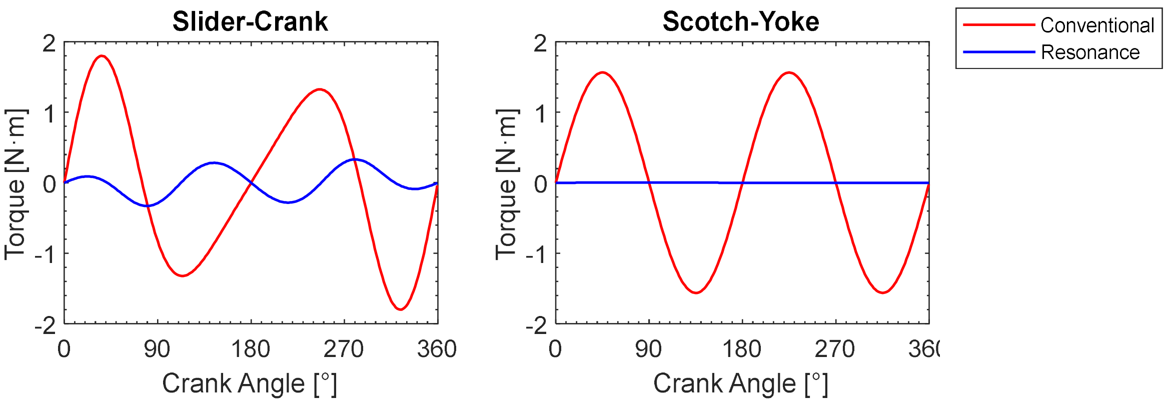

Figure 3.1. Input torques of the slider-crank and Scotch-yoke mechanism at angular velocity of 25 rad/s in one cycle. Red curves represent the setups without spring elements, and blue curves represent the setups at resonance with spring element of 1250 N/m and compensated gravity. Simulations are done without involving friction and externally

applied forces.

$$
\begin{aligned}
\tau(\alpha) = {} & \frac{m_2 l_1 \sin\alpha \cos 2\alpha}{2\sqrt{{l_2}^2 - {l_1}^2 \sin^2\alpha}} \left(\dot{\alpha}^2 l_1 - \frac{\dot{\alpha} r_2 {l_1}^2 \sin 2\alpha}{l_2} \right) \\
& - m_2 \dot{\alpha}^2 \left(l_1 \cos\alpha + \frac{{l_1}^2 \cos 2\alpha \left(1 - \frac{r_2}{l_2}\right)}{\sqrt{{l_2}^2 - {l_1}^2 \sin^2\alpha}} \right) \left(l_1 \sin\alpha \right. \\
& \left. + \frac{{l_1}^2 \sin 2\alpha \left(1 - \frac{r_2}{l_2}\right)}{2\sqrt{{l_2}^2 - {l_1}^2 \sin^2\alpha}} \right) \\
& + \frac{1}{2} I_2 \dot{\alpha}^2 \sin\alpha \cos\alpha \left(\frac{l_1}{\left(\sqrt{{l_2}^2 - {l_1}^2 \sin^2\alpha}\right)^3} + \frac{{l_1}^3 \sin 2\alpha}{2\left(\sqrt{{l_2}^2 - {l_1}^2 \sin^2\alpha}\right)^5} \right) \\
& - \frac{2 I_2 \dot{\alpha}^2 {l_1}^2 \sin\alpha \cos^3\alpha}{({l_2}^2 - {l_1}^2 \sin^2\alpha)^2} + \frac{m_3 \dot{\alpha}^2 {l_1}^2 \sin\alpha \cos 2\alpha}{2\sqrt{{l_2}^2 - {l_1}^2 \sin^2\alpha}} \\
& - m_3 \dot{\alpha}^2 \left(l_1 \cos\alpha + \frac{{l_1}^2 \cos 2\alpha}{\sqrt{{l_2}^2 - {l_1}^2 \sin^2\alpha}} \right) \left(l_1 \sin\alpha \right. \\
& \left. + \frac{{l_1}^2 \sin 2\alpha}{2\sqrt{{l_2}^2 - {l_1}^2 \sin^2\alpha}} \right)
\end{aligned}
\tag{3.2}
$$

$$
\begin{aligned}
\tau(\alpha) = {} & \frac{m_2 l_1 \sin\alpha \cos 2\alpha}{2\sqrt{{l_2}^2 - {l_1}^2 \sin^2\alpha}} \left(\dot{\alpha}^2 l_1 - \frac{\dot{\alpha} r_2 {l_1}^2 \sin 2\alpha}{l_2} \right) - \frac{2 I_2 \dot{\alpha}^2 {l_1}^2 \sin\alpha \cos^3\alpha}{({l_2}^2 - {l_1}^2 \sin^2\alpha)^2} \\
& + \frac{m_3 \dot{\alpha}^2 {l_1}^2 \sin\alpha \cos 2\alpha}{2\sqrt{{l_2}^2 - {l_1}^2 \sin^2\alpha}} \\
& - m_2 \dot{\alpha}^2 \left(l_1 \cos\alpha + \frac{{l_1}^2 \cos 2\alpha \left(1 - \frac{r_2}{l_2}\right)}{\sqrt{{l_2}^2 - {l_1}^2 \sin^2\alpha}} \right) \left(l_1 \sin\alpha \right. \\
& \left. + \frac{{l_1}^2 \sin 2\alpha \left(1 - \frac{r_2}{l_2}\right)}{2\sqrt{{l_2}^2 - {l_1}^2 \sin^2\alpha}} \right) \\
& + \frac{1}{2} I_2 \dot{\alpha}^2 \sin\alpha \cos\alpha \left(\frac{l_1}{\left(\sqrt{{l_2}^2 - {l_1}^2 \sin^2\alpha}\right)^3} + \frac{{l_1}^3 \sin 2\alpha}{2\left(\sqrt{{l_2}^2 - {l_1}^2 \sin^2\alpha}\right)^5} \right) \\
& - m_3 \dot{\alpha}^2 \left(l_1 \cos\alpha + \frac{{l_1}^2 \cos 2\alpha}{\sqrt{{l_2}^2 - {l_1}^2 \sin^2\alpha}} \right) \left(l_1 \sin\alpha \right. \\
& \left. + \frac{{l_1}^2 \sin 2\alpha}{2\sqrt{{l_2}^2 - {l_1}^2 \sin^2\alpha}} \right) \\
& - k l_1 \sin\alpha \left(l_1 (1 - \cos\alpha) + l_2 - \sqrt{{l_2}^2 - {l_1}^2 \sin^2\alpha} \right)
\end{aligned}
\tag{3.3}
$$

$$\tau(\alpha) = I_1\ddot{\alpha} + (m_2 + m_3){l_1}^2(\ddot{\alpha}\cos^2\alpha - \dot{\alpha}^2\sin\alpha\cos\alpha) + k{l_1}^2\sin\alpha\cos\alpha \tag{3.4}$$

$$\tau(\alpha) = -(m_2 + m_3){l_1}^2\dot{\alpha}^2\sin\alpha\cos\alpha \tag{3.5}$$

$$\tau(\alpha) = (k{l_1}^2 - (m_2 + m_3){l_1}^2\dot{\alpha}^2)\sin\alpha\cos\alpha \tag{3.6}$$

Figure 3.1 presents a comparative analysis of the conventional and resonance models for both the slider-crank and Scotch-yoke mechanisms. The two systems share identical rigid body parameters, as specified in Table 2.1 and depicted in Figure 2.8, and are operated at a crank angular velocity of 25 rad/s. This operating speed corresponds to the resonant frequency of the resonance model, identified in Chapter 2 as the condition associated with the narrowest torque response in Figure 2.11.

In both the slider-crank and Scotch-yoke mechanisms, the reciprocating bodies m_t undergo two acceleration and deceleration phases within each crank cycle. In the conventional model of the slider-crank mechanism, higher inertia forces are observed during specific segments of the cycle. In particular, the reciprocating bodies generate greater inertial loading when moving from top dead center (TDC) to the mid-stroke position (MID), corresponding to crank angles from 0° to approximately 90°, and again during the return from MID to TDC, i.e., from approximately 270° to 360°. This phenomenon arises from the kinematic configuration of the slider-crank mechanism, wherein the linear acceleration and deceleration of the reciprocating bodies are highest over these angular ranges at constant crank angular velocity. In contrast, during the motion from MID to bottom dead center (BDC) (around 90° to 180°) and from BDC back to MID (180° to about 270°), the acceleration and deceleration of the reciprocating mass are lower, resulting in reduced inertia forces. This asymmetry in inertial loading is reflected in the red-colored input torque curve of the conventional model in Figure 3.1 (Slider-Crank).

On the other hand, the Scotch-yoke mechanism follows a different kinematic trajectory. Due to its geometric configuration, the motion of the reciprocating mass follows a sinusoidal displacement pattern. Consequently, the resulting inertia forces remain more uniform, with less pronounced variation compared to the slider-crank system. This characteristic is evident in the red-colored input torque profile of the Scotch-yoke mechanism shown in Figure 3.1.

At resonance, the system is tuned such that the crank angular velocity matches the natural frequency of the translational subsystem, as defined by Equation 3.7. In the resonance model of the slider-crank mechanism, substituting this angular velocity (from Equation 3.7) into the torque expression derived in Equation 3.3 yields the resonance-specific formulation presented in Equation 3.8.

As illustrated by the blue-colored (Resonance) input torque curve in Figure 3.1 (Slider-Crank), the system does not reach a condition in which the restoring torque from the spring completely offsets the inertia-induced torque across all crank angles. Instead, a nonzero residual torque persists throughout the cycle, varying with crank position. This residual torque necessitates a continuous external torque input to maintain uniform rotational motion even under resonant conditions.

$$\dot{\alpha} = \sqrt{\frac{k}{m_2 + m_3}} \tag{3.7}$$

$$\begin{aligned}
\tau(\alpha) = {} & \frac{m_2 l_1 \sin\alpha \cos 2\alpha}{2\sqrt{{l_2}^2 - {l_1}^2 \sin^2\alpha}} \left(\frac{k l_1}{m_2 + m_3} - \frac{r_2 {l_1}^2 \sin 2\alpha}{l_2} \sqrt{\frac{k}{m_2 + m_3}} \right) \\
& + \frac{k}{m_2 + m_3} \left(-\frac{2 I_2 {l_1}^2 \sin\alpha \cos^3\alpha}{({l_2}^2 - {l_1}^2 \sin^2\alpha)^2} + \frac{m_3 {l_1}^2 \sin\alpha \cos 2\alpha}{2\sqrt{{l_2}^2 - {l_1}^2 \sin^2\alpha}} \right) \\
& - \frac{m_2 k}{m_2 + m_3} \left(l_1 \cos\alpha + \frac{{l_1}^2 \cos 2\alpha \left(1 - \frac{r_2}{l_2}\right)}{\sqrt{{l_2}^2 - {l_1}^2 \sin^2\alpha}} \right) \left(l_1 \sin\alpha \right. \\
& \left. + \frac{{l_1}^2 \sin 2\alpha \left(1 - \frac{r_2}{l_2}\right)}{2\sqrt{{l_2}^2 - {l_1}^2 \sin^2\alpha}} \right) \\
& + \frac{I_2 k \sin\alpha \cos\alpha}{2(m_2 + m_3)} \left(\frac{l_1}{\left(\sqrt{{l_2}^2 - {l_1}^2 \sin^2\alpha}\right)^3} + \frac{{l_1}^3 \sin 2\alpha}{2\left(\sqrt{{l_2}^2 - {l_1}^2 \sin^2\alpha}\right)^5} \right) \\
& - \frac{m_3 k}{m_2 + m_3} \left(l_1 \cos\alpha + \frac{{l_1}^2 \cos 2\alpha}{\sqrt{{l_2}^2 - {l_1}^2 \sin^2\alpha}} \right) \left(l_1 \sin\alpha \right. \\
& \left. + \frac{{l_1}^2 \sin 2\alpha}{2\sqrt{{l_2}^2 - {l_1}^2 \sin^2\alpha}} \right) \\
& - k l_1 \sin\alpha \left(l_1 (1 - \cos\alpha) + l_2 - \sqrt{{l_2}^2 - {l_1}^2 \sin^2\alpha} \right)
\end{aligned} \tag{3.8}$$

For the resonance model of the Scotch-yoke mechanism, substituting the angular velocity defined in Equation 3.7 into the torque expression given in Equation 3.6 results in the formulation presented in Equation 3.9. As depicted by the blue-colored input torque profile in Figure 3.1 (Scotch-Yoke), the distinct kinematic constraints and motion characteristics of the Scotch-yoke mechanism results in a unique resonance condition, wherein the restoring torque generated by the spring precisely cancels the inertia torque arising from the reciprocating mass. Under idealized conditions—specifically, in the absence of damping, friction, or external loads—the net input torque required to sustain uniform crank rotation reduces to zero at all crank angles. From a physical standpoint, this represents a state of dynamic equilibrium, in which energy continuously oscillates between kinetic and potential forms within the system without any net energy exchange with the input. Consequently, no external torque is necessary to maintain motion.

$$\tau(\alpha) = \left(k{l_1}^2 - (m_2 + m_3){l_1}^2 \left(\sqrt{\frac{k}{m_2 + m_3}} \right)^2 \right) \sin\alpha \cos\alpha = 0 \tag{3.9}$$

Based on the data presented in Figure 3.1 and summarized in Table 3.1, the implementation of resonance significantly reduces the torque demands in the absence of non-conservative forces. Specifically, for the slider-crank mechanism, the peak inertia torque is reduced by approximately 81.6%, while the root-mean-square (RMS) torque decreases by 82.2% when operating under resonant conditions. As previously discussed, in the case of the Scotch-yoke mechanism, resonance results in complete elimination of torque fluctuations, owing to the perfect dynamic cancellation between the spring's restoring torque and the inertia torque of the reciprocating mass. These findings demonstrate that resonance effectively counterbalance the inertia forces associated with reciprocating motion, resulting in significantly more uniform and stable load torque requirements on the driving source. Note that, in this analysis, the mechanical work done by all configurations is zero, as no energy dissipation occurs under the idealized conditions considered.

Table 3.1. Peak and RMS input torque of the conventional (without spring element) and resonance (with spring element and gravity compensation) setups at 25 rad/s. Simulations are done without involving friction and externally applied forces.

Mechanism	Peak Torque [N · m]		RMS Torque [N · m]	
	Conventional	Resonance	Conventional	Resonance
Slider-Crank	1.79	0.33	1.07	0.19
Scotch-Yoke	1.56	0	1.10	0

The instantaneous mechanical power input $P_{\text{in}}(t)$ required by the driver is defined as the product of the input torque $\tau_{\text{in}}(t)$ and the crank's angular velocity $\omega(t)$, as expressed in Equation 3.10.

$$P_{\text{in}}(t) = \tau_{\text{in}}(t) \cdot \omega(t) \tag{3.10}$$

For a system driven at a constant angular velocity $\omega = \dot{\alpha}$ stated in Equation 3.7, this simplifies to Equation 3.11.

$$P_{\text{in}}(\alpha) = \tau(\alpha) \cdot \dot{\alpha} \tag{3.11}$$

As previously discussed, the input torque $\tau(\alpha)$ varies cyclically with the crank angle due to inertial and kinematic constraint forces arising from the motion of the reciprocating masses. During portions of the cycle in which the reciprocating mass undergoes deceleration, the associated inertia torque becomes negative. This signifies that, in principle, the mechanism is capable of returning energy to the driver. However, in practical implementations, this reverse energy flow is seldom recovered due to limitations in the driver's regenerative capabilities or the absence of appropriate energy storage systems.

In an idealized, energy-conservative system with no dissipation, the net mechanical energy exchanged over a full cycle is zero, as stated in Equation 3.12.

$$\int_0^{2\pi} P_{\text{in}}(\alpha)\ d\alpha = 0 \tag{3.12}$$

However, in a non-regenerative driving system, negative power—associated with deceleration of the reciprocating mass—cannot be effectively absorbed or stored. In such cases, the system is incapable of utilizing the reverse energy flow, and these intervals are treated as instances of zero or near-zero power acceptance. As a result, the effective power delivered by the driver becomes a rectified version of the input power, defined by Equation 3.13.

$$P_{\text{eff}}(\alpha) \begin{cases} P_{\text{in}}(\alpha), & if\ P_{\text{in}}(\alpha) > 0 \\ 0, & otherwise \end{cases} \tag{3.13}$$

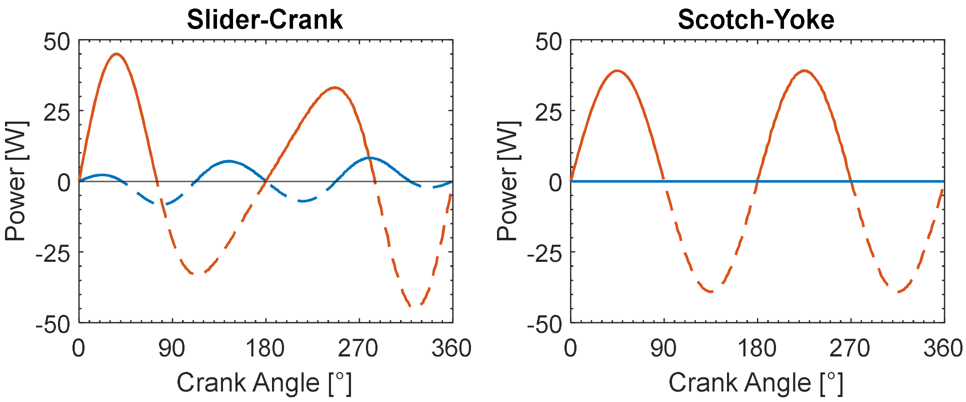

Figure 3.2. Input mechanical power of the slider-crank and Scotch-yoke mechanism at an angular velocity of 25 rad/s in one cycle. Dark red curves represent the models without spring elements, and dark blue curves represent the models at resonance with spring element of 1250 N/m and compensated gravity. Simulations are done without involving friction and externally applied forces.

This effect is illustrated in Figure 3.2, which shows both the ideal and effective mechanical input power profiles. The solid line represents the power delivered during acceleration phases of the reciprocating mass, while the dashed line indicates intervals of kinetic and potential energy recovery during deceleration—energy that, in a non-regenerative system, is essentially lost. Consequently, the average effective mechanical power input over a cycle is no longer zero, in contrast to the ideal case. The resonant model significantly reduces the area under the positive portion of the rectified power curve $P_{\text{eff}}(t)$, thereby minimizing the effective energy that must be supplied by the driver. This reduction contributes to improved energy efficiency and reduced driver load in practical applications.

3.2. Reaction Forces on Joints

In both the slider-crank and Scotch-yoke mechanisms, radial reaction forces are imposed by the joints as a result of force and torque transmission during dynamic operation [114]. As established in Chapter 2, the kinematic constraint conditions are incorporated into the system's equations of motion via the expressions defined by Equation 2.58 for the slider-crank mechanism and Equation 2.59 for the Scotch-yoke mechanism. In these formulations, the Lagrange multipliers λ_1 and λ_2 represent the constraint forces exerted by the joint in the global X- and Y-directions, respectively. The total reaction force acting at the joint—i.e., the net constraint force vector—can therefore be expressed as Equation 3.14.

$$\Phi_\alpha^T \lambda = \left(-2l_1 \sin\alpha - \frac{2{l_1}^2 \sin\alpha\cos\alpha}{\sqrt{{l_2}^2 - {l_1}^2\sin^2\alpha}}\right)\lambda_1 + (2l_1\cos\alpha)\lambda_2 \tag{2.58}$$

$$\Phi_\alpha^T \lambda = (-l_1\sin\alpha - l_1\cos\alpha)\lambda_1 + (l_1\cos\alpha)\lambda_2 \tag{2.59}$$

$$\vec{F}_{joint} = \lambda_1\hat{\imath} + \lambda_2\hat{\jmath} \tag{3.14}$$

Figures 3.3 and 3.4 present the joint reaction forces for two different configurations of both mechanisms. While both setups share the same input angular velocity and rigid body parameters, as specified in Table 2.1, they differ in the stiffness of the spring element. A summary of the data extracted from these figures is provided in Table 3.2. The results indicate that, in resonance-based models, tuning the crank's angular velocity to match the natural frequency of the spring–reciprocating mass system can lead to a significant reduction in the reaction forces experienced at the joints. The extent of this reduction varies depending on the body connection, which is influenced by factors such as mass, spring element stiffness, and angular velocity configuration.

For Case-1, illustrated in Figure 3.3, the mechanism operates at an angular velocity of 25 rad/s with a spring stiffness of 1250 N/m. According to the analytical estimate given by Equation 2.3, the corresponding resonant mass is 2 kg. In this configuration, the effective reciprocating mass precisely matches the combined mass of the connecting rod and the slider, as defined in Equation 3.7. In the slider-crank mechanism, the most significant reduction in joint reaction force occurs at the crank–connecting rod connection (joint B), with a peak value reduction of approximately 79.99% and an RMS reduction of 76.74%. In contrast, the slider–connecting rod connection (joint C) experiences minimal change. For the Scotch-yoke mechanism, the harmonic nature of the slider's motion allows resonance to practically eliminate reaction forces at joints B, C, and E—corresponding to the crank–connecting rod, connecting rod–ground, and slider–ground connections, respectively. However, joint D (slider–connecting rod) shows the least reduction in reaction force, similar to the behavior observed in the slider-crank mechanism. This limited reduction is attributed to the fact that the spring element supports the entire reciprocating mass, comprising both the slider and the connecting rod. Consequently, the joints that derive the greatest benefit from resonance tuning are those located between the crank and ground, crank and connecting rod, connecting rod and ground (in the Scotch-yoke), and the slider and ground.

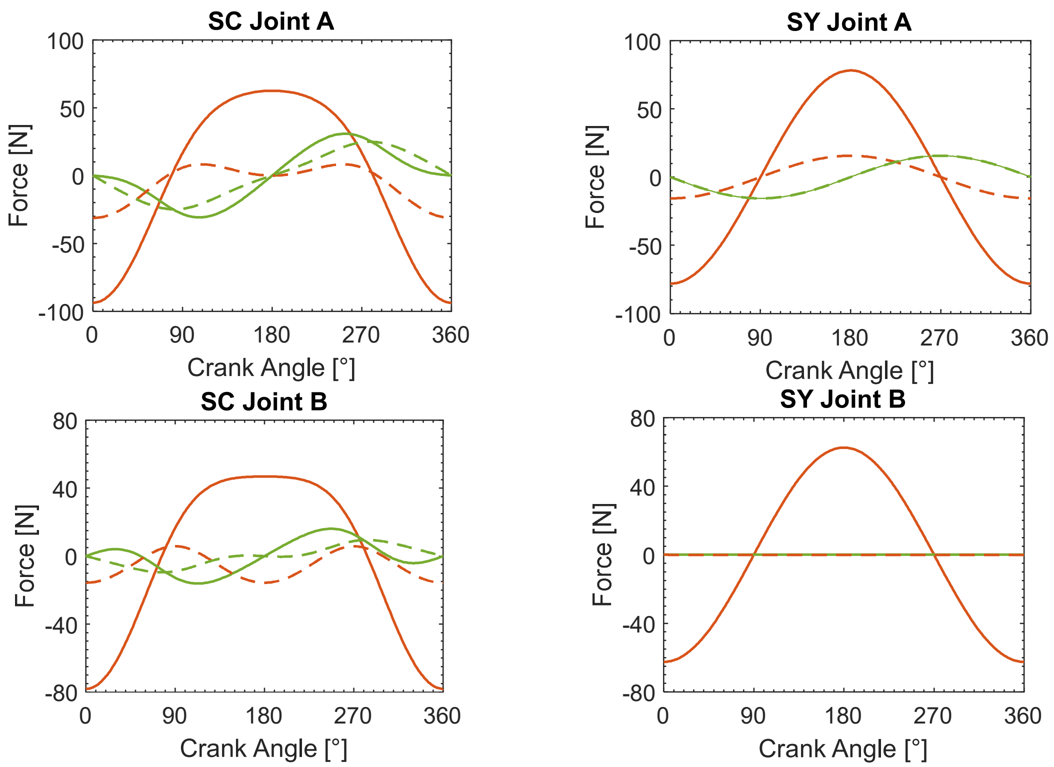

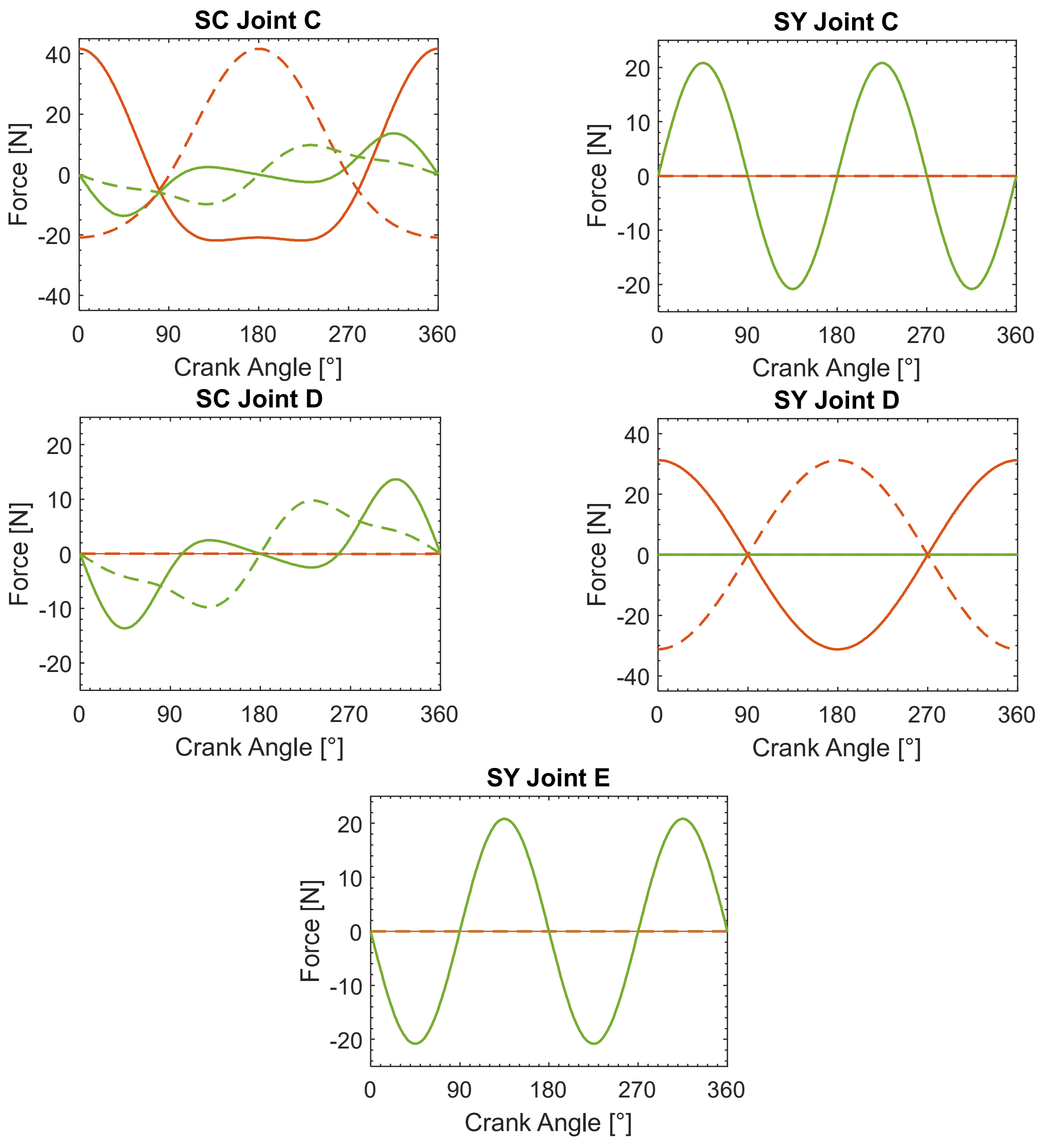

Figure 3.3. Reaction forces on the joints of the slider-crank (SC) and Scotch-yoke (SY) mechanisms in conventional (solid line) and resonance (dashed line) setups along the X-axis (red) and Y-axis (green) at angular velocity of 25 rad/s. Case-1, using a spring element k of 1250 N/m and compensated gravity, connecting rod and slider are supported in resonance. Simulations are done without involving friction and externally applied forces.

For Case-2, presented in Figure 3.4, the mechanism operates at an angular velocity of 25 rad/s with a spring element stiffness of 625 N/m. According to Equation 2.3, the corresponding resonant mass is 1 kg, which in this configuration matches the mass of the slider alone. In the slider-crank mechanism, the most significant reduction in joint reaction force occurs at the slider–connecting rod connection (joint C), with reductions of approximately 74.97% in the peak value and 66.24% in the RMS value. Additionally, in this case, other joints also experience notable reductions in reaction forces. In the Scotch-yoke mechanism, unlike Case-1, the slider–connecting rod joint (joint D) experiences a much greater reduction in both peak (68.05%) and RMS (72.37%) reaction forces. This improvement is attributed to the fact that, under the current configuration, the spring element supports only the slider mass (1 kg), which enables more effective resonance tuning at this specific joint. As a result, joint D benefits most from resonance in this scenario.

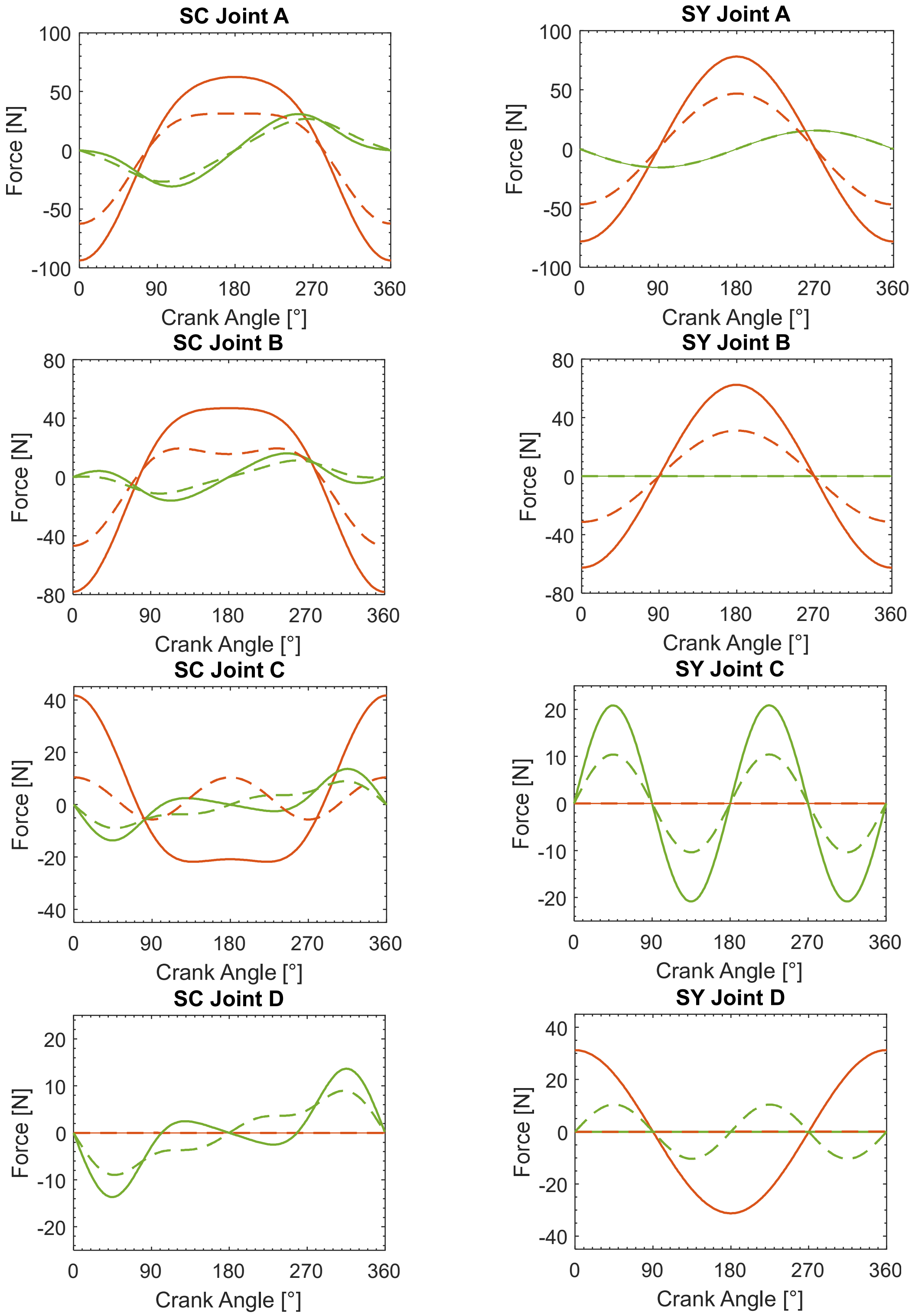

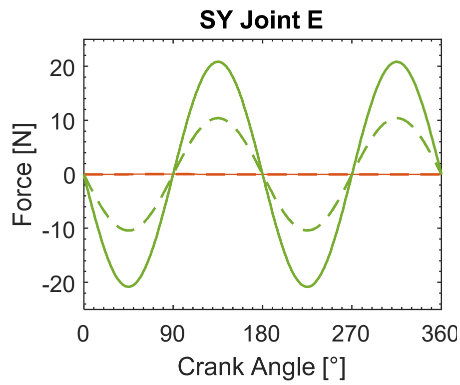

Figure 3.4. Reaction forces on the joints of the slider-crank (SC) and Scotch-yoke (SY) mechanisms in conventional (solid line) and resonance (dashed line) setups along the X-axis (red) and Y-axis (green) at angular velocity of 25 rad/s. Case-2, using a spring element k of 625 N/m and compensated gravity, only slider is supported in resonance. Simulations are done without involving friction and externally applied forces.

Table 3.2. Joint reaction forces magnitude comparison of the conventional (without spring element) and resonance (with spring element and gravity compensation) setups run at the resonant speed of 25 rad/s. Case-1 k = 1250 N/m, connecting rod and slider are supported in resonance; case-2 k = 625 N/m, only slider is supported in resonance. Simulations are done without involving friction and externally applied forces.

	Joint	Type	Connection	Peak Force [N]			RMS Force [N]		
				Conv.	Resonance		Conv.	Resonance	
					Case-1	Case-2		Case-1	Case-2
Slider-Crank	A	Revolute	Crank-Ground	93.75	31.25	62.5	59.69	21.86	38.77
	B	Cylindrical	Connecting Rod-Crank	78.13	15.63	46.88	46.69	10.86	25.14
	C	Spherical	Slider-Connecting Rod	41.67	41.65	10.43	24.47	23.84	8.26
	D	Translational	Slider-Ground	13.66	9.78	8.96	7.06	6.20	5.36
Scotch-Yoke	A	Revolute	Crank-Ground	78.13	15.63	46.88	56.40	15.62	34.95
	B	Cylindrical	Connecting Rod-Crank	62.50	0.020	31.25	44.25	0.017	22.11
	C	Inline	Connecting Rod-Ground	20.83	0.013	10.40	14.71	0.009	7.34
	D	Spherical	Slider-Connecting Rod	32.55	31.25	10.40	26.57	22.11	7.34
	E	Translational	Slider-Ground	20.83	0.013	10.40	14.71	0.009	7.34

The distribution of resonance-induced force reduction across the joints depends strongly on the configuration of the spring element and the input angular frequency. When the spring–frequency setup is tuned to support both the connecting rod and slider masses, the most significant reduction in reaction forces occurs at the connecting rod–crank joint. Conversely, if the configuration supports only the slider mass, the most substantial reduction is observed at the slider–connecting rod joint.

The effective reciprocating mass that participates in resonance can be analytically estimated using Equation 2.3. By adjusting the spring stiffness and crank angular velocity, designers can intentionally target specific mass contributions—either the combined slider and connecting rod, or the slider alone—to tailor the location of maximum joint force reduction. This tunability provides a valuable design flexibility, allowing selection of joint loading based on the system's dynamic requirements and operational priorities.

3.3. Shaking Forces and Moments

In dynamic mechanism design, particular attention is given to the forces transmitted to the machine's frame or foundation, which arise due to the inertia of moving components [115-118]. Variations in the magnitude and direction of these forces produce shaking forces and shaking moments, which can induce vibrations or oscillatory motion in the mechanism and its support structure [53, 119].

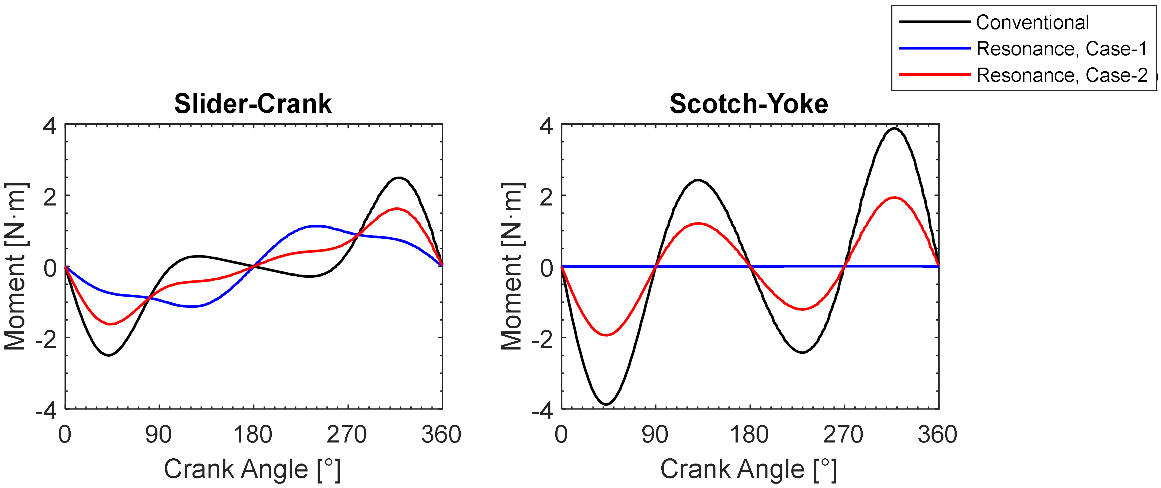

Figure 3.5. Shaking moments of the slider-crank (SC) and scotch-yoke (SY) mechanisms in conventional (solid line) and resonance (dashed line) setups at angular velocity of 25 rad/s. Case-1 (blue line), connecting rod and slider are supported in resonance; case-2 (red line), only slider is supported in resonance. Simulations are done without involving friction and externally applied forces.

As demonstrated in Figures 3.3 and 3.4, the shaking forces are observable as the red curves at Joint A (the crank–ground connection) for both the slider-crank (SC) and Scotch-yoke (SY) mechanisms. Shaking moments are calculated by multiplying the vertical (Y-axis) reaction force at the slider–ground connection by the distance between the slider–connecting rod joint and the crank–ground joint over a full motion cycle [14]. The resulting shaking moment profiles are presented in Figure 3.5. For the slider-crank mechanism, the conventional model generates an RMS shaking moment of 1.25 $N \cdot m$. Implementing the resonance model in Case-1 reduces this to 0.81 $N \cdot m$—a reduction of approximately 35.2%. In Case-2, the shaking moment is further reduced to 0.89 $N \cdot m$, corresponding to a 28.8% decrease.

In the Scotch-yoke mechanism, the conventional model produces an RMS shaking moment of 2.27 $N \cdot m$. With the resonance model in Case-1, this value drops significantly to 0.0013 $N \cdot m$, representing a reduction of approximately 99.94%. In Case-2, the resonance model achieves an RMS value of 1.13 $N \cdot m$, which constitutes a reduction of approximately 50.22% compared to the conventional model.

3.4. Stresses in the Bodies

It is well-established that elevated forces at mechanical joints—particularly at points of articulation and load transfer—induce significant mechanical consequences within the structure. Foremost among these are increased internal stresses and a corresponding rise in strain energy stored within the system's components. Stress, defined as the internal resistance of a material to deformation under external loading, scales proportionally with the magnitude of the applied forces at the joints. As stress increases, so does strain energy, which quantifies the elastic energy stored due to deformation.

This elevated strain energy can lead to greater elastic deformation of critical components, such as the crank or connecting rod. Such deformations may adversely affect the precision of the slider's displacement, which is a key performance metric in both slider-crank and Scotch-yoke mechanisms. When these structural members deviate from their ideal rigid-body motion due to force-induced deflections, the resulting path of the slider may no longer follow its intended trajectory. This leads to displacement errors and degraded system accuracy, ultimately compromising the performance and reliability of the mechanism.

This section investigates the strain energy characteristics of the slider-crank and Scotch-yoke mechanisms through combined multibody dynamics and finite element analyses, as illustrated in Figures 3.6 and 3.7. The analysis quantifies both peak and average strain energy levels within the system components under conventional and resonance configurations. A summary of the simulation results is provided in Table 3.3.

The flexible multibody modeling in this study employs the Floating Frame of Reference Formulation (FFRF). In this framework, each deformable body is assigned a local coordinate system, and its geometry is discretized into a set of rigidly connected finite elements [120]. This allows the model to capture both large rigid-body motions and small elastic deformations simultaneously. The governing equations for each flexible body are derived using Lagrange's equations of motion, as outlined in Equation 3.15, while the resulting coupled differential equations in terms of generalized coordinates are expressed in Equation 3.16. Due to their complexity, a detailed derivation of these equations is omitted here.

$$\frac{d}{dt}\left(\frac{\partial \mathcal{L}}{\partial \dot{\xi}}\right) - \frac{\partial \mathcal{L}}{\partial \xi} + \frac{\partial F}{\partial \dot{\xi}} + \left[\frac{\partial \psi}{\partial \xi}\right]^T \lambda - Q = 0 \tag{3.15}$$

$$M\ddot{\xi} + \dot{M}\dot{\xi} - \frac{1}{2}\left[\frac{\partial M}{\partial \xi}\dot{\xi}\right]^T \dot{\xi} + K\xi + f_g + D\dot{\xi} + \left[\frac{\partial \psi}{\partial \xi}\right]^T \lambda - Q = 0 \tag{3.16}$$

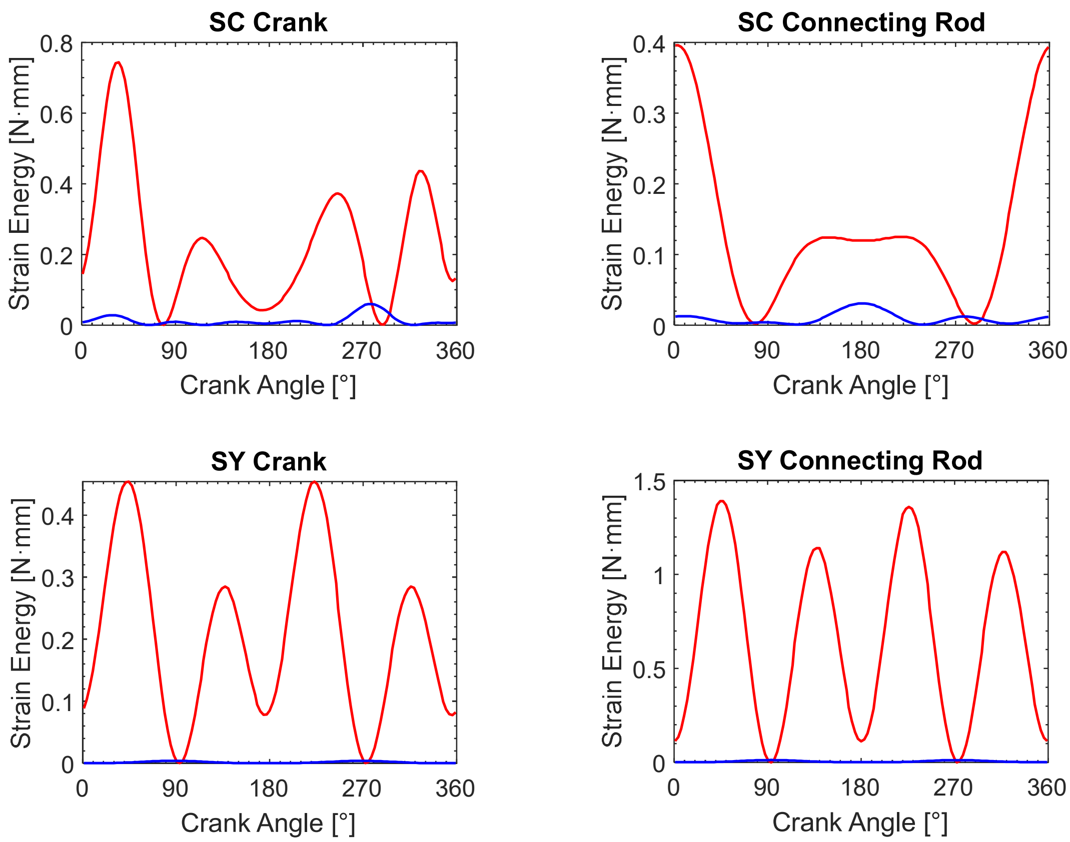

Figure 3.6. Flexible body strain energy of the crank and connecting rod in conventional (red) and resonance (blue) setups of the slider-crank (SC) and Scotch-yoke (SY) mechanisms. Simulations are done without involving friction and externally applied forces.

The flexible body used in this analysis is modeled based on the specifications provided in Table 2.1. The strain energy within the flexible body is computed using the ADAMS Solver, which evaluates deformation energy according to the formulation given in Equation 3.17 [121]. In this equation, $\{q\}$ denotes the vector of generalized modal coordinates associated with the active vibration modes (modal deformations) of the flexible body, while $[K]$ represents the generalized modal stiffness matrix. This matrix captures the stiffness characteristics of the flexible body projected onto the modal basis. The product of Equation 3.17 provides the instantaneous strain energy stored in the body due to elastic deformation during dynamic operation.

$$U = \frac{1}{2}\{q\}^T[K]\{q\} \tag{3.17}$$

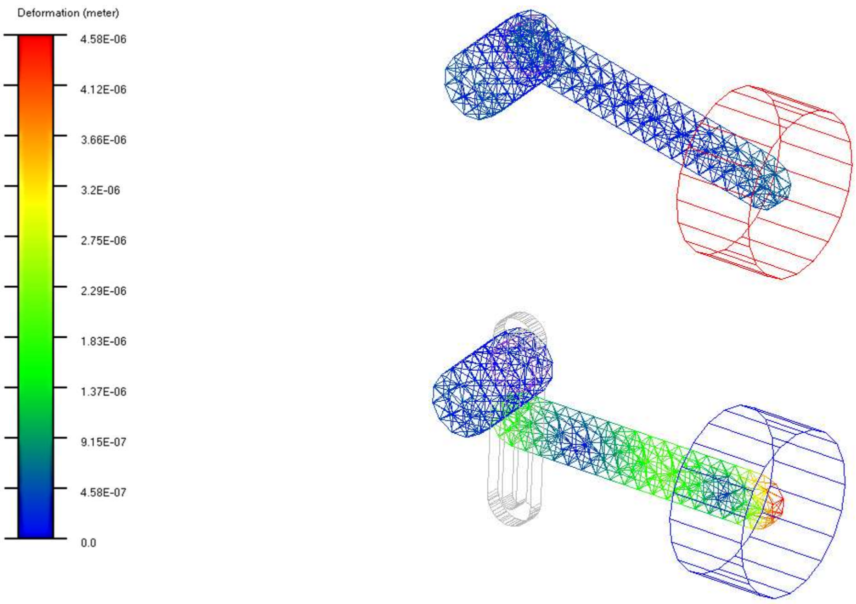

(a) Conventional setups. Frame showing at crank angle of 44.3°

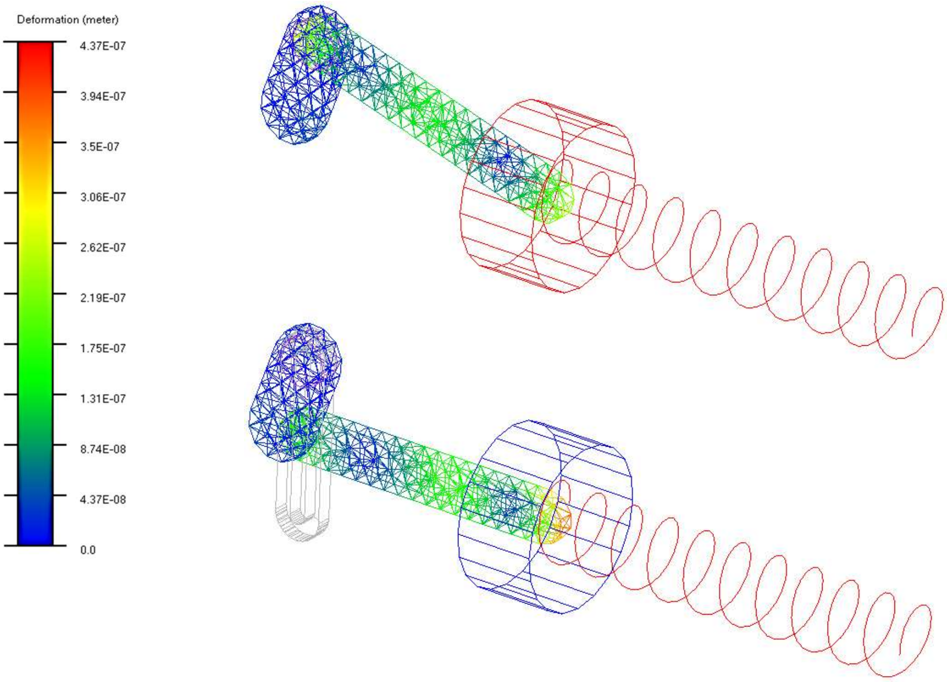

(b). Resonance setups. Frame showing at crank angle of 65.4°

Figure 3.7. Flexible body deformation of the crank and connecting rod in conventional (a) and resonance (b) setups of the slider-crank (SC) and Scotch-yoke (SY) mechanisms.

Table 3.3. Flexible body strain energy of the crank and connecting rod in conventional and resonance setups of the slider-crank and Scotch-yoke mechanisms. Simulations are done without involving friction and externally applied forces.

Mechanism	Body	Peak Strain Energy [N · mm]		Average Strain Energy [N · mm]	
		Conventional	Resonance	Resonance	Conventional
Slider-Crank	Crank	0.744	0.059	0.231	0.013
	Connecting Rod	0.397	0.031	0.135	0.009
Scotch-Yoke	Crank	0.455	0.004	0.206	0.002
	Connecting Rod	1.394	0.013	0.656	0.005

The application of resonance results in an improvement in the dynamic performance of the system, as also demonstrated by significant reductions in strain energy and corresponding structural deformations. Under resonance conditions, the slider-crank mechanism demonstrates significant improvements: the crank experiences a 91.9% reduction in peak strain energy and a 94.5% reduction in average strain energy relative to the conventional configuration. The connecting rod also benefits considerably, with reductions of 92.2% and 92.9% in peak and average strain energy, respectively. In the Scotch-yoke mechanism, the advantages of resonance are even more pronounced. The crank exhibits a 99.1% reduction in peak strain energy and a 99.2% reduction in average strain energy, while the connecting rod shows equivalent improvements of 99.1% (peak) and 99.2% (average).

3.5. Influence of Reciprocating Body Mass

This section examines the effect of reciprocating body mass on the dynamic behavior of both the slider-crank and Scotch-yoke mechanisms through a series of multibody dynamic simulations. Figure 3.8 presents the input torque profiles over a complete cycle for both conventional and resonance configurations of the slider-crank and Scotch-yoke mechanisms, evaluated using three different reciprocating masses. For the resonance configurations, the corresponding angular velocity for each mass is determined based on Equation 3.7. A constant spring stiffness of 1250 N/m is used within all simulations, with gravitational forces compensated and both friction and external loads excluded to isolate the inertial effects. The figure shows that the resonance configurations produce nearly identical torque profiles regardless of the reciprocating mass used. Interestingly, the input torque curves for the conventional configurations also remain identical across all mass values and angular velocities. In particular, for the slider-crank mechanism, if the mass of the connecting rod remains constant and only the slider mass is adjusted, the input torque profile remains essentially unchanged.

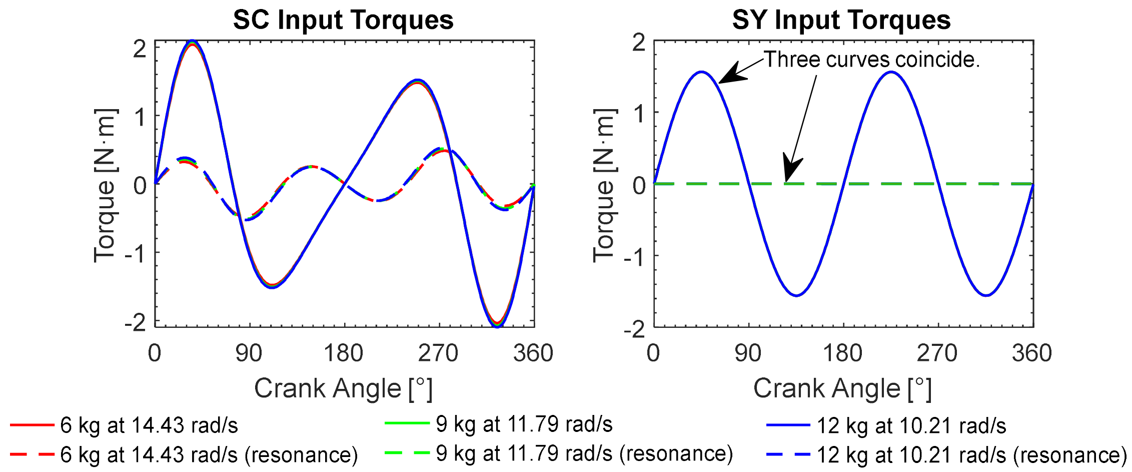

Figure 3.8. Input torque per cycle of the conventional and resonance slider-crank (SC) and scotch-yoke (SY) mechanisms using three different reciprocating body masses at $\sqrt{k/m}$ rad/s. All resonance setups use a spring element stiffness of 1250 N/m and gravity compensation. Simulations are done without involving friction and externally applied forces.

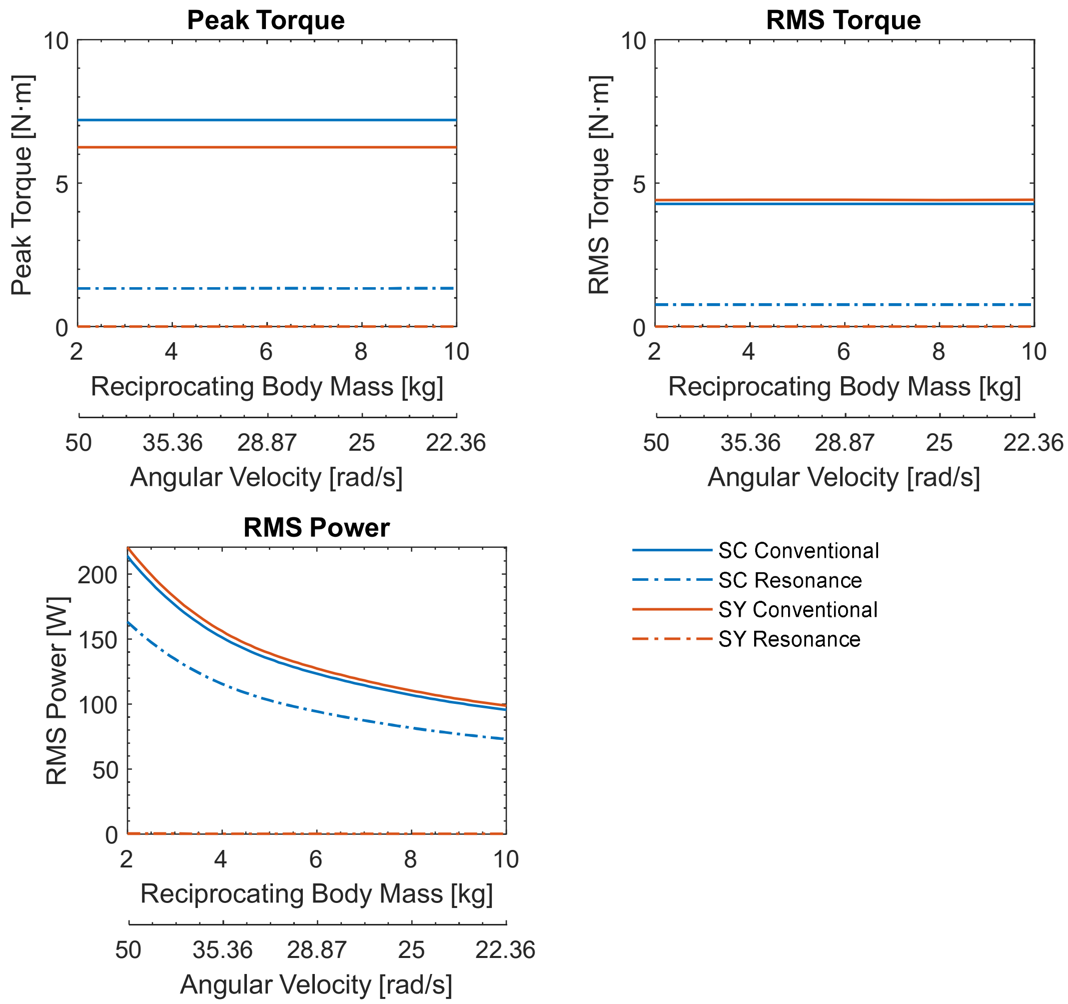

Figure 3.9. Input torque and input power of the conventional and resonance slider-crank (SC) and scotch-yoke (SY) mechanisms at different reciprocating body masses and their corresponding resonant frequencies. All resonance setups use a spring element stiffness of

5000 N/m and gravity compensation. Simulations are done without involving friction and externally applied forces.

To give another example, consider the scenario in which the simulation setup employed a spring element with the stiffness of 5 kN/m, gravity compensation, and excluded both frictional effects and external load forces to again isolate the effects of mass variation. Figure 3.9 presents the results, showing the peak input torque, RMS input torque, and RMS mechanical power as functions of the reciprocating mass. Despite changes in mass, the use of similar spring stiffness leads to similar magnitudes of spring-compensated inertia forces, as depicted in Figure 3.10(a). This outcome is attributed to the proportional adjustment in resonant frequency with reciprocating mass, in accordance with the relation stated in Equation 2.3. As the reciprocating mass increases, the corresponding resonant angular velocity decreases, maintaining comparable levels of inertial forces. In the absence of dissipative forces, both the peak and RMS input torque values are observed to be essentially equivalent across varying masses, with only minor differences arising due to numerical errors. Notably, in the slider-crank mechanism, this equivalence holds most precisely when the mass of the connecting rod remains constant. If the connecting rod mass is also varied along with the slider, slight deviations may emerge, but the overall trend remains consistent. An important consequence of this relationship is that systems with heavier reciprocating masses exhibit lower RMS mechanical power consumption. This is due to the inverse relationship between mass and resonant frequency: larger masses correspond to lower natural frequencies and, thus, reduced operating speeds for a given spring stiffness. As a result, despite identical torque demands, the overall power requirement decreases with increasing reciprocating mass.

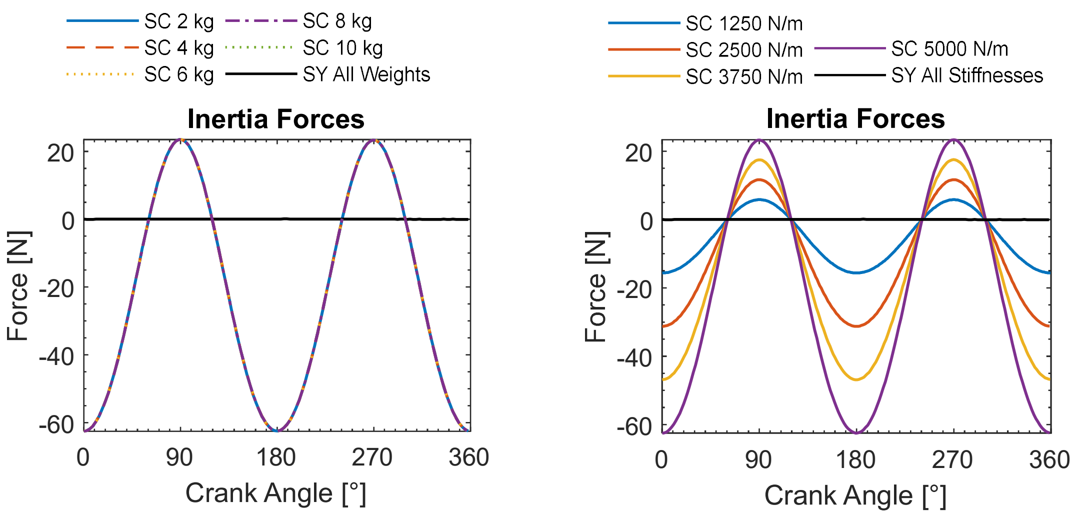

(a) (b)

Figure 3.10. Inertia forces of the reciprocating bodies compensated by the spring force, the mechanisms operate at their corresponding resonant frequencies with: (a) varying

reciprocating body masses with a consistent spring element stiffness, and (b) maintaining the same mass while varying spring element stiffness. Simulations are done without involving friction and externally applied forces.

3.6. Influence of Spring Element Stiffness

This section examines the influence of varying spring element stiffness on the dynamic performance of the slider-crank and Scotch-yoke mechanisms. The simulations were carried out under idealized conditions, excluding dissipative forces, and employed a fixed reciprocating mass of 5 kg for both mechanisms. As depicted in Figure 3.10(b), the magnitude of spring-compensated inertia forces increases with higher spring stiffness, corresponding to the increase in resonant frequency, as defined by Equation 2.3. This behavior is particularly apparent in the slider-crank mechanism, where each configuration of spring stiffness results in a distinctive combination of resonant frequency and inertia force magnitude. In contrast, the Scotch-yoke mechanism exhibits a similar behavior: due to the inherent harmonic nature of its motion, the resulting compensated inertia forces remain relatively uniform across different stiffness values.

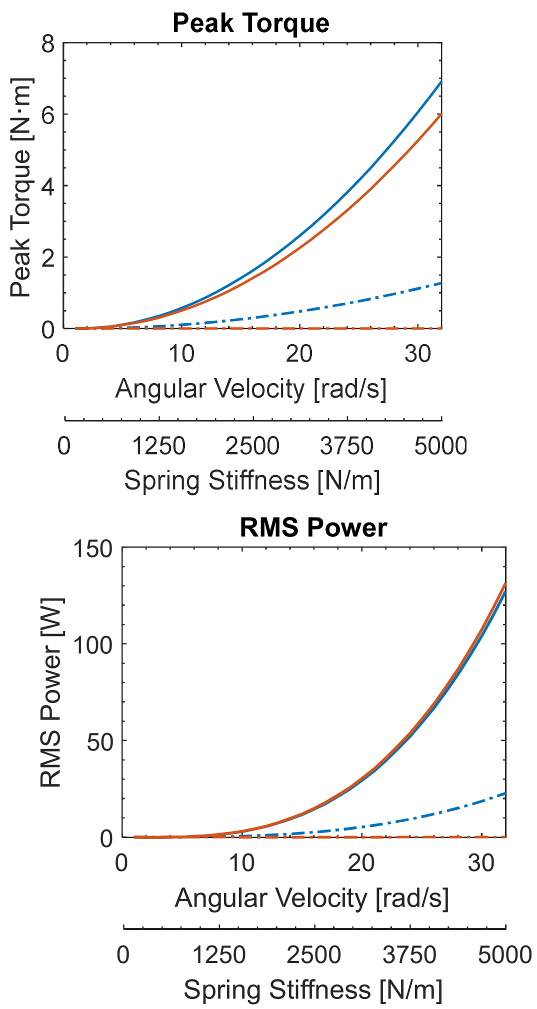

Figure 3.11. Input torque and input power of the conventional and resonance slider-crank

(SC) and Scotch-yoke (SY) mechanisms as functions of spring element stiffness, together with the corresponding resonant frequencies. All setups use a reciprocating body mass of 5 kg. Simulations are performed without friction or externally applied forces. Note that the "SY Resonance" curve is present but appears nearly indistinguishable from the zero baseline due to its consistently low and weakly varying magnitude over the investigated stiffness range.

Figure 3.11 presents the dynamic behavior of the slider-crank and Scotch-yoke mechanisms under varying spring element stiffness configurations. An important observation is the exponential difference between conventional and resonance setups in terms of peak torque, RMS torque, and RMS mechanical power as spring stiffness increases. In conventional setups, the rise in angular velocity leads to a marked exponential increase in torque and power demands, demonstrating the relationship between rotational speed and inertial loading. In contrast, when operating under resonance setups, both mechanisms demonstrate significantly reduced peak torque, RMS torque, and RMS mechanical power across all tested stiffness values. This indicates that resonance operation not only enhances torque uniformity but also yields reductions in mechanical power demands. The effect becomes increasingly pronounced as spring stiffness—and thus the system's natural frequency—rises, pointing out the efficiency advantages of resonance-based design, particularly in high-speed applications.

3.7. Influence of Frictional Forces on Joints

This section presents several essential findings regarding the behavior and performance of the system under varying damping conditions, as detailed in Table 3.4. The simulations were conducted using joint geometries and component specifications outlined in Table 2.1. Since the simulation data are collected at discrete time intervals, the work done by the input torque on the crank over one full revolution (i.e., a cycle of 2π radians) is computed numerically. The work, W, is determined using Equation 3.18.

$$W = \frac{2\pi}{n}\sum_{i=1}^{n}\tau_i \tag{3.18}$$

where τ_i denotes the instantaneous torque at the i^{th} discrete time step, and n is the total number of discrete time steps within one crank revolution.

As demonstrated in Figure 3.12 and detailed in Table 3.4, irrespective of the friction coefficients and damping parameters employed, the resonance model consistently requires notably less work per cycle than its conventional counterpart. Although viscous damping influences the magnitude of the damping force, which depends on the relative velocity, it has a negligible effect on the total work done per cycle under the simulated conditions since in these simulations, viscous damping is implemented within the spring element damper and primarily acts solely on the slider. Nonetheless, it is important to recognize that in practical applications, viscous damping may also arise from other sources—such as lubricated joints or material hysteresis—which could impact the dynamic response of the system. Therefore, while the model isolates viscous damping within the spring-slider interface, real-world implementations may exhibit more complex damping behavior that warrants further consideration.

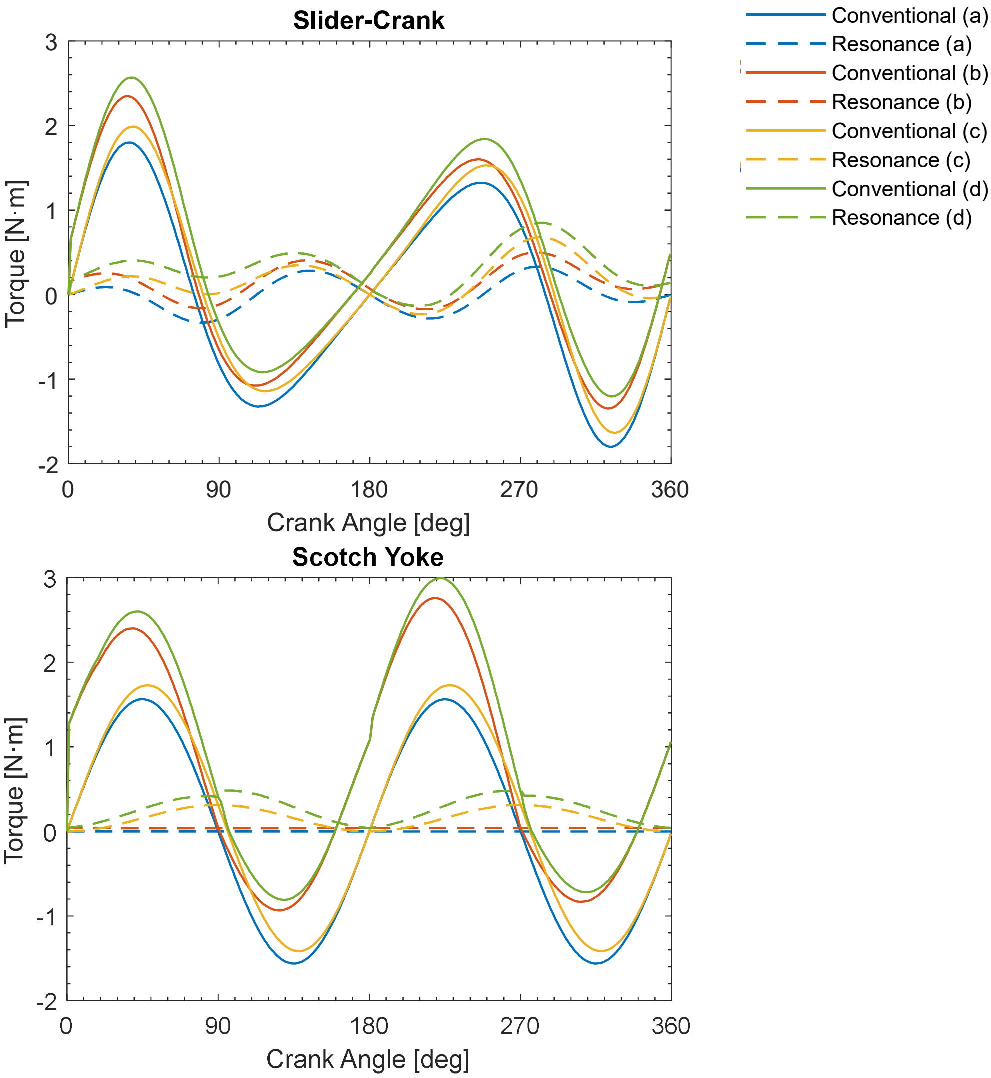

Figure 3.12. Input torque of the conventional and resonance slider-crank and Scotch-yoke mechanisms under various magnitudes of damping specified in Table 3.4. Simulations are done without involving the externally applied forces.

The influence of both static and dynamic coefficients of friction on the radial forces at the joints of the slider-crank and Scotch-yoke mechanisms has been found to be insignificant, with virtually no variation observed across a range of friction coefficients. Instead, these coefficients primarily govern the frictional torque generated at the joints. As highlighted in Table 3.4, Coulomb damping appears as the predominant source of energy dissipation affected by the dynamic performance of these mechanisms. Specifically, poorer dynamic performance—characterized by elevated radial forces at the joints—leads to increased frictional torque and, consequently, greater work done per cycle. This observation aligns with the findings of Arakelian and Briot [1], who reported that in practical scenarios, motion generation in balanced and unloaded systems generally requires only minimal input torque, primarily to overcome frictional resistance.

Table 3.4. Input torque of both the conventional (Con.) and resonance (Res.) slider-crank and Scotch-yoke mechanisms under various magnitudes of damping. Simulations are done without involving the externally applied forces.

Slider-Crank Mechanism									
Case	Coefficient of Friction		Damping Coefficient [N · s/m]	Peak Torque [N · m]		RMS Torque [N · m]		Rotational Work per Cycle [J]	
	μ_s	μ_d		Con.	Res.	Con.	Res.	Con.	Res.
a	0	0	0	1.79	0.33	1.07	0.19	0	0
b	0.5	0.25	0	2.35	0.50	1.14	0.25	2.04	0.94
c	0	0	5	1.99	0.68	1.09	0.28	1.01	1.01
d	0.5	0.25	5	2.57	0.85	1.23	0.39	3.08	1.96
Scotch-Yoke Mechanism									
Case	Coefficient of Friction		Damping Coefficient [N · s/m]	Peak Torque [N · m]		RMS Torque [N · m]		Rotational Work per Cycle [J]	
	μ_s	μ_d		Con.	Res.	Con.	Res.	Con.	Res.
a	0	0	0	1.56	0	1.10	0	0	0
b	0.5	0.25	0	2.76	0.04	1.45	0.04	4.71	0.25
c	0	0	5	1.73	0.31	1.12	0.19	1.01	1.01
d	0.5	0.25	5	2.99	0.48	1.58	0.30	5.78	1.67

3.8. Influence of Externally Applied Forces

Given the infinite range of possible externally applied forces acting on the slider-crank and Scotch-yoke mechanisms, there exists an equally countless variety of force profiles within a single operational cycle. In this section, a representative selection of common external load types is investigated—namely constant, linear, exponential, and logarithmic double-acting force profiles, as illustrated in Figure 3.13. These loading scenarios are selected based on their relevance to practical applications, particularly in manufacturing and related industrial processes where these mechanisms are widely employed. The constant force profile simulates applications that demand uniform resistance throughout the slider's motion, such as power hacksaws [122]. Linear double-acting forces correspond to operations like incremental component adjustments in automated assembly systems. Exponential force profiles model applications involving progressively increasing resistance, such as material compaction. Conversely, logarithmic double-acting forces represent scenarios where resistance diminishes with continued motion, as observed in precision cutting machines where cutting resistance decreases as the tool penetrates deeper into the material.

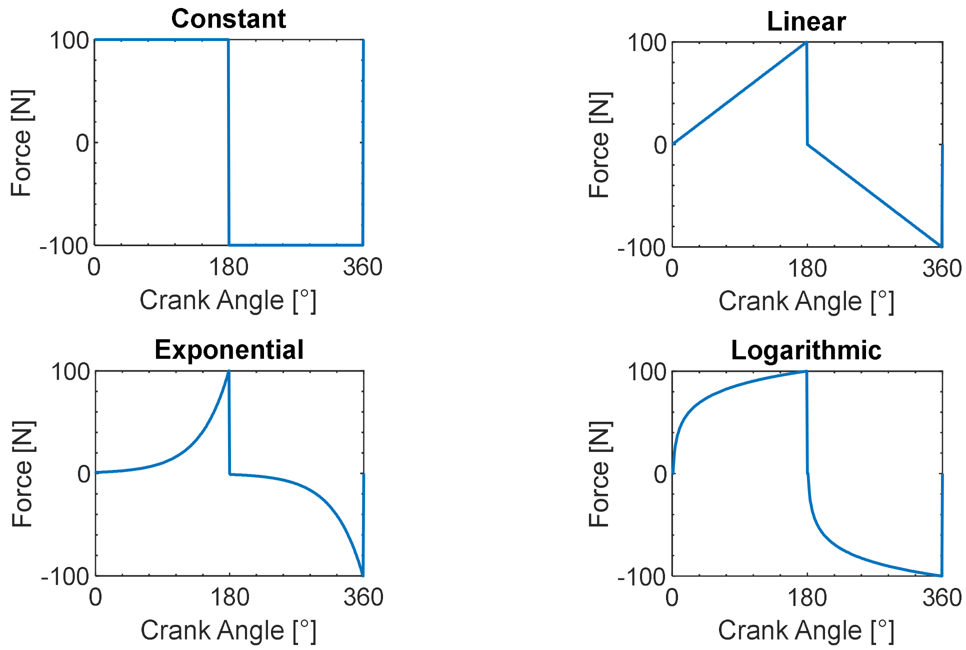

Figure 3.13. Selected external force profiles applied on the slider within one cycle: constant double acting, linear increase double acting, exponential double acting, and logarithmic double acting.

The specifications of the mechanisms used in the simulations for this section are provided in Table 2.1, while the corresponding joint friction coefficients are listed under case-b in Table 3.4. A consistent observation across both the slider-crank and Scotch-yoke mechanisms is that the output work per cycle is consistently lower than the input rotational work per cycle. This is primarily attributed to energy losses caused by frictions at the joints. Friction, as discussed in the previous section, affects the magnitude of the input torque required to drive the mechanisms, thereby impacting the overall work done per cycle.

Figures 3.14 and 3.15 present the simulation results for the scenario in which a constant load is applied to the slider during each stroke (double-acting), as illustrated in Figure 3.13 (*Constant*). Comparatively, the Scotch-yoke mechanism exhibits slightly higher work done per cycle than the slider-crank mechanism. This difference in energy consumption arises due to the kinematic pair differences between the two mechanisms. The Scotch-yoke, characterized by its additional joints and corresponding frictional losses, requires more energy input to achieve the same mechanical output.

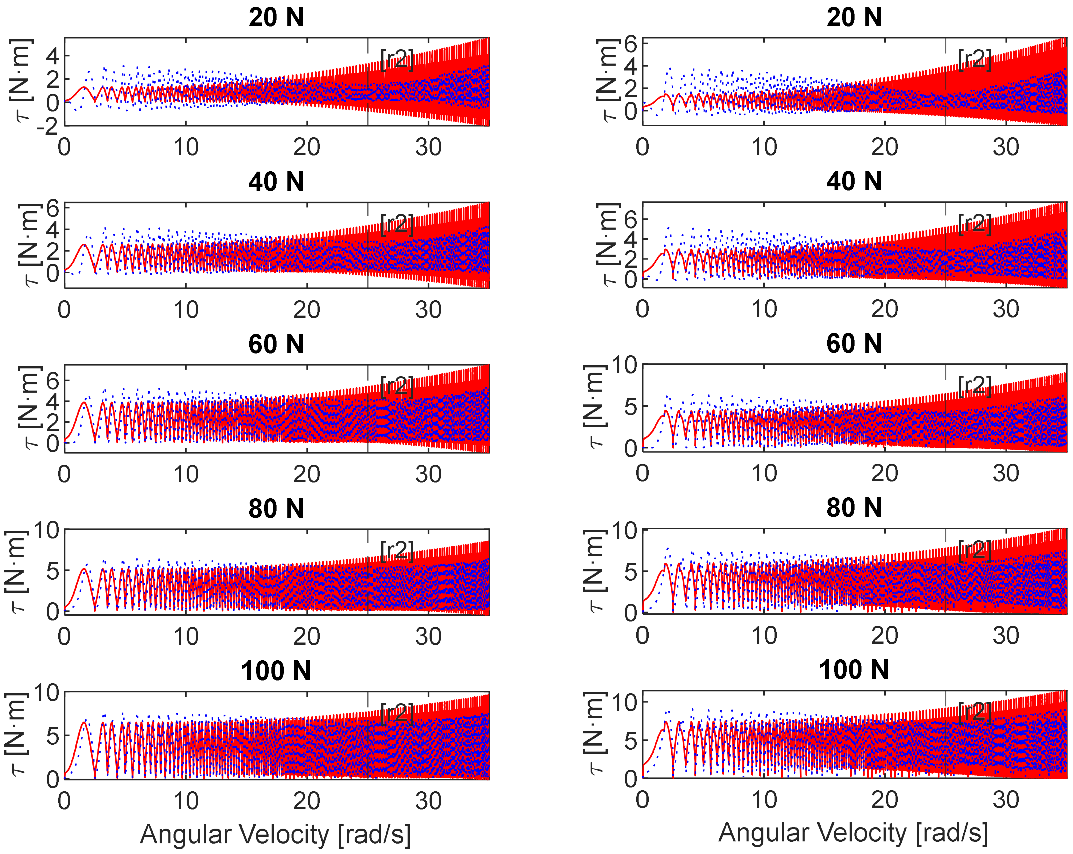

(a) (b)

Figure 3.14. Input torques of the slider-crank (a) and Scotch-yoke (b) mechanisms under various magnitudes of constant double-acting external force. Red curves represent the setups without spring elements, and blue curves represent the setups with spring element of 1250 N/m and gravity compensation. Simulations involve joint coefficients of friction μ_s = 0.5 and μ_d = 0.25.

When evaluating the performance of the slider-crank and Scotch-yoke mechanisms under varying constant loads, several important observations can be noted. The resonant frequency remains unchanged across different load magnitudes for both mechanisms, as shown in Figure 3.14. However, as the external load increases, the difference in RMS torque and work per cycle between the conventional and resonance setups progressively diminishes. The behavior arises because, as the load approaches or exceeds the mechanism's capability, the dynamic benefits of operating at resonance become less significant, ultimately reducing the effectiveness of resonance-based energy reduction.

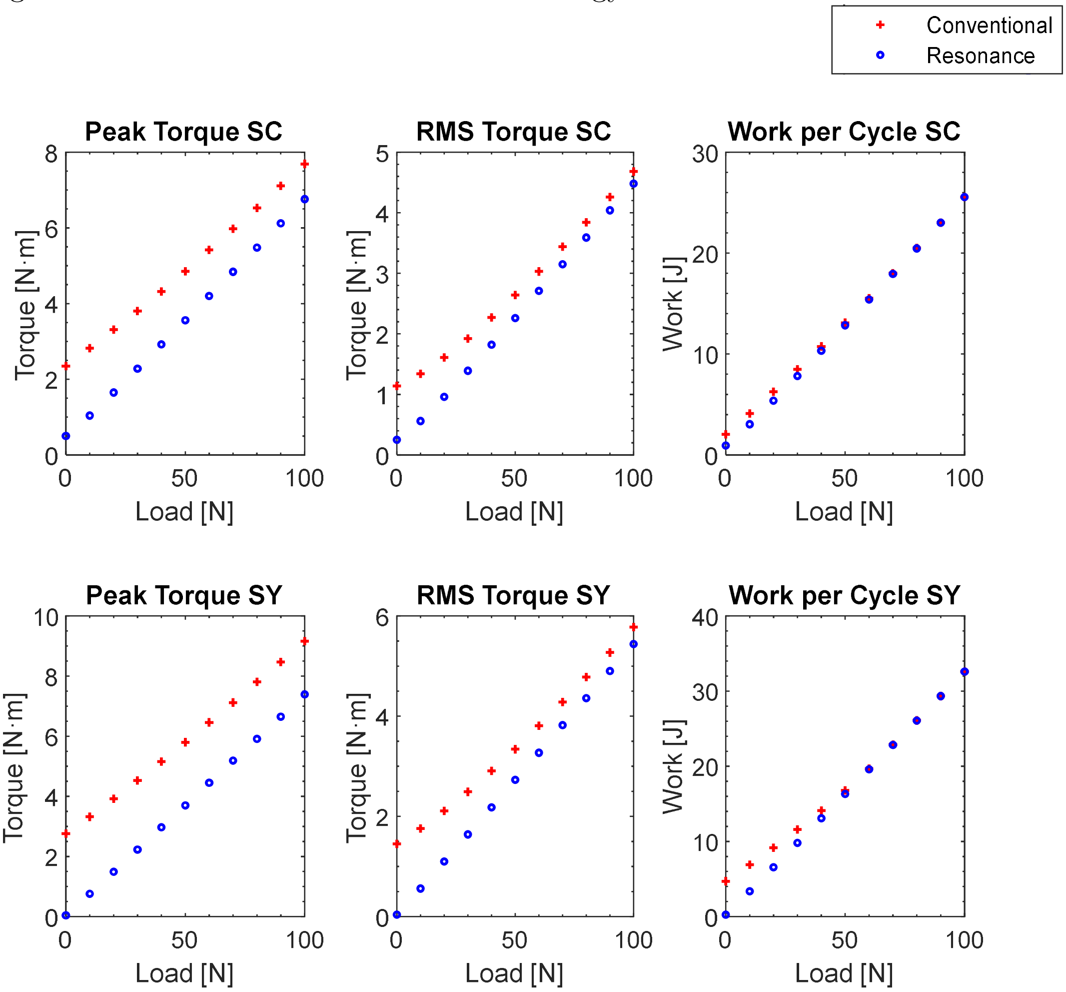

Figure 3.15. Input torque and work done per cycle of the slider-crank (SC) and Scotch-yoke (SY) mechanisms under various magnitudes of constant double-acting external force at resonant frequency (25 rad/s). Simulations involve joint coefficients of friction $\mu_s = 0.5$ and $\mu_d = 0.25$.

Under varying magnitudes of increasing linear double-acting external force, as depicted in Figure 3.13 (*Linear*), a key observation is the load-dependent nature of the resonant frequency for both the slider-crank and Scotch-yoke mechanisms, as shown in Figure 3.16. Referring to these results, Figure 3.17 presents the corresponding torque and work done per cycle for both mechanisms. It can be observed that, as the magnitude of the linear load increases, the resonant frequency also increases, indicating a direct correlation between load magnitude and resonant behavior. Across all linear load cases, both without spring and with spring configurations exhibit narrow resonance regions, demonstrating the ability of the mechanisms to achieve resonance conditions under different linear loading scenarios.

When identical linear loads are applied to both the conventional and resonance setups, the resonance setup incorporating the spring element always achieves resonance at higher angular velocities. This emphasizes the influence of the spring element in altering resonant behavior and its potential utility in tuning the system's operating speed in resonance, as previously discussed in Section 3.5. Another noteworthy finding is the near equivalence in resonant frequencies between the slider-crank and Scotch-yoke mechanisms under the same linear load magnitudes. This similarity holds regardless of whether the spring element is present.

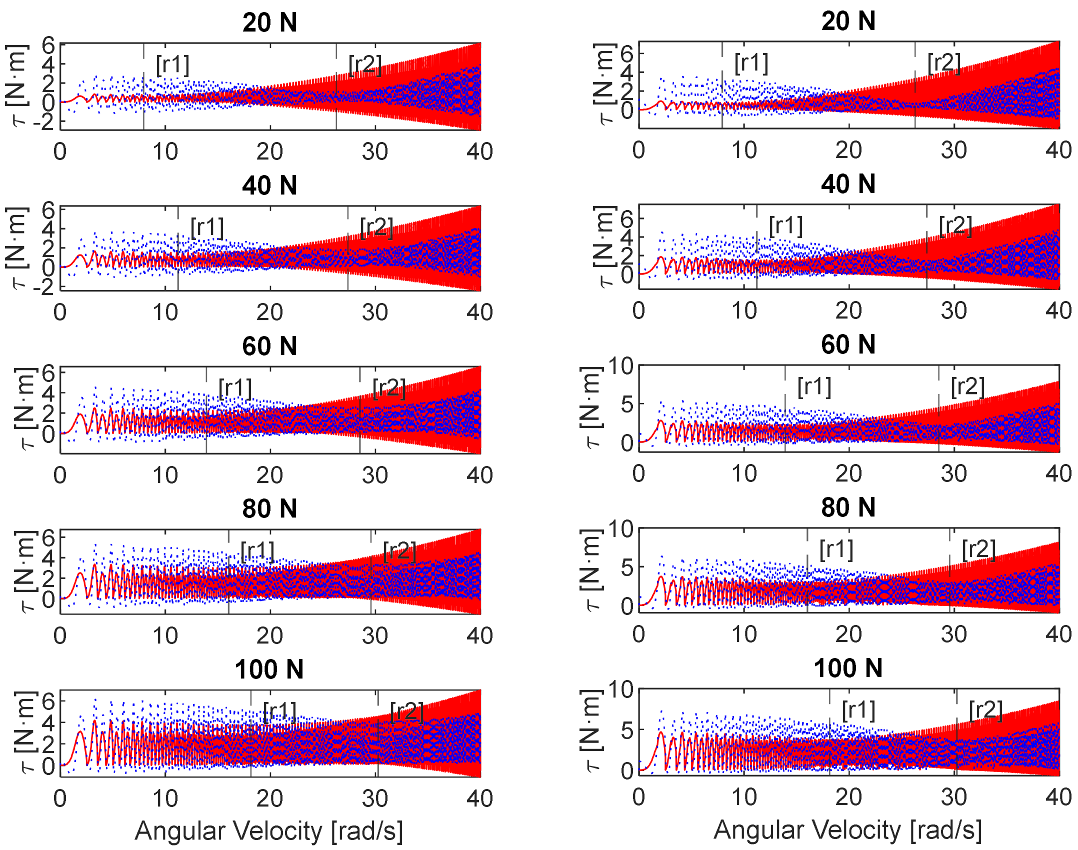

(a) (b)

Figure 3.16. Input torques of the slider-crank (a) and Scotch-yoke (b) mechanisms under various magnitudes of increasing, linear double-acting external force. Red curves represent the setups without spring elements, and blue curves represent the setups with spring element of 1250 N/m and gravity compensation. Simulations involve joint coefficients of friction $\mu_s = 0.5$ and $\mu_d = 0.25$.

Furthermore, despite differences in the resonant frequencies achieved, the Scotch-yoke mechanism displays comparable peak torque, RMS torque, and work done per cycle in both conventional and resonance configurations. These results demonstrate that the mechanisms employing spring elements can enable operation at higher rotational speeds while maintaining equivalent torque behavior and energy requirements to conventional setups operating at lower speeds.

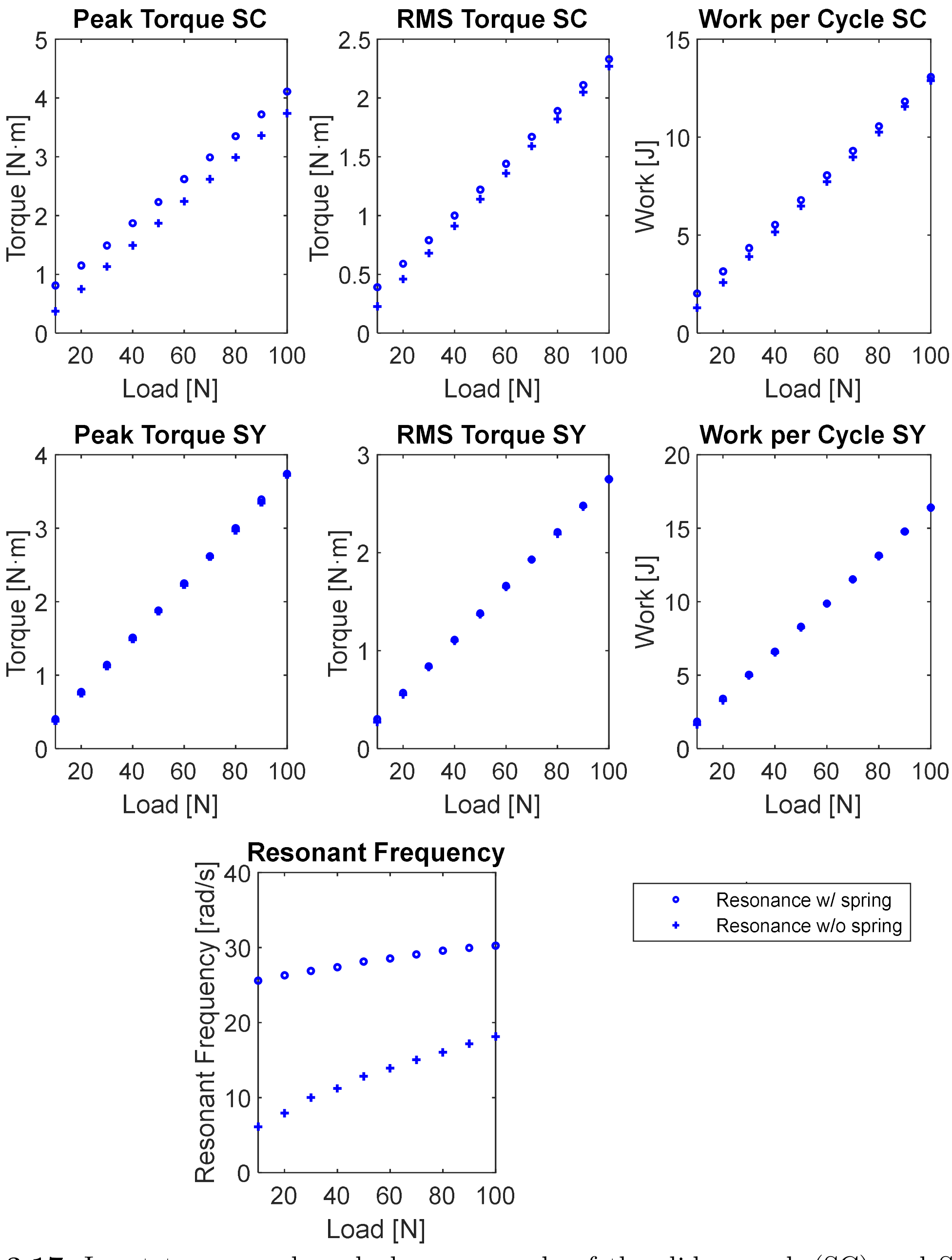

Figure 3.17. Input torque and work done per cycle of the slider-crank (SC) and Scotch-yoke (SY) mechanisms under various magnitudes of increasing, linear double-acting external force at their corresponding resonant frequency. Simulations involve joint coefficients of friction $\mu_s = 0.5$ and $\mu_d = 0.25$.

In the context of exponential loads, as illustrated in Figure 3.13 (*Exponential*), both the slider-crank and Scotch-yoke mechanisms exhibit a load-dependent resonant frequency, similar with the trends observed under increasing linear loads. This relationship is shown in Figure 3.18, while Figure 3.19 presents the corresponding torque and work done per cycle under varying magnitudes of exponential double-acting external force. As the magnitude of the load increases, the resonant frequency also increases, implying a correlation between load intensity and the system's dynamic response.

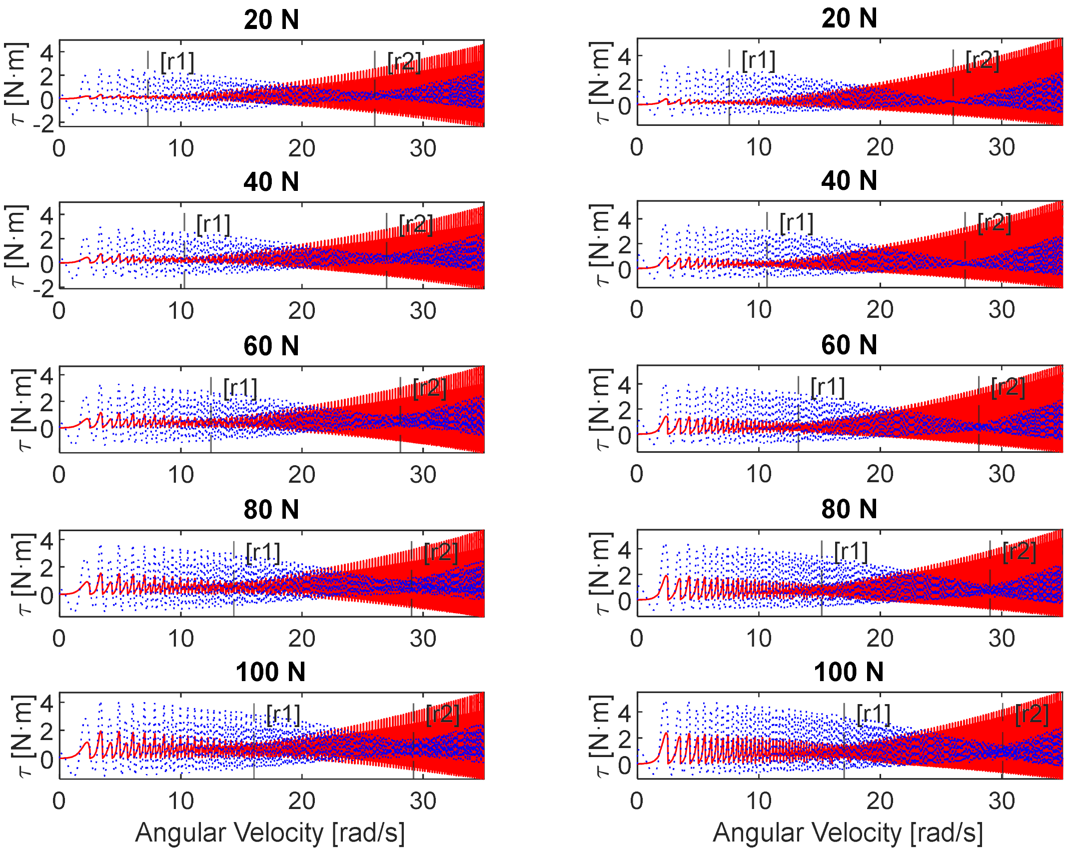

(a) (b)

Figure 3.18. Input torques of the slider-crank (a) and Scotch-yoke (b) mechanisms under different magnitudes of exponential double-acting external force. Red curves represent the setups without spring elements, and blue curves represent the setups with spring element of 1250 N/m and gravity compensation. Simulations involve joint coefficients of friction μ_s = 0.5 and μ_d = 0.25.

Across all exponential load cases, both without and with spring configurations consistently present narrow resonance regions, demonstrating their ability to achieve resonance within a range of exponential load conditions. Notably, for identical exponential load magnitudes, the presence of a spring element enables the resonance setup to achieve resonance at higher angular velocities. This outcome highlights the potential of the spring element to adjust operational speeds in resonance. An additional observation is the slight difference in resonant frequencies between the slider-crank and Scotch-yoke mechanisms under the same exponential loading. Specifically, the Scotch-yoke mechanism tends to exhibit marginally higher resonant frequencies compared to the slider-crank mechanism, irrespective of the inclusion of the spring element.

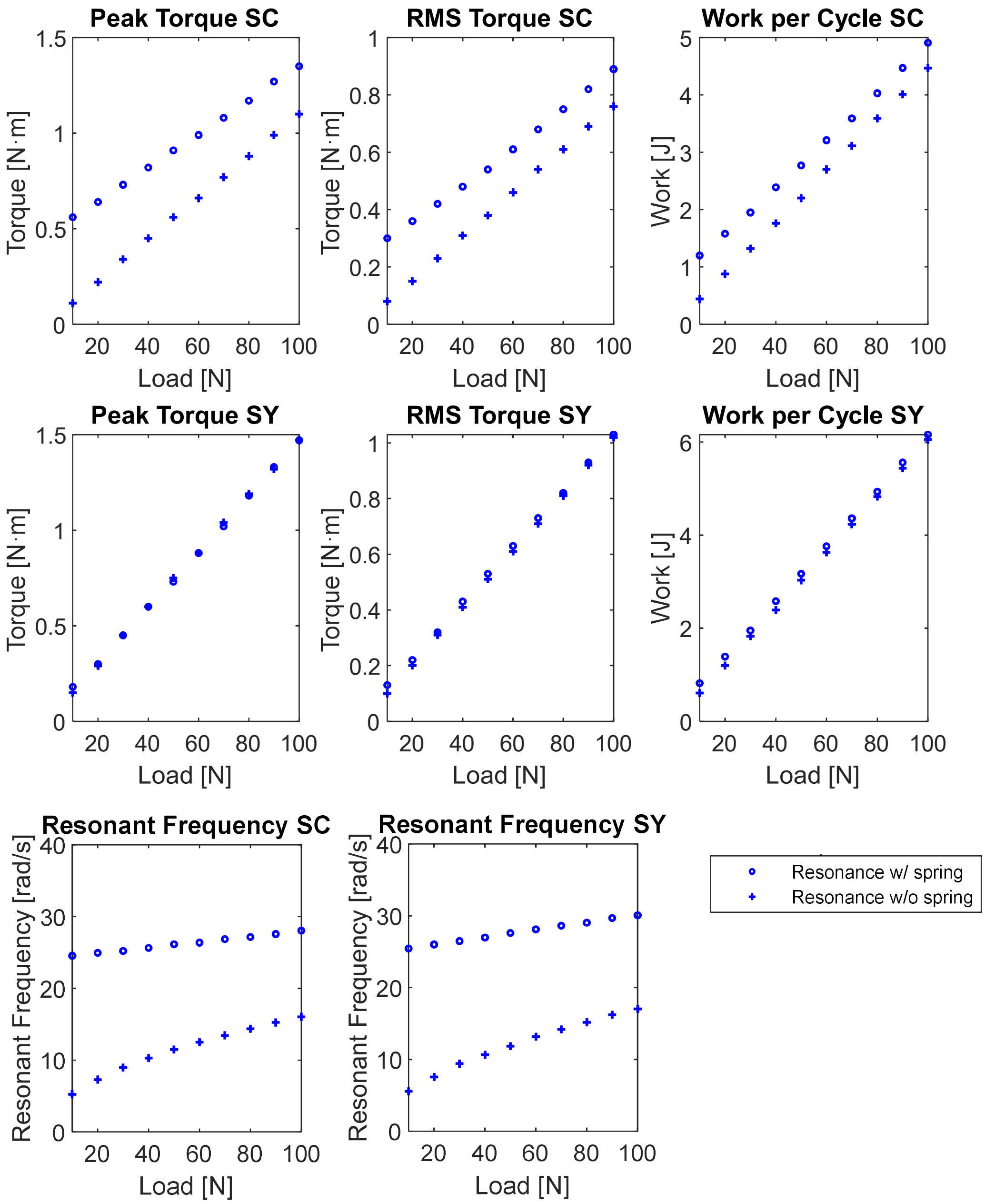

Figure 3.19. Input torque and work done per cycle of the slider-crank (SC) and Scotch-yoke (SY) mechanisms under different magnitudes of exponential double-acting external force at their corresponding resonant frequency. Simulations involve joint coefficients of friction $\mu_s = 0.5$ and $\mu_d = 0.25$.

In the final case example, presented in Figures 3.20 and 3.21, a logarithmic load profile—depicted in Figure 3.13 (*Logarithmic*)—is applied to the slider. A narrow resonance region is observed exclusively in the configurations incorporating a spring element, provided that the load magnitude remains within a manageable range, as shown in Figure 3.20. As the applied load increases significantly, the resonance region remains present; however, its effectiveness diminishes, as indicated by the convergence of the red marker (conventional setup) and the blue marker (resonance setup) in Figure 3.21.

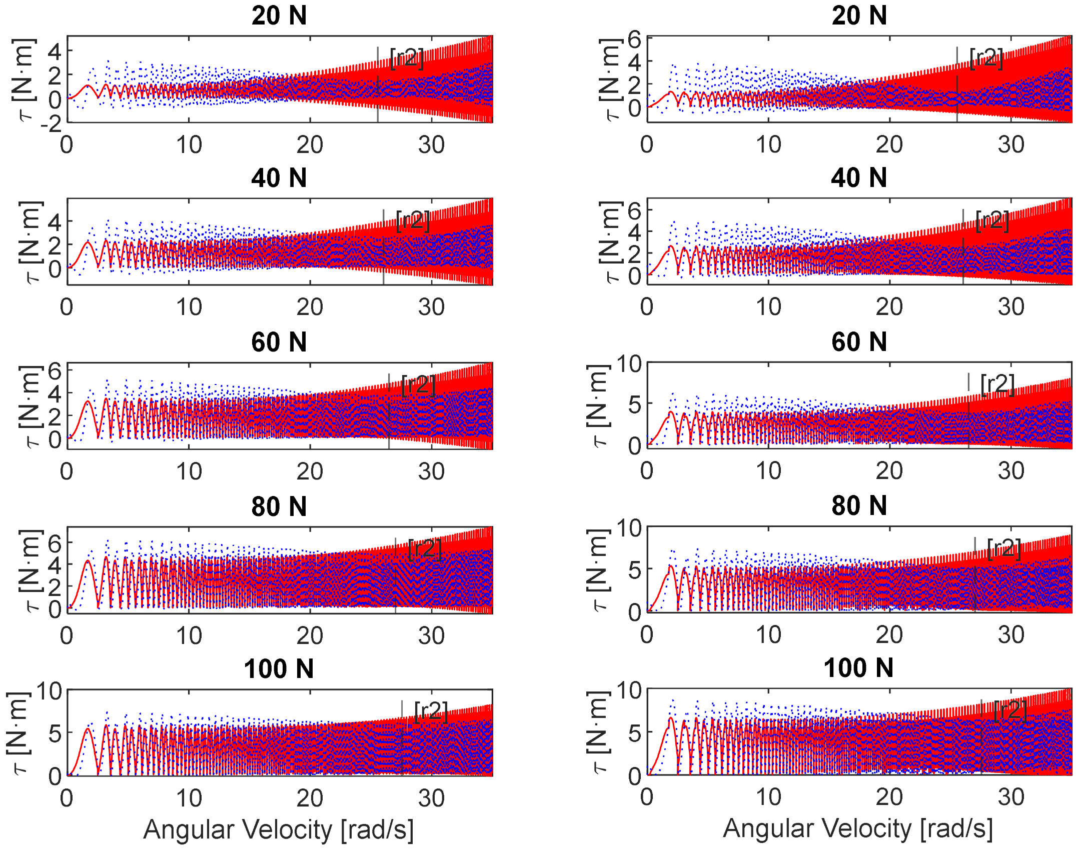

Figure 3.20. Input torques of the slider-crank (a) and Scotch-yoke (b) mechanisms under various magnitudes of logarithmic double-acting external force. Red curves represent the setups without spring elements, and blue curves represent the setups with spring element of 1250 N/m and gravity compensation. Simulations involve joint coefficients of friction μ_s = 0.5 and μ_d = 0.25.

At the corresponding resonant frequency, the resonance setup consistently demonstrates significant reductions in both peak torque and RMS torque relative to the conventional setup. This behavior is analogous to the observations made under constant load conditions, where resonance-induced energy savings become more evident under moderate loading. Nevertheless, as the external load magnitude continues to rise, the performance gap between the conventional and resonance setups progressively narrows. Specifically, the difference in RMS torque and work done per cycle diminishes, demonstrating the limitations of resonance-based efficiency gains under high-load conditions.

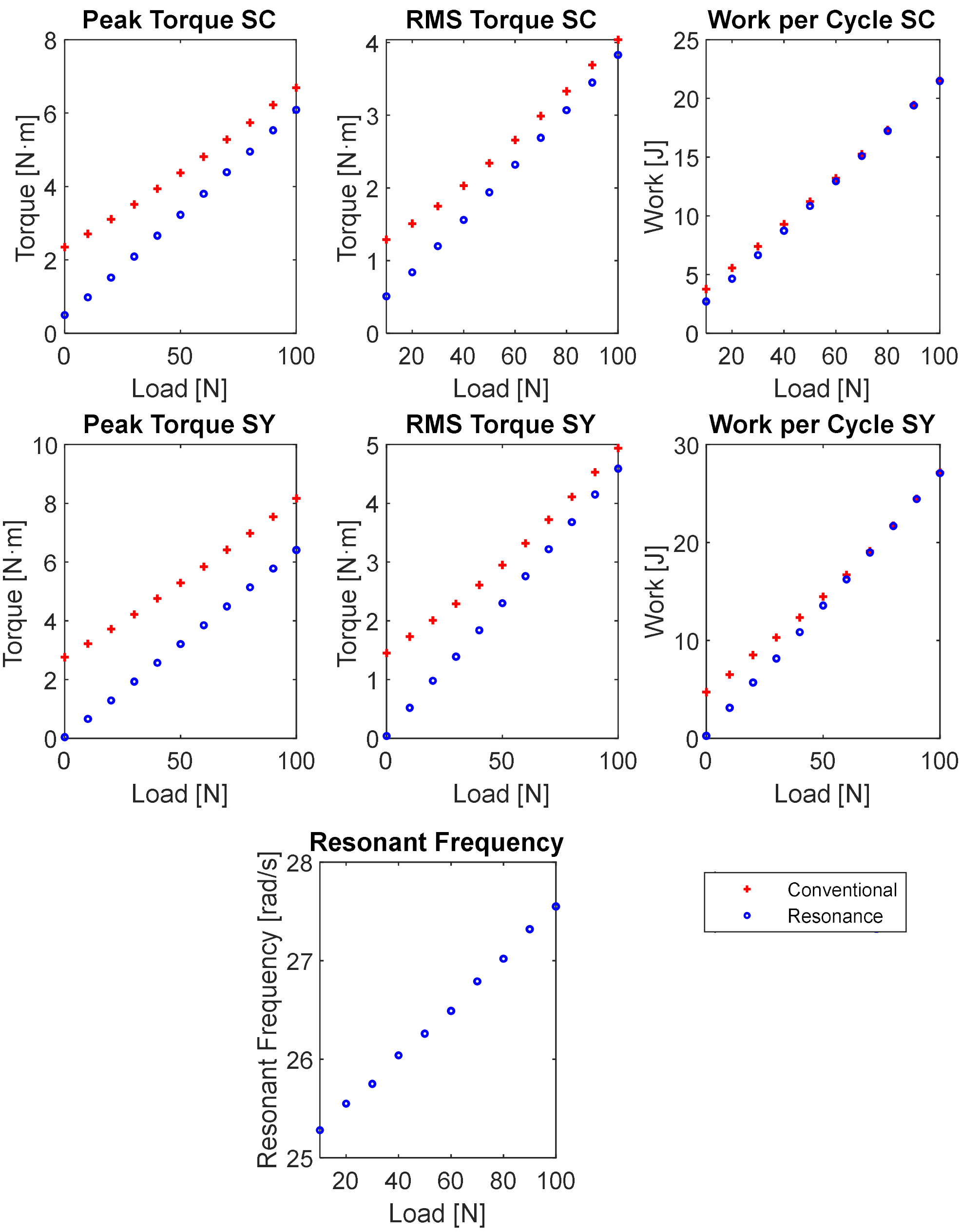

Figure 3.21. Input torque and work done per cycle of the slider-crank (SC) and Scotch-yoke (SY) mechanisms under various magnitudes of logarithmic double-acting external force at their corresponding resonant frequency. Simulations involve joint coefficients of friction $\mu_s = 0.5$ and $\mu_d = 0.25$.

3.9. Dynamics Under Electric Motor Drive

DC electric motors are mechanically commutated machines powered by a direct current (DC) electrical source. In these motors, the rotor (armature) current is switched using a mechanical commutator, ensuring that the relative angle between the stator and rotor magnetic flux remains close to 90°, thereby maximizing torque generation. DC motors are characterized by a rotating armature winding and a stationary magnetic field, which is produced either by a field winding or a permanent magnet. The configuration of the field and armature windings significantly influences the motor's inherent speed–torque characteristics. Speed control of DC motors can be achieved by varying the voltage applied to the armature or by adjusting the field current. A recurring control objective for the machine is to regulate its speed in the occurrence of parametric changes, unknown dynamics, and external disturbances [123].

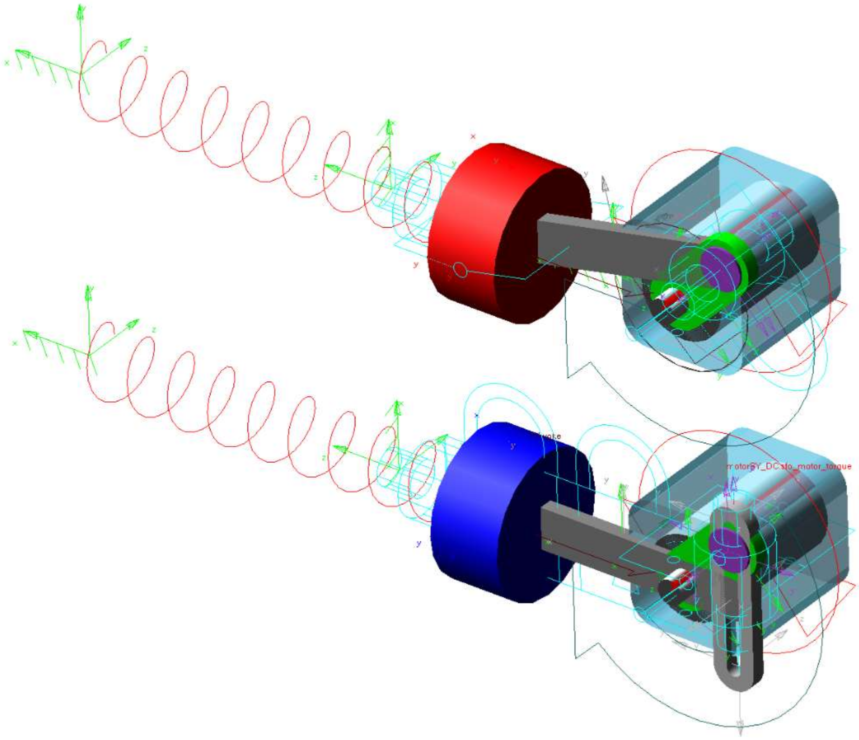

Figure 3.22. Multibody dynamics models of the slider-crank (red slider) and Scotch-yoke (blue slider) mechanisms driven by DC motor. Mechanism specifications are given in Table 2.1 and motor parameters in Table 3.5. Conventional configurations are compared with resonance configurations employing a spring stiffness of 1817.98 N/m and gravity compensation. Simulations are performed without friction or externally applied forces.

In this section, the dynamics of both the conventional and resonance-based slider-crank and Scotch-yoke mechanisms are analyzed when driven by an analytical electric motor [121], shown in Figure 3.22. A shunt DC motor is selected for this analysis due to its good speed regulation characteristics even under varying loads. The torque τ produced by a DC shunt motor is governed by Equation 3.19, measured in newton-meters. The torque constant is represented by K, ϕ denotes the magnetic flux per pole in Webers, while the armature current is given by I_a, measured in amperes.

$$\tau = K\boldsymbol{\phi}I_a \tag{3.19}$$

The torque constant K, armature current I_a, and back electromotive force induced E_b (in volts) are calculated by Equations 3.20-3.22; where z is the total number of conductors, p indicates the number of magnetic poles, and a refers to the number of parallel paths in the armature. The source voltage supplied to the motor is denoted by E_s (in volts). The armature resistance is denoted by R_a, measured in ohms (Ω). Lastly, n denotes the rotational speed of the armature, expressed in revolutions per minute (RPM).

$$K = \frac{zp}{2\pi a} \tag{3.20}$$

$$I_a = \frac{E_s - E_b}{R_a} \tag{3.21}$$

$$E_b = \frac{z\phi np}{60a} \tag{3.22}$$

The specifications of the simulated motor are listed in Table 3.5. Simulations were conducted under gravity-compensated conditions, with no friction or external forces applied. Figure 3.23 presents the simulation results showing the angular velocity profiles of the slider-crank and Scotch-yoke mechanisms driven by the DC motor, targeting an angular velocity of approximately 30.15 rad/s—corresponding to the resonance condition for a spring element stiffness of 1817.98 N/m.

Table 3.5. Motor specification.

DC type	Shunt
Rotor length	100 mm
Rotor radius	30 mm
Stator length	100 mm
Stator width	90 mm
Number of conductors z	100
Armature resistance R_a	0.2 Ω
Flux per pole ϕ	0.025 Wb
Number of poles p	8
Number of parallel paths in the armature a	2
Source voltage E_s	48 V

It can be observed that the motor ramps up to the target angular velocity in both configurations. The figure also includes a zoomed-in view of the crank angular displacement ranging from 360° to 1440°, showing up the dynamic behavior within a few full revolutions. In the conventional setup, significant fluctuations in angular velocity are evident, indicating instability and increased inertial loading during operation. In contrast, the resonance setup exhibits a much more stable angular velocity profile, indicating smoother dynamic performance due to the compensating effects of the spring element.

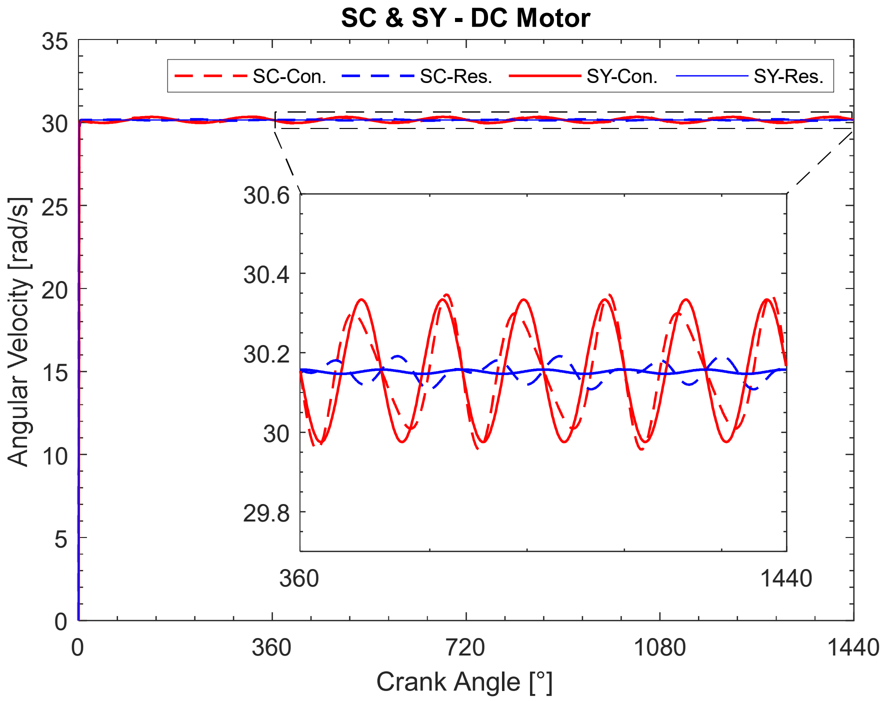

Figure 3.23. Angular velocity of the slider-crank and Scotch-yoke mechanisms driven by the DC motor. Red curves represent the setups without spring elements, and blue curves represent the setups at resonance with spring element of 1817.98 N/m and compensated gravity. Simulations are done without involving friction and externally applied forces.

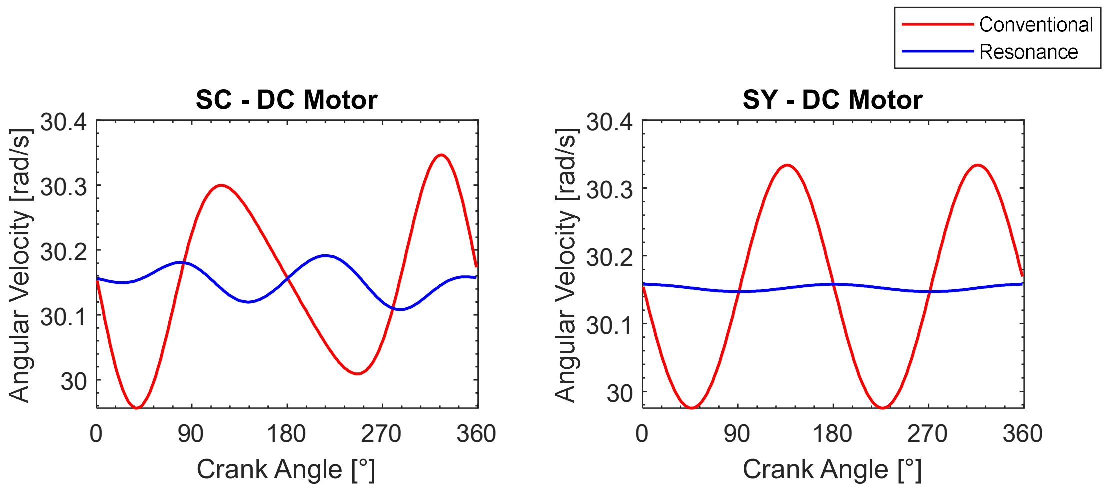

Figure 3.24. Angular velocity of the slider-crank (SC) and Scotch-yoke (SY) mechanisms driven by the DC motor in one cycle. Red curves represent the setups without spring elements, and blue curves represent the setups at resonance with spring element of 1817.98 N/m and compensated gravity. Simulations are done without involving friction and externally applied forces.

This behavior is further illustrated in Figure 3.24, which presents the angular velocity profiles of both configurations over a single cycle. For the slider-crank mechanism, the conventional setup exhibits angular velocity fluctuations ranging from 29.96 rad/s to 30.35 rad/s. In contrast, its resonance configuration shows significantly reduced variation, with angular velocities ranging from 30.11 rad/s to 30.19 rad/s—closer to the target value of 30.15 rad/s. Similarly, the conventional Scotch-yoke mechanism fluctuates between 29.98 rad/s and 30.33 rad/s, while its resonance counterpart demonstrates better stability, maintaining angular velocity within a narrow range of 30.15 rad/s to 30.16 rad/s.

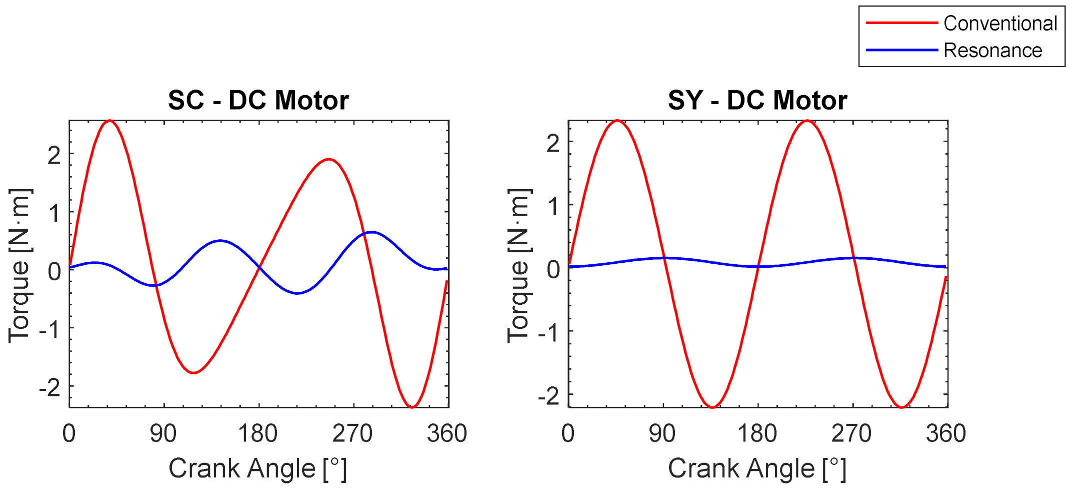

Figure 3.25. Motor torque driving the slider-crank and Scotch-yoke mechanisms in one cycle. Red curves represent the setups without spring elements, and blue curves represent the setups at resonance with spring element of 1817.98 N/m and compensated gravity. Simulations are done without involving friction and externally applied forces.

Figure 3.25 illustrates the motor output torque required to sustain the angular velocity profiles shown in Figure 3.24 for both the slider-crank and Scotch-yoke mechanisms. The torque fluctuations closely follow the trends observed in the angular velocity variations. Specifically, when the angular velocity drops below the target value, the motor responds by increasing torque output to restore it. Conversely, when the angular velocity exceeds the target, the motor torque becomes theoretically negative, indicating a resisting effect.

The resonance setup of the slider-crank mechanism results in a significantly more stable motor output torque, with an RMS torque of 0.31 $N \cdot m$, compared to 1.49 $N \cdot m$ in the conventional configuration. Similarly, the Scotch-yoke mechanism demonstrates even greater improvement under resonance conditions, where the RMS torque drops to 0.09 $N \cdot m$, in contrast to 1.61 $N \cdot m$ in the conventional setup. Overall, these results demonstrate the enhanced dynamic stability achieved through resonance, particularly in maintaining consistent operating speeds.

3.10. Multiple Slider Configuration

Application of resonance in slider-crank and Scotch-yoke mechanisms with multiple sliders can enhance dynamic performance, provided the mechanisms are primarily balanced. *Primary balance* refers to a condition in which the inertial forces generated by the rotating and reciprocating components are effectively canceled at the crankshaft-to-ground joint (joint-A, as shown in Figure 2.8) [124]. In this state, the mechanism exerts no net reaction force on the frame during crankshaft rotation. Achieving primary balance typically involves configuring the mechanism such that the inertial forces produced by each slider assembly are counteracted by those of another assembly [125]. In systems with multiple sliders, employing an even number of symmetrically arranged slider units allows the opposing forces to cancel each other out, leading to a more stable and balanced operation [126].

For the slider-crank mechanism, further dynamic improvements can be realized through *secondary balance*. This involves mitigating higher-order inertial effects—especially those from the reciprocating components—which are not addressed by primary balancing alone. A common method to achieve secondary balance is the use of a counterweighted crankshaft, where additional masses are attached to the crank to offset the forces arising from the connecting rods and sliders [124]. Alternatively, a combined approach using both a counterweighted crankshaft and a *balance shaft* can be employed. The balance shaft, rotating at twice the crankshaft speed, is designed to counteract second-order harmonic forces, thereby reducing overall vibration and enabling lighter crankshaft counterweights [120].

This section presents common layout examples, such as four sliders arranged in-line or in a horizontally opposed configuration. As illustrated in Figure 3.26, these layouts achieve primary balance by pairing sliders that move in opposite directions, with adjacent crank arms offset by 180°. The plots compare configurations without spring elements (red curves) to those with spring elements (blue curves) under gravity-compensated conditions. It is evident that, when operated at their respective resonant frequencies, setups with spring element exhibit a significantly reduced input torque fluctuation. Despite having similar mass and inertia specifications, the slider-crank mechanism exhibits a notably higher resonant frequency—approximately 32 rad/s versus 25 rad/s for the Scotch-yoke—primarily due to the rotational motion of the connecting rod. As discussed earlier, this rotational motion introduces a varying component of force along the slider's direction, which is absent in the purely translational motion of the Scotch-yoke. When properly balanced and configured, this resonance-based approach can also be extended to other common multi-slider layouts, such as V-type, W-type, and radial configurations.

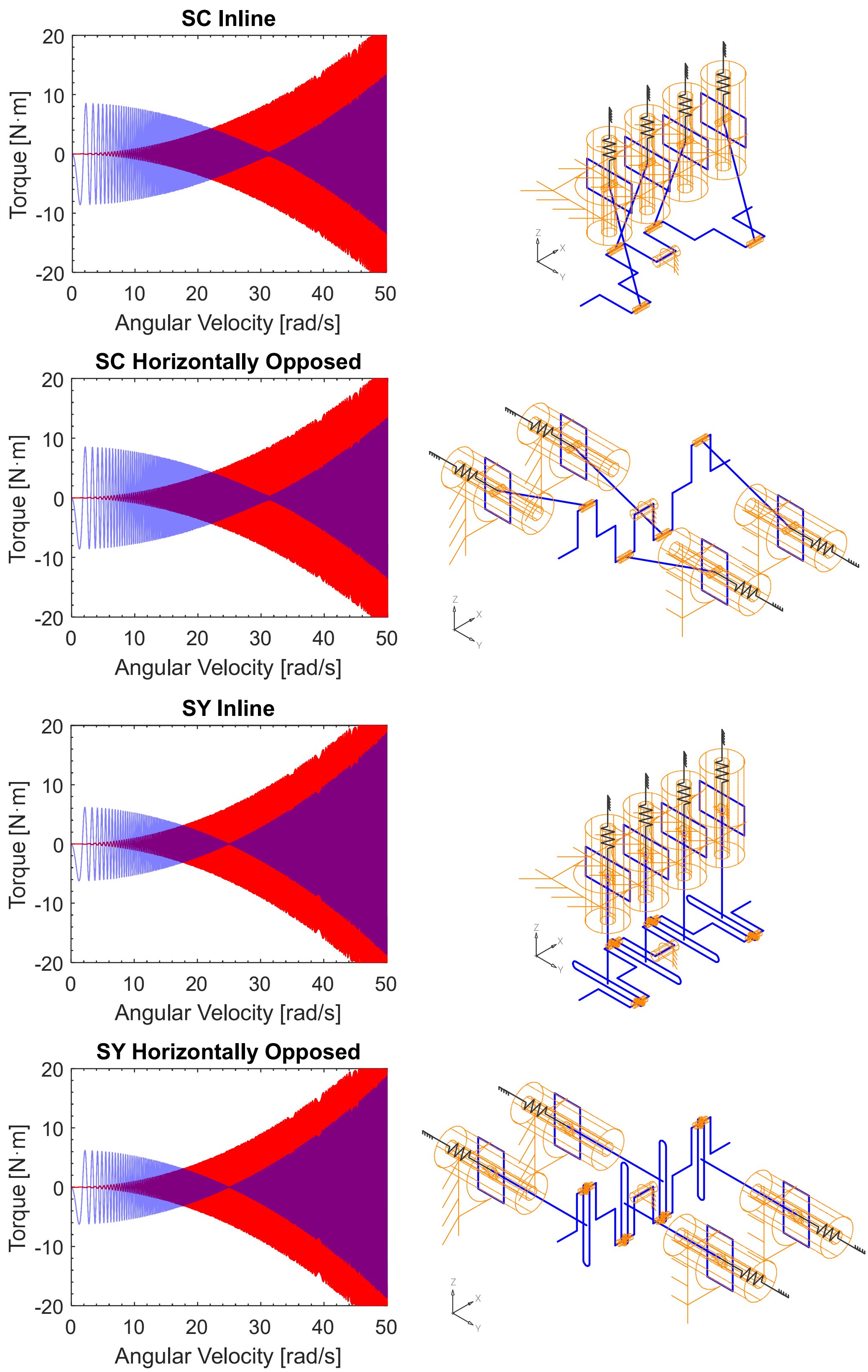

Figure 3.26. Input torques of the slider-crank (SC) and Scotch-yoke mechanism (SY) under a ramp crank angular velocity input at different layouts. Red curves represent the setups without spring elements, and blue curves represent the setups with spring elements k of 1250 N/m. Simulations are done without involving friction, externally applied forces, and gravity.

Chapter 4

Experimental Validation

4.1. Physical Prototype

As shown in Figures 4.1 and 4.2, the experimental prototypes used for validation comprise several essential components, including an electric motor, crank, connecting rod, slider, adjustable reciprocating mass, spring elements, a rack-and-pinion mechanism, and a brake system with an adjuster. The entire assembly is mounted in a horizontal-flat orientation to compensate the influence of gravitational forces on the system dynamics. In accordance with the design synthesis, spring elements are integrated between the slider and the frame to facilitate resonant behavior. The brake system applies an external force to the slider via the rack-and-pinion mechanism, with the adjuster enabling tuning of the applied load. Additionally, a force sensor is installed in-line with the connecting rod to measure

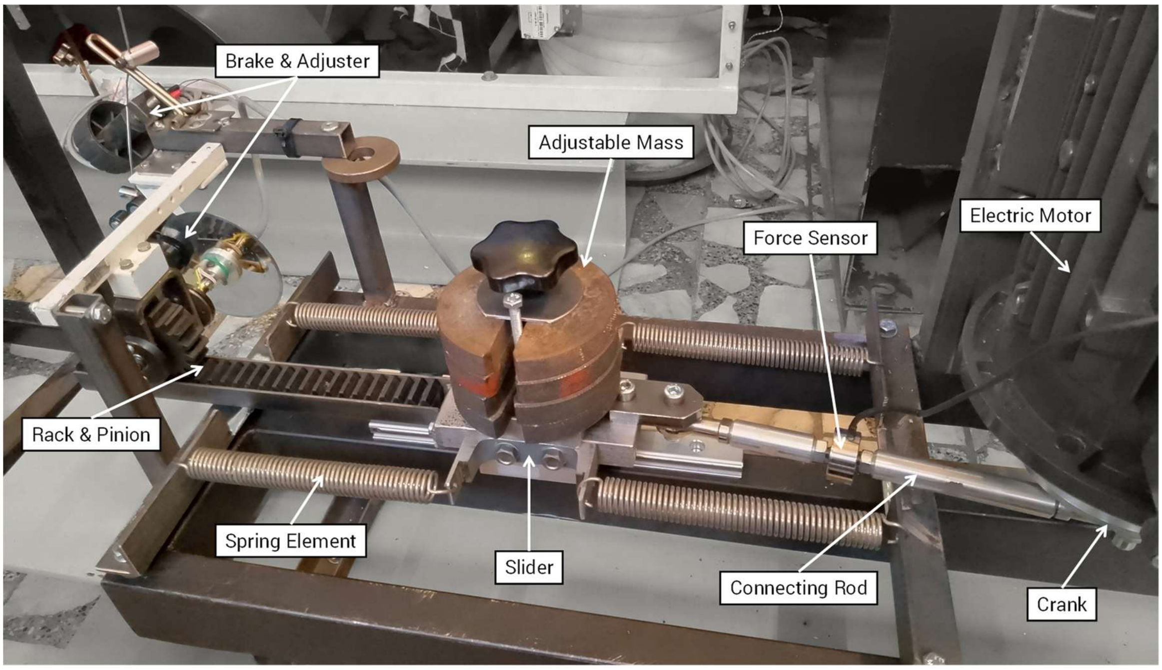

Figure 4.1. Slider-crank physical prototype.

the dynamic forces during operation, thereby providing insight into the system's behavior. A detailed view of the force measurement instrument is provided in Figure 4.3. To measure the force in the connecting rod, a force sensor is integrated inline with the rod assembly. The sensor is positioned such that it directly senses the axial force transmitted between the crank (or yoke) and the slider. The output, typically a millivolt-level signal proportional to force, is transmitted to the DAQ system.

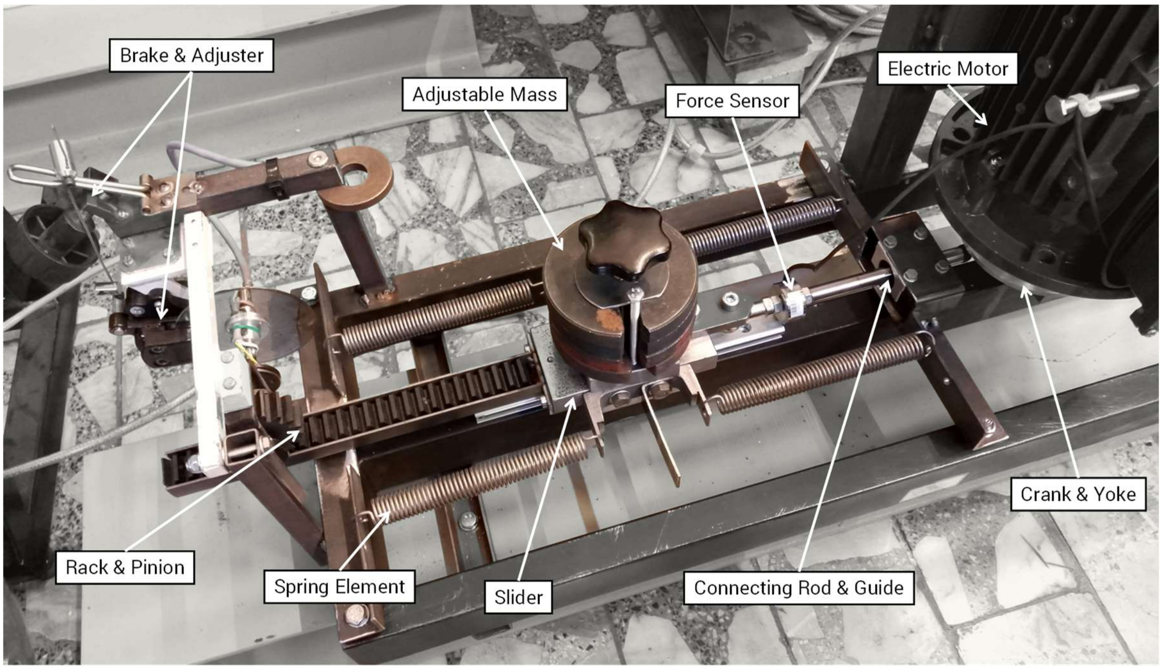

Figure 4.2. Scotch-yoke physical prototype.

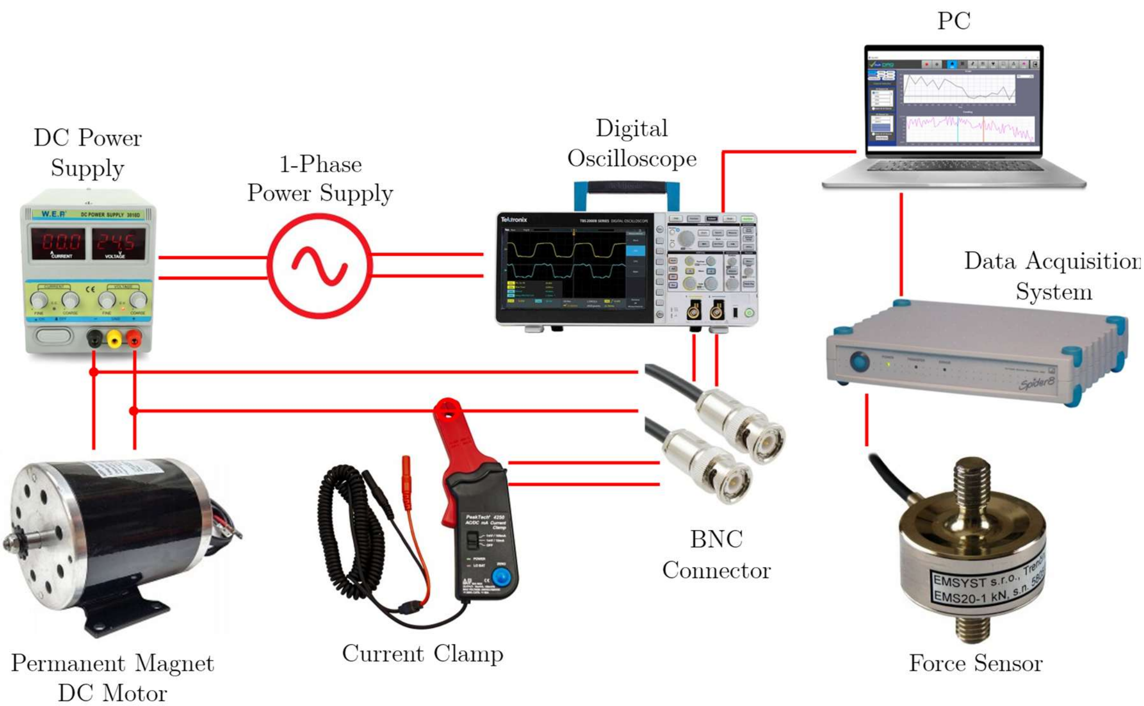

Figure 4.3. Schematic diagram of the power measurement of the slider-crank and Scotch-yoke mechanisms prototype.

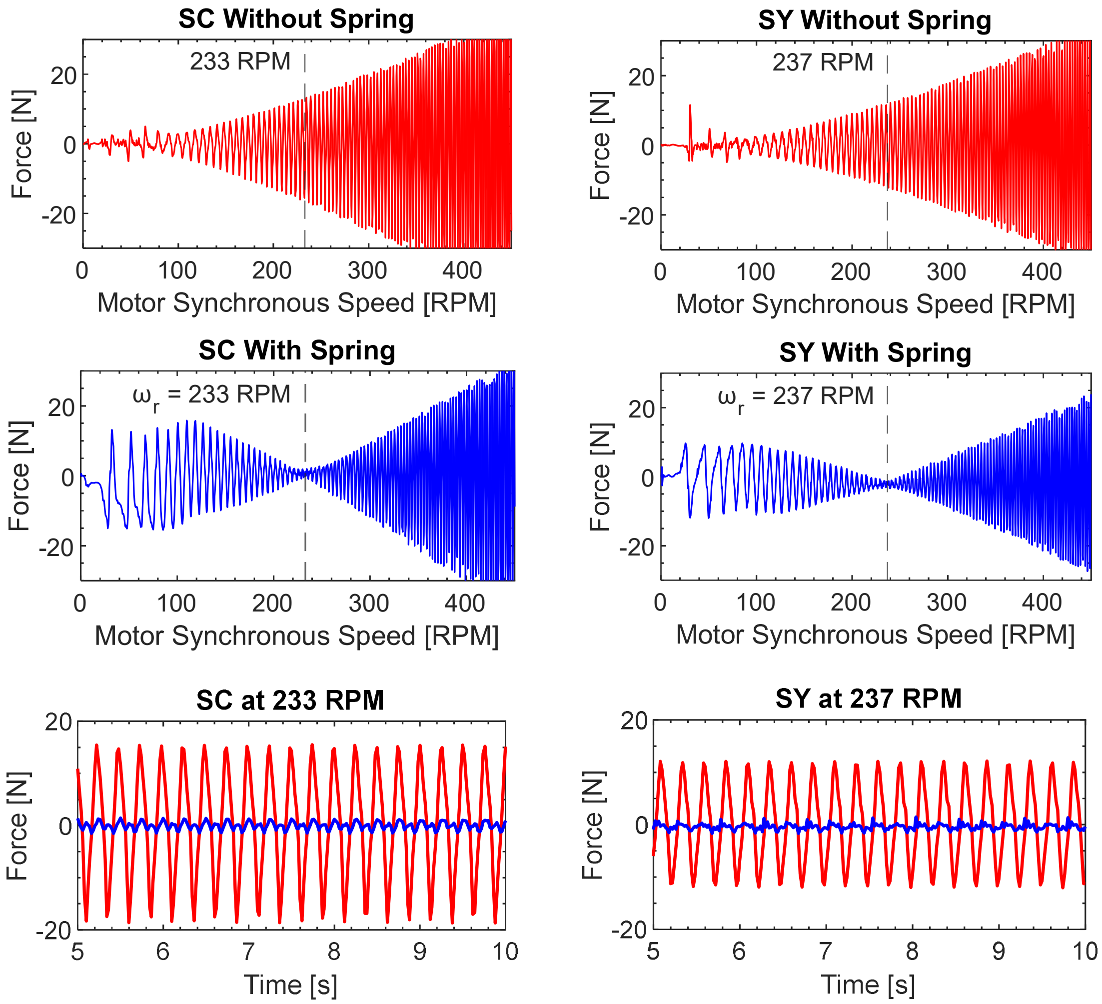

Figure 4.4. Forces on the connecting rod of the slider-crank and Scotch-yoke prototypes without externally applied load condition. Positive values indicate compressive force, while negative values indicate tensile force.

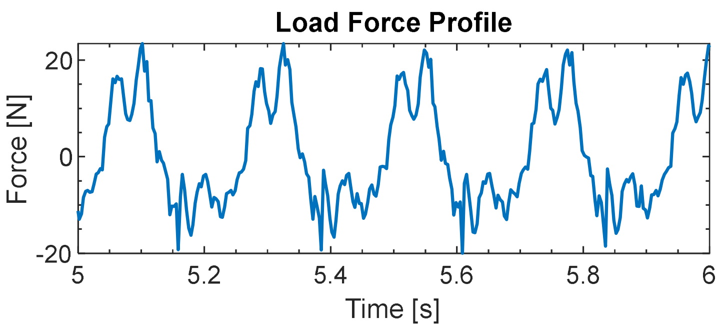

Figure 4.5. Example of an externally applied force profile generated by the prototype brake.

Experimental testing under no-load conditions shows the most pronounced differences between the conventional and resonance configurations, as illustrated in Figure 4.4. For the slider-crank mechanism, the resonance setup—incorporating a spring element and operating at its resonant frequency—achieves a 91.7% reduction in the peak-to-peak force measured on the connecting rod compared to the conventional configuration. Similarly, the Scotch-yoke mechanism operating under resonance conditions demonstrates an 87.4% reduction in peak-to-peak connecting rod force relative to its conventional counterpart. In the following subsections, both mechanisms are further evaluated under externally applied loads introduced via the brake system, with the corresponding force profile shown in Figure 4.5.

4.2. Influence of Reciprocating Body Mass

Simulations presented in Section 3.5 demonstrate that, in the absence of dissipative forces, reciprocating bodies generate comparable magnitudes of inertia force at their respective resonant frequencies when using the same spring element stiffness, irrespective of the mass of the reciprocating body. In spite of this, experimental results reveal slight differences from this behavior in both mechanisms, as illustrated in Figure 4.6 and detailed in Table 4.1. The externally applied force profile from the brake system is shown in Figure 4.5, with all tests conducted at a force amplitude of around 14.7 N. The results indicate that the peak-to-peak force increases for both conventional and resonance configurations as the reciprocating mass increases. For the slider-crank mechanism, the difference between the conventional and resonance setups becomes more pronounced with heavier reciprocating bodies. In contrast, the Scotch-yoke mechanism exhibits a less consistent trend. These deviations from the simulation results are attributed to the presence of Coulomb damping and the applied external force in the experimental setup, where larger masses induce higher frictional forces. Despite these discrepancies, the resonance setups consistently demonstrate superior dynamic performance, evidenced by reduced peak-to-peak forces and improved system response.

Table 4.1. Forces exerted on the connecting rod of both the conventional setup (without the spring element) and the resonance setup (with the spring element), operating at a resonant frequency under varying masses of the reciprocating bodies. All setups are characterized by the same spring stiffness of 4116.08 N/m and an externally applied force of 14.7 N.

Mechanism	Additional Mass [kg]	Resonant Frequency [RPM]	Peak-to-peak Force		
			Conventional [N]	Resonance [N]	Difference [%]
Slider-Crank	1	216	35.12	9.28	73.6
	2	199	41.54	10.08	75.7
	3	184	49.02	11.12	77.3
Scotch-Yoke	1	215	27.33	4.8	82.4
	2	190	30.64	5.12	83.2
	3	177	30.8	5.52	82.1

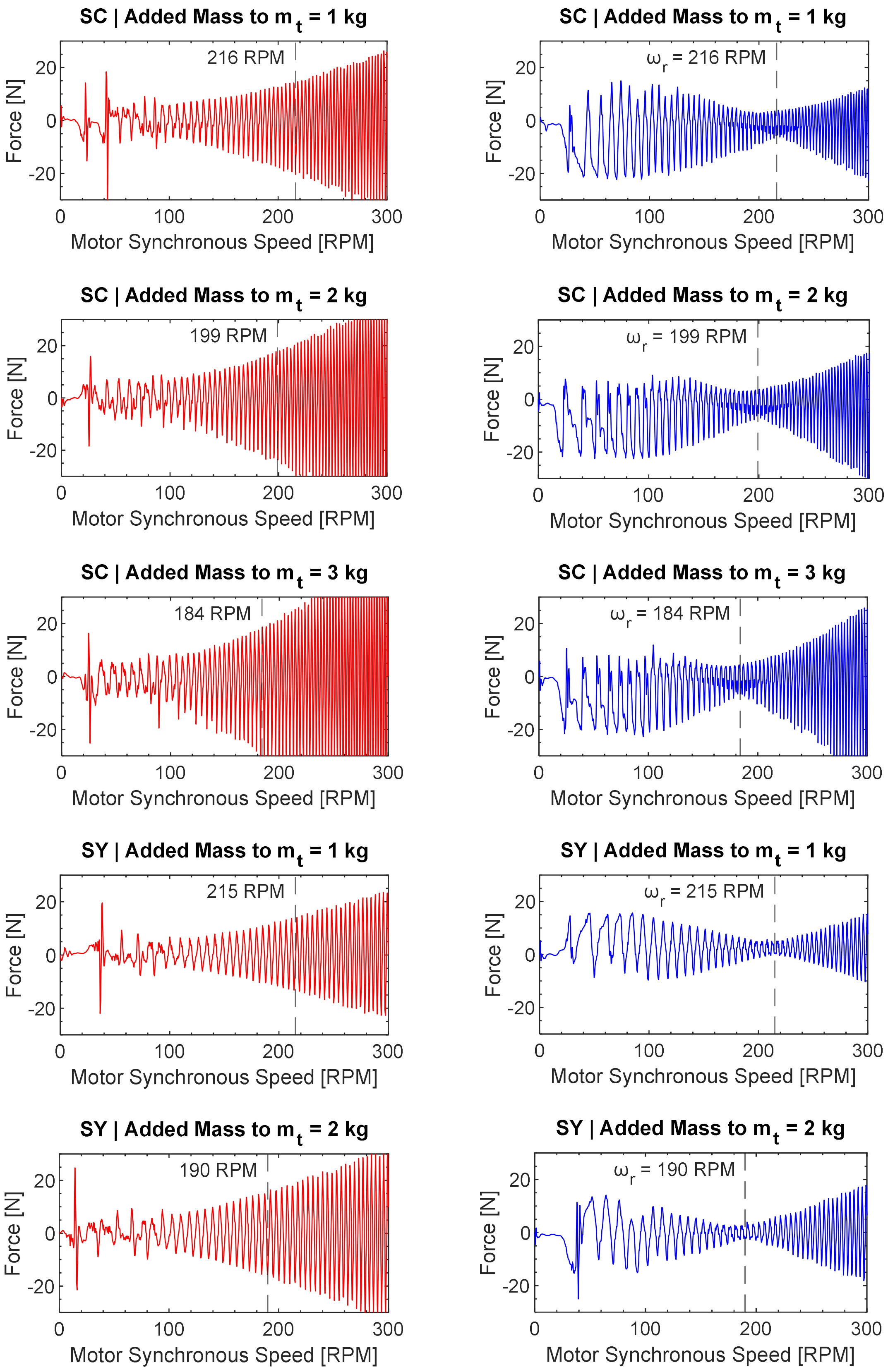
SC | Added Mass to m_t = 1 kg
216 RPM
SC | Added Mass to m_t = 1 kg
ω_r = 216 RPM
SC | Added Mass to m_t = 2 kg
199 RPM
SC | Added Mass to m_t = 2 kg
ω_r = 199 RPM
SC | Added Mass to m_t = 3 kg
184 RPM
SC | Added Mass to m_t = 3 kg
ω_r = 184 RPM
SY | Added Mass to m_t = 1 kg
215 RPM
SY | Added Mass to m_t = 1 kg
ω_r = 215 RPM
SY | Added Mass to m_t = 2 kg
190 RPM
SY | Added Mass to m_t = 2 kg
ω_r = 190 RPM
Force [N]
Motor Synchronous Speed [RPM]
20
0
-20
0
100
200
300

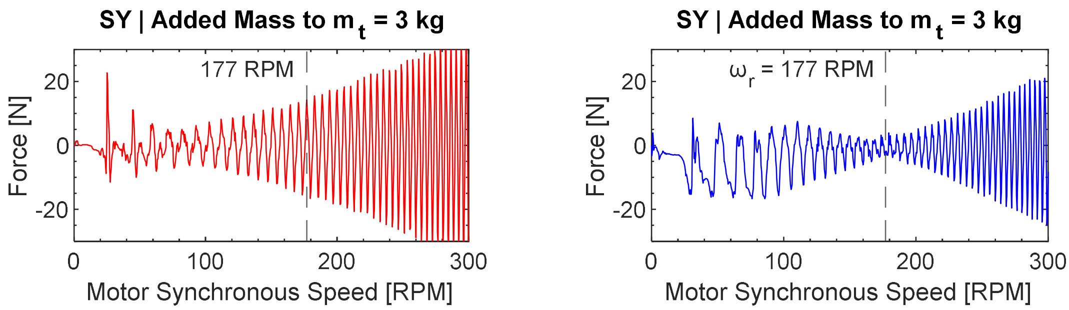

Figure 4.6. Forces on the connecting rod of the slider-crank and Scotch-yoke prototypes under different reciprocating masses. All setups are characterized by the same externally applied force of 14.7 N. The red curves represent setups without springs, while the blue curves represent setups with a spring stiffness of 4116.08 N/m.

4.3. Influence of Spring Element Stiffness

In investigating the influence of spring element stiffness, key parameters such as reciprocating mass and externally applied force were held constant across all setups. Both simulation and experimental results exhibit consistent trends. Definitely, an increase in spring stiffness corresponds to higher resonant frequencies and elevated forces acting on the joints. As illustrated in Figure 4.7 and detailed in Table 4.2, the difference in force experienced by the connecting rod between the conventional and resonance setups becomes increasingly pronounced with higher spring stiffness. This observation is in strong agreement with the trends predicted by simulation.

Table 4.2. Forces exerted on the connecting rod of both the conventional setup (without the spring element) and the resonance setup (with the spring element), operating at resonant frequency under varying spring stiffness. All setups are characterized by the same reciprocating body mass and an externally applied force of 14.7 N.

Mechanism	Spring Stiffness [N/m]	Resonant Frequency [RPM]	Peak-to-peak Force		
			Conventional [N]	Resonance [N]	Difference [%]
Slider-Crank	2058.04	194	23.22	11.32	51.2
	4116.08	254	37.39	10.56	71.8
	5130.9	327	55.36	10.31	81.4
Scotch-Yoke	2058.04	188	18.8	7.04	62.6
	4116.08	253	26.72	5.2	80.5
	5130.9	327	40.01	4.24	89.4

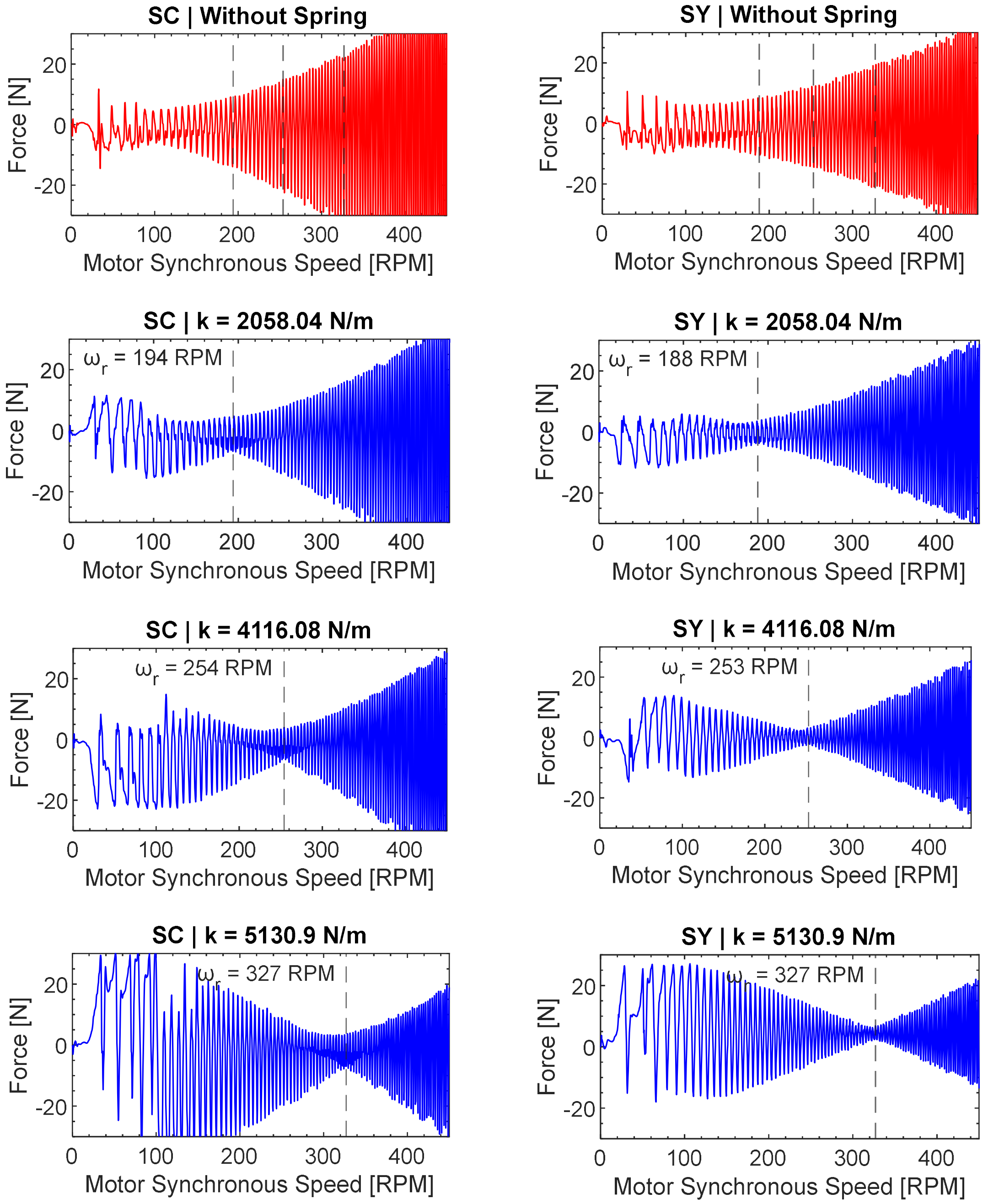

Figure 4.7. Forces on the connecting rod of the slider-crank and Scotch-yoke prototypes under different spring stiffnesses. All setups are characterized by the same reciprocating body mass and an externally applied force of 14.7 N.

4.4. Influence of Externally Applied Forces

Consistent with the simulation results, experimental tests evaluating varying externally applied forces emphasize the presence of limits to the beneficial effects of resonance utilization in both mechanisms. As shown in Figure 4.8 and detailed in Table 4.3, when the applied load remains below a certain threshold, the resonance setup yields a significant reduction in the force exerted on the connecting rod compared to the conventional setup. However, as the magnitude of the applied load increases, the difference in connecting rod force between the two configurations progressively decreases. This trend suggests that although resonance significantly improves force reduction under moderate loading conditions, its effectiveness diminishes as the externally applied load exceeds a certain level, thereby indicating the presence of an upper operational limit for resonance-based performance benefits.

Table 4.3. Forces exerted on the connecting rod of both the conventional setup (without the spring element) and the resonance setup (with the spring element), operating at resonant frequency under varying externally applied forces. All setups are characterized by the same reciprocating body mass and spring stiffness of 4116.08 N/m.

Mechanism	Setup		Peak-to-peak Force		
	Externally Applied Force [N]	Resonance Speed [RPM]	Conventional [N]	Resonance [N]	Difference [%]
Slider-Crank	9.8	236	35.33	5.44	84.6
	14.7	240	35.72	8.48	76.3
	19.6	259	37.14	13.76	62.9
Scotch-Yoke	9.8	240	25.12	4.08	83.8
	14.7	249	25.76	5.9	77.1
	19.6	251	26.48	6.16	76.7

When a non-constant external force is applied, the system may exhibit a shift in its dominant frequency, influenced by the force profile, amplitude, and frequency content. Nonlinear phenomena—such as displacement-dependent stiffness or nonlinear energy dissipation—can alter the system's dynamic response, including its resonant behavior. Consequently, both numerical simulations and experimental investigations are necessary for accurately capturing and analyzing these nonlinear effects. Unlike linear systems, where the resonant frequency can be defined through a simple analytical expression, nonlinear systems often defy such simplification due to their inherent complexity. The resonant frequency in these cases becomes highly dependent on the specific nature and severity of the nonlinearities, often resulting in amplitude-dependent or multi-valued resonance characteristics.

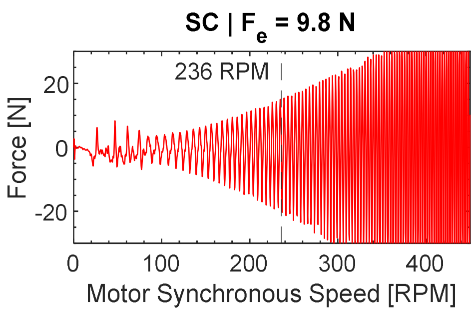

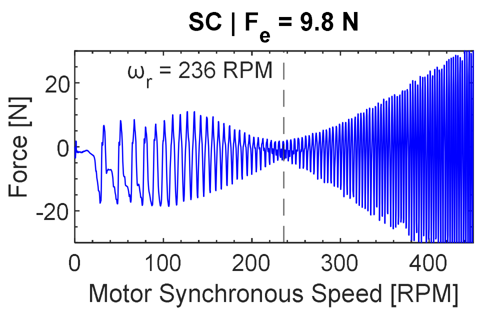

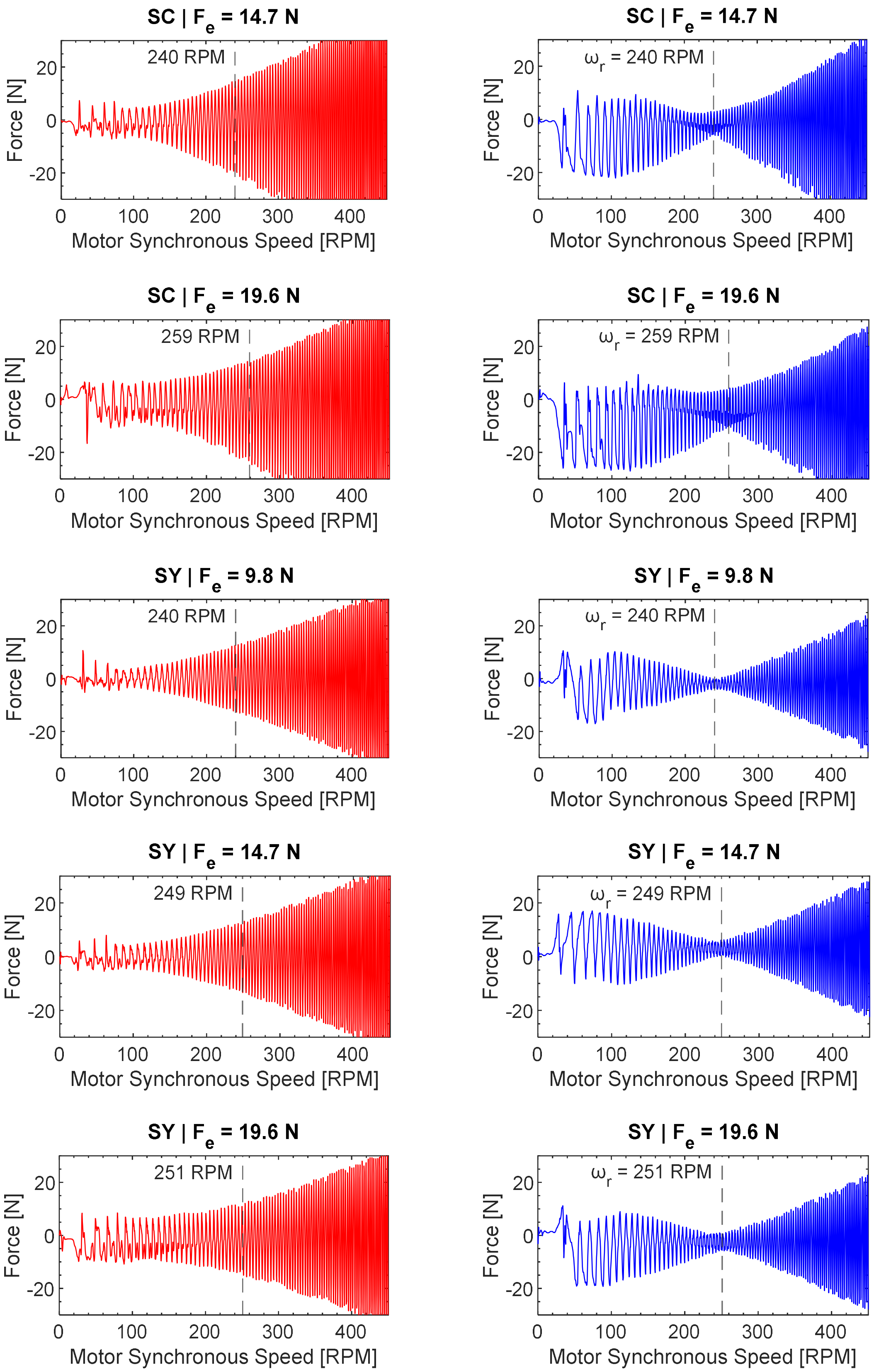

Figure 4.8. Forces on the connecting rod of the slider-crank and Scotch-yoke prototypes under different externally applied forces. All setups are characterized by the same reciprocating body mass. The red curves represent setups without springs, while the blue curves represent setups with a spring stiffness of 4116.08 N/m.

4.5. Comparison of Electric Power Demand

This section presents a systematic comparison of the electric power demand of the slider–crank and Scotch-yoke mechanisms operating in both conventional and resonance configurations. The analysis focuses on quantifying the influence of spring usage, motor speed, reciprocating mass, and externally applied load on the average and peak electrical power drawn by the drive motor. The experimental results are discussed for two main operating scenarios. First, the case without externally applied force is examined to isolate the effects of inertial forces and resonance on motor power demand. Second, the mechanism is analyzed under externally applied forces to evaluate the effectiveness of the resonance configuration when performing mechanical work, as occurs in actual applications.

The electric power measurements were obtained using the instrument setup illustrated in Figure 4.3, which shows a schematic diagram of the power and reaction force measurement system implemented on the slider–crank and Scotch-yoke mechanisms prototype. Electrical power consumption is determined by monitoring both the supply voltage and the current drawn by the drive motor. A regulated DC power supply feeds the motor, and voltage is measured across the motor terminals; while current is measured using a current clamp. These signals are routed to a digital oscilloscope, which records time-resolved voltage and current data. The instantaneous electrical power is obtained as the product of the measured voltage and current signals, and time-averaged power consumption is computed over steady-state operating intervals.

4.5.1. Electric Power Demand of the Slider–Crank Mechanism

The electric power demand characteristics summarized in Figure 4.9 and Table 4.4 provide a comparison between the conventional and the resonance slider–crank mechanism, under operating conditions without externally applied forces and for two quantities of additional reciprocating mass. For the conventional configuration without a spring element, both average and peak power demands increase with motor speed for the two tested reciprocating masses. Increasing the additional mass from 1 kg to 2 kg results in a rise in both average and peak power at all speeds, indicating higher torque requirements imposed on the motor due to amplified inertia forces.

When the spring element with stiffness of 4116.08 N/m is installed, a reduction in average power demand is observed over a range of motor speeds for both mass configurations. For the 1 kg reciprocating mass, the average power with the spring reaches a minimum around 175–200 RPM, where it is approximately 40–45% lower than that of the conventional setup. A similar tendency is also observed for the 2 kg case. These operating points correspond to resonance conditions where the spring force effectively compensates the inertia force of the reciprocating mass, leading to reduced motor torque demand. As motor speed increases beyond the resonance region, both average and peak powers rise again, gradually approaching the levels of the conventional mechanism.

The stiffer spring configuration with 5130.9 N/m demonstrates a shift of the resonance operating region toward higher motor speeds. For the 1 kg reciprocating mass, the minimum average power is observed in the range of approximately 225–275 RPM, while for the 2 kg mass the minimum shifts slightly lower but remains above that of the softer spring case. In these regions, the average power is lower than both the conventional setup and the softer spring configuration. Notably, the stiffer spring results in lower peak power values in the resonance range compared to the softer spring, particularly for the 1 kg mass case.

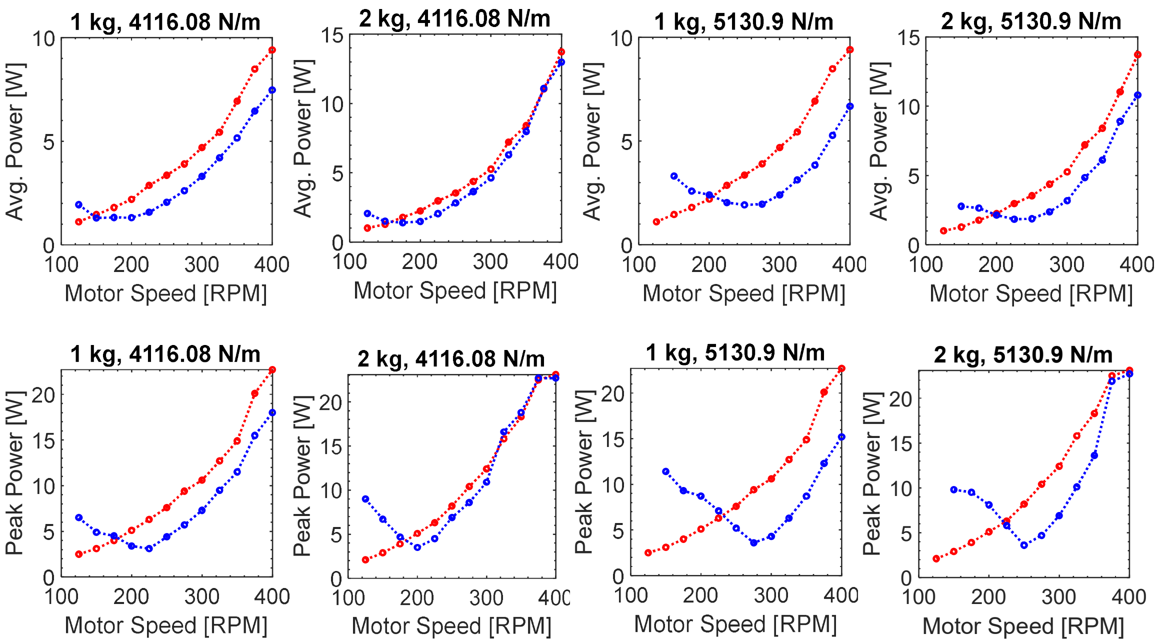

Figure 4.9. Electric power demand characteristics of both the conventional setup (without the spring element in red curves) and the resonance setup (with the spring element in blue curves) of the slider-crank mechanism under varying speed of the electric motor without externally applied load.

Table 4.4. Electric power demand characteristics of both the conventional setup (without the spring element) and the resonance setup (with the spring element) of the slider-crank mechanism under varying speed of the electric motor without externally applied load.

Additional Reciprocating Mass = 1 kg						
Motor Speed [RPM]	Without Spring		With Spring, k = 4116.08 N/m		With Spring, k = 5130.9 N/m	
	Average Power [W]	Peak Power [W]	Average Power [W]	Peak Power [W]	Average Power [W]	Peak Power [W]
125	1.11	2.50	1.94	6.50	-	-
150	1.46	3.10	1.30	4.90	3.31	11.40
175	1.80	4.00	1.32	4.50	2.59	9.30

200	2.20	5.10	1.31	3.40	2.41	8.70
225	2.87	6.30	1.57	3.10	2.04	7.10
250	3.36	7.60	2.06	4.40	1.92	5.20
275	3.90	9.40	2.61	5.70	1.96	3.60
300	4.69	10.60	3.30	7.30	2.40	4.30
325	5.44	12.70	4.20	9.50	3.13	6.30
350	6.93	14.90	5.16	11.50	3.84	8.70
375	8.48	20.10	6.45	15.50	5.27	12.30
400	9.41	22.70	7.47	18.00	6.68	15.20
Additional Reciprocating Mass = 2 kg						
Motor Speed [RPM]	Without Spring		With Spring, k = 4116.08 N/m		With Spring, k = 5130.9 N/m	
	Average Power [W]	Peak Power [W]	Average Power [W]	Peak Power [W]	Average Power [W]	Peak Power [W]
125	1.01	2.10	2.06	9.00	-	-
150	1.28	2.90	1.50	6.70	2.78	9.80
175	1.78	3.90	1.39	4.70	2.65	9.50
200	2.25	5.10	1.49	3.50	2.14	8.10
225	2.97	6.30	2.05	4.50	1.85	5.80
250	3.54	8.20	2.82	6.90	1.88	3.60
275	4.37	10.40	3.64	8.60	2.38	4.70
300	5.26	12.40	4.63	10.90	3.18	6.90
325	7.21	15.80	6.29	16.60	4.85	10.10
350	8.41	18.30	7.97	18.80	6.11	13.60
375	11.04	22.50	11.08	22.70	8.91	21.90
400	13.72	23.10	12.99	22.70	10.81	22.70

The electric power demand results presented in Figure 4.10 and Table 4.5 extend the analysis to conditions with externally applied loads, while maintaining identical reciprocating mass and spring stiffness across all configurations. The data compare the conventional and resonant slider–crank mechanisms under increasing motor speed and three discrete levels of external force. For the conventional configuration without the spring element, similar to the case without externally applied force, both average and peak power demands increase with motor speed for all three externally applied forces. At a given speed, higher external force leads to a proportional increase in average power. The peak power also rises with increasing load, although the relative increment is smaller than that observed in the average power.

When the spring element is introduced, for all external force levels, under tolerable external loading the resonance condition yields a reduction in average power demand over a range of motor speeds. For instance, at 250 RPM and an external force of 14.7 N, the average power decreases from 9.1 W in the conventional setup to

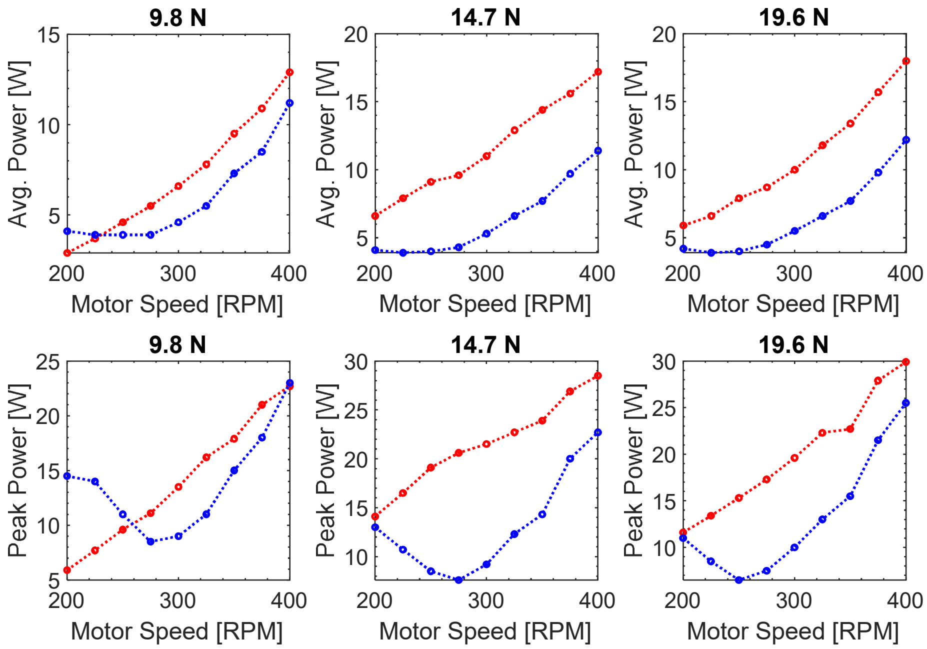

Figure 4.10. Electric power demand characteristics of both the conventional setup (without the spring element in red curves) and the resonance setup (with the spring element in blue curves) of the slider-crank mechanism under varying speed of the electric motor with externally applied load.

Table 4.5. Electric power demand (in Watt) of both the conventional setup (without the spring element) and the resonance setup (with the spring element) of the slider-crank mechanism under varying speed of the electric motor with externally applied load. All setups are characterized by the same reciprocating body mass and spring stiffness.

Motor Speed [RPM]	Externally Applied Force 9.8 N				Externally Applied Force 14.7 N				Externally Applied Force 19.6 N			
	Without Spring		With Spring		Without Spring		With Spring		Without Spring		With Spring	
	Avg.	Peak	Avg.	Peak	Avg.	Peak	Avg.	Peak	Avg.	Peak	Avg.	Peak
200	2.9	5.9	4.1	14.5	6.6	14.1	4.1	13.0	5.9	11.6	4.2	11.0
225	3.7	7.7	3.9	14.0	7.9	16.5	3.9	10.7	6.6	13.4	3.9	8.5
250	4.6	9.6	3.9	11.0	9.1	19.1	4.0	8.5	7.9	15.3	4.0	6.5
275	5.5	11.1	3.9	8.5	9.6	20.6	4.3	7.6	8.7	17.3	4.5	7.5
300	6.6	13.5	4.6	9.0	11.0	21.5	5.3	9.2	10.0	19.6	5.5	10.0
325	7.8	16.2	5.5	11.0	12.9	22.7	6.6	12.3	11.8	22.3	6.6	13.0
350	9.5	17.9	7.3	15.0	14.4	23.9	7.7	14.3	13.4	22.7	7.7	15.5
375	10.9	21.0	8.5	18.0	15.6	26.9	9.7	20.0	15.7	27.9	9.8	21.5
400	12.9	22.7	11.2	23.0	17.2	28.5	11.4	22.7	18.0	29.9	12.2	25.5

approximately 4.0 W with the spring in resonance, corresponding to a reduction of more than 55%. At the lower end of the speed range, the peak power with the spring is higher than that of the conventional mechanism for all load cases. As motor speed increases toward the resonance region, the peak power in the resonance setup decreases significantly and, in several cases, becomes comparable to or lower than that of the conventional configuration. For example, at 275 RPM and 9.8 N external force, the peak power is reduced from 11.1 W without the spring to 8.5 W with the spring. At higher speeds beyond approximately 325 RPM, both average and peak power demands in the resonant setup increase steadily and begin to converge toward those of the conventional setup. This behavior indicates a gradual loss of resonance effectiveness as the excitation frequency departs from the natural frequency of the mass–spring subsystem.

4.5.2. Electric Power Demand of the Scotch-Yoke Mechanism

The power demand characteristics of the Scotch-yoke mechanism in general showed similar behavior with the slider-crank mechanism. As shown in Figure 4.11 and Table 4.6, in the conventional configuration, the average and peak power show an increase with rotational speed. For the 1 kg added mass, the average power increases from approximately 2.04 W at 125 RPM to 11.80 W at 400 RPM, indicating the expected dependence of power demand on rotational speed and inertial loading. When the additional mass is increased to 2 kg, both average and peak power rise considerably due to greater inertial loading. In this case, the average power increases from about 3.38 W at 125 RPM to 26.70 W at 400 RPM, while the peak power increases from 7.31 W to 60.50 W over the same speed range.

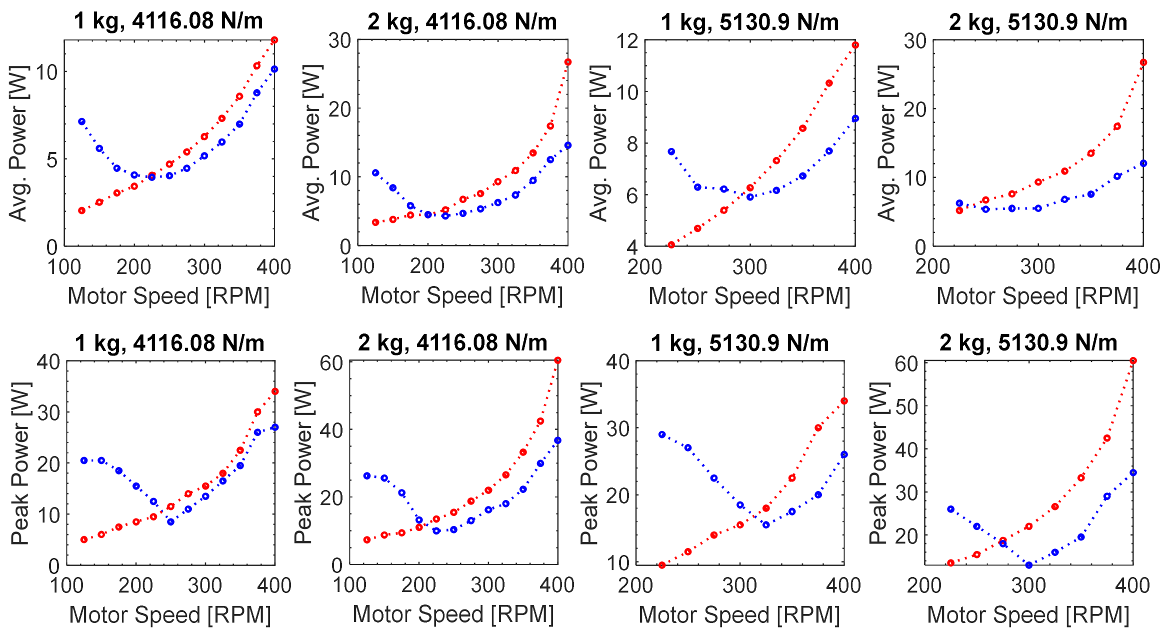

Figure 4.11. Electric power demand characteristics of both the conventional setup (without the spring element in red curves) and the resonance setup (with the spring element in blue curves) of the Scotch-yoke mechanism under varying speed of the electric motor without externally applied load.

With springs of stiffness 4116.08 N/m installed and a 1 kg added mass, the system demonstrates higher power demand in the low-speed region (125–175 RPM) compared with the no-spring configuration, indicating the additional work required to compress and extend the springs when the operating frequency is well below the resonant frequency of the spring–mass system. As speed increases, the power demand progressively converges toward or even falls slightly below the no-spring configuration. At speeds within the resonance range of approximately 225–325 RPM, the spring restoring forces begin to interrelate constructively with the inertial forces, reducing the average and peak power demand. At higher speeds, inertial effects again dominate, leading to increasing average and peak power, although the presence of the springs continues to yield reductions relative to the configuration without springs.

A similar tendency is observed when the added mass is increased to 2 kg, though the characteristic speed ranges shift downward due to the lower resonant frequency of the heavier spring–mass assembly. In this case, the low-speed region of approximately 125–175 RPM also shows an increase in power demand relative to the no-spring setup. In the mid-speed range of roughly 200–300 RPM, resonance condition reduces the required average and peak power demand. At higher speeds, inertial forces dominate once more, and both average and peak power rise, although remaining somewhat lower than in the no-spring configuration. For both the 1 kg and 2 kg cases, increasing the spring stiffness to 5130.9 N/m shifts the system's resonant frequency to higher rotational speeds. Compared with the lower-stiffness configuration, a key distinction is that the deviations in both average and peak power demand relative to the no-spring setup become more pronounced over a broader range of operating speeds.

Table 4.6. Electric power demand characteristics of both the conventional setup (without the spring element) and the resonance setup (with the spring element) of the Scotch-yoke mechanism under varying speed of the electric motor without externally applied load.

Additional Reciprocating Mass = 1 kg						
Motor Speed [RPM]	Without Spring		With Spring, k = 4116.08 N/m		With Spring, k = 5130.9 N/m	
	Average Power [W]	Peak Power [W]	Average Power [W]	Peak Power [W]	Average Power [W]	Peak Power [W]
125	2.04	5.00	7.14	20.50	-	-
150	2.52	6.00	5.60	20.50	-	-
175	3.04	7.50	4.47	18.50	-	-
200	3.43	8.50	4.08	15.50	-	-
225	4.05	9.50	3.94	12.50	7.67	29.00
250	4.69	11.50	4.03	8.50	6.29	27.00
275	5.40	14.00	4.46	11.00	6.22	22.50
300	6.27	15.50	5.17	13.50	5.91	18.50

325	7.32	18.00	5.97	16.50	6.17	15.50
350	8.57	22.50	6.99	19.50	6.73	17.50
375	10.33	30.00	8.77	26.00	7.69	20.00
400	11.80	34.00	10.14	27.00	8.96	26.00
Additional Reciprocating Mass = 2 kg						
Motor Speed [RPM]	Without Spring		With Spring, k = 4116.08 N/m		With Spring, k = 5130.9 N/m	
	Average Power [W]	Peak Power [W]	Average Power [W]	Peak Power [W]	Average Power [W]	Peak Power [W]
125	3.38	7.31	10.57	26.25	-	-
150	3.80	8.75	8.40	25.63	-	-
175	4.43	9.38	5.80	21.25	-	-
200	4.50	11.00	4.50	13.20	-	-
225	5.19	13.50	4.30	9.94	6.24	26.00
250	6.71	15.44	4.70	10.33	5.34	22.00
275	7.58	18.75	5.34	13.00	5.48	18.00
300	9.31	22.00	6.25	16.20	5.49	13.00
325	10.90	26.56	7.36	18.05	6.79	16.00
350	13.49	33.25	9.47	22.31	7.55	19.50
375	17.41	42.50	12.50	29.90	10.17	29.00
400	26.70	60.50	14.59	36.75	12.04	34.50

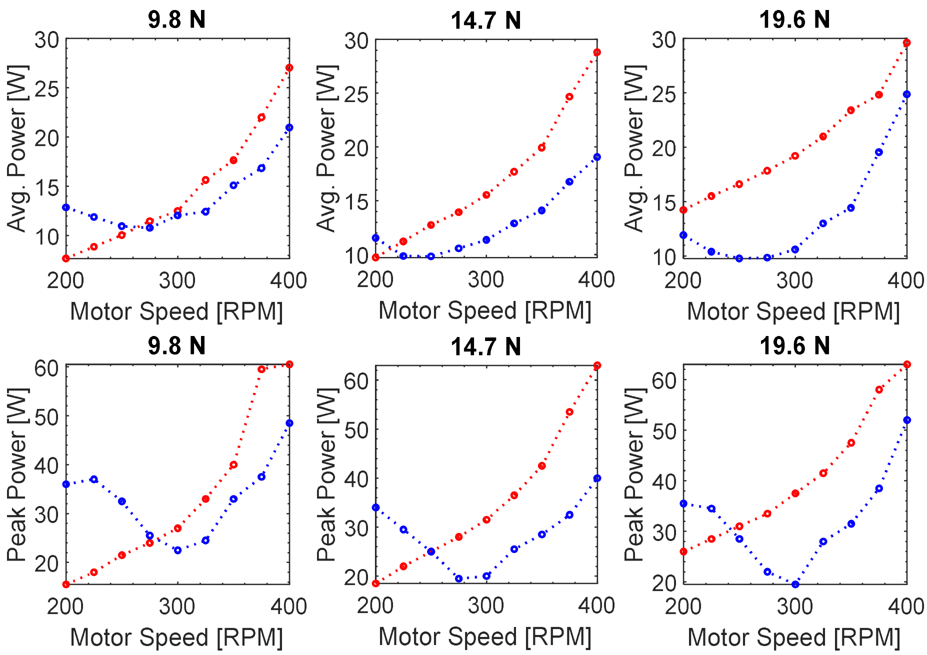

Figure 4.12. Electric power demand characteristics of both the conventional setup (without the spring element in red curves) and the resonance setup (with the spring element in blue curves) of the Scotch-yoke mechanism under varying speed of the electric motor with externally applied load.

Figure 4.12 and Table 4.7 summarize the measured electric power demand of the Scotch–yoke mechanism under externally applied loads, while the reciprocating mass and spring stiffness are held constant. Across all load cases, the conventional configuration without springs demonstrates a practically proportional increase in both average and peak power with increasing motor speed, similar to the findings in the slider-crank cases. Increasing the externally applied force raises both average and peak power across all speeds and configurations. The influence of the spring remains across load levels: higher power demand at low speeds, a distinct mid-speed region of reduced power due to resonance, and moderated but rising power at higher speeds.

Overall, the investigation results demonstrate that the incorporation of a properly tuned spring element can reduce the average electric power demand of a slider–crank and Scotch-yoke mechanisms under unloaded and loaded conditions, particularly within a targeted speed range and bearable external loading. The effectiveness of this resonance-based approach depends critically on the matching between motor speed, spring stiffness, and reciprocating mass, and careful selection of system parameters enables both reduced torque ripple and energy savings.

Table 4.7. Electric power demand (in Watt) of both the conventional setup (without the spring element) and the resonance setup (with the spring element) of the Scotch-yoke mechanism under varying speed of the electric motor with externally applied load. All setups are characterized by the same reciprocating body mass and spring stiffness.

Motor Speed [RPM]	Externally Applied Force 9.8 N				Externally Applied Force 14.7 N				Externally Applied Force 19.6 N			
	Without Spring		With Spring		Without Spring		With Spring		Without Spring		With Spring	
	Avg.	Peak	Avg.	Peak	Avg.	Peak	Avg.	Peak	Avg.	Peak	Avg.	Peak
200	7.7	15.5	12.9	36.0	9.7	18.5	11.5	34.0	14.2	26.0	11.9	35.5
225	8.9	18.0	11.9	37.0	11.2	22.0	9.9	29.5	15.5	28.5	10.4	34.5
250	10.1	21.5	11.0	32.5	12.8	25.0	9.8	25.0	16.6	31.0	9.8	28.5
275	11.5	24.0	10.8	25.5	13.9	28.0	10.6	19.5	17.8	33.5	9.9	22.0
300	12.5	27.0	12.1	22.5	15.5	31.5	11.4	20.0	19.2	37.5	10.6	19.5
325	15.6	33.0	12.4	24.5	17.7	36.5	12.9	25.5	21.0	41.5	13.0	28.0
350	17.6	40.0	15.1	33.0	19.9	42.5	14.1	28.5	23.4	47.5	14.4	31.5
375	22.0	59.5	16.8	37.5	24.7	53.5	16.8	32.5	24.8	58.0	19.6	38.5
400	27.0	60.5	21.0	48.5	28.8	63.0	19.1	40.0	29.6	63.0	24.9	52.0

4.6. Overview of the Design Methodology

Based on the results of numerical simulations and experimental tests, a practical procedure for utilizing mechanical resonance in slider–crank and Scotch–yoke mechanisms is formulated. The approach combines dynamic modeling with the selection and tuning of system parameters so that kinetic and potential energy are exchanged in a controlled manner, thereby reducing inertial forces and input torque fluctuations. The resulting design and implementation steps are outlined in Figure 4.13.

1. Identify the external load.

The initial step is identifying the operational requirements of the mechanism. This involves analyzing the magnitude and profile of the external load establishing a desired work.

2. Specify the target resonant frequency.

After defining the operational requirements, the target operating speed of the mechanism is determined. This involves selecting a suitable angular velocity that enables the mechanism to deliver the desired output while ensuring dynamic stability and operational reliability.

3. Determine the suitable reciprocating mass.

Once the external load and target angular velocity have been established, the appropriate reciprocating mass must be determined. The inertia force generated by this mass should be sufficient to effectively counteract the external load, thereby enabling the mechanism to operate efficiently at or near resonance while maintaining operational reliability under the applied loads.

4. Install the appropriate spring element.

Subsequently, the appropriate spring element is installed between the reciprocating mass and the ground. The selection of this spring requires consideration of its stiffness, damping characteristics, and overall compatibility with the system's dynamic behavior, with the objective of facilitating resonance at the specified target angular velocity.

5. Adjust the reciprocating mass to the middle position.

After the spring element is installed, the reciprocating mass is positioned at its equilibrium point. This adjustment is critical for maximizing the beneficial effects of resonance. It is achieved by applying an appropriate spring preload and/or repositioning the moving bodies to compensate for gravitational forces, thereby ensuring a balanced initial configuration.

6. Operate the mechanism at resonant frequency.
Finally, the mechanism is operated at its target angular velocity, which corresponds to the resonant frequency of the system. By aligning the input angular frequency with the natural frequency of the spring–reciprocating mass assembly, resonance is achieved, resulting in enhanced dynamic performance.

Figure 4.13. Design methodology of the resonance slider-crank and Scotch-yoke mechanisms.

Chapter 5
Application Examples

5.1. Reciprocating Compressors

In this section, a technique for reducing input torque and joint forces through the use of mechanical resonance is presented, with gas compression in a reciprocating compressor employing slider-crank mechanism serving as a practical application example [82, 127]. The results demonstrate that resonance utilization offers advantages, including reduced input torque requirements and reduced rotating joint forces when compared to conventional operation. Notably, during the gas compression process, the compressibility of the air itself acts analogously to a spring, storing potential energy. As a result, a narrow region of reduced torque and force around the resonant frequency can be achieved, even in the absence of an external spring element.

5.1.1. Modeling

Initially, a CAD model of the reciprocating compressor is developed and imported into ADAMS/View. As illustrated in Figure 5.1, the model comprises the crankshaft (as the crank), and the crosshead, push rod, and piston (collectively modeled as the slider). The connecting rod links the crank to the slider, and coil springs are mounted around guide rails, fixed between the main frame and the crosshead, such that the slider rests at the midpoint of the stroke in its equilibrium position. The mass and moment of inertia of each component are assigned based on the predetermined physical properties. The assembly is converted into an MBD model by defining mechanical joints—each with appropriate friction characteristics—between the interconnected parts. Furthermore, as ADAMS is not capable of simulating fluid dynamics directly, an equivalent multi-domain system model of the compressor is built in Simcenter Amesim. This model is used to compute the suction and compression forces acting on the piston due to the gas dynamics.

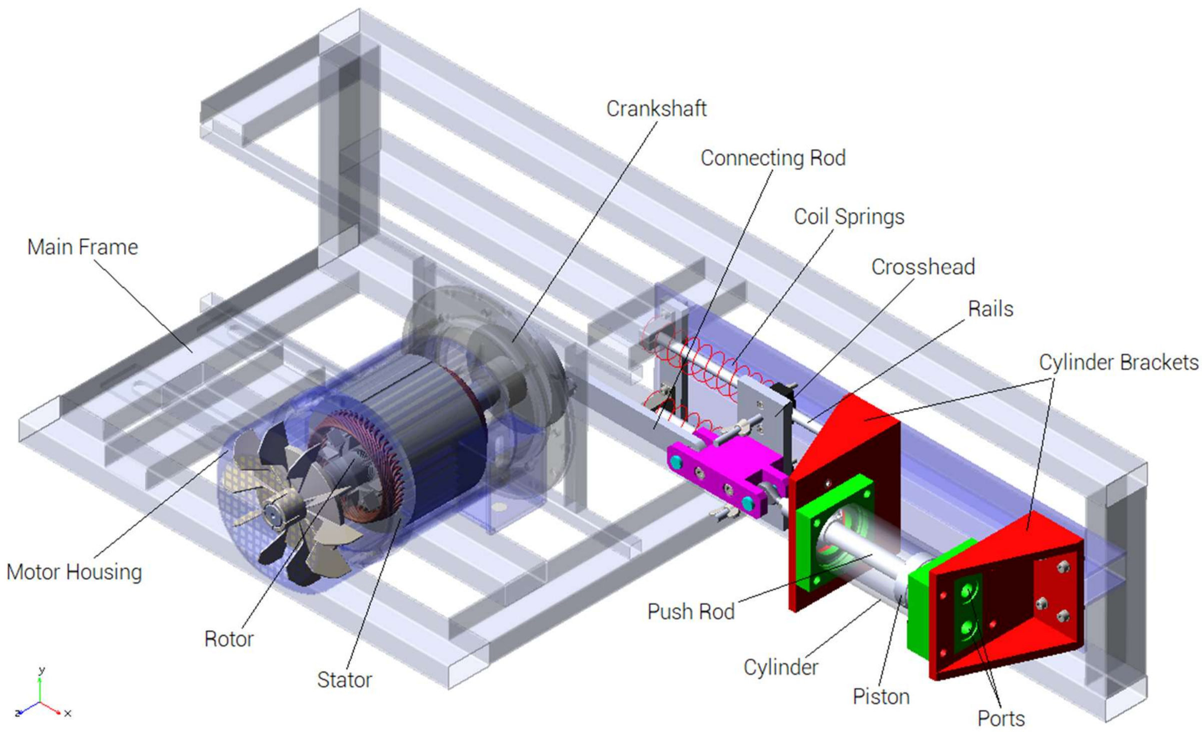

Figure. 5.1. CAD-MBD model of the reciprocating compressor prototype. Electric motor is adapted from [32].

Initially, the crank angular position versus piston-top force data—representing the air suction and compression effects—are exported from Simcenter Amesim simulation results and imported into ADAMS. Within ADAMS, this dataset is implemented as a spline-based time-varying force, applied directly to the top of the piston in the MBD model. Two principal operating configurations are investigated: (1) a conventional setup without spring elements, and (2) a resonance setup incorporating springs. Both configurations share identical component specifications and boundary constraints. The complete assemblies are simulated using ADAMS to evaluate the input torque and mechanical power requirements.

In addition to these primary scenarios, the influence of various secondary parameters on system performance is also analyzed, including joint friction, pressure loading, component mass, and crankshaft speed. Finally, comparative results are presented to highlight the improvements associated with mechanical resonance utilization, particularly in terms of reduced input torque and enhanced energy performance.

Multi-domain system modeling and simulations are performed to determine the air pressure—and consequently, the forces acting on the piston—during the suction and compression strokes. As illustrated in Figure 5.2, the model comprises 16 components, with their parameters listed in Table 5.1. The system's operation begins with the prime mover (component 1) rotating the crank (component 4), which transmits rotary motion into linear displacement, thereby driving the piston (component 5). During the piston's movement from top dead center (TDC) to bottom dead center (BDC), the resulting pressure differential opens the inlet valve (component 9, lower), allowing ambient air to be drawn into the cylinder. As the piston returns from BDC to TDC, the compressed air exits through the outlet valve (component 9, upper) and is directed into the storage tank (component 14). To protect the pneumatic circuit from overpressure, a relief valve (component 13) is incorporated, regulating the upstream pressure.

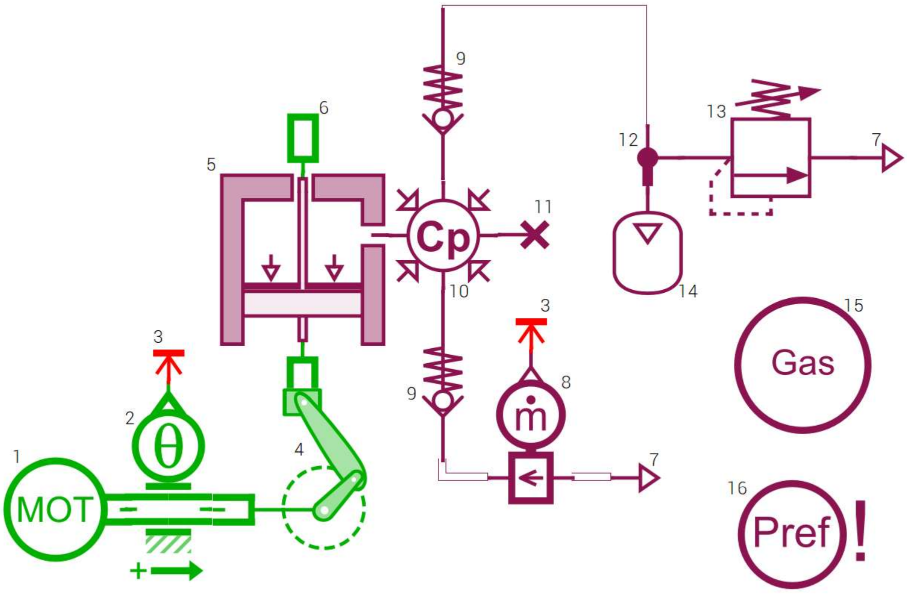

Figure 5.2. Multi-domain system sketch of the reciprocating compressor prototype.

Table 5.1. Parameters for the multi-domain system simulations.

	Components	Parameters	Value
1	Constant speed prime mover	Shaft speed	[a]-
2	Angular displacement sensor	Sign convention: positive from	Port 1 to 3
		Offset to be subtracted from angle	0 degree
		Gain for signal output	1/degree
3	Plug for signal port	-	-
4	Ideal crank without friction or inertia with state variable	Angular position of crank (initial)	0 degree
		Radius of crank	50 mm
		Length of connecting rod	168 mm
		Offset of displacement	0 mm
		Offset perpendicular to displacement	0 mm
5	Pneumatic piston	Piston diameter	60 mm
		Rod diameter	0 mm
		Chamber length at zero displacement	0 mm
6	Zero force source	-	-
7	Source of atmospheric	Temperature at port 1	293.15 K

	pressure and temperature		
8	Pneumatic mass flow sensor	Offset to be subtracted from mass flow	0 g/s
		Gain for signal output	1/(g/s)
9	Pneumatic check valve with saturation (suction valve)	Maximum flow coefficient (Cv)	22 (inlet), 20 (outlet)
		Check valve cracking pressure	0 bar (both inlet & outlet)
		Maximum opening pressure	1 bar (both inlet & outlet)
		Valve hysteresis	0 bar (both inlet & outlet)
10	Variable volume pneumatic chamber with heat exchange	Dead volume	0.62 L
		Thermal exchange coefficient	0 $J/m^2/K/s$
		Thermal exchange area	0.1 m^2
11	Zero pneumatic flow source	-	-
12	Pneumatic junction three ports	-	-
13	Pneumatic relief valve	Relief valve cracking pressure	[a]-
		Relief valve mass flow rate pressure gradient	10 g/s/bar
		Valve hysteresis	0 bar
14	Fixed volume pneumatic chamber with heat exchange	Volume	1 L
		Thermal exchange coefficient	0 $J/m^2/K/s$
		Thermal exchange area	0.1 m^2
15	Generic gas definition	Specific heat ratio	1.4
		Specific gas constant	287 J/kg/K
		Absolute viscosity	0.0182 cP
		Thermal conductivity	0.0264 W/m/K
		Enthalpy of formation	−125.53 J/mol
		Properties definition	Air, perfect gas
16	Set reference pressure	Reference pressure	1.013 barA

[a]depends on the setup and comparison scenario

Each simulation step within the multi-domain model is time-synchronized with the MBD simulations. The thermal exchange coefficient is set to 0 $J/m^2/K/s$, as heat transfer is considered negligible for the purposes of this study. The crank (component 4) is modeled as an ideal converter between rotary and linear motion, with no frictional losses or inertia. In modeling the piston (component 5), the piston rod diameter d_r is set to zero, indicating the absence of a rod on the upper side of the piston. The instantaneous chamber length s and the chamber volume V are calculated using Equations 5.1 and 5.2 respectively, where x_0 is the chamber length at zero displacement, x is the translational displacement of reciprocating mass, and d_p is the piston diameter. Furthermore, the total force acting towards the connecting rod F_l is calculated by Equation 5.3, where p_l is the pressure at the top of the piston.

$$s = x_0 - x \tag{5.1}$$

$$V = \frac{s\pi}{4}({d_p}^2 - {d_r}^2) \tag{5.2}$$

$$F_l = \frac{p_l\pi}{4}({d_p}^2 - {d_r}^2) \tag{5.3}$$

The pneumatic check valve (9) is normally closed and open when the pressure drop across the valve exceeds the cracking pressure p_c. The maximum opening pressure is the pressure differential at which the valve becomes fully open, and this value is greater than the cracking pressure. In the simulation, to improve computational efficiency, the valve is modeled using static behavior, meaning no valve dynamics are included. The net opening pressure Δp across the valve is defined in Equation 5.4, where p_1 is the pressure at the outlet side while p_2 is at the inlet side.

$$\Delta p = p_2 - p_1 - p_c. \tag{5.4}$$

The static fractional valve opening of the valve o_v is given by Equation 5.5, where Δp is the valve net opening pressure and p_{max} is the maximum opening pressure.

$$o_v = \frac{\Delta p}{p_{max} - p_c} \tag{5.5}$$

Relief valve (13) works rather comparably to the check valve, with the aim that the pressure drop gets regulated to the cracking pressure. The opening of the relief valve is determined by the pressure drop p_d in Equation 5.6.

$$p_d = p_2 - p_1 - p_c. \tag{5.6}$$

If $p_d \leq 0$, the relief valve is closed, and the flow rates are null. Otherwise, the relief valve is open, and the flow rate $\dot{m}_d$ is given by Equation 5.7.

$$\dot{m}_d = G \cdot p_d \tag{5.7}$$

Here, the relief valve mass flow rate pressure gradient G is defined as Equation 5.8

$$G = p_2 - p_1 \tag{5.8}$$

To define the gas characteristics in the pneumatic circuit, component 15 is used. The simulation assumes the behavior of an ideal (perfect) gas, governed by the equation of state presented in Equation 5.9, where p is the pressure, R is the specific gas constant, and T is the temperature.

$$p = \frac{R \cdot T}{V} \tag{5.9}$$

The specifications of each component in the MBD model are assigned according to the properties listed in Table 5.2. For most parts, such as the piston, push rod, crosshead, connecting rod, and crankshaft, the mass and moment of inertia are predefined based on design requirements. For all other components, ADAMS/View automatically calculates mass and inertia based on their geometry and material properties.

Table 5.2. Components' dimensions, mass, and moment of inertia of the MBD model.

Essential dimensions		
Component	**Link**	**Length [mm]**
Crank radius l_1	AB	50
Connecting rod length l_2	BC	168

Mass, and moment of inertia						
Component	**Mass [kg]**	**Moment of Inertia [kg.mm²]** I_{xx}	I_{yy}	I_{zz}	**Connected with**	**Joint**
Main frame	24.59	3.08×10^6	2.80×10^6	5.76×10^5	Ground	Fixed
Stator	2.80	1.103×10^4	8562.18	8555.26	Motor housing	Fixed
Connecting rod	0.15*	451.95	441.64	12.76	Crankshaft	Revolute
					Crosshead	Revolute
Crankshaft	0.85*	1350.89	798.75	772.66	Connecting rod	Revolute
					Rotor	Fixed
Cylinder	1.53	4056.40	4054.44	1688.46	Cylinder brackets	Fixed
					Piston	Cylindrical
Front cylinder	4.13	1.59×10^4	1.07×10^4	7412.01	Main frame	Fixed

bracket					Cylinder	Fixed
Motor housing	2.12	1.69×10^4	1.62×10^4	1.37×10^4	Main frame	Fixed
					Rotor	Fixed
Piston (including pin)	0.25*	335.87	292.34	290.84	Push rod	Fixed
					Cylinder	Cylindrical
Push rod	0.25*	2358.69	2357.44	35.95	Piston	Fixed
					Crosshead	Revolute
Rail	1.22	1.89×10^4	1.66×10^4	2664.15	Main frame	Revolute
					Crosshead	Translational
Rear cylinder bracket	3.93	1.90×10^4	1.09×10^4	1.01×10^4	Main frame	Fixed
					Cylinder	Fixed
Rotor	2.59	1.32×10^4	1.32×10^4	2554.61	Crankshaft	Fixed
					Motor housing	Revolute
Crosshead	*varied*	4850.21	4338.28	3509.18	Rail	Translational
					Connecting rod	Revolute
					Push rod	Revolute

Coefficient of friction		
	μ_s	μ_d
Cylindrical joint (F)	0.035	0.03
Translational joint (E)	0.004	0.002
Revolute joint (A, B, C, & D)	0.0015	0.001

*defined.

5.1.2. Simulation

As described in Table 5.1, the initial position of the crank is set to 0°, indicating that the piston is initially located at TDC. The cycle begins with the suction stroke, where the crank rotates from 0° to 180°, moving the piston from TDC to BDC. This is followed by the compression stroke, covering 180° to 360°, during which the piston returns from BDC to TDC. During the compression phase, the compressed air is accumulated in the storage tank, and the pressure inside the cylinder increases gradually until it reaches the cracking pressure of the relief valve. As illustrated in Figures 5.3a and 5.3b, setting the relief valve cracking pressure to 8.7 bar, for example, results in a maximum cylinder pressure $p_{l_{max}}$ of approximately 8.84 bar. Correspondingly, the downward force acting on the piston due to the compressed air reaches approximately 2500 N.

Figure 5.3b shows the force–crank angle curve in one cycle. To await pressure build-up as the tank is filled up which takes place for the first 0.85 seconds (in Figure 5.3a), crank angle from 14400° to 14760° is taken for the plot so that the expected steady load upon the piston is achieved. Within one cycle, there are several stages that take place. At BDC, point ‘d’, the cylinder is already filled with the air after suction as the piston moves from TDC to BDC and the inlet valve opens at point ‘c’ to ‘d’. When the piston moves toward TDC, from ‘d’ to ‘e’ air is compressed and the pressure, so does the force upon the piston, rises up until the outlet check valve opens at point ‘e’. Discharge occurs from point ‘e’ to ‘a’, and between ‘a’ and ‘b’, there is left-over pressure inside the cylinder before the outlet valve is finally closed at ‘b’ and so the piston displacement from ‘b’ to ‘c’ is only expansion without having any valve open.

a.

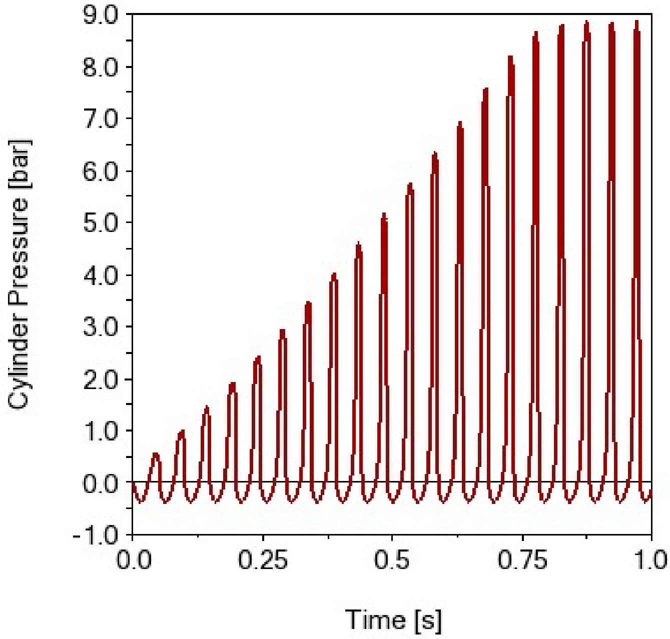

b.

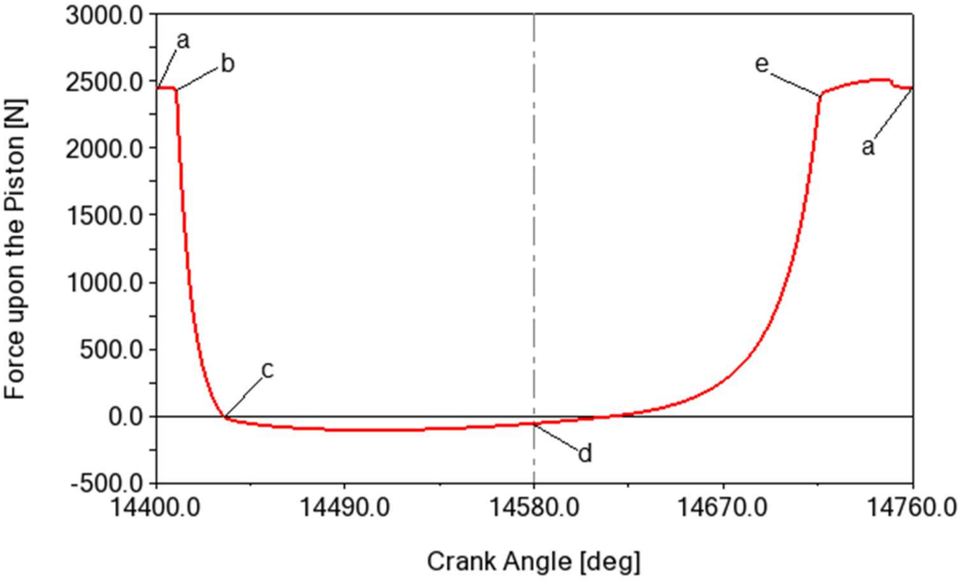

Figure 5.3. a. Air pressure inside the cylinder as the tank is filled up, and b. Force acting on the piston in one cycle, 0° to 360° of crank. The process consists of expansion (a-c), effective suction (c-d), compression (d-e), and discharge (e-a).

Multiple simulations in Amesim were conducted at 2.5, 5, 7.5, and 10 bar of air pressure. From these simulations, the piston force F_l as a function of crank angle modulo 360° was extracted and imported into ADAMS/View as a spline curve. This spline defines the applied force input on the top of the piston in the MBD model.

To evaluate the maximum possible torque reduction between the two configurations, this section presents a comparative analysis conducted without any dissipative forces (e.g., friction or damping). The simulation parameters are defined as specified in the description of Figure 5.4. In the setup incorporating the spring element, an equilibrium configuration is reached where the crank angle at rest deviates from the typical 270° position observed in the configuration without a spring. It is critical to ensure that, as stated in Chapter 2, following the spring installation, the reciprocating masses are positioned at the midpoint of their stroke in the equilibrium state.

a. Without Spring

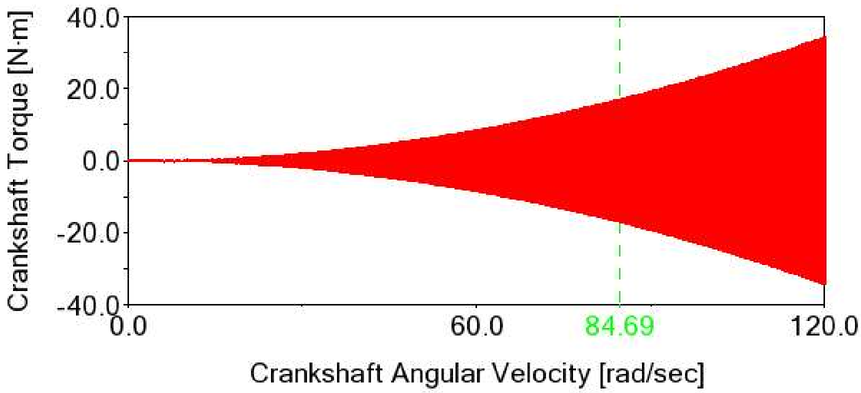

b. With Spring

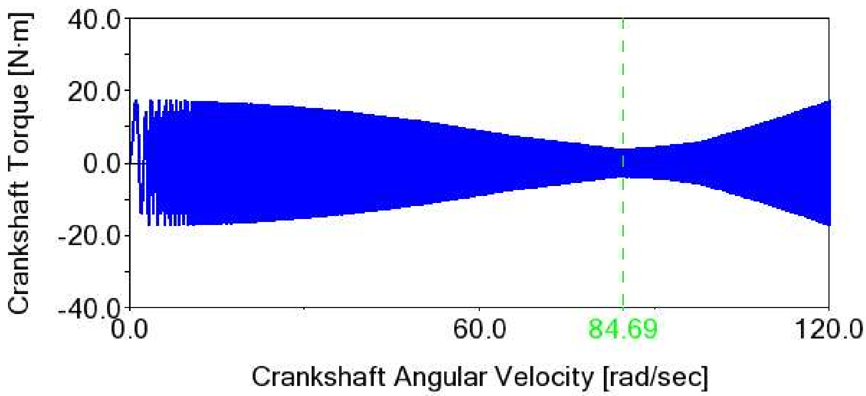

Figure 5.4. Torque–angular velocity curves of a. without spring, b. with spring. $M = 1.5$ kg, $k = 6.25$ kN/m.

Figure 5.4a illustrates that the configuration without a spring exhibits a progressive increase in input torque as the crankshaft angular velocity rises. In contrast, Figure 5.4b demonstrates that the configuration with installed springs experiences a significantly lower input torque magnitude at its resonant frequency, approximately 84.69 rad/s. At resonance, the system efficiently stores and exchanges energy between the kinetic energy of the reciprocating mass and the potential energy of the spring, thereby reducing the torque required to maintain crankshaft rotation.

From the front view of the model (the XY plane in Figure 5.1), any quantity directed counterclockwise is determined as positive, while clockwise values are considered negative. As shown in Figure 5.5a, at a constant angular velocity of 84.69 rad/s, corresponding to the system's resonant frequency, the torque alternates between positive and negative values within a single cycle.

a.

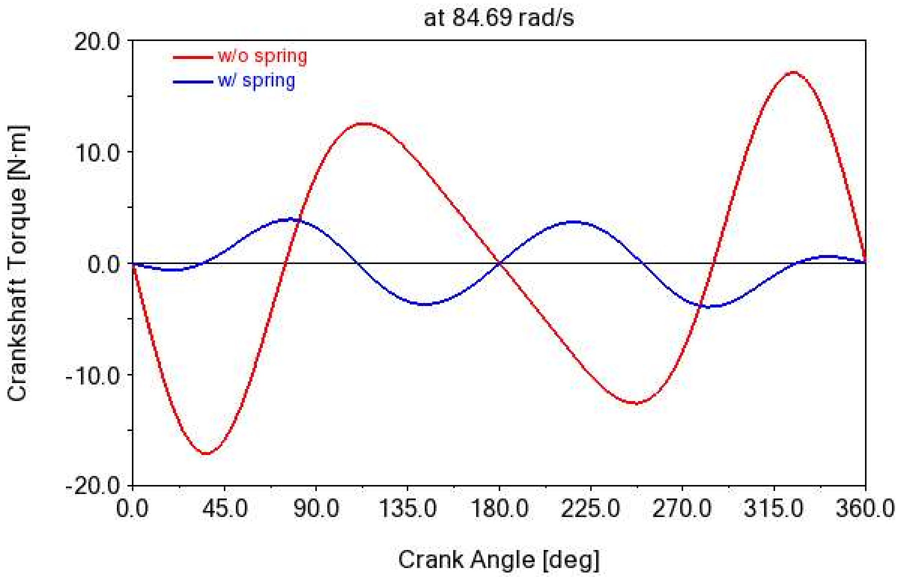

b.

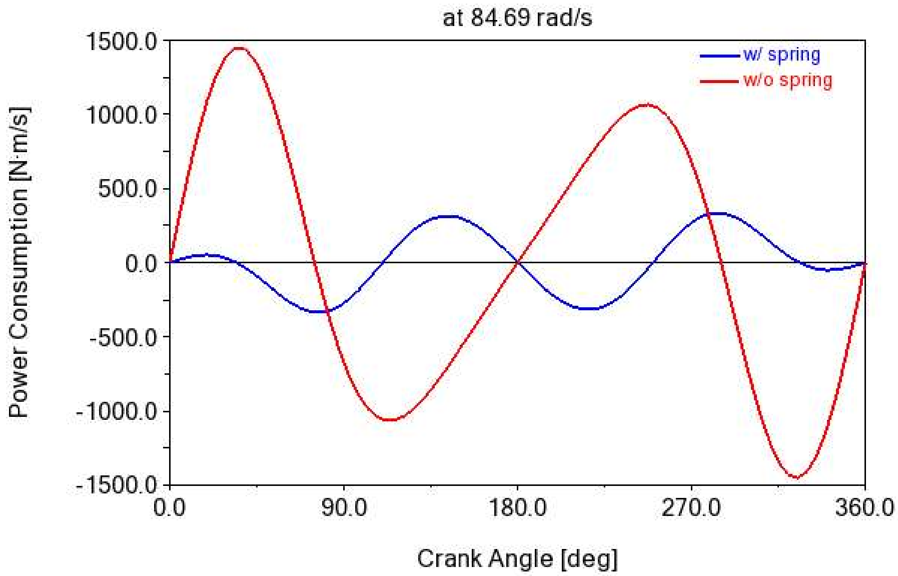

Figure 5.5. Torque–crank angle (a) and mechanical power–crank angle (b) curves within one cycle at resonant frequency $\omega_r = 84.69$ rad/s.

In the setup without a spring, during crank rotation from 0° to approximately 74°, the torque becomes negative, as the reciprocating mass is accelerated from rest at TDC toward the middle of the stroke. As the crank continues to rotate at constant angular velocity, the torque shifts to positive values from 74° to 180°, as the reciprocating mass undergoes deceleration, eventually coming to rest at BDC. A similar but opposite pattern occurs from 180° to 360°, completing the full cycle.

As discussed in Chapter 3, in practice, a system requiring higher input torque—often associated with greater inertia torque—presents several drawbacks, including increased component stresses, higher joint friction, and greater driving power demands, which collectively tend to result in higher energy dissipation. In contrast, as shown in Figure 5.5a, the setup with spring operating at resonance shows a distinctive torque pattern, characterized by three crests and three troughs within a single cycle, with significantly reduced magnitudes compared to the conventional setup.

During the initial crank displacement from 0° to approximately 33°, the dynamic torque is negative but of much smaller magnitude, as the pre-extended spring helps the motion driver by pulling the reciprocating mass, thereby reducing the torque demand for acceleration. From 33° to 108°, the combined effect of the spring force and the inertia force exceeds the required torque to continue accelerating the mass, resulting in positive torque. Between 108° and 180°, the spring is being compressed, generating a restorative force that opposes the crank motion, thus producing negative torque once again. These dynamics are mirrored in reverse as the crank rotates from 180° to 360°, completing the cycle. As with the conventional setup, the net work done over one full cycle remains zero, indicating that mechanical energy is conserved.

Furthermore, as illustrated in Figure 5.5b, it is evident that power consumption—defined as the product of torque and angular velocity—can assume positive values even when the torque is negative (i.e., in the clockwise direction), provided the system maintains a constant positive angular velocity. This reflects moments where the motion driver must exert energy to sustain the prescribed motion against the opposing torque.

Figure 5.6 shows the power demand plotted against angular velocity, where only positive values are shown to represent the magnitude of power required for system operation. In the setup with spring, as seen in Figure 5.6b, a pronounced drop in power demand is observed near the resonant frequency, where the required input power is approximately 300 W. In contrast, the conventional setup (Figure 5.6a) demonstrates a significantly higher power requirement, reaching around 1400 W at comparable operating speeds. The negative power values observed in Figure 5.5b—but intentionally excluded from Figure 5.6—correspond to periods where the motion driver theoretically receives energy, as a result of the inertia torque contributions discussed earlier.

a. Without Spring

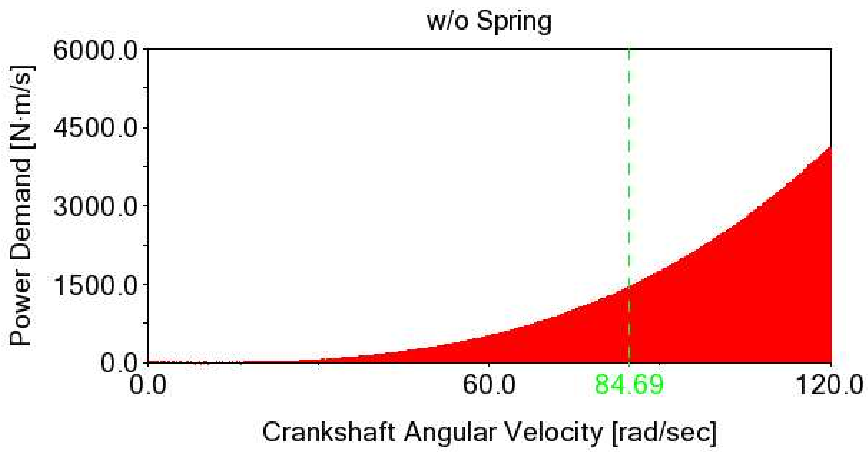

b. With Spring

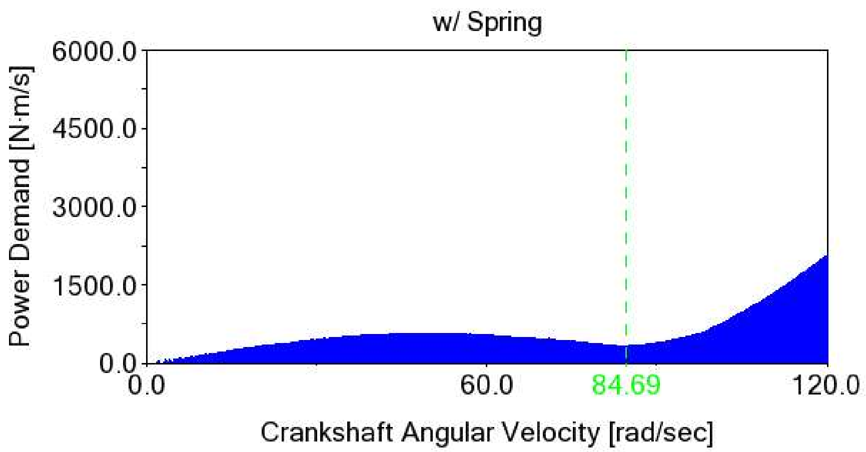

Figure 5.6. Mechanical power demand of the MBD model of reciprocating compressor prototype.

The following discussion elaborates on the effectiveness of resonance utilization in a slider-crank mechanism of a reciprocating compressor subjected to varying levels of external loading. In the MBD simulations, the external load—represented by the force applied at the top of the piston—is implemented as a single-component applied force whose magnitude is defined via a runtime function using the Akima Spline Fitting Method. This runtime function incorporates the modulo operation of the crank angle as the independent variable, and the force data previously imported from Simcenter Amesim—as shown in Figure 5.3b—as the dependent variable. These spline data represent the pressure-induced piston force profiles under different operating conditions. In ADAMS/View, the syntax for the Akima Spline runtime function is defined as:

```
AKISPL(1st_Indep_Var, 2nd_Indep_Var, Spline_Name, Deriv_Order)
```

The modulo operation is implemented using:

```
MOD(x1, x2)
```

Here, the first independent variable (`1st_Indep_Var`) of the `AKISPL` function is assigned the modulated crank angle, calculated via `MOD(x1, x2)`, where `x1` is the cumulative crank angle and `x2` is 360 degrees, representing a full revolution or cycle. The second independent variable (`2nd_Indep_Var`) is not used in this case and may be omitted or set to a constant. The `Spline_Name` corresponds to the specific imported data set representing the desired force profile. The `Deriv_Order` is set to 0, indicating that the function returns the interpolated force value, not its derivative.

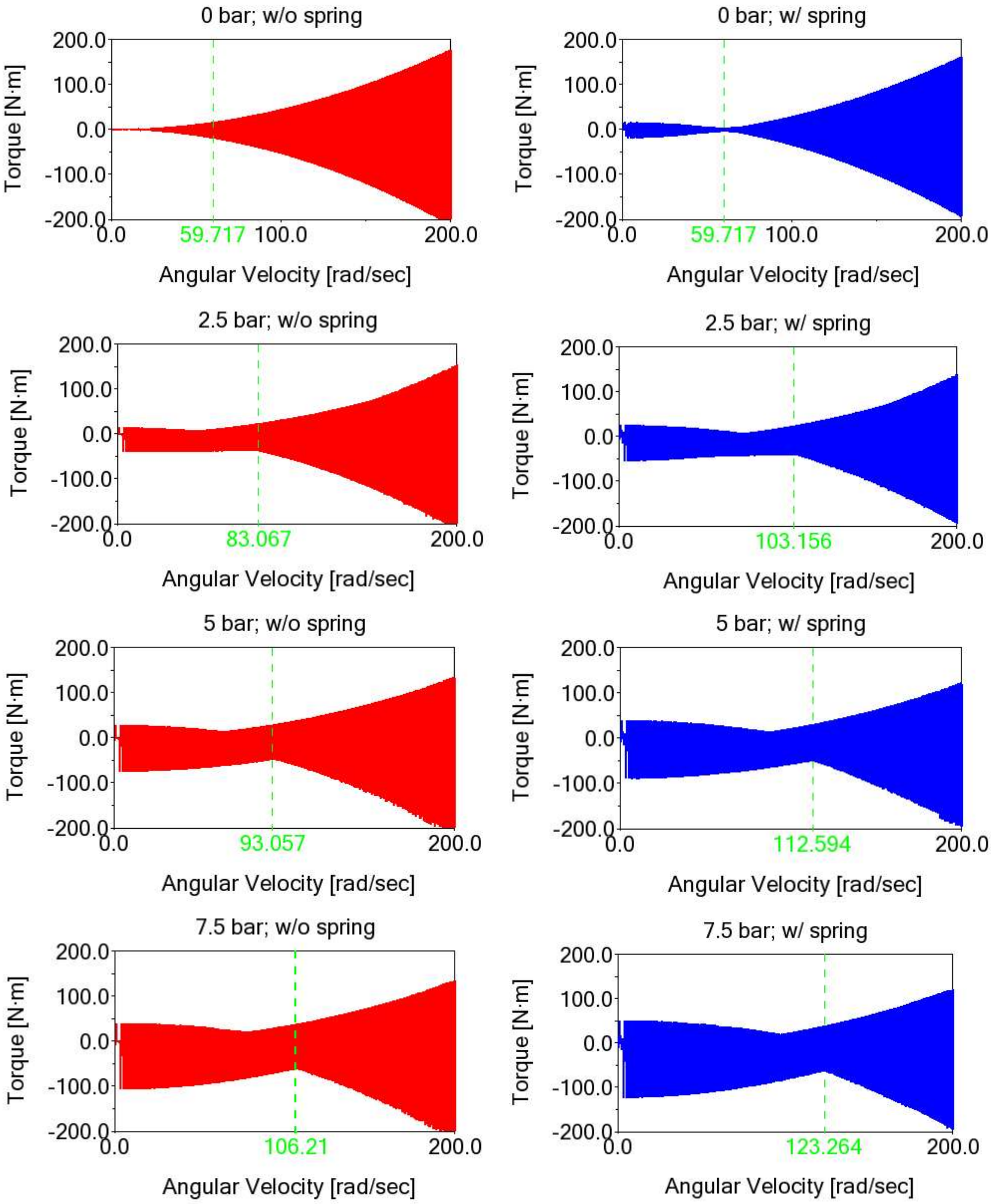

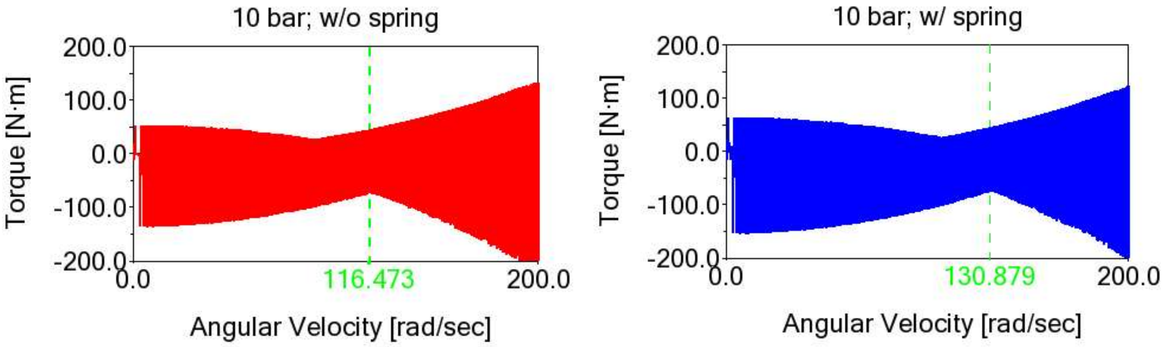

Figure 5.7. Torque–angular velocity curves loaded with different values of external forces. The setup uses $M = 3$ kg, and $k = 6.25$ kN/m.

Figure 5.7 demonstrates that when the system is operated at its resonant frequency, the required input torque is significantly reduced. Notably, this phenomenon is observed in both setups—with and without the mechanical spring. In the configuration without spring, the air compression itself functions as a source of stiffness, effectively acting like a spring. Consequently, the system still exhibits a narrow region of reduced input torque around its natural resonant frequency, indicating that pneumatic loading can inherently enable resonance in such reciprocating systems.

Based on the simulation results, when each setup is operated at its respective resonant frequency, there is no significant difference in the RMS input torque and driver power demand between the spring-assisted and the springless configurations. This implies that resonance-based efficiency benefits can be achieved even in the absence of mechanical springs, provided that the system is operated at the appropriate resonant speed induced by its own pneumatic load characteristics.

In practical terms, for systems equipped with adjustable driver angular velocity, resonance may be achieved through careful speed tuning alone, thereby eliminating the need for mechanical springs. However, if the operational speed of the prime mover is fixed or limited, installing springs with tunable stiffness can serve as a practical means to shift the resonant frequency of the system to align with the available driving conditions.

5.1.3. Experimental Investigation

As illustrated in Figure 5.8, a physical prototype was built to resemble the MBD model, with some differences in the drivetrain and spring configuration. In the MBD simulations, only two extension-compression springs were implemented, whereas the physical prototype utilizes four extension springs, as shown in Figure 5.8(c).

The prototype consists primarily of two sections: the compressor unit and the electric drive system. A pulley-and-belt drivetrain is incorporated to increase the available torque from the motor, also enabling lower starting angular velocities. Moreover, the external load on the slider, represented by the magnitude of air pressure, can be manually adjusted using the relief valve, allowing for controlled testing of system performance under varying pneumatic conditions.

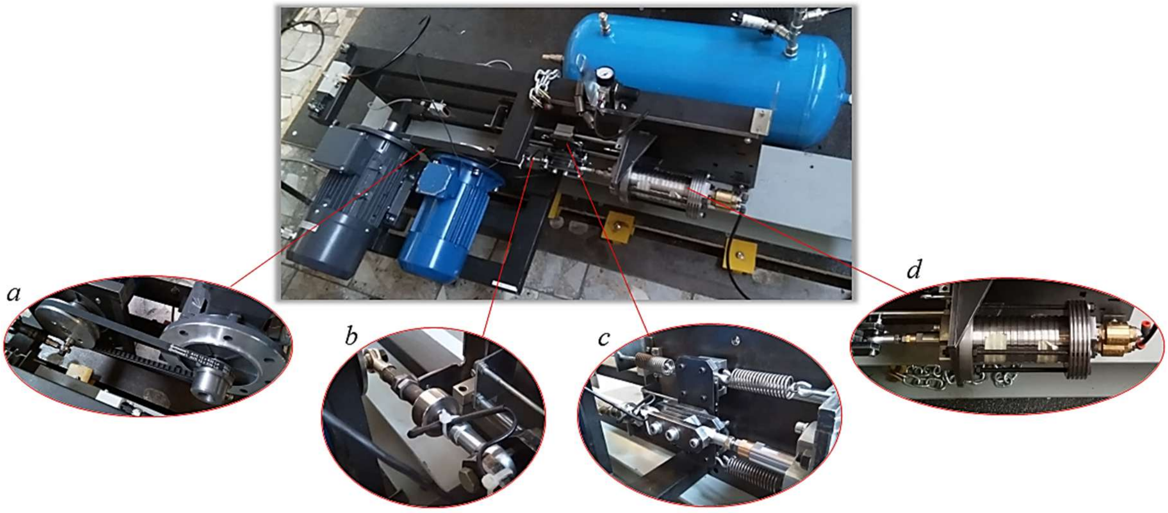

Figure 5.8. *a.* Pulley and belt drivetrain, *b.* Force sensor on the connecting rod joint, *c.* Crosshead and springs, and *d.* Valves, cylinder, and piston connected to the crosshead.

The electric drive system primarily consists of a three-phase induction motor, programmable logic controller (PLC), variable frequency drive (VFD), relays, circuit breakers, switches, cabling, and a control panel enclosure. The assembled control unit is programmed to enable the motor to operate under two modes: at a constant predefined speed or with a linearly increasing speed profile (ramp function), which facilitates a frequency sweep of the slider motion. This allows for the identification of the system's resonant speed through experimental observation. Subsequently, experimental tests are conducted on setups with and without spring elements, allowing a comparison of the resulting forces at the connecting rod joints under identical loading and boundary conditions.

Due to limitations of the physical prototype, experimental testing was restricted to a maximum air pressure of 1 bar. The test results are illustrated in Figure 5.9, with key data summarized in Table 5.3. It is observed that, for all configurations incorporating springs, the force variation across the connecting rod joints exhibits a narrow region near the resonance speed, consistent with the simulated behavior. In the spring-only configuration without pressure load and without valves, the peak-to-peak force is reduced by approximately 60.34% at resonance compared to the non-resonant condition. However, the installation of inlet and outlet valves introduces additional external loading, which reduces the effectiveness of resonance-induced force reduction. Under these conditions, the peak-to-peak force reduction drops to 20.9%.

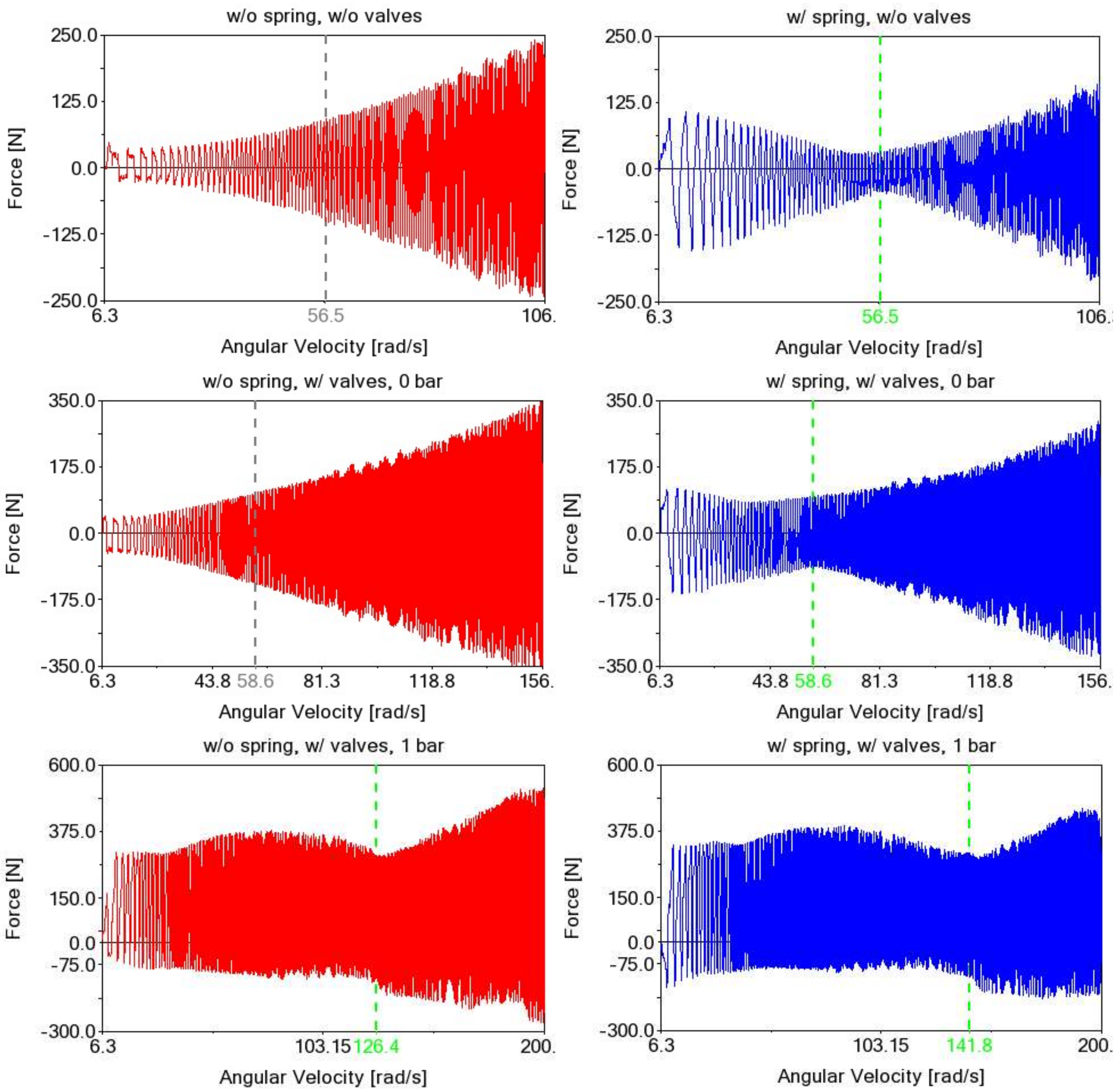

Figure 5.9. Force–angular velocity curves. Force is measured on the connecting rod as shown in Figure 5*b*. Red curves: without spring, blue curves: with spring; M = 3.9 kg, k_{eq} = 2.5 kN/m.

As demonstrated in the simulations, air compression itself acts as a spring, contributing to the system's overall stiffness. Consequently, even without the installation of mechanical springs, a narrow force region is observable. At a compression load of 1 bar, the peak-to-peak force reduction is measured at 6.26% for the conventional setup (without spring) at 126.4 rad/s, and 16.24% for the setup with spring at 141.8 rad/s, corresponding to their respective resonant speeds. However, when both setups are operated at their own resonance frequencies—126.4 rad/s for the conventional case and 141.8 rad/s for the mechanical spring-assisted case—the difference in peak-to-peak force becomes less pronounced, amounting to only 1.53%. This indicates that, depending on the system's parameters and available operating speeds, the use of mechanical springs may be optional. As long as the system is tuned to operate at its natural frequency, either by mechanical or pneumatic means, dynamic performance improvements—such as reduced reaction forces and smoother operation—can still be achieved.

Table 5.3. Comparison of the generated force on the connecting rod of the physical prototype; M = 3.9 kg, k_{eq} = 2.5 kN/m.

Load F_l [bar]	Resonance Speed ω_r [rad/s]	Pulling Force F_{min} [N]		Pushing Force F_{max} [N]		Peak-to-peak Amplitude of Force F_{pp} [N]		Decrease of peak-to-peak amplitude of Force [%]
		w/o spring	w/ spring	w/o spring	w/ spring	w/o spring	w/ spring	
w/o valves	56.5	−99.84	−43.92	93.2	32.64	193.04	76.56	60.34
0	58.6	−134.64	−92.08	106.08	98.32	240.72	190.4	20.90
1	126.4	−133.28	−84.08	295.04	317.44	428.32	401.52	6.26
1	141.8	−181.68	−121.04	321.84	300.72	503.52	421.76	16.24

5.2. Punch Press Machine

This section presents a resonance-based slider-crank mechanism developed to enhance the dynamic performance of a punch press machine as an application example. A comparative analysis is conducted between the proposed resonance model and a conventional counterpart to evaluate improvements in mechanical behavior and energy utilization.

5.2.1. Modeling

The designs investigated in this section comprise two distinct configurations: a conventional setup and a resonance setup. These configurations are subjected to comparative analysis to assess their respective performances and to validate the effectiveness of the resonance-based design.

As shown in Figure 5.10, the resonance setup retains the core components of the conventional system—crankshaft, connecting rod, and slider—while additionally incorporating spring elements. These springs are placed between the slider and the frame, enabling the system to resonate at a specific frequency. In contrast, the conventional setup follows standard design practices without the use of springs. Moreover, Figure 5.11 presents the multibody model, showing the detailed design of the developed punch press machine.

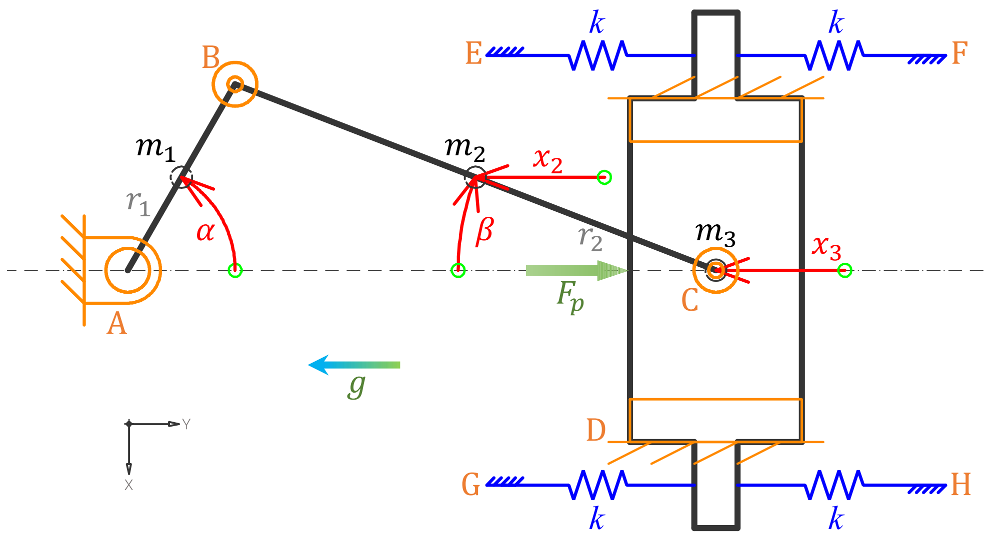

Figure 5.10. Body diagram of the developed resonance punch press machine. The arrow g denotes the gravitational force, while F_p represents the punching force.

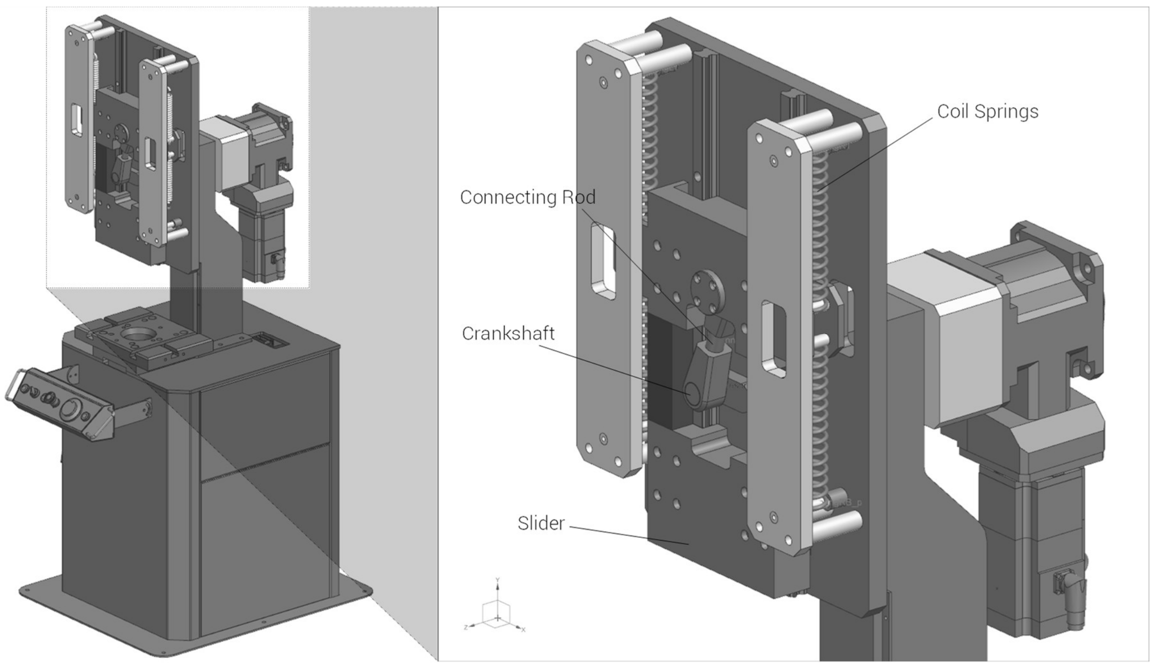

Figure 5.11. Multibody model of the developed punch press machine.

5.2.2. Simulation

In the comparative analysis, both mechanisms are designed with identical parameters, as summarized in Table 5.4. The crankshaft angular velocity for both configurations is set to the resonant frequency of the resonance model, approximated using Equation 3.7.

Table 5.4. Multibody model of the developed punch press machine specification.

Rigid Body		
Crank length l_1		50 mm
Connecting rod length l_2		170.13 mm
Mass of each body	m_1	4.33 kg
	m_2	1.8 kg
	m_3	42.71 kg
Moments of inertia	I_{xx}, I_{yy}, I_{zz} of m_1	81715.14 kg · mm², 81049.98 kg · mm², 1532.18 kg · mm²
	I_{xx}, I_{yy}, I_{zz} of m_2	6926.56 kg · mm², 6810.36 kg · mm², 465.71 kg · mm²
	I_{xx}, I_{yy}, I_{zz} of m_3	1401856.49 kg · mm², 1084119.48 kg · mm², 346652.14 kg · mm²
Joints		
Revolute	Pin Radius	20 mm
	Bending Reaction Arm	200 mm
	Friction Arm	20 mm
Cylindrical	Pin Radius	20 mm
Translational	Reaction Arm	4 × 12.5 mm
Spherical	Ball Radius	20 mm

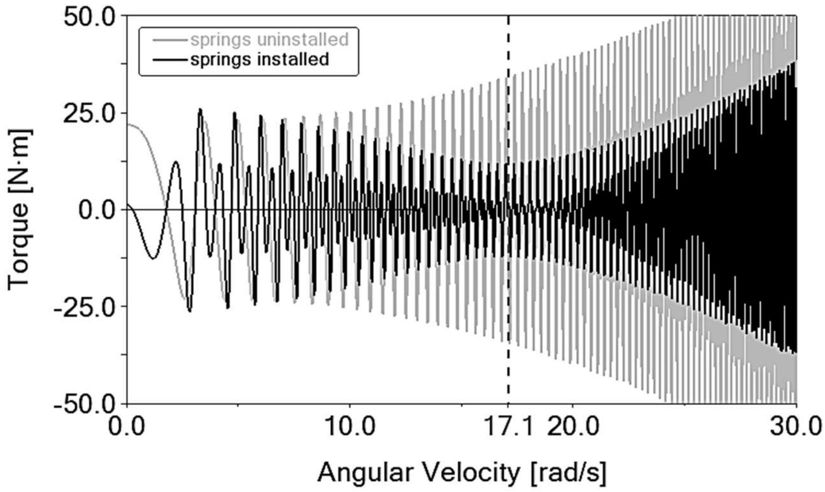

Figure 5.12. Input torque of the punch press machine with and without the spring installed. Both setups were simulated without dissipative forces and gravity.

Figure 5.12 presents the crank input torque profiles of the presented punch press machine under two distinct configurations: conventional setup (springs uninstalled) and resonance setup (springs installed). Both are subjected to a uniformly increasing angular velocity, ramped at a rate of 1 rad/s², while disregarding dissipative forces and gravitational effects to isolate the dynamic response. The results show a noticeable contrast in behavior between the two setups. In the configuration without springs, torque fluctuations remain relatively broad and persistent throughout the entire angular velocity range. In contrast, the model with spring elements demonstrates a significantly narrower region of torque fluctuations, particularly apparent as the crankshaft angular velocity approaches the system's natural frequency at 17.1 rad/s.

As discussed in Chapter 2, the presence of gravity affects the distribution of potential energy within the reciprocating components, particularly in vertically oriented systems such as punch press machines. To maintain dynamic equilibrium and ensure proper resonance behavior, it is essential to balance the periodic gravitational potential energy with the periodic potential energy stored in the spring element. The approach involves configuring the spring system such that the slider reaches its equilibrium position at the midpoint of its stroke, independent of any external conservative forces. In the vertical configuration of a punch press, this condition requires the application of a constant upward (opposing) force equal in magnitude to the gravitational force acting on the slider. This is achieved by preloading the spring with a force, whose magnitude is determined by Equation 2.61 with angle θ is taken as 0°. Practically, this preload is implemented by introducing an initial spring displacement, calculated using Equation 2.62.

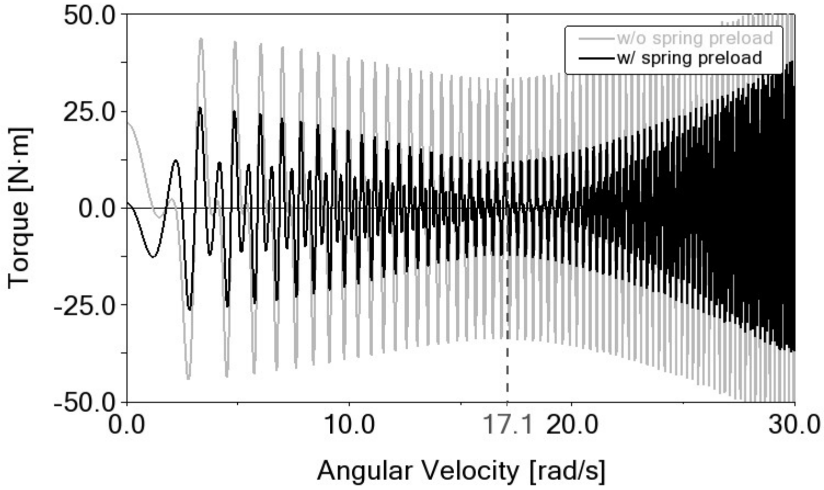

Figure 5.13. Input torque of the punch press machine with and without the spring preload. Both setups were run under the gravity acting towards the negative Y-axis illustrated in Figure 5.10.

The influence of spring preload on the dynamics behavior of the mechanism is illustrated in Figure 5.13. The figure compares two configurations: one in which the spring element is installed at the midpoint of the slider stroke but without any preload (represented by the gray curves and labeled *w/o spring preload*), and another where a calculated preload is applied to the spring (represented by the black curves and labeled *w/ spring preload*). The preloaded configuration demonstrates a notable reduction in input torque fluctuations near the system's resonant frequency. This behavior more closely resembles the ideal resonance condition observed in the absence of gravitational effects presented in Figure 5.12.

Furthermore, the comparison of input torque over a single cycle at the resonant frequency (17.1 rad/s) is shown in Figure 5.14, with the corresponding data summarized in Table 5.5. Consistent with the trends observed in Figures 5.12 and 5.13, Figure 5.14 confirms that incorporating spring elements and operating at the resonant frequency significantly reduces input torque fluctuations.

Figure 5.14. Input torque within one cycle under constant 17.1 rad/s angular velocity of the crank.

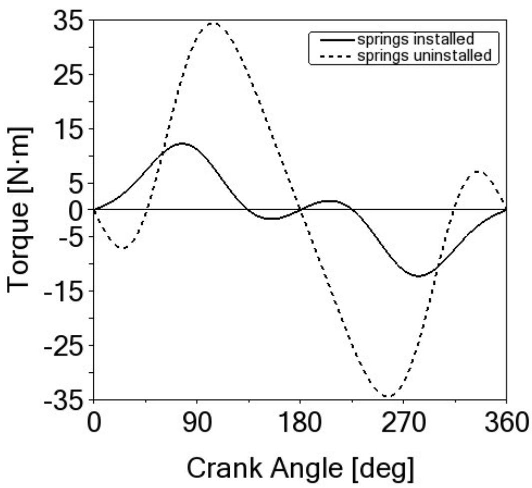

Table 5.5. Input torque within one cycle under constant 17.1 rad/s angular velocity of the crank.

Setup	Peak Torque [N · m]	RMS Torque [N · m]
Resonance (springs installed)	12.21	6.59
Conventional (springs uninstalled)	34.48	20.14

Table 5.6. Joint reaction forces magnitude of the conventional and resonance models run at the resonant speed of 17.1 rad/s.

Joint	Peak Force [N]				RMS Force [N]			
	Conventional		Resonance		Conventional		Resonance	
	x-axis	y-axis	x-axis	y-axis	x-axis	y-axis	x-axis	y-axis
A	243.91	950.24	84.29	270.18	143.61	680.06	46.65	172.44
B	238.0	902.11	78.06	228.90	139.76	647.81	42.68	147.73
C	224.71	863.89	64.03	213.89	131.22	622.67	34.17	148.84
D	224.78	-	64.03	-	131.22	-	34.17	-

Figure 5.15 presents the joint reaction forces of the conventional and resonance setups at the same resonant frequency, with the corresponding data provided in Table 5.6. The results show that the resonance setup achieves a substantial reduction in joint reaction force fluctuations; which is in practice, lower joint forces potentially reduce energy dissipation due to friction. According to

Table 5.6, the most significant reduction occurs in the crankshaft-to-frame connection (joint A), with decreases of approximately 66.57% in peak force and 65.36% in RMS force compared to the conventional model.

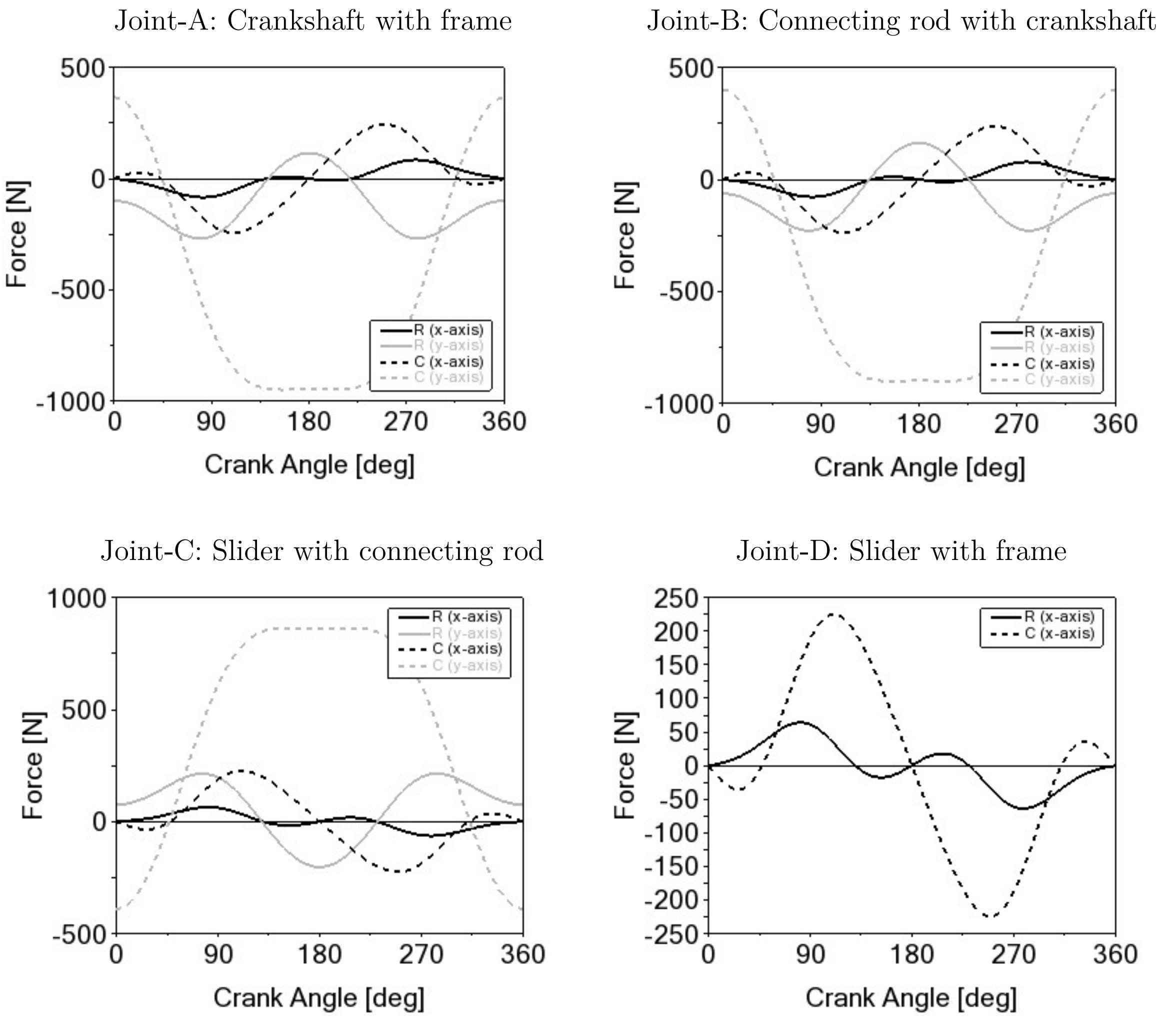

Figure 5.15. Joint reaction forces within one cycle under constant 17.1 rad/s angular velocity of the crank.

The subsequent discussion presents the results of simulations conducted to evaluate the dynamic behavior of the system under varying Coulomb damping conditions. The joint configurations are modeled using the geometric specifications provided in Table 5.4, while the joint coefficient of frictions are stated in Table 5.7. Variations in the coefficient of friction significantly influence the magnitude of joint tangential forces and, consequently, the input torque, as shown in Figure 5.16. An increase in the friction coefficient shifts the input torque curve downward, indicating a rise in the average work required per cycle. Throughout all simulated friction scenarios, the resonance setup consistently demonstrates reduced work per cycle compared to the conventional setup. The essential data of the curves in Figure 5.16 are further noted in Table 5.7.

Table 5.7. Input torque and rotational work per cycle of the conventional and resonance models under different cases of joint frictions.

Friction Case	Coefficient of Friction		Peak Torque [N · m]		RMS Torque [N · m]		Rotational Work per Cycle [J]	
	μ_s	μ_d	Conv.	Reso.	Conv.	Reso.	Conv.	Reso.
a	0.2	0.1	17.35	12.86	8.42	6.61	6.18	2.30
b	0.4	0.2	18.69	13.43	8.61	6.64	11.89	4.29
c	0.6	0.3	20.04	13.99	8.91	6.69	17.61	6.29

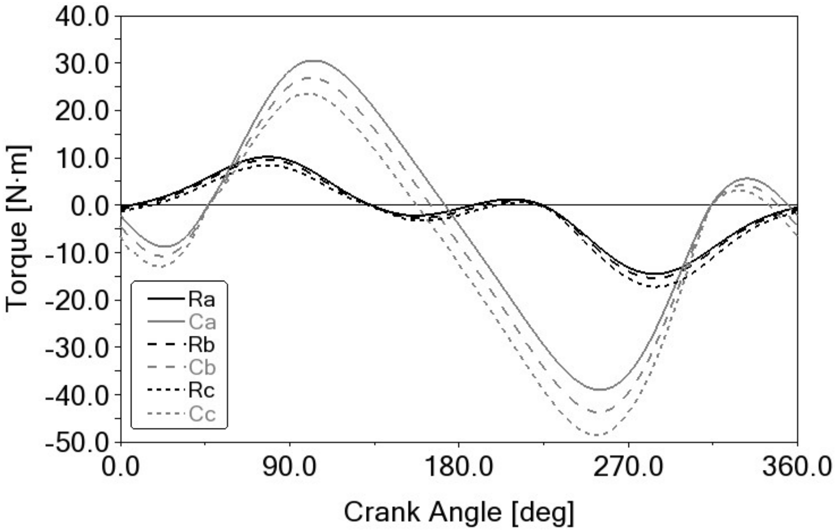

Figure 5.16. Input torque of the conventional (C) and resonance (R) models under different cases of joint frictions.

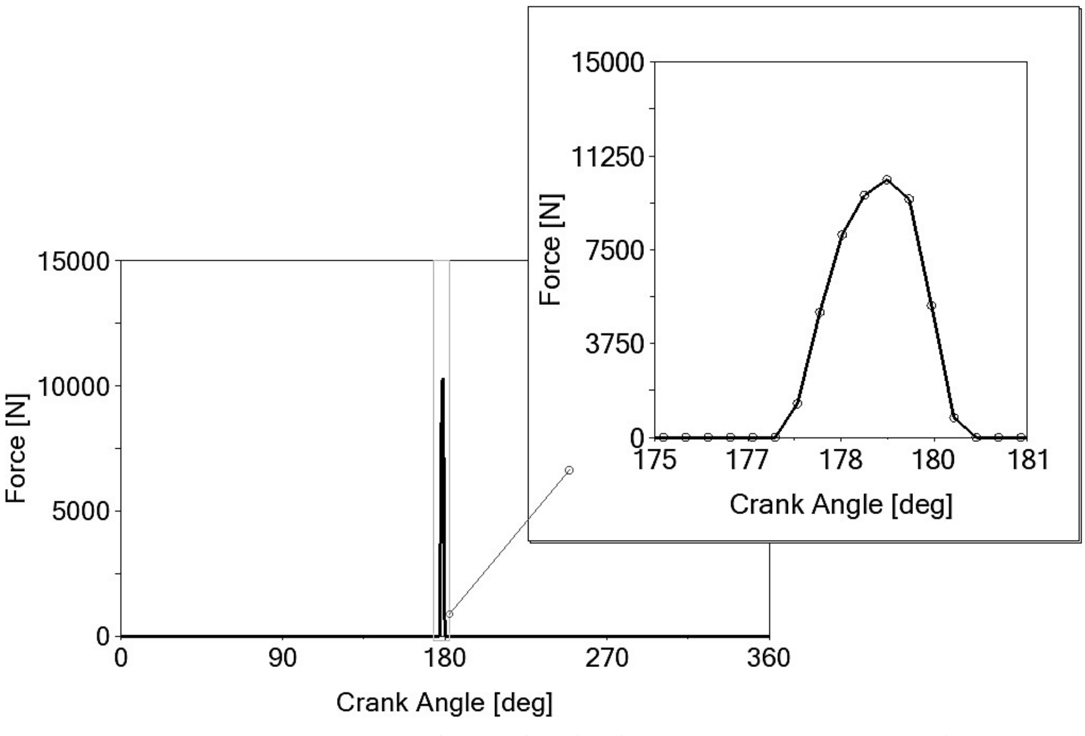

Figure 5.17. Force-crank angular displacement curve in one cycle.

Further analyses explore the influence of the punching process within a single cycle, using a case study derived from the work of Kubik et al. [128], which presents characteristic force–displacement curves for the blanking process. As illustrated in Figure 5.17, the example punching force profile exhibits a peak force of 10.3 kN during the punching phase, resulting in an estimated work input of approximately 10 J per cycle. When this force profile is applied, the resulting input torque is shown in Figure 5.18, with important numerical data summarized in Table 5.8. The results clearly indicate that the resonance setup exhibits lower work done per cycle, in comparison to the conventional setup.

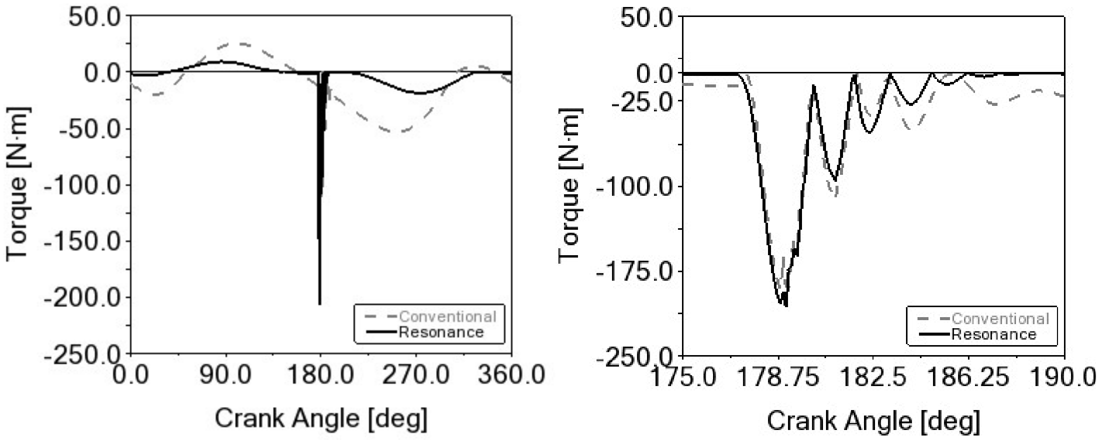

Figure 5.18. Input torque in one cycle under punching process (with zoom section from 175 to 190 degrees).

Table 5.8. Input torque and work done per cycle of the conventional and resonance models during punching process.

	Peak Torque [N · m]	RMS Torque [N · m]	Rotational Work per Cycle [J]
Conventional	191.39	28.16	72.58
Resonance	207.18	14.88	22.7

5.2.3. Experimental Investigation

Building on the previously described multibody model, Figure 5.19 presents the physical prototype of the developed punch press machine, designed for the experimental investigations conducted in this work. The working mechanism consists of a slider–crank mechanism with a spring element, and a die assembly mounted beneath the slider. The slider–crank mechanism is driven by a servo motor through a belt-and-pulley arrangement, with motion controlled by a servo drive and its associated components and measurement equipment shown in Figure 5.20, with the schematic diagram shown in Figure 5.21. The entire press is mounted on a rigid frame equipped with an integrated control panel for operational safety and adjustment.

Figure 5.19. Working mechanism of the physical prototype of resonance punch press machine.

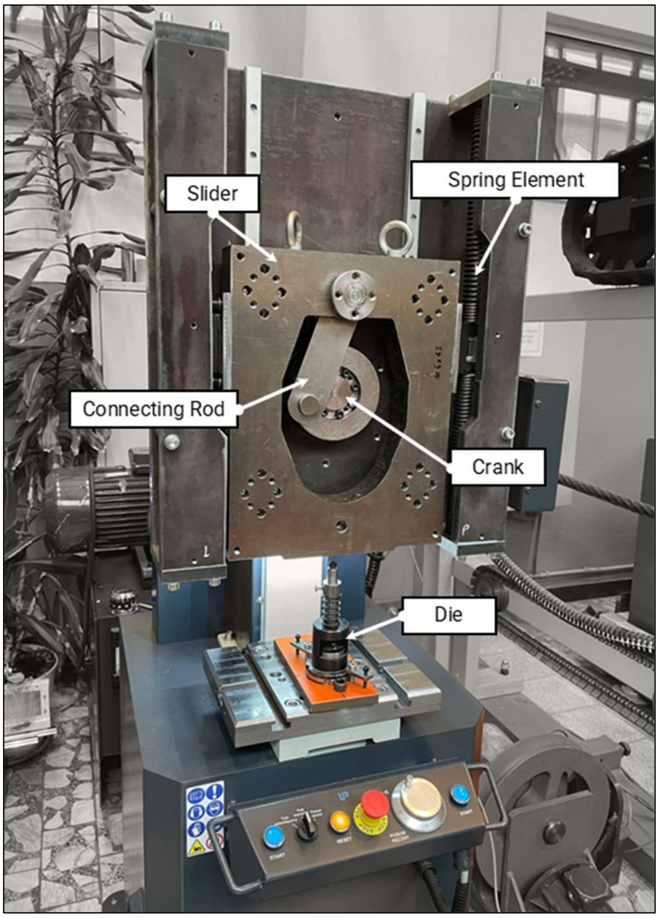

In detail, Figure 5.21 illustrates the primary schematic configuration of power measurement system implemented for the punch press machine prototype. The setup is aimed to monitor the instantaneous power characteristics of the machine during operation. The system is supplied by a three-phase power source, which provides the electrical input to the punch press machine. A circuit breaker is installed upstream of the system to provide overcurrent protection and safe isolation. Downstream of the circuit breaker, an electromagnetic relay is incorporated to enable controlled switching of the power supply to the servo drive. To enable electrical measurement, current transformers (CTs) are installed on the three-phase lines. The CTs measure the phase currents non-intrusively and provide scaled signals proportional to the line currents. These signals, together with the measured phase voltages, are transmitted to the three-phase energy and power measurement terminals. This measurement unit computes electrical parameters including phase current, line voltage, active power, reactive power, and apparent power. The servo drive receives the three-phase input power and performs AC–DC–AC conversion to supply controlled electrical power to the servo motor, allowing control of motor torque, speed, and position. A regenerative resistor is connected to the servo drive to dissipate excess electrical energy during deceleration or braking events, preventing overvoltage in the DC bus. For data acquisition and monitoring, the energy and power measurement unit is integrated with an embedded PC and a power supply unit. The embedded PC collects the processed electrical measurement signals and transmits them to a host PC for real-time visualization, recording, and further analysis.

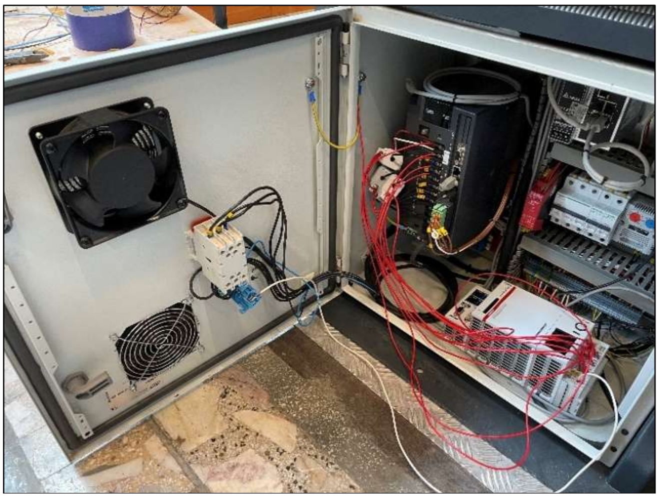

Figure 5.20. Drive system of the physical prototype of resonance punch press machine and its measurement equipment.

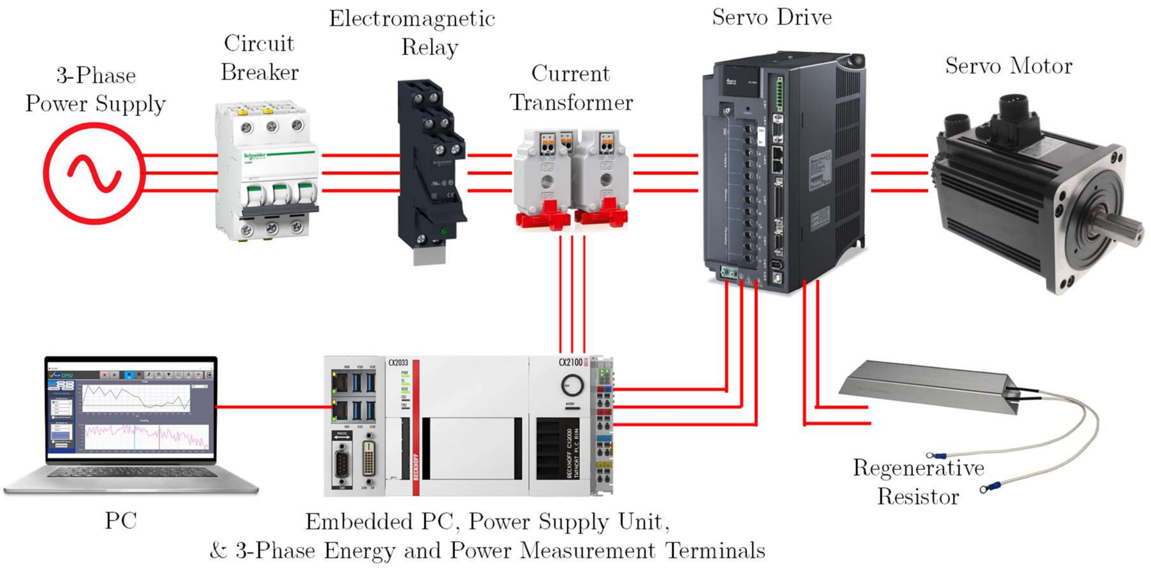

Figure 5.21. Schematic diagram of the energy and power measurement of the punch press machine prototype.

Figure 5.22 illustrates the active power response of the punch press machine drive system under two setups: conventional (without spring) and resonance (with spring and preload). Both cases were tested at a rotational speed of approximately 1787 RPM, which corresponds to resonant speed for the setup with spring. The equipment used to measure the active power applies the formula given in Equation 5.10, where P denotes the active power, n is the number of samples, $u_{(t)}$ is the instantaneous voltage, and $i_{(t)}$ is the instantaneous current.

$$P = \frac{1}{n}\sum_{n}^{1} u_{(t)} . i_{(t)} \tag{5.10}$$

Without the punching process and the die is not installed, in the conventional setup, the active power is consistently at higher magnitude, oscillating between approximately 20–400 W, with an RMS value of 243.2 W and average of 211.8 W over one cycle during steady operation. On the other hand, in the resonance setup (with a spring and preload, at resonance), the active power fluctuation is reduced to approximately 70–300 W, with an RMS value of 221.9 W and average of 205.9 W over one cycle at the corresponding operating speed.

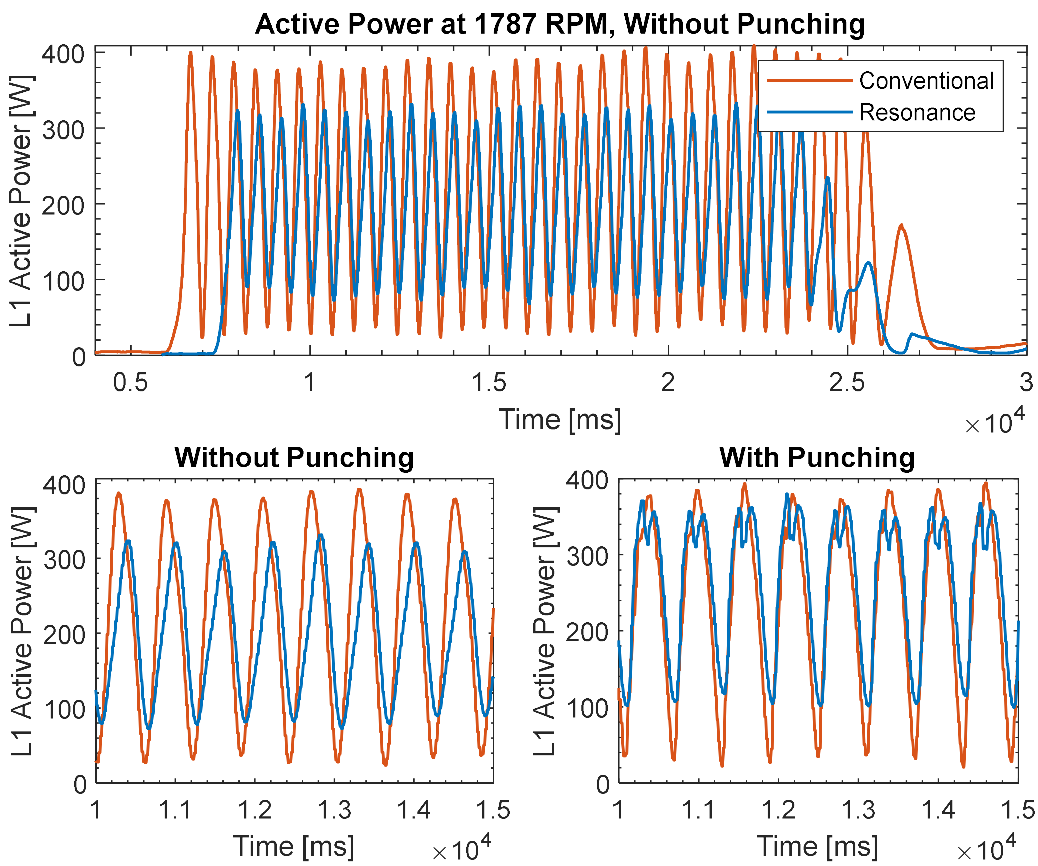

Figure 5.22. L1 active power response of the punch press machine prototype. The upper plot shows the complete test sequence, whereas the lower plots show the zoomed-in segment for detailed observation.

Table 5.9. Electrical active power (L1 phase) of the conventional and resonance setups in experimental tests.

Setup		RMS Active Power [W]	Average Active Power [W]
Without Punching	Conventional	243.2	211.8
	Resonance	221.9	205.9
With Punching	Conventional	273.1	250.3
	Resonance	255.6	238.8

When the punching process of the plate is included, the active power increases in both configurations due to the additional mechanical load. In the conventional setup, the active power oscillates with an RMS value of 273.1 W and an average of 250.3 W over one cycle. In contrast, when operating in resonance setup, these values decrease to an RMS of 255.6 W and an average of 238.8 W. The resonance configuration demonstrates a slight reduction in both RMS and mean active power of approximately 6.4% and 4.6%, respectively, compared with the conventional setup. Overall, the main findings discussed above are presented in Table 5.9.

For future work, it is necessary to perform a systematic experimental comparison between the power demand of the presented resonance punch press prototype and that of conventional punch press machines currently available on the market. Such a comparative study should be conducted under equivalent operating conditions, including identical properties, stroke rates, and forming loads, to ensure a reasonable evaluation of energy consumption and power requirements.

Chapter 6
Conclusions and Future Work

Unbalanced inertia forces, moments, and torques have a significant impact on the dynamic performance of slider-crank and Scotch-yoke mechanisms. These imbalances introduce vibrations, elevated dynamic stresses, and accelerated wear of mechanical components, thereby limiting operational reliability, efficiency, and service life. Conventional mitigation strategies often rely on geometric balancing, additional counterweights, or structural reinforcements, which can increase system complexity, mass, and cost. In contrast, this dissertation investigates the deliberate utilization of mechanical resonance as an alternative and fundamentally different approach to dynamic load mitigation. By tuning the system such that the excitation frequency coincides with the natural frequency of the elastic–inertial subsystem, resonance is utilized to compensate inertia-induced forces over the operating cycle. The results demonstrate that, when properly designed and operated, resonance enables a systematic reduction in force, moment, and torque fluctuations without extensive structural modification, offering a scalable and energy-efficient solution for reciprocating mechanisms. The principal outcomes of this study are summarized below in terms of scientific and application-oriented contributions.

6.1. Summary of Scientific Results

This dissertation advances the theory and practice of dynamic balancing in reciprocating mechanisms by demonstrating that mechanical resonance can be deliberately synthesized and utilized as a cyclic inertia load reduction, rather than avoided as a source of vibration. A generalized resonance-based synthesis framework is developed, in which the inertia forces of reciprocating bodies are balanced by elastic restoring forces through controlled energy exchange. By explicitly linking reciprocating mass, spring stiffness, and operating speed via the natural frequency of the equivalent mass–spring subsystem, the work establishes the precise conditions under which kinetic energy of the reciprocating body is cyclically converted into elastic potential energy and returned with minimal net torque demand over a full operating cycle.

Secondly, in addition to global force reduction, the dissertation provides a mechanism-level understanding of how resonance redistributes dynamic loads within the kinematic chain. Through systematic variation of spring stiffness and excitation frequency, it is shown that the internal force transmission paths can be altered during resonance, enabling selective reduction of reaction forces at specific joints (e.g., crank–connecting rod or connecting rod–slider). This in turn allows balancing strategies to be tailored toward protecting fatigue-critical components such as crank pins, connecting rods, or slider guides, depending on application requirements.

Third, the scientific contribution of this work is the identification of equilibrium positioning and gravity compensation as necessary conditions for realizable resonance in practical mechanisms. The dissertation shows that resonance-assisted balancing is only achievable when the reciprocating body is positioned at the midpoint of its stroke in the static equilibrium configuration, ensuring symmetric spring deformation and minimizing torque fluctuation. In the presence of gravity, it is demonstrated that spring installation alone is insufficient to produce resonance; gravitational potential energy variations introduce an undesired influence that disrupts energy exchange unless compensated through appropriate spring element preload, and/or mechanism reorientation.

Fourth, the robustness and limits of resonance-assisted operation are quantified through an analysis incorporating viscous and Coulomb damping, externally applied forces with different temporal profiles, and variations in reciprocating mass and spring element stiffness. The results show that effective resonance can be load-dependent, with externally applied forces shifting the effective resonant frequency and constraining the operating range over which inertia compensation remains effective.

Fifth, by extending the analysis to flexible multibody dynamics, the dissertation further demonstrates that resonance-based balancing yields significant reductions in structural strain energy and elastic deformation in main components. This establishes a direct causal link between resonance utilization and improved structural durability.

Finally, the theoretical and numerical findings are experimentally validated using physical prototypes of both slider–crank and Scotch–yoke mechanisms. The experimental results confirm significant reductions in dynamic force amplitudes and electric power demand under both unloaded and externally loaded conditions. These results demonstrate that the proposed resonance-based design methodology is not only theoretically rigorous but also experimentally robust in the presence of friction, manufacturing tolerances, and real-world disturbances.

6.2. Implications for Engineering Practice

A primary application-oriented contribution is that, as mentioned earlier, the resonance-based operation mitigates peak inertia forces and torque fluctuations, leading to lower reaction forces at joints and reduced stress amplitudes in load-bearing components. These outcomes directly contribute to enhanced durability and extended service life of mechanical systems. Reductions in electric power demand through resonance-based design are also demonstrated, under both unloaded and externally loaded operating conditions. Experimental results for both slider–crank and Scotch–yoke mechanisms show that, when operated at resonance, the average electrical power drawn by the drive motor can be reduced by up to 40–55% relative to conventional configurations without elastic elements.

Closely related to this, the dissertation provides evidence of peak power and torque reduction at resonance, which has direct implications for actuator selection and drivetrain sizing. The measured reduction in peak electrical power—particularly in the resonance speed range—indicates that motors, power electronics, and transmission components can be downsized or operated with increased reliability margins. This is especially relevant for electrically driven systems where peak power constraints often determine component selection and cost in industrial machinery employing slider–crank or Scotch–yoke mechanisms.

Another important application-oriented contribution is the identification of operational trade-offs and safe operating ranges for resonance-based mechanisms. The experimental results show that the inclusion of springs increases power demand at low rotational speeds and that resonance benefits diminish at speeds far above the tuned natural frequency. By explicitly indicating these regions, the dissertation provides guidance on when resonance-based designs are advantageous and when conventional configurations may be preferable.

Finally, the dissertation delivers a practical, step-by-step design methodology for implementing resonance in reciprocating mechanisms, bring in together from numerical and experimental findings. The methodology integrates external load identification, target speed selection, reciprocating mass sizing, spring stiffness tuning, gravity compensation, and resonant operation. This procedure is explicitly validated through prototype testing and measurements, making it transferable to industrial practice and future product development. The presented methodology in principle can be adapted to existing designs or incorporated into new systems with relatively minor structural changes, making it appealing for a wide range of engineering applications.

6.3. Limitations and Future Work

While this dissertation demonstrates that mechanical resonance can be utilized to improve the dynamic performance of slider–crank and Scotch–yoke mechanisms, several limitations must be acknowledged. Recognizing these limitations is essential for interpreting the results and for guiding future research efforts.

First, the resonance-based mechanisms rely on spring elements with fixed stiffness and constant reciprocating mass. While this design choice ensures simplicity, robustness, and ease of implementation, it also constrains the system to a single dominant resonant frequency. As a result, optimal performance cannot be maintained when operating conditions vary significantly over time. This limitation is particularly relevant for applications involving variable-speed drives, intermittent loading, or frequent start–stop operation, where resonance tuning cannot be continuously maintained. Second, the experimental investigation focused on steady-state cyclic operation. Transient effects such as start-up, shut-down, speed ramping, and impact-dominated loading were not investigated in great detail. These conditions may introduce additional dynamic effects that influence stability and durability in industrial applications. Third, although stresses in the bodies were evaluated, long-term fatigue of the spring element was not addressed. The durability of the spring element under prolonged resonance operation remains an important topic for future investigation.

These limitations suggest several directions for future research. One important path is the development of adaptive or semi-active resonance control strategies capable of maintaining near-resonant operation under varying load and speed conditions. Such approaches may involve real-time adjustment of drive speed, controlled auxiliary masses, or effective stiffness through feedback control. Additionally, the investigation of alternative elastic elements—such as variable-stiffness springs, magnetic springs, or pneumatic springs—may extend the effective resonance range and improve robustness. Finally, applying the proposed methodology to more complex mechanisms and full-scale industrial systems would further validate its practicality and broaden its applicability.

References

[1] V. Arakelian and S. Briot, “Balancing of linkages and robot manipulators,” *Mechanisms and Machine Science*, 2015. doi:10.1007/978-3-319-12490-2.

[2] V. Arakelian, J.-P. Le Baron, and M. Mkrtchyan, “Design of Scotch yoke mechanisms with improved driving dynamics,” *Proceedings of the Institution of Mechanical Engineers, Part K: Journal of Multi-body Dynamics*, vol. 230, no. 4, pp. 379–386, Dec. 2016, doi: 10.1177/1464419315614431.

[3] V. Arakelian and M. R. Smith, “Shaking Force and Shaking Moment Balancing of Mechanisms: A Historical Review with New Examples,” *Journal of Mechanical Design*, vol. 127, no. 2, pp. 334–339, Mar. 2005, doi: 10.1115/1.1829067.

[4] E. N. Stevensen, “Balancing of Machines,” *Journal of Engineering for Industry*, vol. 95, no. 2, pp. 650–656, May 1973, doi: 10.1115/1.3438205.

[5] J. L. Wiederrich, “Analysis of Drive Shaft Speed Variations in a Scotch Yoke Mechanism,” *Journal of Mechanical Design*, vol. 104, no. 1, pp. 239–246, Jan. 1982, doi: 10.1115/1.3256317.

[6] R. H. Avanço *et al.*, “Remarks on the dynamics of a DC motor moving a cart horizontally,” *Springer Proceedings in Mathematics & Statistics*, pp. 69–80, 2024. doi:10.1007/978-3-031-56492-5_6.

[7] H. Nigus, “Kinematics and Load Formulation of Engine Crank Mechanism,” *Mechanics, Materials Science & Engineering Journal*, 2015, doi: 10.13140/RG.2.1.3257.1928.

[8] B. Zappa, V. Lorenzi, P. Righettini, and R. Strada, “Design of Torque Balancing Mechanisms,” *Journal of Mechanics Engineering and Automation*, vol. 7, no. 6, Jun. 2017, doi: 10.17265/2159-5275/2017.06.004.

[9] M. T. Orvananos-Guerrero, M. Acevedo, C. N. Sanchez, N. Ivan Giannoccaro, P. Visconti, and R. Velazquez, “Efficient Balancing Optimization of a Simplified Slider-Crank Mechanism,” in *2020 IEEE ANDESCON*, IEEE, Oct. 2020, pp. 1–6. doi: 10.1109/ANDESCON50619.2020.9272109.

[10] A. K. Abdul Jawwad, N. AlShabatat, and M. Mahdi, “The effects of joint design, bolting procedure and load eccentricity on fatigue failure characteristics of high-strength steel bolts,” *Engineering Failure Analysis*, vol. 122, p. 105279, Apr. 2021. doi:10.1016/j.engfailanal.2021.105279.

[11] T. Ren, W. T. Qu, and W. Sun, “Dynamics Study of a Dynamic Balancing Linkage

with Small Fluctuations in Load," *Applied Mechanics and Materials*, vol. 86, pp. 176–179, Aug. 2011, doi: 10.4028/www.scientific.net/AMM.86.176.

[12] J. Hu, C. Deng, D. Yang, Y. Yang, and M. Jia, "Optimal energy consumption and torque fluctuation control of integrated electric drive system based on mechanical-electromagnetic-thermal coupling characteristics," *Energy*, vol. 247, p. 123504, May 2022, doi: 10.1016/j.energy.2022.123504.

[13] F. Zi-Ming, D. Huan-Huan, and J. Min-Zheng, "New Secondary Balancing Method Saves Energy for Crank-Balanced Rod-Pumping Application," *SPE Production & Operations*, vol. 30, no. 02, pp. 141–145, May 2015, doi: 10.2118/173889-PA.

[14] J. J. Uicker, G. R. Pennock, and J. E. Shigley, *Theory of machines and Mechanisms,* 5th ed. New York: Oxford University Press, 2017.

[15] F. Freudenstein, J. P. Macey, and E. R. Maki, "Optimum Balancing of Combined Pitching and Yawing Moments in High-Speed Machinery," *Journal of Mechanical Design*, vol. 103, no. 3, pp. 571–577, Jul. 1981, doi: 10.1115/1.3254956.

[16] V. Votrubec, "An influence of balancing on non-uniform motion of crank-slider mechanism," *Journal of Vibration Engineering and Technologies*, vol. 3, no. 6, pp. 711–720, 2015.

[17] R. S. Berkof, "The input torque in linkages," *Mechanism and Machine Theory*, vol. 14, no. 1, pp. 61–73, Jan. 1979, doi: 10.1016/0094-114X(79)90042-9.

[18] J. L. Elliott and D. Tesar, "The Theory of Torque, Shaking Force, and Shaking Moment Balancing of Four Link Mechanisms," *Journal of Engineering for Industry*, vol. 99, no. 3, pp. 715–722, Aug. 1977, doi: 10.1115/1.3439303.

[19] O. Fischer. "Über die reduzierten Systeme und die Hauptpunkte der Glieder eines Gelenkmechanismus", *Zeitschrift für Angewandte Mathematik und Physik*, 1902, 47, pp. 429-466.

[20] V. P. Goryachkin, "The Forces of Inertia and Their Balancing", *Collection of Scientific Works*, Moscow, Russia: Kolos, 1914, pp. 283–418

[21] V.A. Yudin, "The balancing of machines and their stability (Russian)". *Edition of Academy of Red Army*, Moscow, 1941, p. 124

[22] F.M. Lanchester, "Engine balancing". *Horseless Age*, 33 (12-16), Mar. 25, Apr. 1,8,15, 22, pp. 494-498, 536-538,571-572, 608-610,644-646 (1914)

[23] F. R. E. Crossley, *Dynamics in machines.* New York, Ronald Press Co, 1954. Accessed: Mar. 09, 2025. [Online]. Available: http://archive.org/details/dynamicsinmachin0000cros

[24] R. L. Maxwell, *Kinematics and dynamics of machinery.* Englewood Cliffs, N.J., Prentice-Hall, 1960. Accessed: Mar. 09, 2025. [Online]. Available: http://archive.org/details/kinematicsdynami00maxw

[25] M. R. Smith and L. Maunder, "Inertia Forces in a Four-Bar Linkage," *Journal of Mechanical Engineering Science*, vol. 9, no. 3, pp. 218–225, Jun. 1967, doi: 10.1243/JMES_JOUR_1967_009_034_02.

[26] H. Hilpert, "Weight balancing of precision mechanical instruments," *Journal of Mechanisms*, vol. 3, no. 4, pp. 289–302, Dec. 1968, doi: 10.1016/0022-2569(68)90005-0.

[27] V. A. Kamenskii, "On the question of the balancing of plane linkages," *Journal of*

Mechanisms, vol. 3, no. 4, pp. 303–322, Dec. 1968, doi: 10.1016/0022-2569(68)90006-2.

[28] R. S. Berkof and G. G. Lowen, "A New Method for Completely Force Balancing Simple Linkages," *Journal of Engineering for Industry*, vol. 91, no. 1, pp. 21–26, Feb. 1969, doi: 10.1115/1.3591524.

[29] C. Bagci, "Complete Shaking Force and Shaking Moment Balancing of Link Mechanisms Using Balancing Idler Loops," *Journal of Mechanical Design*, vol. 104, no. 2, pp. 482–493, Apr. 1982, doi: 10.1115/1.3256371.

[30] M. A. K. Zobairi, S. S. Rao, and B. Sahay, "Kineto-elastodynamic balancing of 4R-four bar mechanisms combining kinematic and dynamic stress considerations," *Mechanism and Machine Theory*, vol. 21, no. 4, pp. 307–315, Jan. 1986, doi: 10.1016/0094-114X(86)90052-2.

[31] M. A. K. Zobairi, S. S. Rao, and B. Sahay, "Kineto-elastodynamic balancing of 4R-four-bar mechanisms by internal mass redistribution," *Mechanism and Machine Theory*, vol. 21, no. 4, pp. 317–323, Jan. 1986, doi: 10.1016/0094-114X(86)90053-4.

[32] Y.-Q. Yu, "Research on complete shaking force and shaking moment balancing of spatial linkages," *Mechanism and Machine Theory*, vol. 22, no. 1, pp. 27–37, Jan. 1987, doi: 10.1016/0094-114X(87)90073-5.

[33] I. Esat and H. Bahai, "A theory of complete force and moment balancing of planer linkage mechanisms," *Mechanism and Machine Theory*, vol. 34, no. 6, pp. 903–922, Aug. 1999, doi: 10.1016/S0094-114X(98)00073-1.

[34] Niu Ming Qi and E. Pennestrí, "Optimum balancing of four-bar linkages," *Mechanism and Machine Theory*, vol. 26, no. 3, pp. 337–348, Jan. 1991, doi: 10.1016/0094-114X(91)90074-E.

[35] C. Bagci, "Complete Balancing of Linkages Using Complete Dynamical Equivalents of Floating Links: CDEL Method," presented at the ASME 1992 Design Technical Conferences, American Society of Mechanical Engineers Digital Collection, Mar. 2021, pp. 477–488. doi: 10.1115/DETC1992-0415.

[36] C. Bagci, "Complete Balancing of Multicylinder Engines Without Requiring Harmonic Balancers," presented at the ASME 1995 Design Engineering Technical Conferences collocated with the ASME 1995 15th International Computers in Engineering Conference and the ASME 1995 9th Annual Engineering Database Symposium, American Society of Mechanical Engineers Digital Collection, Mar. 2021, pp. 317–324. doi: 10.1115/DETC1995-0587.

[37] C. Bagci, "Complete Balancing of Multicylinder Engines Without Requiring Harmonic Balancers," presented at the ASME 1995 Design Engineering Technical Conferences collocated with the ASME 1995 15th International Computers in Engineering Conference and the ASME 1995 9th Annual Engineering Database Symposium, American Society of Mechanical Engineers Digital Collection, Mar. 2021, pp. 317–324. doi: 10.1115/DETC1995-0587.

[38] V. Arakelian, M. Dahan, and M. Smith, "A Historical Review of the Evolution of the Theory on Balancing of Mechanisms," in *International Symposium on History of Machines and Mechanisms Proceedings HMM 2000*, M. Ceccarelli, Ed., Dordrecht: Springer Netherlands, 2000, pp. 291–300. doi: 10.1007/978-94-015-9554-4_33.

[39] P. Nehemiah, B. S. K. Sundara Sivarao, and K. Ramji, "Complete balancing of

planar linkages," *Advances in Vibration Engineering*, vol. 12, no. 2, pp. 203–214, 2013.

[40] B. Demeulenaere and J. De Schutter, "Input Torque Balancing Using an Inverted Cam Mechanism," *Journal of Mechanical Design*, vol. 127, no. 5, pp. 887–900, Oct. 2004, doi: 10.1115/1.1876452.

[41] B. Demeulenaere, P. Spaepen, and J. De Schutter, "Input torque balancing using a cam-based centrifugal pendulum: design procedure and example," *Journal of Sound and Vibration*, vol. 283, no. 1, pp. 1–20, May 2005, doi: 10.1016/j.jsv.2004.03.029.

[42] B. Demeulenaere, P. Spaepen, and J. De Schutter, "Input torque balancing using a cam-based centrifugal pendulum: design optimization and robustness," *Journal of Sound and Vibration*, vol. 283, no. 1, pp. 21–46, May 2005, doi: 10.1016/j.jsv.2004.04.003.

[43] B. Demeulenaere *et al.*, "Experimental Validation of Input Torque Balancing Applied to Weaving Machinery," *Journal of Mechanical Design*, vol. 130, no. 022307, Jan. 2008, doi: 10.1115/1.2821386.

[44] C.-J. Wu and J. Angeles, "The optimum synthesis of an elastic torque-compensating cam mechanism," *Mechanism and Machine Theory*, vol. 36, no. 2, pp. 245–259, Feb. 2001, doi: 10.1016/S0094-114X(00)00042-2.

[45] D. M. Tsay, H. C. Ho, and K. C. Wang, "Design of Torque Balancing Cams for Globoidal Cam Indexing Mechanisms," *Journal of Mechanical Design*, vol. 124, no. 3, pp. 441–447, Aug. 2002, doi: 10.1115/1.1479690.

[46] S. Briot, I. A. Bonev, C. M. Gosselin, and V. Arakelian, "Complete shaking force and shaking moment balancing of planar parallel manipulators with prismatic pairs," *Proceedings of the Institution of Mechanical Engineers, Part K: Journal of Multi-body Dynamics*, vol. 223, no. 1, pp. 43–52, Mar. 2009, doi: 10.1243/14644193JMBD161.

[47] S. Briot, V. Arakelian, and J.-P. Le Baron, "Shaking force minimization of high-speed robots via centre of mass acceleration control," *Mechanism and Machine Theory*, vol. 57, pp. 1–12, Nov. 2012, doi: 10.1016/j.mechmachtheory.2012.06.006.

[48] V. Arakelian and S. Briot, "Simultaneous inertia force/moment balancing and torque compensation of slider-crank mechanisms," *Mechanics Research Communications*, vol. 37, no. 2, pp. 265–269, Mar. 2010, doi: 10.1016/j.mechrescom.2009.11.007.

[49] V. Arakelian, "Shaking moment cancellation of self-balanced slider–crank mechanical systems by means of optimum mass redistribution," *Mechanics Research Communications*, vol. 33, no. 6, pp. 846–850, Nov. 2006. doi:10.1016/j.mechrescom.2006.03.003.

[50] V. Arakelian, "Reduction of input torque and joint reactions in high-speed mechanical systems with reciprocating motion," *WSEAS Transactions on Applied and Theoretical Mechanics*, vol. 19, pp. 88–96, Jul. 2024. doi:10.37394/232011.2024.19.10.

[51] V. Arakelian, "Reduction of Input Torque and Joint Reactions in High-Speed Mechanical Systems with Reciprocating Motion," *WSEAS Transactions on Applied and Theoretical Mechanics*, vol. 19, pp. 88–96, Jul. 2024, doi: 10.37394/232011.2024.19.10.

[52] J. Sun and Y.-A. Yao, “An Active Gear Balancer for Torque Compensation,” *Journal of Mechanical Design*, vol. 133, no. 1, Jan. 2011, doi: 10.1115/1.4003141.
[53] K. Chaudhary and H. Chaudhary, “Optimum Balancing of Slider-crank Mechanism Using Equimomental System of Point-masses,” *Procedia Technology*, vol. 14, pp. 35–42, 2014, doi: 10.1016/j.protcy.2014.08.006.
[54] K. Chaudhary and H. Chaudhary, “Optimal dynamic balancing and shape synthesis of links in planar mechanisms,” *Mechanism and Machine Theory*, vol. 93, pp. 127–146, Nov. 2015, doi: 10.1016/j.mechmachtheory.2015.07.006.
[55] D. Groza, “Balancing of a Slider-Crank Mechanism by Using a Counter Mass and a Progressive Spring with Two Rates,” *Applied Mechanics and Materials*, vol. 823, pp. 37–42, 2016, doi: 10.4028/www.scientific.net/AMM.823.37.
[56] D. Groza and C. Antonya, “Dynamically Spring Balanced Slider-Crank Mechanism for Reciprocating Machines,” *IJME*, Accessed: Mar. 07, 2025. [Online]. Available: https://www.internationaljournalssrg.org/IJME/paper-details?Id=184
[57] L. Moussafir and V. Arakelian, “Investigation on Inertia Force Balancing and Torque Compensation of Slider-Crank Mechanisms,” *Journal of Robotics and Mechanical Engineering Research* 3(3): 1-4. doi: https://doi.org/10.24218/jrmer.2020.34.
[58] G. Etesami, M. E. Felezi, and N. Nariman-Zadeh, “Optimal transmission angle and dynamic balancing of slider-crank mechanism with joint clearance using Pareto Bi-objective Genetic Algorithm,” *Journal of the Brazilian Society of Mechanical Sciences and Engineering*, vol. 43, no. 4, 2021, doi: 10.1007/s40430-021-02834-8.
[59] J. C. Frantz, L. Mejia Rincon, H. Simas, and D. Martins, “A New Methodology for the Balancing of Mechanisms Using the Davies’ Method,” in *Multibody Mechatronic Systems*, J. C. M. Carvalho, D. Martins, R. Simoni, and H. Simas, Eds., Cham: Springer International Publishing, 2018, pp. 203–212. doi: 10.1007/978-3-319-67567-1_19.
[60] N. Levecque, J. Mahfoud, D. Violette, G. Ferraris, and R. Dufour, “Vibration reduction of a single cylinder reciprocating compressor based on multi-stage balancing,” *Mechanism and Machine Theory*, vol. 46, no. 1, pp. 1–9, Jan. 2011, doi: 10.1016/j.mechmachtheory.2010.09.004.
[61] V. Arakelian and M. Mkrtchyan, “Design of scotch yoke mechanisms with balanced input torque,” *Volume 5B: 39th Mechanisms and Robotics Conference*, Aug. 2015. doi:10.1115/detc2015-46709.
[62] S.-R. Kwon, D.-Y. Lee, U. Jeong, Y.-J. Park, and K.-J. Cho, “Development of Efficiency Enhanced Scotch Yoke Mechanism for Robotic Fish,” *International Journal of Precision Engineering and Manufacturing*, vol. 19, no. 10, pp. 1507–1513, Oct. 2018, doi: 10.1007/s12541-018-0177-x.
[63] G. J. Lee, J. Kim, and T. S. Lee, “The rolling scotch yoke mechanism applied to a small air compressor for oil-free operations,” *Int. J. Precis. Eng. Manuf.*, vol. 15, no. 1, pp. 97–103, Jan. 2014, doi: 10.1007/s12541-013-0310-9.
[64] W. Funk and J. Han, “On the Complete Balancing of the Inertia-Caused Input Torque for Plane Mechanisms,” presented at the ASME 1996 Design Engineering Technical Conferences and Computers in Engineering Conference, American Society of Mechanical Engineers Digital Collection, Feb. 2021. doi: 10.1115/96-

DETC/MECH-1570.

[65] Y.-A. Yao and H.-S. Yan, “A new method for torque balancing of planar linkages using non-circular gears,” *Proceedings of the Institution of Mechanical Engineers, Part C: Journal of Mechanical Engineering Science*, vol. 217, no. 5, pp. 495–503, May 2003, doi: 10.1243/095440603765226786.

[66] W.-B. Shieh and B.-S. Chou, “A Novel Spring Balancing Device on the Basis of a Scotch Yoke Mechanism,” *Proceedings of the 14th IFToMM World Congress*, pp. 206–212, Nov. 2015, doi: 10.6567/IFToMM.14TH.WC.OS8.004.

[67] H.-N. Nguyen and W.-B. Shieh, “Realization of Statically Balanced Articulated Mechanisms and Scotch Yoke Type Balancers,” in *Advances in Mechanism and Machine Science*, T. Uhl, Ed., Cham: Springer International Publishing, 2019, pp. 1345–1354. doi: 10.1007/978-3-030-20131-9_132.

[68] I. S. Kochev, “General theory of complete shaking moment balancing of planar linkages: a critical review,” *Mechanism and Machine Theory*, vol. 35, no. 11, pp. 1501–1514, Nov. 2000, doi: 10.1016/S0094-114X(00)00015-X.

[69] L. Ni, Y. Y. Huang, and C. K. Zhou, “The Dynamic Simulation of Engine Slider-Crank Mechanism Based on ANSYS and ADAMS,” *Advanced Materials Research*, vol. 842, pp. 347–350, 2014, doi: 10.4028/www.scientific.net/AMR.842.347.

[70] J. J. de Jong, Y. Wu, M. Carricato, and J. L. Herder, “A Pure-Inertia Method for Dynamic Balancing of Symmetric Planar Mechanisms,” in *Advances in Robot Kinematics 2018*, J. Lenarcic and V. Parenti-Castelli, Eds., Cham: Springer International Publishing, 2019, pp. 277–284. doi: 10.1007/978-3-319-93188-3_32.

[71] R. S. Berkof, “Complete force and moment balancing of inline four-bar linkages,” *Mechanism and Machine Theory*, vol. 8, no. 3, pp. 397–410, Sep. 1973, doi: 10.1016/0094-114X(73)90076-1.

[72] Liu Der Yong and Huang Zhen, “Input torque balancing of linkages,” *Mechanism and Machine Theory*, vol. 24, no. 2, pp. 99–103, Jan. 1989, doi: 10.1016/0094-114X(89)90016-5.

[73] N. Van Khang and N. Phong Dien, “Balancing conditions of spatial mechanisms,” *Mechanism and Machine Theory*, vol. 42, no. 9, pp. 1141–1152, Sep. 2007, doi: 10.1016/j.mechmachtheory.2006.08.007.

[74] H. Chaudhary and S. K. Saha, “Balancing of four-bar linkages using maximum recursive dynamic algorithm,” *Mechanism and Machine Theory*, vol. 42, no. 2, pp. 216–232, Feb. 2007, doi: 10.1016/j.mechmachtheory.2006.02.008.

[75] V. Van Der Wijk, J. L. Herder, and B. Demeulenaere, “Comparison of Various Dynamic Balancing Principles Regarding Additional Mass and Additional Inertia,” *Journal of Mechanisms and Robotics*, vol. 1, no. 4, p. 041006, Nov. 2009, doi: 10.1115/1.3211022.

[76] S. Erkaya and I˙. Uzmay, “Effects of balancing and link flexibility on dynamics of a planar mechanism having joint clearance,” *Scientia Iranica*, vol. 19, no. 3, pp. 483–490, Jun. 2012, doi: 10.1016/j.scient.2012.04.011.

[77] V. Arakelian, S. Briot, and J.-P. Le Baron, “Shaking force minimisation of slider-crank mechanisms via optimal motion control,” presented at the Conference Proceeding - 5th International Conference, TAE 2013: Trends in Agricultural

Engineering 2013, 2013, pp. 67–71.
[78] G. Destradi, “Generation of Optimized Rotation of Counterweights from Balancing Device for Slider-Crank Mechanisms,” *SAE Technical Papers*, vol. 2019-January, no. January, 2019, doi: 10.4271/2019-01-5020.
[79] V. Arakelian, “Design of Torque-Compensated Mechanical Systems With Two Connected Identical Slider-Crank Mechanisms,” *Journal of Mechanisms and Robotics*, vol. 14, no. 024503, Sep. 2021, doi: 10.1115/1.4052320.
[80] J. Buśkiewicz, “Kinematic synthesis of the mechanism for static balancing of an input torque in three positions,” *Archive of Mechanical Engineering*, pp. 571–594, Sep. 2022, doi: 10.24425/ame.2022.143095.
[81] A. M. Albaghdadi, M. B. Baharom, and S. A. Sualiman, “Balancing and Simulation of a Double Crank-Rocker Engine Model for Optimum Reduction of Shaking Forces and Shaking Moments | IIETA.” Accessed: Mar. 08, 2025. [Online]. Available: https://www.iieta.org/journals/mmep/paper/10.18280/mmep.080210.
[82] S. S. Bajiya, K. Chaudhary, and H. Chaudhary, “A Review on Dynamic Balancing and Link Shape Synthesis of Planar Mechanisms,” in *Mechanism and Machine Science*, D. Sen, S. Mohan, and G. K. Ananthasuresh, Eds., Singapore: Springer, 2021, pp. 87–106. doi: 10.1007/978-981-15-4477-4_7.
[83] W. Fiebig and W. Prastiyo, “Utilization of Mechanical Resonance for the Enhancement of Slider-Crank Mechanism Dynamics in Gas Compression Processes,” *Energies*, vol. 15, no. 20, p. 7769, Oct. 2022, doi: 10.3390/en15207769.
[84] J. Sun and Y. Yao, “Integrated Design of an Active Torque Balancing Mechanism and a Planetary Gear Reducer,” *JSDD*, vol. 4, no. 3, pp. 391–405, 2010, doi: 10.1299/jsdd.4.391.
[85] K. Chaudhary and H. Chaudhary, “Optimal design of planar slider-crank mechanism using teaching-learning-based optimization algorithm,” *J Mech Sci Technol*, vol. 29, no. 12, pp. 5189–5198, Dec. 2015, doi: 10.1007/s12206-015-1119-5.
[86] M. M. Ettefagh, F. Abbasidoust, H. Milanchian, and M. Y. Asr, “Complex crank-slider mechanism dynamic balancing by Binary Genetic Algorithm(BGA),” in *2011 International Symposium on Innovations in Intelligent Systems and Applications*, Jun. 2011, pp. 277–281. doi: 10.1109/INISTA.2011.5946075.
[87] W. Prastiyo and W. Fiebig, “Balancing of slider-crank and Scotch-yoke mechanisms by the use of mechanical resonance: Simulation and experiment,” *Simulation Modelling Practice and Theory*, vol. 142, p. 103137, July 2025, doi: 10.1016/j.simpat.2025.103137.
[88] W. Fiebig and J. Wróbel, “Energy accumulation in mechanical resonance and its use in drive systems of impact machines,” *Archiv.Civ.Mech.Eng*, vol. 20, no. 1, p. 30, Mar. 2020, doi: 10.1007/s43452-020-00036-y.
[89] M. Aiple, J. Smisek, and A. Schiele, “Increasing Impact by Mechanical Resonance for Teleoperated Hammering,” *IEEE Transactions on Haptics*, vol. 12, no. 2, pp. 154–165, Apr. 2019, doi: 10.1109/TOH.2018.2882401.
[90] W. Fiebig, “Accumulation of the Energy in Mechanical Resonance,” in *Dynamical Systems in Applications*, J. Awrejcewicz, Ed., Cham: Springer International Publishing, 2018, pp. 115–124. doi: 10.1007/978-3-319-96601-4_11.

[91] Y. Zhang, C. Peng, and Y. D. Wang, "Study on a Kind of Active Balancer Using Planetary Gear Train," *Applied Mechanics and Materials*, vol. 701–702, pp. 761–768, 2015, doi: 10.4028/www.scientific.net/AMM.701-702.761.

[92] D. J. Inman and R. C. Singh, *Engineering vibration*, 4. ed., Internat. ed. in Always Learning. Boston, Mass. München: Pearson, 2014.

[93] W. J. Palm, *Mechanical vibration*. Hoboken, NJ: John Wiley, 2007.

[94] D. García-Violini, N. Faedo, Y. Peña-Sanchez, V. Nava, and J. V. Ringwood, "Revisiting excitation force estimation in WECs: On the (mis)use of structure-based estimation approaches," *Ocean Engineering*, vol. 311, p. 118864, Nov. 2024, doi: 10.1016/j.oceaneng.2024.118864.

[95] C. Cerini, V. Yotov, and G. S. Aglietti, "Structural system modelling from base excitation measurements using swarm intelligence," *Mechanical Systems and Signal Processing*, vol. 209, p. 111084, Mar. 2024, doi: 10.1016/j.ymssp.2023.111084.

[96] C. Shi, Y. Ma, X. Chen, Z. Song, and J. Hong, "Research on coupled angular-torsional vibration of unbalanced rotor," *Mechanical Systems and Signal Processing*, vol. 234, p. 112808, Jul. 2025, doi: 10.1016/j.ymssp.2025.112808.

[97] J. McConville and J. McGrath, *Introduction to ADAMS Theory*, vol. MDI-073190. Mechanical Dynamics, Inc., 1998.

[98] F. Schwarzfischer, B. Corves, and M. Hüsing, "The Dynamic Synthesis of an Energy-Efficient Slider-Crank-Mechanism," 2017. Accessed: Mar. 25, 2025. [Online]. Available: https://www.semanticscholar.org/paper/The-Dynamic-Synthesis-of-an-Energy-Efficient-Schwarzfischer-Corves/394e282f11f751af96938cb4dbf9056873ffda5e

[99] J. Krivošej, P. Beneš, J. Zavřel, A. Balon, V. Halamka, and Z. Šika, "Energy efficient robots based on structures with tensegrity features and cable-driven mechanisms," *Mechanism and Machine Theory*, vol. 187, p. 105364, Sep. 2023, doi: 10.1016/j.mechmachtheory.2023.105364.

[100] V. Arakelian, "Gravity compensation in robotics," *Advanced Robotics*, vol. 30, no. 2, pp. 79–96, Jan. 2016, doi: 10.1080/01691864.2015.1090334.

[101] D. G. Chung, M. Hwang, J. Won, and D.-S. Kwon, "Gravity compensation mechanism for roll-pitch rotation of a robotic arm," in *2016 IEEE/RSJ International Conference on Intelligent Robots and Systems (IROS)*, IEEE, Oct. 2016, pp. 338–343. doi: 10.1109/IROS.2016.7759076.

[102] C. Gosselin, "Gravity Compensation, Static Balancing and Dynamic Balancing of Parallel Mechanisms," in *Smart Devices and Machines for Advanced Manufacturing*, L. Wang and J. Xi, Eds., London: Springer, 2008, pp. 27–48. doi: 10.1007/978-1-84800-147-3_2.

[103] C.-H. Hsu, Y.-H. Lin, C.-S. Jhuang, and D.-Z. Chen, "Spring Perfectly Statically Balanced 1-DOF Mechanisms Using Slider-Crank," in *Advances in Mechanism and Machine Science*, M. Okada, Ed., Cham: Springer Nature Switzerland, 2023, pp. 429–437. doi: 10.1007/978-3-031-45770-8_43.

[104] H.-C. Hsieh, L. Chien, and C.-C. Lan, "Mechanical design of a gravity-balancing wearable exoskeleton for the motion enhancement of human upper limb," in *2015 IEEE International Conference on Robotics and Automation (ICRA)*, May 2015, pp. 4992–4997. doi: 10.1109/ICRA.2015.7139893.

[105] H.-N. Nguyen and W.-B. Shieh, “On the design of the gravity balancer using Scotch yoke derivative mechanism,” *New Advances in Mechanism and Machine Science*, pp. 13–25, 2018. doi:10.1007/978-3-319-79111-1_2.
[106] V. Arakelyan and Y. Zhang, “Improvement of the Balancing Accuracy in Gravity Compensators Based on the Inverted Slider Crank Mechanism,” presented at the ASME 2018 International Design Engineering Technical Conferences and Computers and Information in Engineering Conference, American Society of Mechanical Engineers Digital Collection, Nov. 2018. doi: 10.1115/DETC2018-85361.
[107] X. Zeng and C.-H. Kuo, “On the Effectiveness and Optimal Performance of Gravity Compensation Design of an Inverted Slider-Crank Mechanism Using Realistic Springs,” presented at the ASME 2022 International Design Engineering Technical Conferences and Computers and Information in Engineering Conference, American Society of Mechanical Engineers Digital Collection, Nov. 2022. doi: 10.1115/DETC2022-89695.
[108] V. Arakelian and Y. Zhang, “An Improved Design of Gravity Compensators Based on the Inverted Slider-Crank Mechanism,” *Journal of Mechanisms and Robotics*, vol. 11, no. 034501, Apr. 2019, doi: 10.1115/1.4043049.
[109] R. S. Haines, “Minimum RMS shaking moment or driving torque of a force-balanced 4-bar linkage using feasible counterweights,” *Mechanism and Machine Theory*, vol. 16, no. 3, pp. 185–195, Jan. 1981, doi: 10.1016/0094-114X(81)90034-3.
[110] D. Chablat, S. Venkateswaran, and F. Boyer, “Mechanical Design Optimization of a Piping Inspection Robot,” *Procedia CIRP*, vol. 70, pp. 307–312, 2018, doi: 10.1016/j.procir.2018.02.015.
[111] Z. X. He and Q. T. Liu, “Synthetical Dynamic Balancing of Mechanism Based on Optimization Simulation,” *Advanced Materials Research*, vol. 774–776, pp. 35–38, 2013, doi: 10.4028/www.scientific.net/AMR.774-776.35.
[112] L. Marino, A. Cicirello, and D. A. Hills, “Displacement transmissibility of a Coulomb friction oscillator subject to joined base-wall motion,” *Nonlinear Dyn*, vol. 98, no. 4, pp. 2595–2612, Dec. 2019, doi: 10.1007/s11071-019-04983-x.
[113] T. Guilan, F. Haibo, and Z. Weiyi, “A New Method of Torque Compensation for High Speed Indexing Cam Mechanism,” *Journal of Mechanical Design*, vol. 121, no. 2, pp. 319–323, Jun. 1999, doi: 10.1115/1.2829462.
[114] Nango J., Yoshizawa T., Kato T., and Koguchi T., “Static analysis of constraint conditions of a rotational-to-linear motion conversion mechanism,” *Transactions of the JSME (in Japanese)*, vol. 87, no. 899, pp. 20-00391-20–00391, 2021, doi: 10.1299/transjsme.20-00391.
[115] V. Arakelian, “Shaking Force Balancing of Mechanisms: An Overview,” *World Academy of Science, Engineering and Technology, International Journal of Mechanical and Mechatronics Engineering*, vol. 15, no. 6, pp. 263 – 266, 2021.
[116] S. Briot, V. Arakelian, N. Sauvestre, and J.-P. Le Baron, “Shaking Forces Minimization of High-Speed Robots via an Optimal Motion Planning,” in *ROMANSY 18 Robot Design, Dynamics and Control*, vol. 524, V. Parenti Castelli and W. Schiehlen, Eds., in CISM International Centre for Mechanical Sciences, vol. 524. , Vienna: Springer Vienna, 2010, pp. 307–314. doi: 10.1007/978-3-7091-0277-0_36.

[117] S. Briot, V. Arakelian, and J.-P. Le Baron, “Shaking Force Minimization of High-Speed Robots via Optimal Trajectory Planning,” in *Advances in Mechanisms Design*, J. Beran, M. Bílek, M. Hejnova, and P. Zabka, Eds., Dordrecht: Springer Netherlands, 2012, pp. 159–166. doi: 10.1007/978-94-007-5125-5_21.

[118] R. Yuan, Y. Sun, W. H. Fan, K. Wu, and Z. J. Chen, “Research on Balancing Method for Inertia Force of Slider-Crank Mechanism with Small Linkage Ratio,” *Advanced Materials Research*, vol. 591–593, pp. 2011–2015, 2012, doi: 10.4028/www.scientific.net/AMR.591-593.2011.

[119] V. Arakelian, “Shaking Force and Shaking Moment Balancing in Robotics: A Critical Review,” in *Advances on Theory and Practice of Robots and Manipulators*, M. Ceccarelli and V. A. Glazunov, Eds., Cham: Springer International Publishing, 2014, pp. 149–157. doi: 10.1007/978-3-319-07058-2_17.

[120] A. A. Shabana, *Dynamics of Multibody Systems*, 4th ed. Cambridge, UK: Cambridge University Press, 2013.

[121] MSC Software Corporation, *Adams View User’s Guide*. Hexagon, 2020.

[122] A. V. Kotov, “Analysis of the balance of the crank-slider drive mechanism of the cutting apparatus by the method of principal point vectors,” *Tractors and Agricultural Machinery*, vol. 91, no. 2, Art. no. 2, Jul. 2024, doi: 10.17816/0321-4443-606653.

[123] I. S. Okoro and C. O. Enwerem, “Robust control of a DC motor,” *Heliyon*, vol. 6, no. 12, p. e05777, Dec. 2020, doi: 10.1016/j.heliyon.2020.e05777.

[124] V. Arakelian and N. Makhsudyan, “Generalized Lanchester balancer,” *Mechanics Research Communications*, vol. 37, no. 7, pp. 647–649, Oct. 2010, doi: 10.1016/j.mechrescom.2010.08.003.

[125] B. F. Yin, J. G. He, Y. Xu, and Y. Q. Li, “The Novel Design of Full-Balancing Mechanism for Single-Cylinder Diesel Engine,” *Applied Mechanics and Materials*, vol. 37–38, pp. 1520–1524, 2010, doi: 10.4028/www.scientific.net/AMM.37-38.1520.

[126] V. van der Wijk and J. L. Herder, “Dynamic Balancing of a Single Crank-Double Slider Mechanism with Symmetrically Moving Couplers,” in *New Trends in Mechanism Science*, D. Pisla, M. Ceccarelli, M. Husty, and B. Corves, Eds., Dordrecht: Springer Netherlands, 2010, pp. 413–420. doi: 10.1007/978-90-481-9689-0_48.

[127] W. Fiebig and W. Prastiyo, “An innovative method of utilization of mechanical resonance for the reduction of dynamical loads in the reciprocating compressors,” presented at the Proceedings of the International Congress on Sound and Vibration, 2023.

[128] C. Kubik, J. Hohmann, and P. Groche, “Exploitation of force displacement curves in blanking—feature engineering beyond defect detection,” The International Journal of Advanced Manufacturing Technology, vol. 113, no. 1–2, pp. 261–278, Jan. 2021. doi:10.1007/s00170-020-06450-z

[129] S. H. Lee, H. J. Lee, K. H. Lee, K. T. Nam, and J. C. Koo, “A novel variable stiffness scotch yoke series elastic actuator for enhanced functional stiffness,” *Microsystem Technologies*, vol. 26, no. 11, pp. 3395–3402, Nov. 2020, doi: 10.1007/s00542-020-04893-8.